PtSnCo/C Nanoparticle Catalysts for Ethanol Electro-oxidation Reaction in an Acidic Medium



Aniwat Pengsawang

Merton College

Hilary Term 2018

A Thesis submitted to the Board of the Mathematical, Physical and Life Sciences Division

for the Degree of Doctor of Philosophy, University of Oxford

Abstract

Title: PtSnCo/C Nanoparticle Catalysts for Ethanol Electro-oxidation Reaction in an Acidic Medium

Student: Aniwat Pengsawang, Merton College, University of Oxford

Supervisor: Prof. S.C. Edman Tsang

Binary PtSn/C and ternary PtSnCo/C catalysts with the nominal Pt:Sn and Pt:Sn:Co atomic ratios of 3:1, 3:1:1, 3:1:2, 3:1:3, and 3:1:4 were synthesised by the modified sodium borohydride reduction method. All the as-synthesised catalysts were characterized by a number of analytical techniques including EDS, ICP-MS, TGA, XRD, TEM, BF-STEM, XPS, and XAS. The electrocatalytic activity towards alcohol electro-oxidation was measured using cyclic voltammetry (CV) and chronoamperometry (CA). Prior to each CV measurement for an activity test, a catalyst-modified glassy carbon electrode was potential cycled in 0.5M H_2SO_4 supporting electrolyte between -0.2 V and 1.0 V (vs. SCE) for 20 cycles to obtain a stable catalyst surface. The results from electrocatalytic activity tests showed that the electrochemically treated PtSnCo/C catalysts of all atomic ratios exhibited higher ethanol electro-oxidation activity than the PtSn/C (3:1) catalyst synthesised by the same preparation method. Moreover, they exhibited higher electro-oxidation activity for ethylene glycol (EG), 2-propanol (2P), and methanol (MeOH) compared to PtSn/C (3:1). These results can lead to the conclusions that carbon supported ternary PtSnCo nanoparticle catalysts would be a candidate for application in direct alcohol fuel cells as anode electrocatalysts.

Acknowledgement

First of all, I would like to express my gratitude to my parents who have always been physically and mentally supporting me throughout the time of my DPhil study. I would like to thank my supervisor, Professor Edman Tsang, for his time and invaluable pieces of advice given to me since I started my DPhil study. His encouragements to get me through some difficulties I have encountered in research over the past few years are greatly appreciated. I would like to gratefully thank Dr. K. Tedsree, Dr. P. Luksirikul, Dr. A. Kolpin, Dr. Feng Xu, Dr. P. Khemthong, and Dr. K. Faungnawakij for their advice and discussions. Also, I would like to acknowledge Miss Panita Kasamechonchung and Dr. Teera Butburee from National Nanotechnology Center (NANOTEC), Thailand, for ICP-MS analysis and STEM images with EDS elemental mapping, respectively, Dr. Molly Li for EXAFS and XANES spectra fitting and data interpretation, and a staff from the surface facility team, department of chemistry, University of Oxford, for the XPS measurements. To my friends and my colleagues, especially May, Wow, Ple, Noo, Un, Aam, N'Kwang, N'Golf, N'Aim, P'Nim, and P'Duang, I am appreciably thankful for your help and support. I am so blessed to have all of you in my life. Last but not least, I would like to thank everyone in Oxford with whom I have met and shared good memories throughout my time here. Finally, I would like to gratefully acknowledge the financial support from the Royal Thai Government, NANOTEC, and Merton College. This thesis would not have been completed without support and encouragement from all the people mentioned above.

Aniwat Pengsawang

Table of Contents

	Page
Abstract	I
Acknowledgement	II
Chapter 1	
-Introduction and Literature Reviews	1
Chapter 2	
-Experimental Theory and Techniques	36
Chapter 3	
-Synthesis and Characterisation	74
Chapter 4	
-Ethanol Electro-oxidation Reaction (EOR) on the PtSn/C and PtSnCo/C Electrodes	126
Chapter 5	
-Electrocatalytic Activities of the PtSnCo/C Nanoparticle Catalysts for Ethylene Glycol (EG), 2-Propanol (2P), and Methanol (MeOH) Oxidation in 0.5M H_2SO_4 Medium	169
Chapter 6	
-Conclusions	203
Chapter 7	
-Experiments	206

List of Tables

	Page
Table 1.1- Summary of a number of electrons released from the complete oxidation of alcohols (n), standard potentials of DAFCs (E^0) at 25 ^oC, theoretical mass energy density (W_s), theoretical volume energy density (W_e), capacity of pure compound (C), and theoretical energy conversion efficiency for alcohol oxidation in a DAFC (η)	11
Table 3.1- A number of moles of Pt(IV), Sn(II), and Co(II) in EG solution for the catalysts preparation	78
Table 3.2 - Bulk compositions of PtSn/C (3:1) and all PtSnCo/C (3:1:1 to 3:1:4)	79
Table 3.3 - Total metal loadings and bulk chemical compositions of the as-prepared catalysts	83
Table 3.4 - Summary of percentages of weight loss in different temperature ranges for the as-prepared PtSn/C (3:1) and PtSnCo/C (3:1:1 to 3:1:4) catalysts	85
Table 3.5 – Summary of the total weight of residues and the temperature for complete oxidation of the carbon support	87
Table 3.6 - Lattice parameters of the fcc structure of Pt and the average crystallite sizes of the carbon supported Pt, PtSn (3:1), and all PtSnCo (3:1:1 to 3:1:4) nanoparticle catalysts	91
Table 3.7 – Summary of the calculated lattice parameters of all the PtSnCo/C catalysts	94
Table 3.8 - XRD analysis of PtSn/C (3:1) and PtSnCo/C (3:1:1 to 3:1:4)	97
Table 3.9 - XPS analysis of the deconvoluted Pt $4f_{7/2}$ peaks of the Pt/C and carbon supported Pt-based electrocatalysts	103
Table 3.10 – Sn $3d_{5/2}$ binding energies of the PtSn/C (3:1) and all PtSnCo/C (3:1:1 to 3:1:4) electrocatalysts	106
Table 3.11 - Co $2p_{3/2}$ binding energies of all PtSnCo/C electrocatalysts	108
Table 3.12 - Co $2p_{3/2}$ binding energies (eV) of different cobalt species	109

Table 3.13- Surface compositions of the PtSn/C (3:1) and all PtSnCo/C catalysts 109

Table 3.14 – Comparison of the bulk and surface Pt/Sn and Pt/Co ratios 110

Table 3.15 - BF-STEM images and EDS elemental maps 112

Table 3.16 - EXAFS fitting results of all the as-prepared and thermally treated PtCo/C (3:1) and PtSnCo/C catalysts 120

Table 4.1 - Summary of the hydrogen desorption charge (Q_H), Pt-EASA, and roughness of the stable catalyst surfaces 136

Table 4.2 - Summary of surface Pt oxidation and Pt-O reduction potentials 137

Table 4.3 - Summary of the ethanol electro-oxidation activities of the Pt/C, PtSn/C (3:1) and all PtSnCo/C catalysts 143

Table 5.1 - Summary of the EG electro-oxidation activities of the PtSn/C (3:1) and all PtSnCo/C catalysts 178

Table 5.2 - Summary of the 2P electro-oxidation activities of the PtSn/C (3:1) and PtSnCo/C catalysts 185

Table 5.3 - Summary of the MeOH electro-oxidation activities of the PtSn/C (3:1) and PtSnCo/C catalysts 193

Table 7.1 - A number of moles of Pt(IV), Sn(II), and Co(II) in EG solution for catalysts preparation 208

List of Figures

	Page
Figure 1.1 Schematic diagram of the reaction mechanism of EOR on the PtSnM/C (M=Ni, Co, Rh, Pd) electrodes	6
Figure 1.2 - Schematic illustration of electricity generation in a DEFC	12
Figure 1.3 - Synthesis of metal nanoparticles	13
Figure 1.4 - Proposed reaction mechanisms of acetaldehyde electro-oxidation on the PtSn/C and tri-metallic PtSnM/C (M = Ni, Co, Rh, Pd) electrodes	26
Figure 2.1 - Three-electrode electrochemical cell with standard calomel electrode (SCE) as RE, a modified glassy carbon electrode (modified GCE) as WE, and a Pt wire as CE	37
Figure 2.2- Schematic illustration of the processes in solution phase electrochemical reactions	42
Figure 2.3- Diffusion process	43
Figure 2.4 - Potential step chronoamperometry measurement	45
Figure 2.5- Current response over time in a potential step chronoamperometry experiment	46
Figure 2.6 - Variation of the applied potential as a function of time in a cyclic voltammetry experiment	48
Figure 2.7 - Cyclic voltammogram for a reversible electron transfer reaction	50
Figure 2.8 - Cyclic voltammogram of an irreversible electron transfer reaction	53
Figure 2.9 - Cyclic voltammograms for (a) a reversible, (b) a quasi-reversible, and (c) an irreversible electron transfer reaction	56
Figure 2.10 - Cyclic voltammogram for the reversible reaction of adsorbed species	59

Figure 2.11- Mettler Toledo TGA/DSC 1 [18] (A) and schematic diagram of Mettler Toledo TGA/DSC 1 [36] (B) 61

Figure 2.12 - Diagram of a modern X-ray tube 63

Figure 2.13- Bremsstrahlung X-ray generation 63
Figure 2.14 - (a) Lattice planes and (b) Bragg's law 64

Figure 2.15 - Powder X-ray diffraction pattern of amylamine stabilised Pt nanoparticles 66

Figure 2.16 - Schematic diagram of X-ray generation in EDS 66

Figure 2.17- Schematic diagram of an X-ray photoelectron spectrometer 69

Figure 2.18 - Diagram of typical TEM working 71

Figure 3.1- EDS spectra of the PtSn/C (3:1) (a) and PtSnCo/C (3:1:1) (b) catalysts 80

Figure 3.2-EDS spectra of the PtSnCo/C (3:1:2) (c) and PtSnCo/C (3:1:3) (d) catalysts 81

Figure 3.3-EDS spectrum of the PtSnCo/C (3:1:4) catalyst 82

Figure 3.4 –TGA profiles of the as-prepared PtSn/C (3:1) and all PtSnCo/C catalysts 84

Figure 3.5 - XRD pattern of the Pt/C catalyst with the nominal Pt loading of 20 wt.% 88

Figure 3.6 - XRD patterns of the Pt/C, PtSn/C (3:1), and PtSnCo/C (3:1:1 to 3:1:4) catalysts 90

Figure 3.7- Proposed structure of the PtSn (3:1) nanoparticles based on the XRD and XPS results 96

Figure 3.8- Plot of the fcc lattice parameters versus the bulk Co content (atomic %) obtained from the EDS measurements 96

Figure 3.9 – TEM images and the histogram of particle size distribution for the PtSn/C (3:1) catalyst 98

Figure 3.10 – TEM images and particle size distribution histograms of the PtSnCo/C (3:1:2) (left) and PtSnCo/C (3:1:4) (right) 99

Figure 3.11 - XPS spectra of the Pt 4f region of the Pt/C (A), PtSn/C (3:1) (B), PtSnCo/C (3:1:1 and 3:1:2) (C-D) electrocatalyst 101

Figure 3.12 - XPS spectra of the Pt 4f region of the PtSnCo/C (3:1:3 and 3:1:4) (E-F) electrocatalysts 102

Figure 3.13 - XPS spectra of the Sn 3d region of the PtSn/C (3:1) (A), PtSnCo/C (3:1:1 to 3:1:4) (B-E) electrocatalysts 106

Figure 3.14 - XPS spectra of Co 2p region of the PtSnCo/C (3:1:1 to 3:1:4) (A-D) electrocatalysts 107

Figure 3.15 -Transitions of three different types of photoelectrons upon absorption of an X-ray quantum 114

Figure 3.16 – Co K-edge XANES spectra of the standard Co foil and all the as-prepared PtSnCo/C catalysts obtained from XAS measurements at room temperature 115

Figure 3.17 – Co K-edge XANES spectra of the PtSnCo/C samples thermally treated at 400 ^{o}C for 2 hours in a H_2 atmosphere at a flow rate of 15 mL/min. 116

Figure 3.18 – Fourier transformed (FT) EXAFS profiles for all the as-prepared PtCo/C (3:1) and PtSnCo/C catalysts 117

Figure 3.19 – FT-EXAFS profiles for all the thermally treated PtCo/C (3:1) and PtSnCo/C catalysts 118

Figure 4.1 - Schematic diagram of the proposed reaction pathways of ethanol electro-oxidation on polycrystalline Pt catalysts in acidic media 126

Figure 4.2 – Summary of the reaction mechanisms of ethanol oxidation on the Pt electrodes 128

Figure 4.3 - Cyclic voltammograms of the Pt/C (A) and PtSn/C (3:1) (B) electrodes recorded in 0.5M H_2SO_4 supporting electrolyte solution at a scan rate of 50 mV/s with an inset showing H desorption charge 130

Figure 4.4 - Cyclic voltammograms of all the investigated PtSnCo/C electrodes recorded in 0.5M H_2SO_4 supporting electrolyte solution at a scan rate of 50 mV/s 133

Figure 4.5 - The Pourbaix diagram for the cobalt-water system 134

Figure 4.6 - Steady-state cyclic voltammograms (cycle 20) of the Pt/C, PtSn/C (3:1) and all PtSnCo/C electrodes recorded in N_2-purged 0.5M H_2SO_4 supporting electrolyte solution at a scan rate of 50 mV/s. 135

Figure 4.7 - Cyclic voltammograms exhibiting the ethanol electro-oxidation activities of the Pt/C, PtSn/C (3:1) and all PtSnCo/C catalysts. CV conditions: 0.5M H_2SO_4 + 1M EtOH electrolyte solution, potential range from -0.2 to 1.0 V (vs. SCE), and a scan rate of 50 mV/s. (A) full voltammograms (B) forward scans (C) reverse scans 139

Figure 4.8 - Cyclic voltammetric profiles of ethanol electro-oxidation on the investigated Pt/C, PtSn/C (3:1) and all PtSnCo/C electrodes. CV conditions: 0.5M H_2SO_4 + 1M EtOH electrolyte solution, potential range from -0.2 to 1.0 V (vs. SCE), and a scan rate of 50 mV/s. 141

Figure 4.9 - Ethanol electro-oxidation activities of the Pt/C, PtSn/C (3:1) and all PtSnCo/C catalysts at 0.3 V and 0.6 V (data taken from the first cyclic voltammograms recorded in N_2-purged 0.5M H_2SO_4 + 1M EtOH solution at room temperature after electrochemical treatment of each electrode between -0.2 V and 1.0 V (vs. SCE) for 20 cycles in N_2-purged 0.5M H_2SO_4 supporting electrolyte solution) 142

Figure 4.10 - Ethanol electro-oxidation activities of the Pt/C, PtSn/C (3:1), PtSnCo/C (3:1:3), and PtSnCo/C (3:1:4) catalysts at 0.3 V and 0.6 V (vs. SCE) 145

Figure 4.11 - Plots showing relationships of the bulk Co/Pt atomic ratio to the oxidation current density for ethanol electro-oxidation at 0.6 V (vs. SCE) and Pt0 4f7/2 core-level binding energy 147

Figure 4.12 - j-t plots for the ethanol electro-oxidation on the PtSn/C and all PtSnCo/C electrocatalysts recorded in 0.5M H_2SO_4 + 1M EtOH solution at 0.6V (vs. SCE) for 500 s after electrochemical treatment in 0.5M H_2SO_4 supporting electrolyte solution 149

Figure 4.13- CO stripping voltammogram of the PtSn/C (3:1) electrode 151

Figure 4.14 - CO stripping voltammograms of all the PtSnCo/C electrodes 152

Figure 4.15 - Comparison of the CO stripping voltammograms of the PtSn/C (3:1) and Pt/C electrodes 153

Figure 4.16 - Comparison of the CO stripping voltammograms of the investigated electrodes 154

Figure 4.17 - Cyclic voltammograms for acetaldehyde electro-oxidation on the PtSn/C (3:1) and all PtSnCo/C electrocatalysts recorded in 0.5M H_2SO_4+0.5M AAL with a scan rate of 50 mV/s 158

Figure 4.18 - Forward scans of the acetaldehyde electro-oxidation reaction on the stable surfaces of the PtSn/C (3:1) and all PtSnCo/C electrocatalysts 159

Figure 4.19 - Ethanol, acetaldehyde (AAL), and acetic acid (AA) electro-oxidation activity of the PtSn/C (3:1) electrode measured by CV in 1.0M EtOH+0.5M H_2SO_4, 0.5M AAL+0.5M H_2SO_4, and 0.5M AA+0.5M H_2SO_4 electrolyte solutions with a scan rate of 50 mV/s 161

Figure 4.20 - Ethanol, AAL, and AA electro-oxidation activities of all the PtSnCo/C electrodes 163

Figure 5.1 - Schematic diagrams for the electro-oxidation reaction of ethylene glycol on the Pt catalysts in acidic media. (I) denotes the dissolved species. 172

Figure 5.2 - Proposed mechanism of 2-propanol electro-oxidation on the Pt single crystal electrodes 174

Figure 5.3 - Cyclic voltammograms (cycle 1) recorded with the PtSn/C (3:1) and all PtSnCo/C electrodes in 0.5M H_2SO_4 + 1M EG electrolyte solution at a scan rate of 50 mV/s. 176

Figure 5.4 - Forward scan (A) and reverse scan (B) voltammograms exhibiting the EG electro-oxidation activities of the PtSn/C (3:1) and all PtSnCo/C catalysts. CV conditions: 0.5M H_2SO_4 + 1M EG electrolyte solution and a scan rate of 50 mV/s. 177

Figure 5.5 - EG electro-oxidation activities of the PtSn/C (3:1) and all PtSnCo/C catalysts at 0.5 V (data were taken from the first cyclic voltammograms recorded in 0.5M H_2SO_4 + 1M EG solution after electrochemical treatment of each electrode in 0.5M H_2SO_4 for 20 cycles between -0.2 V and 1.0 V (vs. SCE)) 181

Figure 5.6 - Plots of the Pt0 4f7/2 core-level binding energies and oxidation current densities at 0.5 V as a function of the bulk Co/Pt atomic ratio 182

Figure 5.7 - 2P electro-oxidation activities of the PtSn/C (3:1) and all PtSnCo/C catalysts. (A) cycle 1, (B) forward scan, and (C) reverse scan cyclic voltammograms. CV conditions: 0.5M H_2SO_4 + 1M 2P electrolyte solution, a potential range from -0.2 to 1.0 V (vs. SCE), and a scan rate of 50 mV/s 186

Figure 5.8 - Summary of 2-propanol electro-oxidation pathways on Pt and Pt-based electrocatalysts based on the findings of S.G. Sun et al., J. Otomo et al., and E.Pastor et al. 188

Figure 5.9 - 2-propanol electro-oxidation activities of the PtSn/C (3:1) and all PtSnCo/C catalysts at 0.3 V (vs. SCE) 189

Figure 5.10 - Plots of the Pt0 4f7/2 core-level binding energies and oxidation current densities at 0.3 V as a function of the bulk Co/Pt atomic ratio 190

Figure 5.11 - Cyclic voltammograms (cycle 1) exhibiting the MeOH electro-oxidation activities of the PtSn/C (3:1) and all PtSnCo/C catalysts (A) forward scan voltammograms (B) reverse scan voltammograms (C). CV conditions: 0.5M H_2SO_4 + 1M MeOH solution and a scan rate of 50 mV/s 192

Figure 5.12 - Methanol electro-oxidation activities of the PtSn/C (3:1) and all PtSnCo/C catalysts at 0.5 V (vs. SCE) 196

List of Standard Subscripts for Theory in Electrochemistry Section

a	anodic
c	cathodic
f	forward
b	backward
O	relating to species O in $O + ne^- \rightleftharpoons R$
R	relating to species R in $O + ne^- \rightleftharpoons R$
ad	referred to an adsorbed species

List of Symbols for Theory in Electrochemistry Section

Symbol	Meaning	Unit	Section Reference
$\Delta\phi_{m/s}$	potential difference at the electrode/solution interface	V	2.1
ϕ_m	electrical potential at an electrode	V	2.1
ϕ_s	electrical potential of a solution	V	2.1
ϕ_{ref}	electrical potential at a reference electrode	V	2.1
i	current	A	2.1, 2.3
R	(a) electrical resistance of a solution (b) universal gas constant	Ω 8.314 J mol^{-1} K^{-1}	2.1 2.2, 2.8, 2.9, 2.10
T	absolute temperature	K	2.2, 2.8, 2.9, 2.10
E	(a) applied potential (b) potential of a half-reaction (c) potential of a redox couple	V	2.1 2.2 2.8
E_e	equilibrium potential of an electrode	V	2.1
E^0	(a) standard potential of an electrode (b) standard potential of a redox couple	V	2.2, 2.10 2.8
n	number of electrons transferred per mole of a reactant		2.1, 2.2, 2.3, 2.5, 2.8, 2.10
F	Faraday's constant	96485 C mol^{-1}	2.1, 2.2, 2.3, 2.5, 2.8, 2.9, 2.10
A	(a) electrode area	cm^2	2.1, 2.5, 2.8, 2.9, 2.10

	(b) fixed electrode area		2.3
j	flux of an electroactive species reaching the electrode surface	mol cm^{-2} s^{-1}	2.1
k	(a) heterogeneous rate constant of the electron transfer reaction (b) rate constant	cm s^{-1}	2.1 2.2, 2.3, 2.9
k_0	standard rate constant	cm s^{-1}	2.2, 2.10
α	charge transfer coefficient		2.2, 2.9, 2.10
I	total current	A	2.2
$[j]_{x=0}$	concentration of species j at the electrode surface	mol cm^{-3}	2.2, 2.3
i_0	exchange current	A	2.2
K	equilibrium constant of a reaction		2.2
t	time	s	2.5
D	diffusion coefficient of a reactant, analyte, or electroactive species	cm^2 s^{-1}	2.5, 2.8, 2.9, 2.10
C	concentration of a reactant in bulk solution	mol cm^{-3}	2.5, 2.8, 2.9, 2.10
i_p	peak current	A	2.8
v	potential scan rate	V s^{-1}	2.8, 2.9, 2.10
$C_j(x,t)$	concentration of species j at distance x at time t	mol cm^{-3}	2.9, 2.10
$C_j(0,t)$	concentration of species j at the electrode surface at time t	mol cm^{-3}	2.9, 2.10
$E_{p/2}$	potential where $i = i_p/2$	V	2.9
E(t)	potential of an electrode at time t	V	2.10

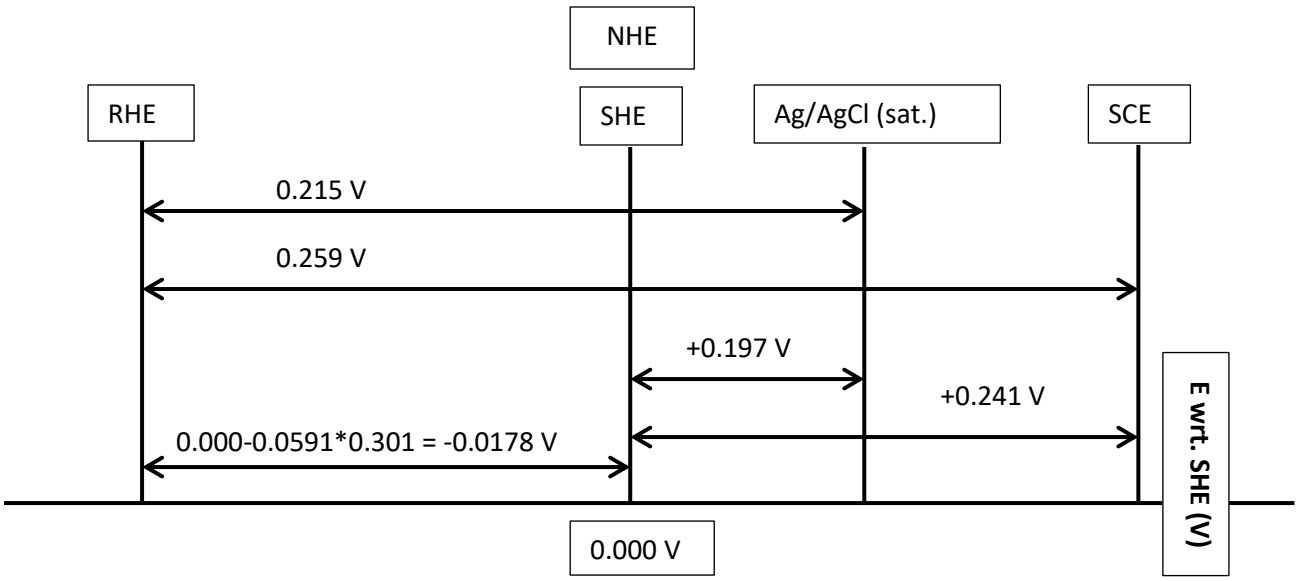
Reference Electrodes Systems

electrode	abbreviation	redox half-cell / redox reaction	potential wrt. SHE (E)/V
Standard Hydrogen Electrode	SHE	$2H^+(aq) + 2e^- \rightarrow H_2(g)$	0.000 with activity of H^+ (a_{H^+}) = 1
Normal Hydrogen Electrode	NHE	$2H^+(aq) + 2e^- \rightarrow H_2(g)$	≈ 0.000 with $[H^+]$ = 1 N
Reversible Hydrogen Electrode	RHE	$2H^+(aq) + 2e^- \rightarrow H_2(g)$	0.000-0.0591*pH (solution pH)
Saturated Calomel Electrode	SCE	$Hg_2^{2+} + 2Cl^- \rightleftharpoons Hg_2Cl_2(s)$	+0.241 , saturated
Silver/Silver Chloride Electrode	Ag/AgCl	$AgCl(s) \rightleftharpoons Ag^+ + Cl^-$	+0.197 , saturated

*wrt. = with respect to

Potential Conversion

The supporting electrolyte solution used in the thesis is 0.5M H_2SO_4 solution. The pH of the solution is 0.301.



In 0.5M H_2SO_4 supporting electrolyte solution at 25 ^oC:

E (V vs. RHE) = E (V vs. SCE) + 0.241 + 0.018 (0.0591*pH)

E (V vs. SHE/NHE) = E (V vs. SCE) + 0.241

Chapter 1

Introduction and Literature Reviews

1.1 Introduction

Fossil fuels are known to be a primary energy supply in the global society. Three kinds of fossil fuels including coal, oil, and natural gas have been used massively to produce energy mainly heat and electricity for consumption [13]. According to BP's Statistical Review of World Energy published in the middle of 2014, the reserves of coal, natural gas, and crude oil will be exhausted in 113, 55, and 53 years, respectively, based on the level of extraction in 2013 [10]. These numbers indicate that the world could possibly face an energy crisis in the upcoming century if the energy we use is solely dependent on these three sources. Many attempts have been made to decrease the use of non-renewable energy sources to generate heat and electricity. One way is to convert renewable energy such as solar and wind energy to electricity by solar cells and wind mills. Another way is to use a fuel cell which is a kind of electrochemical device. Hydrogen gas (H_2) is the first fuel used in a Polymer Electrolyte Membrane Fuel Cell (PEMFC) to generate electricity. Although hydrogen gas is a promising candidate for electricity generation due to its high energy density, its production and storage are still problematic [6]. Naturally, hydrogen does not exist as a separate form of matter, but combines with other elements. To extract hydrogen gas from its companion substances, a lot of work and time must be taken. Subsequently, hydrogen gas itself is fairly expensive, making it a source of fuel that is not for everyone. As we know that hydrogen gas is light and highly flammable. Therefore, a state-of-the-art infrastructure and secure methods are needed for transporting hydrogen gas from one place to another. Such requirements can be costly, making the use of hydrogen gas impractical for most functions [1]. The use of alcohols in

liquid form as a fuel in a PEMFC can simplify the production and storage problems arising from the use of hydrogen gas. Liquid alcohols can be transported by a reasonable fashion, such as pipelines and trucks. Reforming process to convert alcohols into hydrogen gas is not required as they can be directly oxidised when fed to fuel cells. Most importantly, the theoretical mass energy density and volume energy density of most alcohols are high [6]. Accordingly, high energy output from fuel cells using liquid alcohols would be expected. Methanol (MeOH) is used to produce electricity in a Direct Methanol Fuel Cell (DMFC) due to its high energy density and ease of handling [15]. However, due to its toxicity to human and animal life, methanol could potentially be an environmental hazard if used extensively. Therefore, an alternative fuel to methanol is needed. Ethanol (EtOH) is a good choice of fuel because it not only has higher energy density than methanol (8.0 kWh/kg vs 6.1 kWh/kg), but it is also non-toxic and quickly biodegradable. Ethanol can be produced in a great quantity from biomass such as sugar cane, wheat, corn, and straw by a fermentation process. This could prevent a shortage of ethanol for fuel cell operation. In addition, the use of biomass-derived ethanol or bioethanol can sustain the natural balance of carbon dioxide (CO_2) in the atmosphere [6]. In a Direct Ethanol Fuel Cell (DEFC), electricity is generated by the oxidation of ethanol molecules at anodes and the reduction of oxygen gas at cathodes. To achieve the performance (current densities) required for various applications, an efficient catalyst for ethanol electro-oxidation reaction (EOR) is needed. It has been known that Pt is a good catalyst for electro-oxidation of many small organic molecules. However, it is known not to be a good anode catalyst for ethanol electro-oxidation reaction at room or moderate temperatures. This is because Pt can be readily poisoned by the strongly adsorbed intermediates such as adsorbed CO (CO_{ads}) [20]. To improve the activity for ethanol electro-oxidation of Pt, an addition of a second metal to Pt has been done [17]. Carbon-supported PtSn (PtSn/C) nanoparticle catalysts have shown higher ethanol electro-oxidation activity in

acidic media compared to pure Pt and other Pt-based bi-metallic electrocatalysts [2-3, 7-9, 11-12, 14, 17, 19, 21]. However, products from the ethanol electro-oxidation reaction on PtSn/C catalysts are mainly the C-C bond containing compounds which will have a negative effect on the performance of fuel cells. Thus, it is necessary to develop novel highly efficient catalysts for the ethanol electro-oxidation reaction. Modification of PtSn/C catalysts by addition of a third metal with an aim to increase the activity for dehydrogenation, C-O and C-C bond cleavage during the electro-oxidation of ethanol has been studied. There are a number of metals selected to be used as an additive to PtSn, but most of the promising candidates are precious metals which are rare in the Earth's crust and quite expensive. Direct ethanol fuel cells using tri-metallic PtSnM/C (where M = precious metals) as anode catalyst could be costly. Subsequently, commercialisation of such fuel cells could be hindered. Development of efficient ternary PtSn-based electrocatalysts by incorporating inexpensive and earth-abundant metals to PtSn nanoparticles is of great interest. Potentially, capital cost for fabricating direct ethanol fuel cells could be reduced. First row transition metals are a good choice for this purpose. According to the literatures [4-5, 16, 89], carbon-supported PtSn-based nanoparticle catalysts with Ni and Co as a third metal have shown higher ethanol electro-oxidation activity than PtSn/C and Pt/C catalysts. While PtSnNi/C nanoparticle catalysts for the ethanol electro-oxidation reaction in acidic media have gained more attention over the past few years, only a few studies of the ethanol electro-oxidation activity in acidic media of carbon-supported PtSnCo (PtSnCo/C) nanoparticle catalysts have been conducted. H. Wang et al.[18] prepared and examined the electrocatalytic activity for ethanol oxidation of the Pt-decorated amorphous CoSn nanoparticles supported on carbon (Pt-CoSn/C) catalyst with the bulk Pt:Sn:Co atomic ratio of 1:0.25:1. The results obtained from cyclic voltammetry measurement showed that Pt-CoSn/C had higher mass activity than the PtSn/C and Pt/C catalysts synthesised by the same method. The enhancement in ethanol electro-oxidation

activity of Pt-CoSn/C could be due to (i) a maximum usage of Pt atoms arranged on the surface of metal nanoparticles, (ii) an increase in the CO oxidation caused by Sn, (iii) the presence of amorphous CoSn alloys which hold some lattice defects that favour the ethanol electro-oxidation, and (iv) the 'anchor effect' of Co to Pt. S. Beyhan *et al.*[4] prepared the tri-metallic PtSnCo/C (nominal Pt:Sn:Co atomic ratio = 80:10:10 atomic percent) using Bönnemann method. The bulk composition in terms of Pt:Sn:Co atomic ratio was determined by energy-dispersive X-ray (EDX) spectroscopy and it was found to be close to the nominal value. The X-ray photoelectron spectroscopy (XPS) analysis revealed that particles surface of the PtSnCo/C catalyst was Pt-enriched and no Co could be detected on the outer surface. The researchers ascribed the undetectability of Co on the outer surface to a random distribution of too small amount of cobalt in the bulk of catalyst. The hydrogen adsorption/desorption feature of the PtSnCo/C catalyst was studied by cyclic voltammetry in 0.1 M $HClO_4$ supporting electrolyte. The obtained cyclic voltammogram showed that hydrogen adsorption on Pt atoms was suppressed by the presence of Co species in comparison to carbon-supported Pt nanoparticle catalyst (Pt/C). The catalytic activity for ethanol electro-oxidation of the PtSnCo/C catalyst was examined by linear sweep voltammetry at a scan rate of 1 mV/s in 1M EtOH + 0.1M $HClO_4$ solution. At 400 mV (vs. RHE), PtSnCo/C catalyst exhibited the highest ethanol electro-oxidation activity among all studied catalysts with the lowest onset potential of 160 mV (vs. RHE). One explanation for such high activity of PtSnCo/C may be a high oxophilicity of Co at relatively low potential. The stability of the PtSnCo/C electrocatalyst during ethanol oxidation was measured by chronoamperometry (CA) at 500 mV (vs. RHE) for 1 hour. In comparison to PtSn/C and Pt/C, PtSnCo/C showed much higher oxidation current for the entire studied time period, indicating its high activity and stability for the ethanol electro-oxidation reaction. However, after the potentiostatic measurement at 500 mV for 1 hour, the surface Pt/Sn atomic ratio

decreased from 4.78 to 0.67. Such decrease could be attributed to the loss of Pt due to a weak interaction between Pt nanoparticles and carbon support. PtSnCo/C also demonstrated high ethanol electro-oxidation activity on the direct ethanol fuel cell (DEFC). The maximum power density obtained from the cell operating at 80 ^{o}C was about 35 mW/cm^{2}. This value is approximately three and six times higher than that obtained from the cells with PtSn/C and Pt/C anode catalysts, respectively. The higher performance of DEFC with the PtSnCo/C anodic electrocatalyst compared to that with PtSn/C could be due to a higher CO_2 production. Due to the obtained ethanol electro-oxidation activity of both Co-containing PtSn/C electrocatalysts, it is worth researching more on PtSnCo/C catalyst materials. Apart from the activity investigation, S. Beyhan et al. also studied the electro-oxidation reaction of ethanol on the synthesised PtSnCo/C catalyst. It was proposed by the researchers that Co can promote dehydrogenation at α-C of ethanol which leads to a high yield in acetaldehyde. The produced acetaldehyde can then be further oxidised to CO_2.The mechanism of ethanol electro-oxidation reaction on the tri-metallic PtSnCo/C catalyst was studied in details by in situ Fourier transform infrared (FTIR) spectroscopy [5]. The results indicated that the formation of adsorbed reaction intermediates was favoured on the PtSnCo/C catalyst. The performance for CO_2 production of PtSnCo/C was inferior to that of PtSnNi/C and PtSnRh/C electrocatalysts, indicating that the electro-oxidation of ethanol via total or complete oxidation pathway was favoured by the presence of Ni and Rh in the PtSn instead of Co. A general scheme for the reaction mechanism of ethanol electro-oxidation reaction on carbon supported tri-metallic PtSnM (M = Ni, Co, Rh, Pd) electrodes was summarised in Figure 1.1.

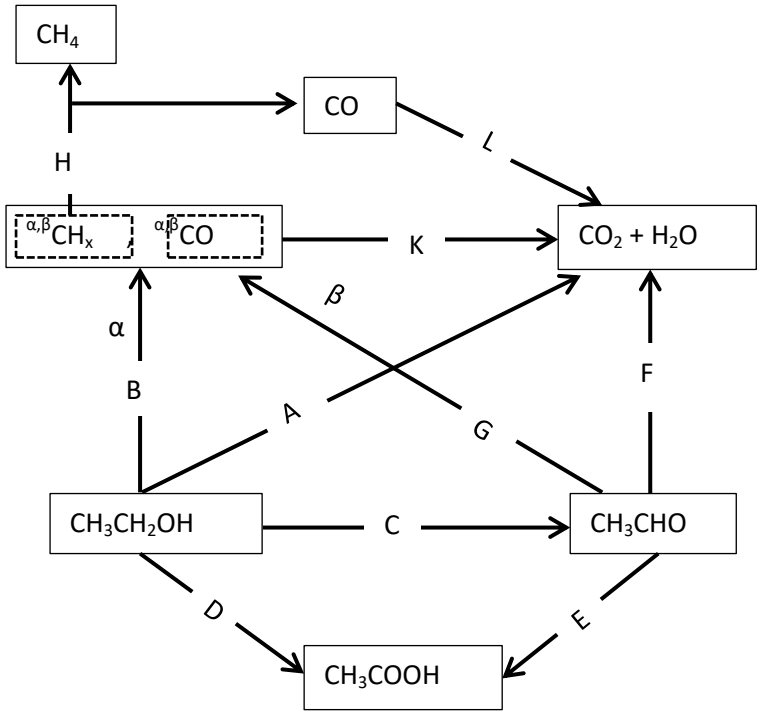


Figure 1.1 Schematic diagram of the reaction mechanism of EOR on the PtSnM/C (M=Ni, Co, Rh, Pd) electrodes [5]

It can be described from the diagram that ethanol can be directly electro-oxidised to acetaldehyde (CH_3CHO) (C) and acetic acid (CH_3COOH) (D). Acetic acid can be produced also by further oxidation of acetaldehyde (E). The production of CO_2 can take place via the C-C bond cleavage of both ethanol (A, B) and acetaldehyde (F, G) molecules. The scission of C-C bond in ethanol and acetaldehyde molecule yields mainly two intermediates namely CH_x and CO. CO can be oxidised to CO_2 (K) by reacting with adsorbed OH (OH_{ads}) species. For CH_x species, it can be either oxidised to CO, which can be further oxidised to CO_2 (L), or electrochemically reduced to methane (CH_4) (H) which could poison the surface of Pt active sites for ethanol electro-oxidation reaction at low potentials. The ethanol electro-oxidation activity of ternary PtSn-based nanoparticle catalysts are dependent on several factors such as type of a third metal, synthesis methods and conditions, particle size, particle size distribution, particle dispersion on support materials, and chemical components. One critical factor which plays an important role in tuning the ethanol electro-oxidation activity of PtSn-

based tri-metallic nanoparticle catalysts is the Pt:Sn:M atomic ratio (where M is a third metal). The studies conducted by H. Wang *et al.* and S. Beyhan *et al.* focus mainly on the electrocatalytic activity for ethanol oxidation in acidic media of carbon supported Co-containing PtSn electrocatalysts prepared with a specific nominal Pt:Sn:Co atomic ratio. The effect of different nominal Pt:Sn:Co atomic ratios on physicochemical properties and ethanol electro-oxidation activity of PtSnCo/C nanoparticle catalysts should be investigated in order to understand a property-activity relationship originating from chemical compositions present in the catalysts. In this research work, PtSnCo/C electrocatalysts with 4 different nominal Pt:Sn:Co atomic ratios are synthesised and their ethanol electro-oxidation activities are examined by means of cyclic voltammetry (CV) and chronoamperometry (CA). The ethanol electro-oxidation reaction on the PtSnCo/C electrocatalysts is investigated and proposed based on electro-oxidation studies of acetaldehyde and acetic acid in an acid supporting electrolyte.

1.2 Aims of Thesis

This thesis aims to study the ethanol electro-oxidation activities in an acidic medium of the carbon supported PtSn (PtSn/C) and PtSnCo (PtSnCo/C) nanoparticle catalysts synthesised by the modified sodium borohydride reduction method with a nominal total metal loading (Pt+Sn and Pt+Sn+Co) of 20 wt. %. It also aims to study the effects of Co content on the ethanol electro-oxidation activity. In addition to the electro-catalytic activities for ethanol oxidation of the PtSn/C and PtSnCo/C catalysts, mechanisms of the ethanol electro-oxidation reaction on the PtSn/C and PtSnCo/C electrodes are aimed to study. A property-activity relationship for the synthesised catalysts is aimed to establish. Furthermore, the electro-catalytic activities of the binary PtSn/C and ternary PtSnCo/C catalysts for ethylene glycol, 2-

propanol, and methanol oxidation and the effects of cobalt species and Co content on the electro-oxidation activity for those alcohols are aimed to investigate. Finally, the property-activity relationships for the electro-oxidation of ethylene glycol, 2-propanol, and methanol are as well aimed to achieve.

1.3 Thesis Overview

This thesis is presented in form of six chapters. In chapter 1, general introduction and literature reviews of ethanol electro-oxidation reaction and activity on PtSn/C and PtSn-based tri-metallic nanoparticle catalysts as well as aims of the thesis are presented. Chapter 2 details theories of an electrochemical cell and electrochemical reactions. Principles of techniques employed to characterise the synthesised catalytic materials and details of experiments are also presented in chapter 2. Physicochemical properties of the catalysts characterised by Energy Dispersive X-ray Spectroscopy (EDX), Powder X-ray Diffraction (PXRD), X-ray Photoelectron Spectroscopy (XPS), Thermogravimetric Analysis (TGA), and Transmission electron microscopy (TEM) are summarised and discussed in Chapter 3. In chapter 4, electrochemical characteristics and ethanol electro-oxidation activities of the synthesised PtSn/C and PtSnCo/C catalysts investigated by cyclic voltammetry (CV) are presented and correlations between the activity and physicochemical properties are discussed. Moreover, stability of the electrocatalysts during ethanol electro-oxidation at a constant potential, the electro-oxidation reaction of adsorbed CO species on the as-synthesised catalysts, and proposed EOR mechanisms are reported. Chapter 5 details the background of ethylene glycol, 2-propanol, and methanol electro-oxidation reactions on Pt and Pt-based electrodes. The electro-oxidation activities for ethylene glycol, 2-propanol, and methanol of the PtSn/C and PtSnCo/C electrocatalysts with proposed mechanisms of ethylene glycol, 2-propanol, and

methanol electro-oxidation reactions are also summarised and discussed in Chapter 5. Chapter 6 and chapter 7 include general conclusions of the research work and future perspectives, respectively.

1.4 Polymer Electrolyte Membrane Fuel Cell (PEMFC)

Polymer electrolyte membrane fuel cell also known as proton exchange membrane fuel cell is a low-temperature fuel cell, which can be used in several applications such as space program electric vehicles, stationary power plants, and portable electronic devices. Well-developed PEMFCs use Nafion (sulfonated tetrafluoroethylene based fluoropolymer-copolymer), which is a type of perfluorosulfonic acid (PFSA) polymer, as electrolyte and membrane [55]. Nafion-based PEMFCs normally operate at temperatures lower than 100 ^{o}C due to the thermal stability of Nafion membrane [39, 55]. Nafion is water-based and it can dehydrate at 100 ^{o}C and higher temperatures. Therefore, operating Nafion-based fuel cells at temperatures higher than 100 ^{o}C can result in a strong decrease in proton conductivity of the membrane [55]. Such decrease, in turn, lowers the performance of the fuel cells.

1.5 Direct Alcohol Fuel Cells (DAFCs)

In principle, DAFCs are electrochemical devices based on the PEMFC technology in which alcohols are directly fed and oxidised at the anodes of fuel cells without reforming [55]. The DAFCs generate electricity from the oxidation of alcohols at an anode and the reduction of oxygen (O_2) at a cathode. Unlike hydrogen fuel cells (HFCs), a heavy and bulky reformer for conversion of liquid alcohols into gas before feeding to DAFCs is not required. The DAFCs are, therefore, convenient for application in transportation and portable electronic devices.

Direct methanol fuel cell (DMFC) and direct ethanol fuel cell (DEFC) are two types of the DAFCs, in which attempts have been made extensively to improve their performance to meet the need of energy markets. In DMFCs with Pt or Pt-based anode electrocatalysts, the complete oxidation of methanol produces carbon dioxide (CO_2) as a final product and releases 6 electrons ($6e^-$) as described in Equation (1.1):

$$CH_3OH + H_2O \rightarrow CO_2 + 6H^+ + 6e^- \quad \text{Equation (1.1)}$$

The formation of CO_2 can occur via adsorbed CO (CO_{ad}), formaldehyde (HCHO), and formic acid (HCOOH) species. Equations (1.2) and (1.3) summarise the total oxidation pathways of methanol electro-oxidation.

$$CH_3OH \rightarrow \text{adsorbed intermediates} \rightarrow CO_{ad} \rightarrow CO_2 \quad \text{Equation (1.2)}$$

$$CH_3OH \rightarrow \text{adsorbed intermediates} \rightarrow HCHO, HCOOH \rightarrow CO_2 \quad \text{Equation (1.3)}$$

In the case of DEFCs with Pt or Pt-based anode electrocatalysts, generally, ethanol electro-oxidation occurs via two reaction mechanisms namely total oxidation and partial oxidation as given by Equation (1.4) and Equation (1.5), respectively.

$$CH_3CH_2OH \rightarrow [CH_3CH_2OH]_{ad} \rightarrow C_{1,ad}, C_{2,ad} \rightarrow CO_2 \text{ (total oxidation)} \quad \text{Equation (1.4)}$$

where C_{1ad} and C_{2ad} refer to adsorbed carbonaceous species with one and two carbon atoms, respectively.

$$CH_3CH_2OH \rightarrow [CH_3CH_2OH]_{ad} \rightarrow CH_3CHO \rightarrow CH_3COOH \text{ (partial oxidation)} \quad \text{Equation (1.5)}$$

To achieve the maximum energy output from 1 mole of ethanol, the total oxidation pathway is preferred to the partial oxidation one. It is because formation of CO_2 involves $12e^-$, while the formation of partial oxidation products, acetaldehyde (CH_3CHO) and acetic acid (CH_3COOH), releases only $2e^-$ and $4e^-$, respectively.

Table 1.1- Summary of the number of electrons (n) released from complete oxidation of alcohols, standard potentials of DAFCs (E^0) at 25 ^oC, theoretical mass energy densities (W_s), theoretical volume energy densities (W_e), capacities of pure compounds (C), and theoretical energy conversion efficiency for alcohol oxidation in a DAFC (η) [39]

Fuel	n	E^0_{cell} with O_2 reduction at cathode (V)	W_s(kWh.kg^{-1})	W_e(kWh.l^{-1})	C(Ah.kg^{-1})	η (%)
hydrogen gas (H_2)	2	1.23	32.80	0.18[a]	26668	83
MeOH	6	1.21	6.07	4.82	5019	97
EtOH	12	1.15	8.03	6.28	6981	97
1-propanol (1-PrOH)	18	1.13	9.07	7.28	8027	97
2-propanol (2-PrOH)	18	1.12	8.99	7.07	8027	97
Ethylene glycol (EG)	10	1.22	5.27	5.87	4318	99
Glycerol	14	1.25	5.09	6.42	4074	N/A

[a]H_2 storage at 70 bar and 25 ^oC, N/A = Not Applicable

1.6 Electrocatalysis

Electrocatalysis is defined as the variation of the rate and selectivity of electrochemical reactions achieved by the catalytic action of electrodes [26, 62]. In electrocatalysis, charge transfer process occurs on the surface of heterogeneous catalyst referred to as electrocatalyst [62]. Adsorption of reactants, intermediates, and final products of the reaction can be observed on the surface of electrocatalysts. Electrocatalysis was first observed in the early 20th century, but became universally known only after 1960, mainly in relation to fuel cells study [26]. Electrocatalysis for ethanol oxidation in DEFCs has been extensively studied [54, 68, 80, 87-88]. The complete oxidation of ethanol to form CO_2 is one of the challenges for applications of DEFCs as the C-C bond in ethanol molecule has to be broken at low temperatures [90].

1.7 Direct Ethanol Fuel Cell (DEFC)

DEFCs generate an electrical energy by the electrochemical redox reactions of liquid ethanol and oxygen gas. Basically, with a sole consideration of the complete oxidation, ethanol is electro-catalytically oxidised to form CO_2 at an anode (see Equation (1.6)).

$$C_2H_5OH + 3H_2O \longrightarrow 12H^+ + 12e^- + 2CO_2 \qquad \text{Equation (1.6)}$$

Protons produced by the electro-oxidation of ethanol migrate to a cathode through polymer electrolyte membrane. Then, they combine with oxygen to produce water as expressed by Equation (1.7).

$$3O_2 + 12H^+ + 12e^- \rightarrow 6H_2O \qquad \text{Equation (1.7)}$$

Overall reaction: $C_2H_5OH + 3O_2 \rightarrow 3H_2O + 2CO_2$ Equation (1.8)

Electrons released from the electro-oxidation of ethanol travel from the anode to the cathode through an external circuit. This movement of electrons provides the electrical current to connected devices [60].

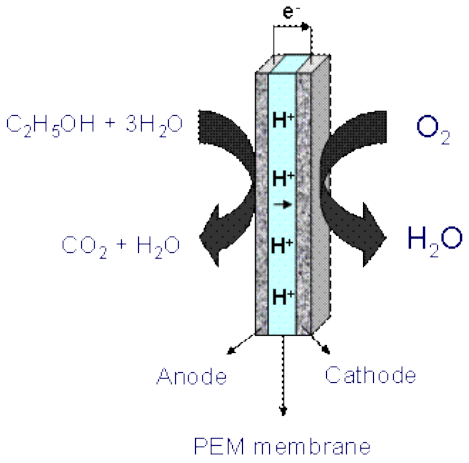


Figure 1.2 - Schematic illustration of electricity generation in a DEFC [27]

1.8 Synthesis of Metal Nanoparticles

A colloidal process, which is the reduction of metal precursors, either metal salts or organometallic compounds, in solution to metal atoms by a reducing agent (e.g. $NaBH_4$) or thermal decomposition process, can be used to synthesise metal nanoparticles [57]. The colloidal process consists of three fundamental steps namely nucleation, growth, and agglomeration or coagulation. Figure 1.3 illustrates the synthesis of metal nanoparticles by the colloidal process. In the first step, a metal precursor (M^+X^-) is reduced to metal atom (M^0). Subsequently, the obtained metal atoms, ions, and metal clusters interact to one another, resulting in metal cluster growth (Step II). Additionally, step I and step II are reversible. The process then becomes irreversible as the cluster grows to a critical size (Step III) due to a thermodynamic condition. Stabilisers added to the metal precursor(s) solution play a role in particle size control (Step IV). The presence of one stabiliser can lead to formation of spherical particles, which occurs under a thermodynamic condition. On the other hand, the presence of two stabilisers may cause a preferential growth due to the preferential adsorption of stabilisers. This process, taking place under a kinetic condition, leads to the formation of anisotropic particles such as nanorods. Particle agglomeration (Step V) can be prevented by the steric hindrance of stabiliser molecules adsorbed on the particle surface. This step is essential in controlling deposition of nanoparticles.

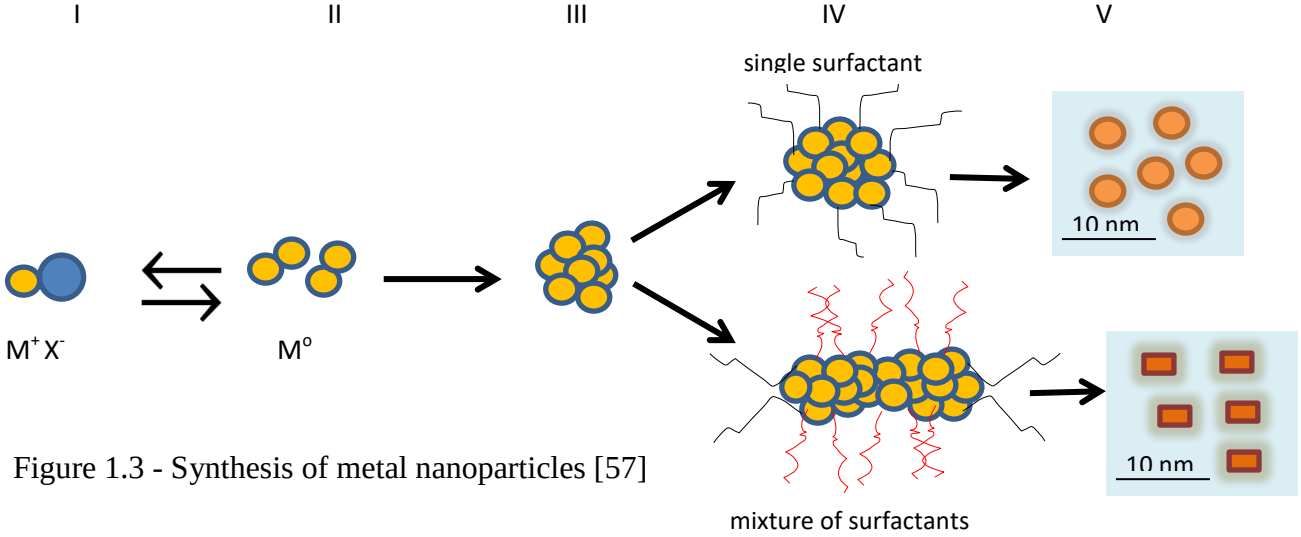


Figure 1.3 - Synthesis of metal nanoparticles [57]

1.9 Catalyst Support

A surface area of catalysts for fuel cell application can be maximised by several approaches. Deposition of a catalytically active component on high surface area materials, such as carbon, is an example. Carbon materials have been used as a catalyst support because they are relatively stable both in acidic and basic media. Moreover, they have good electrical conductivity and high specific surface area suitable for application in fuel cells [76]. The properties of supported catalytic metal nanoparticles including particle size, particle size distribution, morphology, degree of alloying, stability, and particles dispersion can be strongly influenced by carbon materials [83]. Not only are the physical properties of the supported metal nanoparticles affected by carbon materials, but their performance such as mass transport, electronic conductivity of catalyst layer, electrochemically active surface area, and stability during fuel cell operation is also affected. Therefore, it is necessary to develop good carbon materials for the use as the catalyst support. Currently, many types of carbon black, such as acetylene Black, Vulcan XC-72, Vulcan XC-72R, and Ketjen Black, are commercially available. Some physical and chemical properties including specific surface area, porosity, electrical conductivity, and surface functionality of individual carbon black materials are different. The most crucial property required for the use of carbon black as a support is the specific surface area. The carbon black with high specific surface area can increase utilisation of catalytic metal nanoparticles. Vulcan XC-72R with specific surface area of ~ 240 m^2g^{-1}, for instance, has been widely used as a support for preparing DEFC anode catalysts [52]. Presently, carbon nanotubes (CNTs) and graphene materials have gained more attention globally from catalyst researchers and developers as potential support materials due to their unique electrical and structural properties [63].

1.10 Electrocatalysts for Ethanol Electro-oxidation Reaction

Pt nanomaterials, especially Pt nanoparticles, have been widely used as a catalyst for ethanol electro-oxidation reaction in acidic media [44]. However, Pt is rapidly poisoned by some strongly adsorbed intermediates [37] mainly carbon monoxide (CO) and acetate anion (CH_3COO^-) produced by the dissociative adsorption of ethanol [41, 48-49]. As a result, the performance of direct ethanol fuel cells using pure Pt as anode electrocatalyst decreases over time. To increase the electro-catalytic activity for ethanol oxidation of Pt, some research on modifying Pt nanoparticles with a second or a third metal have been conducted. The addition of metals such as Ru [46, 69], Sn [43, 81], W [24], Mo [61], and Pd [24] to Pt has been studied in order for efficient catalysts for the ethanol electro-oxidation to be identified. It was found that carbon supported PtSn (PtSn/C) catalysts exhibited higher activity for ethanol electro-oxidation in acidic media than other bi-metallic catalysts studied. Also, the performance of DEFCs with PtSn/C as anode catalyst was improved compared to that with pure Pt/C as anodic catalyst.

1.10.1 PtSn Nanoparticle Catalysts for Ethanol Electro-oxidation Reaction

The ethanol electro-oxidation activity of PtSn nanoparticle catalysts has been extensively studied. Based on a degree of alloying, the ethanol electro-oxidation on non-alloyed, fully alloyed, and partially alloyed PtSn electrocatalysts was reported [23]. In this section, a review on the ethanol electro-oxidation activity of the three PtSn nanoparticle catalysts is presented.

1.10.1.1 Ethanol Electro-oxidation on Non-alloyed Pt-Sn Electrocatalysts : cases of Pt-SnO_x

L. Jiang et al.[51] prepared the carbon supported PtSn alloy and Pt-SnO_x nanoparticles using the modified polyol method. The data collected from chronoamperometry (CA) measurement and DEFC test showed that the Pt-SnO_x/C catalyst had higher activity for ethanol electro-oxidation than the PtSn/C electrocatalyst with PtSn alloy phase. They attributed the higher EOR activity of the Pt-SnO_x/C electrocatalyst to unchanged Pt lattice parameter which could favour ethanol adsorption and to convenient removal of CO-like species adsorbed on the Pt active sites. The removal was suggested to occur via the oxidation of adsorbed CO with adsorbed hydroxyl species (OH_{ads}) possibly formed on the surface of tin(IV)oxide (SnO_2) located in the vicinity of Pt nanoparticles. Hable and Wrighton [47] investigated the ethanol electro-oxidation activity of the Pt-SnO_2 catalyst and compared it with that of Pt. They found that Pt-SnO_2 had superior activity to Pt, but did not promote the C-C bond oxidation. At relatively negative potentials, both ethanol and acetaldehyde could be oxidised on the surface of the Pt-SnO_2 catalyst, while acetic acid was quite stable. The products of the ethanol electro-oxidation reaction on the Pt-SnO_2 electrode were analysed and the results showed that at potentials lower than 0.5V (vs. SCE), acetic acid was a major product. Regarding the electro-oxidation of alcohols containing C-C bond, the Pt-SnO_2 catalyst did not suffer from the CO poisoning at low temperatures and low potentials. It is because under such conditions the C-C bond cleavage is not activated. Lamy et al. [54] prepared the Pt-Sn/C catalyst (Pt:Sn atomic ratio of 9:1) by the Bönneman method. According to the XRD pattern of the catalyst, tin was not alloyed with Pt and should be in an oxide form. The activity for ethanol electro-oxidation of the prepared PtSn/C (9:1) electrocatalyst was higher than that of Pt/C especially at low potentials. The ethanol electro-oxidation reaction on the PtSn/C (9:1) electrode was investigated in details [68]. It was found that SnO_x present in the electrocatalyst led to an

increase of acetic acid (AA) and a decrease of acetaldehyde (AAL) and CO_2 yields. The electro-oxidation of ethanol without the C-C bond breaking at potentials greater than 0.2-0.3 V was suggested. The role of SnO_x species was discussed. Pt nanoparticles modified by SnO_x oxidises ethanol to acetaldehyde. The adsorbed acetaldehyde then reacts with adsorbed OH species (OH_{ads}) provided by SnO_x to form acetic acid (bi-functional mechanism). The effect of Pt and SnO_x compositions on the ethanol electro-oxidation activity of the Pt-SnO_x catalysts has also been investigated. Jiang et al.[50] prepared the Pt-SnO_x/C catalysts with different nominal Pt:Sn atomic ratios by a colloidal method and tested their ethanol electro-oxidation activity at two temperatures. The results showed that the EOR activity decreased with increasing tin content at room temperature, but increased at 80 ^oC. The products analysis revealed that AA and AAL were two major products of the ethanol electro-oxidation reaction on all Pt-SnO_x/C electrodes. In accordance with the DEFC test at 90 ^oC, the fuel cell using the Pt-SnO_x/C catalyst with SnO_x/Pt ratio of ~ 0.57 exhibited the highest maximum power density (MPD). Simoes et al.[70] also investigated the ethanol electro-oxidation activity of the Pt-SnO_x (Pt-SnO_2) catalysts prepared by thermal decomposition method. The DEFC with $Pt_{0.9}Sn_{0.1}O_2$ anode catalyst exhibited the largest power density. AA and AAL were found to be the main products of the ethanol electro-oxidation reaction on the Pt-SnO_2 catalysts. The thermal decomposition-prepared Pt-SnO_2 catalysts could activate the C-C bond cleavage as evidenced by the presence of adsorbed CO_L species and CO_2. The promoting effect of tin oxide on the ethanol electro-oxidation activity of PtSn/C catalysts was reported by C. Lamy et al. [54]. Non-alloyed SnO_2 species could activate water molecules to produce the adsorbed hydroxyl (-OH_{ads}) species at lower potentials than Pt. The reaction of adsorbed C_1 and C_2 intermediates with OH_{ads} species formed on the surface of SnO_2 adjacent to Pt then liberated the Pt active sites [24].

1.10.1.2 Ethanol Electro-oxidation on Partially Alloyed Pt-Sn Catalysts

The ethanol electro-oxidation activity of partially alloyed Pt-Sn catalysts has been reported. Vigier et al. [80] prepared the Pt-Sn/C electrocatalysts by co-impregnation reduction method and characterised them with Extended X-ray Absorption Fine Structure (EXAFS) technique to identify phases present in the catalysts. It was found that these catalysts consisted of Pt-Sn alloy phases, Pt particles, and Pt-O-Sn^{2+} species. The ethanol electro-oxidation activity of the Pt-Sn/C catalyst was about two times higher than that of Pt/C. A reaction mechanism of the ethanol electro-oxidation on these catalysts was also studied by High Performance Liquid Chromatography (HPLC), Subtractively Normalised Interfacial Fourier Transform Infrared Reflection Spectroscopy (SNIFTIRS), and Single Potential Alteration Infrared Reflectance Spectroscopy (SPAIRS) techniques. The adsorbed species including adsorbed CO and adsorbed acetyl ($CH_3CO_{ads)}$, CO_2, CH_3CHO, and CH_3COOH were detected. They explained that the EOR on the Pt-Sn/C electrodes involves two effects: bi-functional mechanism due mainly to non-alloyed tin and ligand effect owing to the alloyed Sn. To maximise the performance of DEFCs using partially alloyed Pt-Sn catalysts, the optimum Sn content in the catalysts prepared by different methods has been searched. Colmati et al. [36] tested the performance of DEFCs operating at 110 ^oC with the Pt-Sn/C anode catalysts consisting of different alloying degrees at high (100 $mA.cm^{-2}$) and low (20 $mA.cm^{-2}$) current densities. They found that increasing lattice parameter had a little effect on power density measured at low current density. However, a linear correlation between power density and lattice parameter was observed at high current density. At low current density, a slight increase of power density with increasing lattice parameter was attributed to an enhanced CO_{ads} oxidation by tin oxide. At high current density, on the other hand, an increase in lattice parameter should promote the C-C bond cleavage or it was associated with an increase in Pt-Sn pairs necessary to oxidising ethanol without the C-C bond breaking. The effect of Sn

content in partially alloyed Pt-Sn anodic electrocatalysts on the performance of single DEFCs was studied by Zhou et al. [84-85]. For DEFCs operating at 60 ^{o}C, the highest maximum power density (MPD) was obtained from the cell with the Pt_3Sn_2/C anode catalyst (Pt lattice parameter (a) = 0.3974 nm), while at the operating temperature of 90 ^{o}C, the cell with the Pt_2Sn_1/C anode catalyst (a = 0.3956 nm) exhibited the highest MPD. Kim et al. [52] performed CV measurement to test the ethanol electro-oxidation activity of the PtSn/C catalysts and found that PtSn/C (2:1 nominal Pt:Sn atomic ratio) with Pt lattice parameter of ~ 0.396 nm showed the highest peak current density. This result is in good agreement with that observed by Tsiakaras [79] who carried out the performance test of DEFCs with different Pt-Sn anode catalysts.

1.10.2 Ternary PtSn-based Nanoparticles Supported on Carbon as a Catalyst for Ethanol Electro-oxidation Reaction in Acid Environment

Although PtSn/C nanoparticle catalysts have exhibited high electrocatalytic activity for ethanol oxidation, final products are mainly acetic acid and acetaldehyde. It is because of the inhibiting effect of Sn to the C-C bond cleavage [54]. To increase the ethanol electro-oxidation activity of PtSn/C catalysts, addition of a third metal to PtSn nanoparticles has been done. The third metal is expected to work synergistically with Sn and Pt to promote the complete oxidation of ethanol on the Pt active sites. A number of efforts have been made to prepare carbon supported tri-metallic PtSn-based (PtSnM where M = Ru [25, 34, 40, 59, 68], Rh [33, 35, 53, 71, 77], Ni [22, 30, 32, 33, 38, 65, 72-73], Ir [64, 66, 74], In [86], W [67], Mo [56], Ce [42], and Re [75] nanoparticles and their activity for ethanol electro-oxidation have been tested. Zhou et al. [84-85] synthesised the carbon supported tri-metallic $Pt_1Ru_1M_1$ (M = W, Mo, and Sn) electrocatalysts using a modified polyol method. The electrocatalytic

activity for ethanol oxidation of the prepared catalysts was tested in single direct ethanol fuel cells and the results showed that the performance of DEFCs with $Pt_1Ru_1M_1/C$ anode electrocatalysts was higher than that of DEFC with Pt_1Ru_1/C, but inferior to the performance of DEFC with Pt_1Sn_1/C. These findings were in agreement with the results of Antolini et al. [25] who used $Pt_1Sn_1Ru_1/C$ prepared by the formic acid reduction method as anodic electrocatalyst in the DEFC. The investigation of ethanol electro-oxidation activity of the $Pt_{86}Sn_{10}Ru_4/C$ electrocatalyst prepared by the Bönnemann method was done by Rousseau et al. [68] by means of single DEFC test. The $Pt_{90}Sn_{10}/C$ and Pt/C electrocatalysts were also prepared by the same method for a comparison purpose. They found that the addition of Ru to PtSn/C enhanced the electrical performance of DEFC. However, this catalyst did not promote the complete oxidation of ethanol (C-C bond breaking pathway) under the cell condition. The observed ethanol electro-oxidation activity in terms of the performance of DEFCs of the PtSnRu/C and PtSn/C electrocatalysts highlights a role of catalyst preparation methods. Apart from Ru, In, Ce, and Re are three metals that have been used as an additive to PtSn nanoparticles. Zhu et al. [86] studied the mechanism of EOR catalysed by the $Pt_{60}Sn_{20}In_{20}/C$ and $Pt_{60}Sn_{40}/C$ catalysts. The catalysts were prepared by a chemical reduction method with sodium borohydride ($NaBH_4$) reducing agent in ethylene glycol solution. They analysed products of the ethanol electro-oxidation reaction occurring in the DEFCs at 0.5 V and found that acetaldehyde and acetic acid are the main products. It can be seen that the complete oxidation of ethanol was not promoted by modifying PtSn/C with In. The $Pt_{68}Sn_{22}Ce_{10}/C$ catalyst was synthesised by Souza et al. [42] using a modified polymeric precursor method and used as anode electrocatalyst in a DEFC. The performance of DEFC with $Pt_{68}Sn_{22}Ce_{10}/C$ and that with the commercial PtSn/C (E-Tek) were compared, and it was found that the former showed higher electrical performance than the latter by 40%. They also studied the reaction mechanism of EOR and proposed that the oxidative removal of CO

intermediate to CO_2 could be favoured by the oxygen-containing species formed on Sn and Ce. Tayal et al. [75] prepared the PtSnRe/C electrocatalysts and investigated their ethanol electro-oxidation activity by single DEFC test. They found that $Pt_{20}Re_5Sn_{15}$/C (by wt. %) was beneficial for the C-C bond breaking and enhanced the DEFC performance compared to PtSn/C synthesised by the same method. They also reported that increasing the weight percentage of Re to 10 ($Pt_{20}Re_{10}Sn_{10}$/C) resulted in a decrease in cell performance because the higher amount of Re blocked further oxidation of intermediates. S. Beyhan et al. [28] studied the ethanol electro-oxidation activity of tri-metallic PtSnM/C (M=Ni, Co, Rh, and Pd) electrocatalysts prepared by the Bönnemann method. The electrocatalytic activity for ethanol oxidation of the tri-metallic PtSnM/C catalysts was measured by LSV and CA techniques. The results showed that PtSnNi/C and PtSnCo/C enhanced the ethanol electro-oxidation activity compared to PtSn/C. The performance of DEFCs with the PtSnNi/C and PtSnCo/C electrocatalysts confirmed the superiority of the ethanol electro-oxidation activity of both tri-metallic catalysts to PtSn/C. The higher activity for ethanol electro-oxidation seemed to be the promotion of the C-C bond breaking by Ni and Co heteroatoms.

1.10.3 PtSnM Compositions on Ethanol Electro-oxidation Reaction in Acidic Media

Ethanol electro-oxidation activity of carbon supported tri-metallic PtSn-based nanoparticle catalysts has been found to be dependent on catalyst compositions. A number of studies have demonstrated a significance of atomic and mass compositions of Pt, Sn, and the third metals on catalytic activity for ethanol electro-oxidation of the PtSnM/C electrocatalysts. S.G. Rodríguez et al. [91] investigated the effect of Rh content of the carbon supported Pt_3Sn electrocatalyst prepared by a controlled impregnation-reduction method on the electro-oxidation of ethanol. It was found that the surface composition affected the ethanol electro-

oxidation activity of the catalysts. Both 1Rh-PtSn/C and 3Rh-PtSn/C (1 and 3 refer to Rh loading in weight %) samples had higher ethanol electro-oxidation activity than the PtSn/C electrocatalyst. The highest activity was obtained from the 1Rh-PtSn/C electrocatalyst and it was attributed to higher production of acetic acid ($4e^-$ route). The study of the effect of metal compositions on the ethanol electro-oxidation activity of PtSnCe/C electrocatalysts was carried out by R. [42]. In this study, the PtSnCe/C electrocatalysts in Pt:Sn:Ce mass ratios of 72:23:5, 68:22:10, and 64:21:15 were prepared by the polymeric precursor method. CA measurement was performed in 0.5M perchloric acid solution in the presence of ethanol to measure the ethanol electro-oxidation activity of the prepared electrocatalysts. Among the three investigated PtSnCe/C electrocatalysts, PtSnCe/C with the mass ratio of 68:22:10 showed the highest activity for the ethanol electro-oxidation. Furthermore, it exhibited about 50% higher activity than that of the commercial PtSn/C (E-Tek).

Ni metal is one of the additives, which has shown a potential to improve the ethanol electro-oxidation activity of PtSn/C nanoparticle catalysts. E. Ribadeneira and B.A. Hoyos [65] employed the alcohol-reduction process to prepare the PtSn/C (75:25), PtSnNi/C (75:15:10), and PtSnNi/C (75:10:15) electrocatalysts and tested their activity for ethanol electro-oxidation in a single DEFC operating at 80 ^oC. The comparison of the DEFC performance in terms of the highest generated current density revealed that both tri-metallic PtSnNi/C electrocatalysts had higher activity than PtSn/C (75:25). The electrocatalyst with higher Sn content showed greater activity. Another tri-metallic PtSn-based nanoparticle material which has been prepared and used as anode catalyst in DEFCs when supported on carbon is PtSnMo. E. Lee et al. [56] prepared the PtSnMo/C electrocatalysts by a polyol method. The effect of Mo addition and atomic compositions of Pt, Sn, and Mo on the ethanol electro-oxidation activity and the DEFC performance were investigated. CV and CA measurements showed that the ternary PtSnMo/C electrocatalysts both $PtSnMo_{0.4}$/C and $PtSnMo_{0.6}$/C had

higher ethanol electro-oxidation activity than PtSn/C synthesised by the same method. Since the actual Pt:Sn atomic ratio of the $PtSnMo_{0.4}$/C and $PtSnMo_{0.6}$/C electrocatalysts is the same as that observed for PtSn/C, the addition of Mo to PtSn proved to have a positive effect on the ethanol electro-oxidation. The $PtSnMo_{0.6}$/C electrocatalyst possesses the higher activity for ethanol electro-oxidation compared to that of $PtSnMo_{0.4}$/C as evidenced both by the voltammetric measurements and single cell test, indicating an importance of metal composition for the oxidation of ethanol molecule. J. Tayal et al. [74] studied the electro-catalytic activity for ethanol oxidation of the tri-metallic PtSnIr/C electrocatalysts prepared by the impregnation-reduction method. CV, LSV, and CA measurement were performed to investigate the ethanol electro-oxidation activity of each catalyst at room temperature. The results showed that the PtSnIr/C electrocatalyst consisting of 20 % Pt, 5 % Ir, and 15 % Sn by weight had the highest activity among all tri-metallic PtSnIr/C electrocatalysts and higher than that of PtSn/C with 20 wt.% Pt and 20 wt.% Sn. The superior activity for ethanol electro-oxidation of the PtSnIr/C (20:15:5) catalyst was confirmed by the performance of DEFC operating at 90 ^{o}C.

1.11 Acetaldehyde Electro-oxidation Reaction

Acetaldehyde has been found to be a major product of ethanol electro-oxidation reaction catalysed by carbon supported Pt or PtSn nanoparticle catalysts. The oxidation of acetaldehyde produces CO_2 and acetic acid as a final product. A quantity of the obtained products is dependent on concentrations of acetaldehyde, temperatures, electrode potentials, and catalyst materials. [29]. Rasch and Iwasita [92] investigated the electro-oxidation of acetaldehyde in acid solution on polycrystalline Pt electrode. In situ Fourier transform infrared (FTIR) spectroscopy was used to monitor the oxidation reaction, identify products,

and determine yields of the products. The results showed that both acetic acid and CO_2 were detected close to the electrode surface at high potentials when the measurement was carried out in 1M acetaldehyde solution. Upon a decrease of the concentration of acetaldehyde to 0.01 M, only CO_2 was produced during acetaldehyde electro-oxidation at high potentials. Nevertheless, the amount of CO_2 produced at both concentrations was similar. CO_2 product is a result from the oxidation of adsorbed CO which could originate from the dissociative chemisorption of acetaldehyde. The electro-oxidation of acetaldehyde in acid solution on the Pt electrode was also studied by using differential electrochemical mass spectroscopy (DEMS) technique [93, 94]. The study showed that electro-oxidation of acetaldehyde produced acetic and CO_2, but methane and ethane were detected during the reduction of the adsorbed intermediates. Pt-based bimetallic alloy electrodes were used to catalyse the acetaldehyde electro-oxidation reaction. Kokoh et al [95] investigated the electro-oxidation of acetaldehyde on PtRu and PtOs alloy electrodes by using the in situ FTIR spectroscopy and high performance liquid chromatography (HPLC) techniques. They found that the majority of the products was acetic acid with the small amount of formic acid and CO_2, suggesting that Pt active sites were low-level poisoned by the adsorbed CO due to the synergistic effect of the Pt sites and neighbouring Ru.

Concerning the electro-oxidation of acetaldehyde in acidic media on PtSn and tri-metallic PtSn-based catalysts, S. Beyhan et al. [29] reported the study of acetaldehyde electro-oxidation reaction on the PtSn/C (90:10) and PtSnM/C (80:10:10) where M = Ni, Co, Rh, and Pd electrodes using in situ FTIR spectroscopy. The results showed that the efficiency of the PtSn/C catalyst for converting acetaldehyde to CO_2 is not appreciable. This is due to the weak adsorption of acetaldehyde on the Pt active sites in the presence of Sn. However, the addition of a third metal to PtSn promotes the CO_2 formation pathway by facilitating the C-C bond cleavage of acetaldehyde. For the PtSnNi/C, PtSnCo/C, and PtSnRh/C electrocatalysts, CO_2

formation seems to originate from the dissociative adsorption of acetaldehyde molecule on the catalyst surface to produce adsorbed CH_3 and CHO species. Such adsorbates are then oxidised to CO_2. Unlike the other tri-metallic catalysts, the formation of CO_2 occurs mainly via the oxidation of CH_3CO species on the surface of the PtSnPd/C electrocatalyst. It can be concluded from the above experimental results that the presence of Ni, Co, Rh, and Pd in the PtSn catalyst affects strongly the adsorption behaviour of acetaldehyde and its oxidation products. The reaction mechanism of the adsorption and electro-oxidation of acetaldehyde on PtSn/C and PtSnM/C (M = Ni, Co, Rh, and Pd) electrodes are shown in Figure 1.4. The electro-oxidation of acetaldehyde begins with the adsorption of acetaldehyde molecule on Pt active sites. Acetaldehyde that weakly adsorbs on the Pt surface via oxygen lone pair electrons tends to molecularly desorb from the catalytic surface to the bulk solution (reaction 1). In the case of strong adsorption, either the production of the adsorbed CH_3 and CHO species from the cleavage of C-C bond in acetaldehyde molecule at low potential or the formation of adsorbed acetyl (CH_3CO) species takes place (reaction 2 and 4). Acetyl species can react with the OH_{ad} species to produce acetic acid (reaction 6). Moreover, the acetyl intermediate can be converted to acetate (CH_3COO^-) via an addition of oxygen atom of the surface oxygen-containing species (reaction 7). The adsorbed acetate species, additionally, are in equilibrium with acetic acid in the solution.

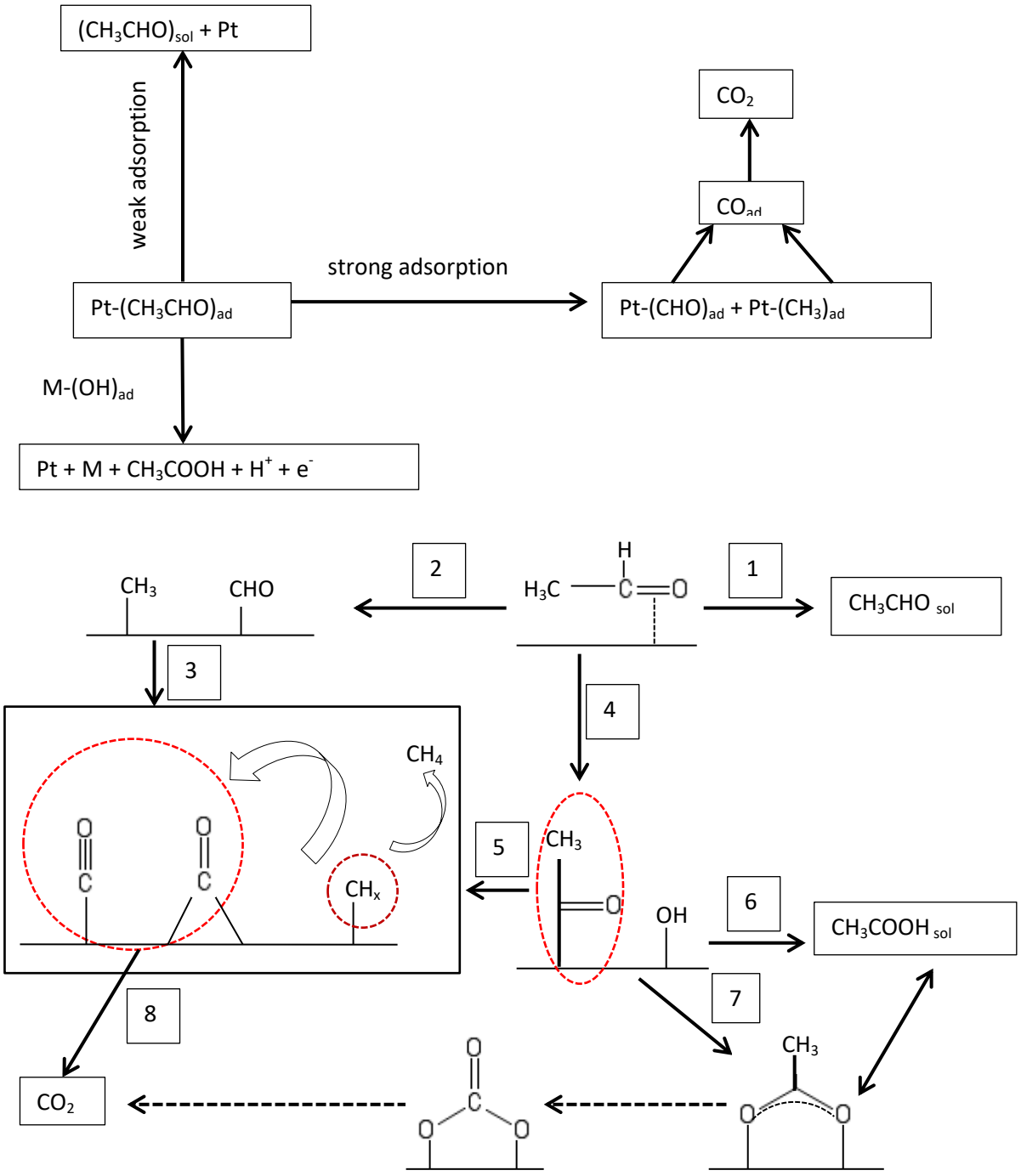


Figure 1.4 - Proposed reaction mechanisms of acetaldehyde electro-oxidation on the PtSn/C and tri-metallic PtSnM/C (M = Ni, Co, Rh, Pd) electrodes [29]

1.12 Electro-oxidation Reaction of Adsorbed CO

Electro-oxidation of ethanol on Pt-based nanoparticle electrodes produces carbon monoxide (CO) via the C-C bond breaking. An adsorbed CO molecule can poison the Pt surface as it has a strong affinity to Pt atoms. As a result, further electro-oxidation of ethanol can be inhibited due to the blockage of Pt active sites by adsorbed CO species. A study of adsorption behaviour and electro-oxidation of CO is, therefore, important to development of Pt-based DEFC anode catalysts. The electro-oxidation of adsorbed CO (CO_{ads}) on Pt single crystal electrodes Pt(hkl) in the absence of dissolved CO in electrolyte was investigated by several research groups. They proposed that the electro-oxidation of adsorbed CO proceeds via the Langmuir-Hinshelwood mechanism which basically is the reaction of CO_{ads} species with adsorbed oxygen-containing species often the adsorbed hydroxyl (OH_{ads}) formed by the dissociation of water on the Pt surface [96]. The reaction mechanism is illustrated by the equations below.

$$Pt + CO \rightarrow Pt - CO_{ad} \qquad \text{Equation (1.9)}$$

$$Pt + H_2O \rightarrow Pt - OH_{ad} + H^+ + e^- \qquad \text{Equation (1.10)}$$

$$Pt - CO_{ad} + Pt - OH_{ad} \rightarrow 2Pt + CO_2 + H^+ + e^- \qquad \text{Equation (1.11)}$$

The electro-oxidation of CO_{ads} referred to as the oxidative stripping of CO_{ads} occurs at relatively positive potentials. This is because an access of water molecules to the electrode surface is blocked by the compact CO adlayer formed. The electro-oxidation of adsorbed CO on Pt single crystal electrodes proceeds in two steps as suggested by a prepeak and a main CO_{ads} stripping peak typically observed at potentials greater than 0.6 V (vs. RHE) in acidic

electrolyte. Crystallographic orientation, type and density of structure defects, and CO coverage define the position and magnitude of the prepeak. The electro-oxidation of adsorbed CO species on binary PtSn/C nanoparticle electrodes has been studied. F. Colmati et al. [37] prepared the carbon supported PtSn electrocatalyst (nominal Pt:Sn atomic ratio = 75:25) by the formic acid reduction method. The as-prepared PtSn/C electrocatalyst consisted of the $Pt_{89}Sn_{11}$ alloy and SnO_2 phases as characterised by XRD. By annealing the as-prepared sample at 200 ^{o}C under H_2 atmosphere, fully alloyed stoichiometric cubic Pt_3Sn phase was found to be the major Pt-Sn alloy phase. Moreover, three PtSn alloy phases namely cubic near-stoichiometric Pt_3Sn phase, $Pt_{88}Sn_{12}$ alloy and hcp PtSn (niggliite) phases were detected upon an increase in the annealing temperature to 500 ^{o}C. The electro-oxidation of adsorbed CO on each electrode was performed and it was found that CO_{ads} started to be oxidised at quite the same potential for the commercial Pt_3Sn/C, the as-prepared, and the PtSn200/C catalysts. The characteristic of Sn dissolution was observed for both thermally treated samples but not the as-prepared PtSn/C and ETEK Pt_3Sn/C catalysts. The experimental results suggested that, probably, Sn present on the surface of the hcp PtSn phase is more likely to dissolve than that of the cubic Pt_9Sn and Pt_3Sn phases. Regarding Arenz et al. [97], Pt-Sn pairs in the surface of Pt_3Sn alloy are most likely the most active sites for CO oxidation at low potentials. In comparison with the Pt/C catalyst, the onset potential of the electro-oxidation of CO_{ads} for the Pt-Sn/C catalysts is lower. The negative shift of the CO_{ads} electro-oxidation onset potential for the Pt-Sn catalysts was also observed by Moromoto and Yeager [98] and Wang et al. [99]. They attributed the shift of the onset potential to oxidative removal of CO_{ads} by the oxygen-containing species formed on Sn sites at lower potentials. The non-alloyed SnOx has also been reported to have a promoting effect for the CO_{ads} electro-oxidation activity of the Pt-SnO_x/C electrocatalysts [100][101]. The Pt-Sn alloy phase is not the only contribution to the CO_{ads} electro-oxidation on PtSn/C nanoparticle catalysts. Y. Ma

et al. [102] prepared the PtSn/C electrocatalysts (nominal Pt:Sn atomic ratio = 3:1) by $NaBH_4$ reduction method in alkaline ethylene glycol solution with different types of stabiliser namely EDTA, NaCitrate, glycine, and PABA. The CO stripping voltammograms of all catalysts showed that oxidation of adsorbed CO occurred at two potentials. In fact, the four prepared PtSn/C catalysts have quite similar bulk compositions (Pt:Sn = 3:1 atomic ratio) and slightly different degrees of alloying. Therefore, the multiple CO stripping peaks were attributed to agglomeration of PtSn nanoparticles. The onset potential of the adsorbed CO electro-oxidation on the PtSn/C electrodes prepared with different stabilisers and degree of particle agglomeration was correlated. It was found that the onset potential shifted more negatively with increasing degree of agglomeration in agreement with the results reported by Friedrich et al. [45] and Maillard et al. [58]. J.Thepkaew et al. [78] investigated the electro-oxidation activity for CO_{ads} of the mesoporous PtSnRu alloy catalyst prepared by the liquid crystalline templating technique. The electro-oxidation of CO adsorbed on the Pt surface of the PtSnRu electrocatalyst is represented by a broad oxidation peak with a peak potential of 0.66 V (vs. RHE). The onset potential of the CO electro-oxidation shifted to the value lower than that of the Pt catalyst prepared by the same method. The highest CO electro-oxidation activity of the PtSnRu catalyst was ascribed to the oxidation of strongly and weakly adsorbed CO promoted by Ru and Sn existing predominantly as SnO on the catalyst surface, respectively. D. Wang et al. [82] studied the CO_{ads} electro-oxidation activity of the sub-monolayer Sn and RuSn decorated Pt/C nanoparticle catalysts. They found that the decorating tin oxides (Sn(II)/Sn(IV)) on Pt nanoparticles of the Sn-decorated Pt/C electrocatalyst induced the oxidation of CO weakly adsorbed on the Pt surface. In the case of the RuSn-decorated Pt/C electrocatalyst, both Ru and Sn cooperatively promoted the electro-oxidation of CO_{ads}, resulting in higher electrocatalytic activity for CO oxidation. The oxidative stripping of adsorbed CO was also studied on the PtSnMo/C electrodes [56]. The adsorbed CO started to

be oxidised at the potential of 0.15 V (vs. NHE) for the $PtSnMo_{0.4}/C$ electrocatalyst. Increasing the Mo content to 0.6 (atomic ratio) did not shift the CO_{ads} electro-oxidation onset potential. The electro-oxidation of CO_{ads} on both electrodes occurred over a broad potential range. This observed phenomenon may be associated with the adsorption of CO on different sites.

References

1. Disadvantages of Hydrogen Energy. http://www.conserve-energy-future.com/Advantages_Disadvantages_HydrogenEnergy.php (accessed 14 November 2014).
2. Antolini, E.; Colmati, F.; Gonzalez, E. R., *Journal of Power Sources* **2009,** *193* (2), 555-561.
3. Antolini, E., *Journal of Power Sources* **2007,** *170* (1), 1-12.
4. Beyhan, S.; Coutanceau, C.; Léger, J.-M.; Napporn, T. W.; Kadırgan, F., *International Journal of Hydrogen Energy* **2013,** *38* (16), 6830-6841.
5. Beyhan, S.; Léger, J.-M.; Kadırgan, F., *Applied Catalysis B: Environmental* **2014,** *144* (0), 66-74.
6. Bommersbach, P.; Mohamedi, M.; Guay, D., *Journal of The Electrochemical Society* **2007,** *154* (8), B876-B882.
7. Colmati, F.; Antolini, E.; Gonzalez, E. R., *Applied Catalysis B: Environmental* **2007,** *73* (1–2), 106-115.
8. Godoi, D. R. M.; Perez, J.; Villullas, H. M., *Journal of Power Sources* **2010,** *195* (11), 3394-3401.
9. Kim, J. H.; Choi, S. M.; Nam, S. H.; Seo, M. H.; Choi, S. H.; Kim, W. B., *Applied Catalysis B: Environmental* **2008,** *82* (1–2), 89-102.
10. Kolesnikov, I. World Reserves of Fossil Fuels. http://knoema.com/smsfgud/world-reserves-of-fossil-fuels. (accessed 14 November 2014)
11. Lim, D.-H.; Choi, D.-H.; Lee, W.-D.; Lee, H.-I., *Applied Catalysis B: Environmental* **2009,** *89* (3–4), 484-493.
12. Liu, Z.; Hong, L.; Tay, S. W., *Materials Chemistry and Physics* **2007,** *105* (2–3), 222-228.
13. McLamb, E. Fossil Fuels vs. Renewable Energy Resources 2011. http://www.ecology.com/2011/09/06/fossil-fuels-renewable-energy-resources/. (accessed 14 November 2014)
14. Neto, A. O.; Dias, R. R.; Tusi, M. M.; Linardi, M.; Spinacé, E. V., *Journal of Power Sources* **2007,** *166* (1), 87-91.
15. Park, K.-W.; Choi, J.-H.; Kwon, B.-K.; Lee, S.-A.; Sung, Y.-E.; Ha, H.-Y.; Hong, S.-A.; Kim, H.; Wieckowski, A., *The Journal of Physical Chemistry B* **2002,** *106* (8), 1869-1877.
16. Parreira, L. S.; da Silva, J. C. M.; D'Villa -Silva, M.; Simões, F. C.; Garcia, S.; Gaubeur, I.; Cordeiro, M. A. L.; Leite, E. R.; dos Santos, M. C., *Electrochimica Acta* **2013,** *96* (0), 243-252.
17. Tsiakaras, P. E., *Journal of Power Sources* **2007,** *171* (1), 107-112.
18. Wang, H.; Zhang, X.; Wang, R.; Ji, S.; Wang, W.; Wang, Q.; Lei, Z., *Journal of Power Sources* **2011,** *196* (19), 8000-8003.
19. Zheng, L.; Xiong, L.; Sun, J.; Li, J.; Yang, S.; Xia, J., *Catalysis Communications* **2008,** *9* (5), 624-629.

20. Zhou, B.; Han, S.; Raja, R.; Somorjai, G. A., Nanotechnology in Catalysis 3. Springer Science & Business Media: 2007; p. 356.
21. Zhu, M.; Sun, G.; Yan, S.; Li, H.; Xin, Q., *Energy & Fuels* **2008,** *23* (1), 403-407.
22. Almeida, T. S.; Kokoh, K. B.; De Andrade, A. R., *International Journal of Hydrogen Energy* **2011,** *36* (6), 3803-3810.
23. Antolini, E.; Gonzalez, E. R., *Catalysis Today* **2011,** *160* (1), 28-38.
24. Antolini, E., *Journal of Power Sources* **2007,** *170* (1), 1-12.
25. Antolini, E.; Colmati, F.; Gonzalez, E. R., *Electrochemistry Communications* **2007,** *9* (3), 398-404.
26. Bagotskii, V. S., Electrocatalysis. In *The Great Soviet Encyclopedia*, 3 ed.; The Gale Group, Inc.: 1979.
27. Baranova, G.Nanoparticles. http://by.genie.uottawa.ca/~baranova/Nano.htm. (accessed 14 December 2014)
28. Beyhan, S.; Coutanceau, C.; Léger, J.-M.; Napporn, T. W.; Kadırgan, F., *International Journal of Hydrogen Energy* **2013,** *38* (16), 6830-6841.
29. Beyhan, S.; Léger, J.-M.; Kadırgan, F., *Journal of Power Sources* **2013,** *242* (0), 503-509.
30. Beyhan, S.; Léger, J.-M.; Kadırgan, F., *Applied Catalysis B: Environmental* **2013,** *130–131* (0), 305-313.
31. Bommersbach, P.; Mohamedi, M.; Guay, D., *Journal of The Electrochemical Society* **2007,** *154* (8), B876-B882.
32. Bonesi, A. R.; Moreno, M. S.; Triaca, W. E.; Luna, A. M. C., *International Journal of Hydrogen Energy* **2010,** *35* (11), 5999-6004.
33. Bonesi, A.; Garaventa, G.; Triaca, W. E.; Castro Luna, A. M., *International Journal of Hydrogen Energy* **2008,** *33* (13), 3499-3501.
34. Chu, Y. H.; Shul, Y. G., *International Journal of Hydrogen Energy* **2010,** *35* (20), 11261-11270.
35. Colmati, F.; Antolini, E.; Gonzalez, E. R., *Journal of Alloys and Compounds* **2008,** *456* (1–2), 264-270.
36. Colmati, F.; Antolini, E.; Gonalez, E. R., *Journal of The Electrochemical Society* **2007,** *154* (1), B39-B47.
37. Colmati, F.; Antolini, E.; Gonzalez, E. R., *Applied Catalysis B: Environmental* **2007,** *73* (1–2), 106-115.
38. Correa, P. d. S.; da Silva, E. L.; da Silva, R. F.; Radtke, C.; Moreno, B.; Chinarro, E.; Malfatti, C. d. F., *International Journal of Hydrogen Energy* **2012,** *37* (11), 9314-9323.
39. Corti, H. R.; Gonzalez, E. R., *Direct Alcohol Fuel Cells: Materials, Performance, Durability and Applications* **2013,** (1), 379.
40. Cunha, E. M.; Ribeiro, J.; Kokoh, K. B.; de Andrade, A. R., *International Journal of Hydrogen Energy* **2011,** *36* (17), 11034-11042.
41. de Souza, J. P. I.; Queiroz, S. L.; Bergamaski, K.; Gonzalez, E. R.; Nart, F. C., *The Journal of Physical Chemistry B* **2002,** *106* (38), 9825-9830.

42. De Souza, R. F. B.; Parreira, L. S.; Silva, J. C. M.; Simões, F. C.; Calegaro, M. L.; Giz, M. J.; Camara, G. A.; Neto, A. O.; Santos, M. C., *International Journal of Hydrogen Energy* **2011,** *36* (18), 11519-11527.
43. Delime, F.; Léger, J. M.; Lamy, C., *Journal of Applied Electrochemistry* **1999,** *29* (11), 1249-1254.
44. Demirci, U. B., *Journal of Power Sources* **2007,** *173* (1), 11-18.
45. Friedrich, K. A.; Henglein, F.; Stimming, U.; Unkauf, W., *Electrochimica Acta* **2000,** *45* (20), 3283-3293.
46. Fujiwara, N.; Friedrich, K. A.; Stimming, U., *Journal of Electroanalytical Chemistry* **1999,** *472* (2), 120-125.
47. Hable, C. T.; Wrighton, M. S., *Langmuir* **1993,** *9* (11), 3284-3290.
48. Hitmi, H.; Belgsir, E. M.; Léger, J. M.; Lamy, C.; Lezna, R. O., *Electrochimica Acta* **1994,** *39* (3), 407-415.
49. Ianniello, R.; Schmidt, V. M.; Rodríguez, J. L.; Pastor, E., *Journal of Electroanalytical Chemistry* **1999,** *471* (2), 167-179.
50. Jiang, L.; Colmenares, L.; Jusys, Z.; Sun, G. Q.; Behm, R. J., *Electrochimica Acta* **2007,** *53* (2), 377-389.
51. Jiang, L.; Sun, G.; Sun, S.; Liu, J.; Tang, S.; Li, H.; Zhou, B.; Xin, Q., *Electrochimica Acta* **2005,** *50* (27), 5384-5389.
52. Kim, J. H.; Choi, S. M.; Nam, S. H.; Seo, M. H.; Choi, S. H.; Kim, W. B., *Applied Catalysis B: Environmental* **2008,** *82* (1–2), 89-102.
53. Kowal, A.; Li, M.; Shao, M.; Sasaki, K.; Vukmirovic, M. B.; Zhang, J.; Marinkovic, N. S.; Liu, P.; Frenkel, A. I.; Adzic, R. R., *Nat Mater* **2009,** *8* (4), 325-330.
54. Lamy, C.; Rousseau, S.; Belgsir, E. M.; Coutanceau, C.; Léger, J. M., *Electrochimica Acta* **2004,** *49* (22–23), 3901-3908.
55. Lamy, C.; Coutanceau, C.; Leger, J.-M., *Catalysis for Sustainable Energy Production* **2009,** (1).
56. Lee, E.; Murthy, A.; Manthiram, A., *Electrochimica Acta* **2011,** *56* (3), 1611-1618.
57. Leite, E. R., Nanocrystals Assembled from the Bottom Up. In *Encyclopedia of Nanoscience and Nanotechnology*, Nalwa, H. S., Ed. American Scientific: 2004 Vol. 6, pp 537-554.
58. Maillard, F.; Schreier, S.; Hanzlik, M.; Savinova, E. R.; Weinkauf, S.; Stimming, U., *Physical Chemistry Chemical Physics* **2005,** *7* (2), 385-393.
59. Neto, A. O.; Dias, R. R.; Tusi, M. M.; Linardi, M.; Spinacé, E. V., *Journal of Power Sources* **2007,** *166* (1), 87-91.
60. Office of Energy Efficiency & Renewable Energy, Fuel Cells-Basics. http://energy.gov/eere/fuelcells/fuel-cells-basics.(accessed14Dec18)
61. Oliveira Neto, A.; Giz, M. J.; Perez, J.; Ticianelli, E. A.; Gonzalez, E. R., *Journal of The Electrochemical Society* **2002,** *149* (3), A272-A279.
62. Piersma, B. J.; Greatbatch, W. *Some Aspects of Electrocatalysis: A Study Of Titanium and Tantalum whenAlloyed with the Platinum Group Metals*; Johnson Matthey Public Limited Company: UK, 1986.

63. Qiao, Y.; Li, C. M.; Bao, S.-J.; Bao, Q.-L., *Journal of Power Sources* **2007,** *170* (1), 79-84.
64. Ramos, S. G.; Calafiore, A.; Bonesi, A. R.; Triaca, W. E.; Castro Luna, A. M.; Moreno, M. S.; Zampieri, G.; Bengio, S., *International Journal of Hydrogen Energy* **2012,** *37* (19), 14849-14853.
65. Ribadeneira, E.; Hoyos, B. A., *Journal of Power Sources* **2008,** *180* (1), 238-242.
66. Ribeiro, J.; dos Anjos, D. M.; Kokoh, K. B.; Coutanceau, C.; Léger, J. M.; Olivi, P.; de Andrade, A. R.; Tremiliosi-Filho, G., *Electrochimica Acta* **2007,** *52* (24), 6997-7006.
67. Ribeiro, J.; dos Anjos, D. M.; Léger, J. M.; Hahn, F.; Olivi, P.; de Andrade, A. R.; Tremiliosi-Filho, G.; Kokoh, K. B., *Journal of Applied Electrochemistry* **2008,** *38* (5), 653-662.
68. Rousseau, S.; Coutanceau, C.; Lamy, C.; Léger, J. M., *Journal of Power Sources* **2006,** *158* (1), 18-24.
69. Schmidt, V. M.; Ianniello, R.; Pastor, E.; González, S., *The Journal of Physical Chemistry* **1996,** *100* (45), 17901-17908.
70. Simões, F. C.; dos Anjos, D. M.; Vigier, F.; Léger, J. M.; Hahn, F.; Coutanceau, C.; Gonzalez, E. R.; Tremiliosi-Filho, G.; de Andrade, A. R.; Olivi, P.; Kokoh, K. B., *Journal of Power Sources* **2007,** *167*(1), 1-10.
71. Song, S.; He, C.; Liu, J.; Wang, Y.; Brouzgou, A.; Tsiakaras, P., *Applied Catalysis B: Environmental* **2012,** *119–120* (0), 227-233.
72. Spinacé, E. V.; Farias, L. A.; Linardi, M.; Neto, A. O., *Materials Letters* **2008,** *62* (14), 2099-2102.
73. Spinacé, E. V.; Linardi, M.; Neto, A. O., *Electrochemistry Communications* **2005,** *7* (4), 365-369.
74. Tayal, J.; Rawat, B.; Basu, S., *International Journal of Hydrogen Energy* **2011,** *36* (22), 14884-14897.
75. Tayal, J.; Rawat, B.; Basu, S., *International Journal of Hydrogen Energy* **2012,** *37* (5), 4597-4605.
76. Tedsree, K. Study of Structure and Electronic Effect Aspects of Nanocatalyst for Formic Acid Electro-oxidation. University of Oxford, 2010.
77. Teran, F. E.; Santos, D. M.; Ribeiro, J.; Kokoh, K. B., *Thin Solid Films* **2012,** *520* (18), 5846-5850.
78. Thepkaew, J.; Therdthianwong, S.; Therdthianwong, A.; Kucernak, A.; Wongyao, N., *International Journal of Hydrogen Energy* **2013,** *38* (22), 9454-9463.
79. Tsiakaras, P. E., *Journal of Power Sources* **2007,** *171* (1), 107-112.
80. Vigier, F.; Coutanceau, C.; Hahn, F.; Belgsir, E. M.; Lamy, C., *Journal of Electroanalytical Chemistry* **2004,** *563* (1), 81-89.
81. Vigier, F.; Coutanceau, C.; Perrard, A.; Belgsir, E. M.; Lamy, C., *Journal of Applied Electrochemistry* **2004,** *34* (4), 439-446.

82. Wang, D.; Wang, J.; Lu, S.; Jiang, S. P., *Journal of Electroanalytical Chemistry* **2014,** *712* (0), 55-61.
83. Zhang, J., PEM Fuel Cell Electrocatalysts and Catalyst Layers: Fundamentals and Applications. Zhang, J., Ed. Springer Science & Business Media: 2008.
84. Zhou, W. J.; Song, S. Q.; Li, W. Z.; Zhou, Z. H.; Sun, G. Q.; Xin, Q.; Douvartzides, S.; Tsiakaras, P., *Journal of Power Sources* **2005,** *140* (1), 50-58.
85. Zhou, W.; Zhou, Z.; Song, S.; Li, W.; Sun, G.; Tsiakaras, P.; Xin, Q., *Applied Catalysis B: Environmental* **2003,** *46* (2), 273-285.
86. Zhu, M.; Sun, G.; Yan, S.; Li, H.; Xin, Q., *Energy & Fuels* **2008,** *23* (1), 403-407.
87. Lamy, C.; Lima, A.; LeRhun, V.; Delime, F.; Coutanceau, C.; Léger, J.-M., *Journal of Power Sources* **2002,** *105* (2), 283-296.
88. Léger, J. M.; Rousseau, S.; Coutanceau, C.; Hahn, F.; Lamy, C., *Electrochimica Acta* **2005,** *50* (25–26), 5118-5125.
89. Bonesi, A.; Triaca, W. E.; Luna, A. C., *Portugaliae Electrochimica Acta* **2009,** *27* (3), 9.
90. Wang, Z.-B.; Yin, G.-P.; Lin, Y.-G., *Journal of Power Sources* **2007,** *170* (2), 242-250.
91. 1. García-Rodríguez, S.; Rojas, S.; Peña, M. A.; Fierro, J. L. G.; Baranton, S.; Léger, J. M., *Applied Catalysis B: Environmental* **2011,** *106* (3–4), 520-528.
92. Rasch, B.; Iwasita, T., *Electrochimica Acta* **1990,** *35* (6), 989-993.
93. Rodríguez, J. L.; Pastor, E.; Xia, X. H.; Iwasita, T., *Langmuir* **2000,** *16* (12), 5479-5486.
94. Silva-Chong, J.; Méndez, E.; Rodríguez, J. L.; Arévalo, M. C.; Pastor, E., *Electrochimica Acta* **2002,** *47* (9), 1441-1449.
95. Kokoh, K. B.; Hahn, F.; Belgsir, E. M.; Lamy, C.; de Andrade, A. R.; Olivi, P.; Motheo, A. J.; Tremiliosi-Filho, G., *Electrochimica Acta* **2004,** *49* (13), 2077-2083.
96. Andreaus, B.; Maillard, F.; Kocylo, J.; Savinova, E. R.; Eikerling, M., *The Journal of Physical Chemistry B* **2006,** *110* (42), 21028-21040.
97. Arenz, M.; Stamenkovic, V.; Blizanac, B. B.; Mayrhofer, K. J.; Markovic, N. M.; Ross, P. N., *Journal of Catalysis* **2005,** *232* (2), 402-410.
98. Morimoto, Y.; Yeager, E. B., *Journal of Electroanalytical Chemistry* **1998,** *441* (1–2), 77-81.
99. Wang, K.; Gasteiger, H. A.; Markovic, N. M.; Ross Jr, P. N., *Electrochimica Acta* **1996,** *41* (16), 2587-2593.
100. Crabb, E. M.; Marshall, R.; Thompsett, D., *Journal of The Electrochemical Society* **2000,** *147* (12), 4440-4447.
101. Götz, M.; Wendt, H., *Electrochimica Acta* **1998,** *43* (24), 3637-3644.
102. Ma, Y.; Wang, H.; Ji, S.; Linkov, V.; Wang, R., *Journal of Power Sources* **2014,** *247* (0), 142-150.

Chapter 2

Experimental Theory and Techniques

2.1 Electrochemical Cells and Electrochemical Reactions

Electrochemical cells are typically composed of two or three electrodes. A two-electrode cell is the simplest system used to study the current/voltage characteristics. For large-scale electrolytic and galvanic cells or experiments carried out in non-aqueous solutions with low conductivity, a three-electrode system is preferable. Figure 2.1 illustrates a three-electrode cell with a reference electrode (RE), a working electrode (WE), and a counter electrode (CE). A current in the three-electrode cell flows between the working electrode, where the electrode reaction under study is occurring [39], and the counter or auxiliary electrode. In fact, the behaviour of working electrodes is not affected by electrochemical properties of counter electrodes. Consequently, an auxiliary electrode material is not specific, but it must not produce substances which will reach the surface of working electrodes and interfere with reactions of interest during electrolysis [31].

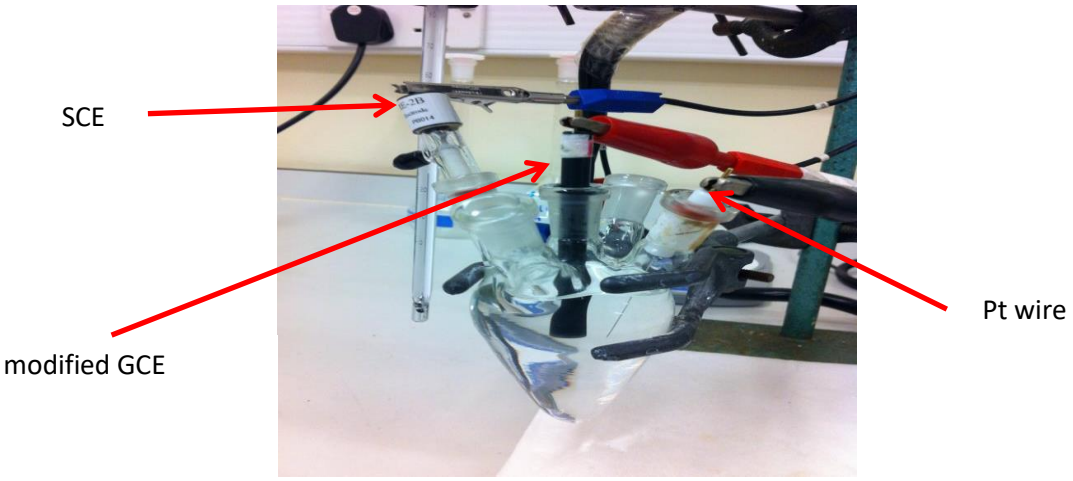


Figure 2.1 - Three-electrode electrochemical cell with standard calomel electrode (SCE) as RE, a modified glassy carbon electrode (modified GCE) as WE, and a Pt wire as CE.

A potential difference at the electrode/solution interface, $\Delta\phi_{m/s,}$ created by the net charge separation developed between the electrode and the solution, is given by Equation (2.1):

$$\Delta\phi_{m/s} = \phi_m - \phi_s \qquad \text{Equation (2.1)}$$

where ϕ_m is the electrical potential at the electrode and ϕ_s is the electrical potential of the solution.

To measure the potential difference, a reference electrode and a complete electrical circuit are required. Due to the electrode/solution potential drop and the constant voltage, the potential difference between the working electrode and the reference electrode, E, can be expressed as:

$$E = (\phi_m^{test} - \phi_{solution}) - (\phi_m^{ref} - \phi_{solution}) = \phi_m^{test} - \phi_m^{ref} \qquad \text{Equation (2.2)}$$

In an electrochemical cell, the potential, E, is applied to the working electrode to trigger a current flow. The difference between the applied potential, E, and the equilibrium potential, E_e, is termed overpotential and it is given by Equation (2.3) [21]:

$$\eta = E - E_e \qquad \text{Equation (2.3)}$$

where η is the overpotential.

The currents that flow into the electrochemical cell, i, is given by Equation (2.4):

$$i = \int nFjdA \qquad \text{Equation (2.4)}$$

where n is the number of electrons transferred per mole of a reactant, F is the Faraday's constant (96485 C mol^{-1}), A is the electrode area (cm^2), and j is the flux of electroactive species reaching the electrode surface (mol cm^{-2} s^{-1}).

For kinetically limited processes, j can be expressed as:

$$j = k[\text{Reactant}]_{surface} \qquad \text{Equation (2.5)}$$

where k is the heterogeneous rate constant of the electron transfer reaction.

In two-electrode cells, a current flow between two electrodes is induced by the applied potential, the solution experiences ohmic drop. By taking the ohmic drop into account, the potential difference between the working electrode and the reference electrode can be expressed as:

$$E = (\phi_m - \phi_s) + iR + (\phi_s - \phi_{ref}) \qquad \text{Equation (2.6)}$$

The ohmic drop in solution of the systems with a small current flow between working and reference electrodes (microelectrode experiments) is negligible. The term *iR* can be ignored and the potentials applied to working electrodes are directly related to the driving force term, (ϕ_m-ϕ_s), accordingly. The *iR* term, however, is no longer negligible with large electrodes. In this case, changes in the applied potential are not limited to changes in (ϕ_m-ϕ_s). Particularly, the iR term is altered by changes in the applied potential due to changes induced by the applied potential change in the current flowing through the cell. Furthermore, passing large currents through the reference electrode can change its chemical compositions. Subsequently, the term $\phi_s - \phi_{ref}$ may no longer be constant. These incidents lead to the current being not readily related to the potential drop at the working electrode/solution interface. To overcome such problems, voltammetric measurements are carried out using a three-electrode system. To ensure that the current flows only between the working and counter electrodes, a potentiostat is employed. The potential of the working electrode is now held relative to the stable reference electrode since the potentiostat used also ensures that no current passes through the reference electrode [21].

2.2 Kinetics of Electrode Reactions

Consider the general aqueous, heterogeneous electron transfer reaction shown by Equation 2.7:

$$O_{(aq)} + ne^- \rightleftarrows R_{(aq)} \qquad \text{Equation (2.7)}$$

where *O(aq)* represents the oxidised species in aqueous solution, *n* is the number of electrons transferred in the reaction, and *R(aq)* is the reduced species in aqueous solution. In this

reaction, the reduction and oxidation reactions proceed with rate constants k_c and k_a, respectively.The reaction kinetics are well described by the Butler-Volmer Equations:

$$k_a = k_0 exp\left[\frac{\alpha_a nF(E - E^0)}{RT}\right] \qquad \text{Equation (2.8)}$$

and

$$k_c = k_0 exp\left[\frac{-\alpha_c nF(E - E^0)}{RT}\right] \qquad \text{Equation (2.9)}$$

where k_0 is the standard rate constant (cm s^{-1}), α_a and α_c are the anodic and cathodic transfer coefficients, respectively, and $\alpha_a = 1-\alpha_c$.

Both Equations are obtained via a linearised free energy transition of O into R. The $\alpha_{c/a}$ value reflects the position of the transition state along the normalised coordinate. Therefore, the $\alpha_{c/a}$ value is approximately 1/2 for most cases. By assuming the reaction operates under kinetic control, the reaction rate observed at the electrode surface is measured in terms of total current (*I*) *via* Equation (2.10):

$$I = i_a + i_c = nFA(k_a[R]_{x=0} - k_c[O]_{x=0}) \qquad \text{Equation (2.10)}$$

where i_a and i_c are anodic current and cathodic current, respectively. The subscript *x=0* refers to a reaction site very close to the electrode surface.

At equilibrium ($\Delta G = 0$ and $\Delta G^o = -RT\ln K$) and under standard conditions, the net current is zero and $i_a = -i_c = i_0$. Thus, the concentrations of R and O at x=0 are given by the Nernst Equation [27]:

$$E^0 = \frac{RT}{nF} lnK = \frac{RT}{nF} ln\frac{[R]_{x=0}}{[O]_{x=0}} \qquad \text{Equation (2.11)}$$

where E^0 is the standard cell potential, R is the universal gas constant (8.314 J mol^{-1} K^{-1}), T is an absolute temperature in K, n is the number of electrons transferred in the reaction, F is Faraday's constant, and K is the equilibrium constant of the reaction 2.7.

2.3 Material Transport

An overall rate of reaction can be affected, or in some cases dominated, by the rate of transport of a species in solution to the electrode surface. Typically, electrolysis involves charge transfer between an electrode and a species in solution. The whole process consists of a series of either simultaneous or consecutive steps including mass transfer, chemical or other surface reactions, and electron transfer (Figure 2.2) [35]. The rate of the electron transfer can be affected by the electrode potential. In fact, the electrode potential and the electron transfer process are related to each other exponentially. Thus, an exponential increase in the reaction rate and the current with increasing electrode potential would be predicted from the electron transfer model. This would mean that it is possible to pass unlimited quantity of current at sufficiently high overpotentials. In reality, this does not occur owing to mass transport limitations [9, 27, 24-25].

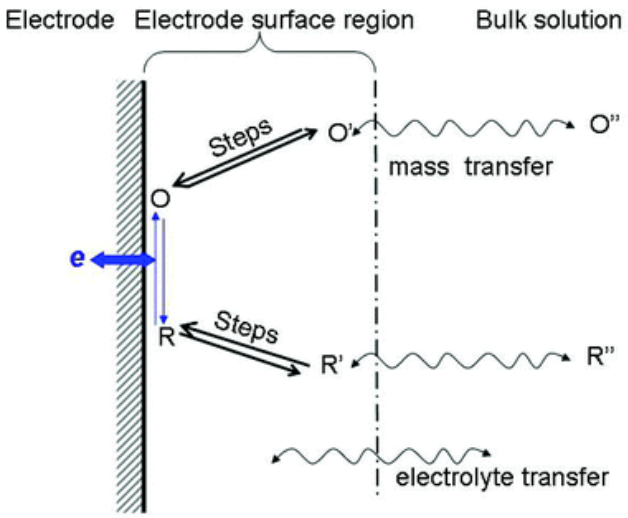


Figure 2.2-Schematic illustration of the processes in solution phase electrochemical reactions [35].

To rationalise this phenomenon, the current encountered in the electrode kinetics (i_c) is considered and expressed as:

$$i_c = -nFAk_c[O]_{x=0} \qquad \text{Equation (2.12)}$$

where A is the fixed electrode area (cm^2), k_c is the rate constant of the forward reaction in Equation (2.7) and $[O]_{x=0}$ is the surface concentration of the oxidised species. Since the electrode area is fixed, the reaction can be controlled explicitly by the rate constant (k_c) and the surface concentration of the reactant ($[O]_{x=0}$). In the case of a large rate constant for the forward electron transfer process made, for example, by holding the electrode at sufficiently negative or positive potentials, any reactant that is close to the electrode/solution interface will immediately be converted into products and the amount of fresh reactants reaching the interface from the bulk solution will control the current. Therefore, the movement of reactants to and from the electrode/solution interface is important in predicting the current flow [8]. Mass transport can be categorised into three forms: diffusion, convection, and migration. In this thesis, only diffusion will be discussed.

2.4 Diffusion

Diffusion is the net movement of a substance, such as an atom, ion, or molecule, from a region of high concentration to a region of low concentration [5]. Diffusion occurs in all solutions and is caused by a concentration gradient of solutes. The maximisation of entropy accounts for the uniformisation of uneven concentration distribution. Therefore, it is the main driving force for this process [16]. In electrolysis, diffusion is particularly significant because the conversion of reactants only takes place at the electrode surface. As a result, a higher concentration of products will be present near the electrode surface than in the bulk solution. In other words, the concentration of reactants at the electrode is lower than that in the bulk solution. Figure 2.3 illustrates the diffusion process of a particle from bulk solution to the electrode surface.

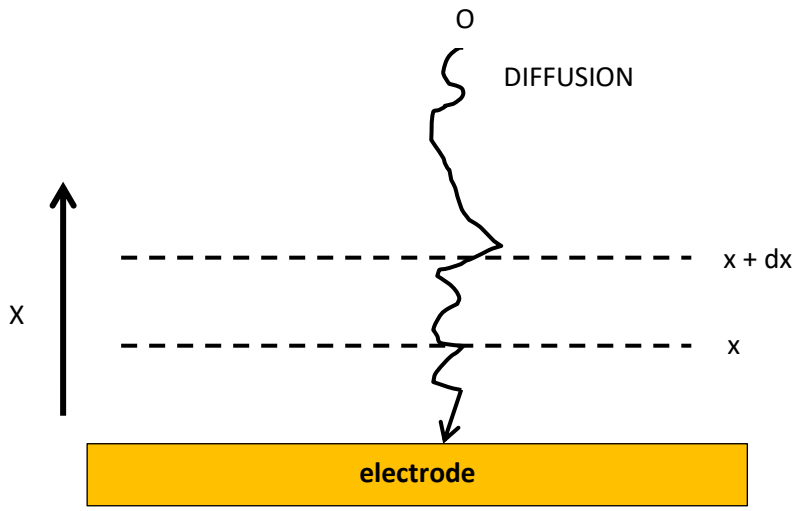


Figure 2.3- Diffusion process [12].

The diffusion rate of substances can be predicted by Fick's laws. The first law is expressed as:

$$J = -D\left(\frac{\partial C}{\partial x}\right) \qquad \text{Equation (2.13)}$$

The first law relates the diffusional flux (J) of species to the concentration gradient in direction x ($\frac{\partial C}{\partial x}$) and the diffusion coefficient (D). The negative sign means that the substance moves down a concentration gradient (i.e. from high to low concentration region). In some measurements, it is crucial to know the variation of concentration with time. This can be predicted from the first law and the result of the prediction is Fick's second law given as:

$$\frac{\partial C}{\partial t} = D\left(\frac{\partial^2 C}{\partial x^2}\right) \qquad \text{Equation (2.14)}$$

The rate of concentration change as a function of time ($\frac{\partial C}{\partial t}$) is proportional to the change in the concentration gradient. It can be stated that the more the concentration changes, the greater the diffusion rate [28]. It is often found that diffusion is the most crucial transport process for many electrolytic reactions. Fick's second law is an important relationship because it allows variations in the concentration of different species with time in an electrochemical cell to be predicted [12].

2.5 Potential Step: Chronoamperometry

Chronoamperometry is the current-time measurement under potentiostatic control (Figure 2.4). The working electrode potential is stepped from a value at which no faradaic reaction or no redox process occurs (E_1) to a potential at which the surface concentration of electroactive species is effectively zero or a value to which the reduction or oxidation is driven (E_2) [21].

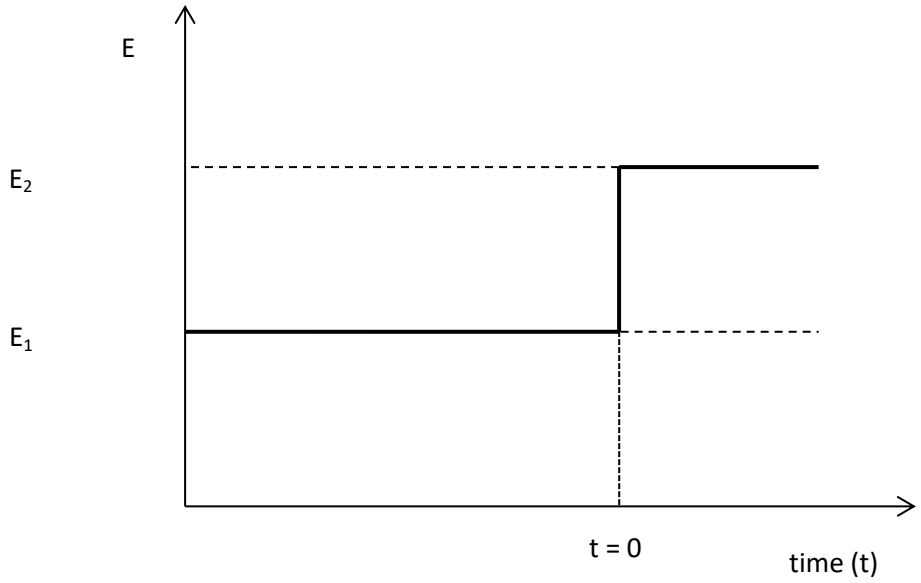


Figure 2.4 - Potential step chronoamperometry measurement.

Immediately after the potential step, a large current is detected which then decreases steadily with time. The initial large current is a non-Faradaic current as it is not produced by any electrochemical reaction at the electrode/electrolyte interface. The concentration gradients are excruciatingly large shortly after the potential step from E_1 to E_2. This is because there has been little time for any depletion of the electroactive species. As a result, a large amount of currents flowing are measured at the beginning of the measurement.

As the depletion progresses, the diffusion layer thickness increases and the current eventually converges to zero [21] (see Figure 2.5).

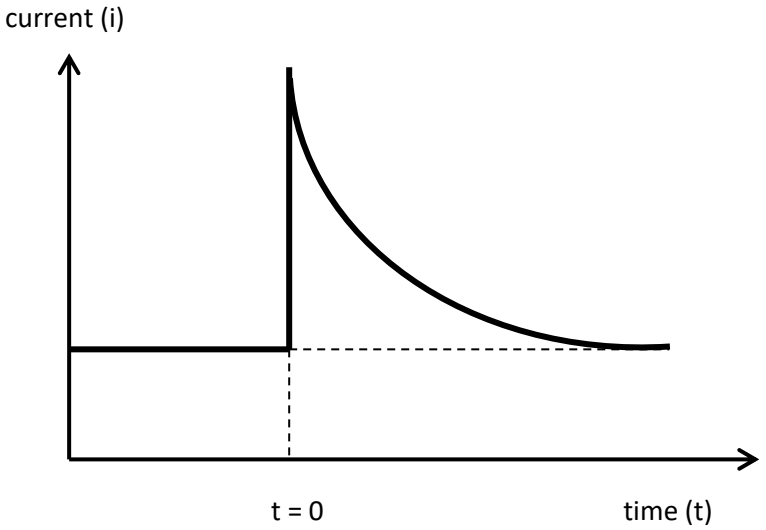


Figure 2.5- Current response over time in a potential step chronoamperometry experiment [13].

In a potentiostatic experiment such as chronoamperometry, the change in electrical current as a function of time is described by the Cottrell Equation (Equation 2.15):

$$|i| = \frac{nFAD^{1/2}C}{\pi^{1/2}t^{1/2}} \qquad \text{Equation (2.15)}$$

where A is the area of the electrode (cm^2), D is the diffusion coefficient of the reactant ($cm^2\ s^{-1}$), C is the concentration of the reactant in bulk solution ($mol\ cm^{-3}$), n is the number of electrons involved in the electrode reaction, and F is Faraday's constant (96485 $C\ mol^{-1}$).

As can be seen in Equation (2.15), the measured current, *i*, is inversely proportional to the square root of time ($t^{1/2}$). An electrode reaction proceeding under diffusion control will demonstrate a linear correlation between the current measured in a potential step experiment and $1/(t^{1/2})$. The slope of the plot of *i* versus $t^{-1/2}$ can be used to estimate diffusion coefficients.

2.6 Cyclic Voltammetry (CV)

Cyclic voltammetry is an electrochemical technique which is generally used to study electrochemical reactions of an analyte in solution [7, 24] and is particularly useful for determining rates of oxidation/reduction reactions and to investigate reaction mechanisms [27]. In a cyclic voltammetric experiment, the potential applied to a working electrode is ascended linearly against time in a similar manner to linear sweep voltammetry (LSV). The potential ramp in the LSV measurement terminates when a set potential is reached. However, in cyclic voltammetry, the electrode potential is further swept in the opposite direction. During a single CV experiment, the potential cycling can take place multiple times (see Figure 2.6). The plot of currents measured at the working electrode versus the applied potentials is referred to as a cyclic voltammogram.

2.7 Cyclic Voltammetry Experiment

In cyclic voltammetry, the electrode potential ramping linearly against time is scanned from E_1 to E_2 and from E_2 back to the original potential value, E_1 as shown in Figure 2.6. The rate of potential change over time during each cyclical phase is referred to as a scan rate. Experimentally, potentials are applied between the working and the reference electrodes, while current is measured between the working and counter electrodes. The current responses (*i*) obtained from the measurements are then plotted against applied potentials (E).

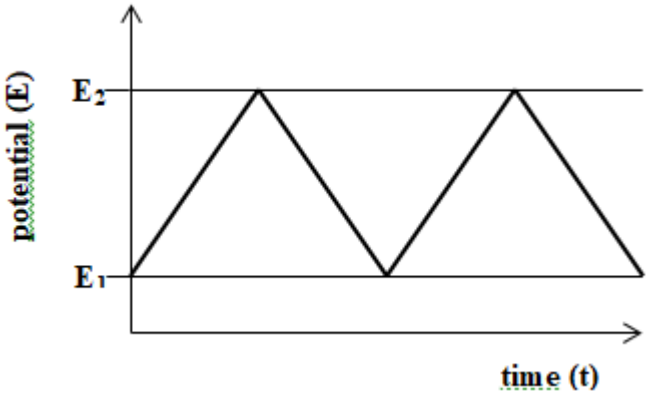


Figure 2.6 – Variation of the applied potential as a function of time in a cyclic voltammetry experiment [21].

In the forward scan of potential cycling, a current peak is produced by reduction or oxidation (depending on an initial sweep direction) of studied analytes over a range of scanned potentials. Assuming that there exist electroactive species capable of undergoing reduction or oxidation at the electrode surface in the system, the cathodic or anodic current begins to rise as potentials, at which electrode reactions can occur, are reached. As the concentration of the analyte close to the electrode surface is diminished, the current begins to fall [27]. For a reversible system, the product of the reduction or oxidation formed in the forward scan is oxidised or reduced, respectively, during the reverse scan at its oxidation or reduction potential. As a result, a current peak corresponding to oxidation or reduction is produced. The reversibility of a redox couple can be reflected by the peak potential and the peak size on the

reverse scan. The peak size or height of the forward current peak is of the same magnitude as that of the reverse current peak and they are separated by approximately 57 mV at 25 ^{o}C. This separation value is not dependent on the scan rate [21]. In cyclic voltammetry, the acquired total current is a sum of Faradaic (I_F) and capacitive charging (I_C) currents. I_F is a contribution from Faradaic reactions and $I_{C,}$ which is proportional to the potential sweep rate, is a contribution from the interfacial region between an electrode and its surrounding electrolytes known as the electrical double layer [27]. The data from CV measurements provide information about redox potentials and the rates of electrochemical reactions. In the case that peak current is proportional to the square root of scan rate (Randles-Sevcik, Equation 2.19), it can be concluded that the reversible electron transfer process at the electrode surface occurs and the diffusion of electroactive species to the electrode surface limits the current due to the much faster electrode kinetics compared to the diffusion rate. If peak current is proportional to scan rate, it can be described that no Faradaic reactions occur on the electrode surface. The currents measured are capacitive contributions arising from charge separation in the electrical double layer. Direct proportionality between peak current and potential scan rate can also be found in the case of adsorbed species undergoing electrochemical reactions at the electrode surface [27]. If peak current is independent of scan rate, it can be described that the system under investigation establishes steady state conditions and a steady-state cyclic voltammogram can be obtained. These conditions can be achieved by scanning microelectrodes with low scan rates [27]. Direct current (DC) cyclic voltammetry is probably the most widely used method for studying electrode processes because both oxidation and reduction reactions can be studied conveniently from experiments [23-24, 26].

2.8 Cyclic Voltammetry with Electrochemically Reversible Systems

Electrochemical systems, either reversible or irreversible, are classified by their electrode kinetics and rate of diffusion. A system with electrode kinetics much faster than the diffusion rate is described as a reversible system. The final boundary condition for a reversible electro-reduction process, $O + ne^- \rightleftharpoons R$, is the Nernst Equation (Equation (2.16)):

$$E = E^0 + \frac{RT}{nF} ln \frac{[Ox]_{x=0}}{[Red]_{x=0}} \quad \text{Equation (2.16)}$$

where $[X]_{x=0}$ is the concentration of the electrode surface species. Figure 2.7 displays the cyclic voltammogram of a reversible electron transfer reaction.

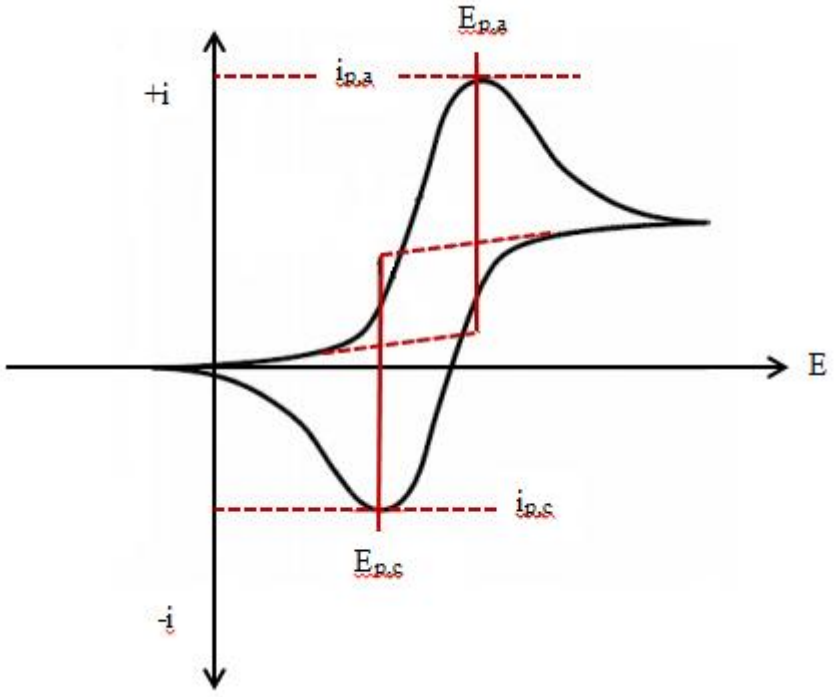


Figure 2.7 - Cyclic voltammogram for a reversible electron transfer reaction [30].

Note: $E_{p,c}$ and $E_{p,a}$ are the peak reduction and oxidation potentials and $i_{p,c}$ and $i_{p,a}$ are the peak cathodic and anodic currents, respectively.

$E_{p,a}$ and $E_{p,c}$ can be obtained directly from the cyclic voltammogram. For a reversible electrode process where n electrons are transferred at 25 ^{o}C, the difference between $E_{p,a}$ and $E_{p,c}$ (ΔE_p), which reflects the separation between the forward and reverse current peaks, can be estimated using Equation (2.17):

$$\Delta E_p\,(\mathrm{mV}) = \frac{56.6}{n} \qquad \text{Equation (2.17)}$$

where n is the number of electrons transferred in the process.

The $i_{p,a}$ to $i_{p,c}$ ratio is given by Equation (2.18):

$$\left|\frac{i_{p,a}}{i_{p,c}}\right| = 1 \qquad \text{Equation (2.18)}$$

The standard potential, E^0, for the reversible system of a redox couple can be estimated by averaging the two peak potentials. The concentration of the analyte involved in the oxidation or reduction reaction at peak potentials can be estimated by the Randles-Sevcik Equation (Equation (2.19)):

$$|i_p| = 0.4463\, n\, FAC\, (^{nFvD}/_{RT})^{1/2} \qquad \text{Equation (2.19)}$$

where i_p is the peak current (A), n is the number of electrons in the half-cell for the redox couple, v is the potential scan rate (V s^{-1}), F is Faraday's constant (96485 C mol^{-1}) , A is the electrode area (cm^2), R is the universal gas constant (8.314 J mol^{-1} K^{-1}), T is the absolute temperature (K), D is the diffusion coefficient of the analyte (cm^2 s^{-1}), and C is the concentration of the analyte in bulk solution (mol cm^{-3}).

At 25 ^oC, Equation (2.19) can be written as:

$$|i_p| = (2.687 * 10^5) n^{\frac{3}{2}} v^{\frac{1}{2}} D^{\frac{1}{2}} AC \qquad \text{Equation (2.20)}$$

The constant in Equation (2.20) has units of C mol^{-1} $V^{-1/2}$.

2.9 Cyclic Voltammetry with Electrochemically Irreversible Systems

A system with electrode kinetics slower than the rate of diffusion is described as an irreversible system. For a completely irreversible one-electron one-step reaction ($R \rightarrow O + e^-$), the same voltammetric profile is obtained from both linear sweep and cyclic voltammetry measurements because reduction cannot occur on reversing the scan direction (see Figure 2.8).

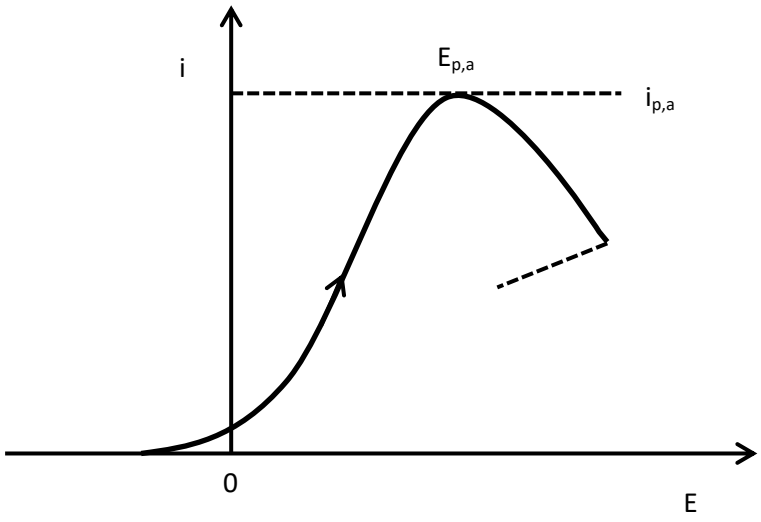


Figure 2.8 - Cyclic voltammogram of an irreversible electron transfer reaction [27].

The anodic peak current for the forward scan of the voltammogram shown in Figure 2.8 at 25 ^{o}C is given by Equarion (2.21).

$$i_{p,a} = 2.99 \times 10^5 \alpha^{1/2} A C_R D_R^{1/2} \nu^{1/2} \qquad \text{Equation (2.21)}$$

where $i_{p,a}$ is the anodic peak current (A), v is the scan rate (V s^{-1}), A is the electrode area (cm^2), D_R is the diffusion coefficient of the analyte (cm^2 s^{-1}), and C_R is the concentration of the analyte in bulk solution (mol cm^{-3}).

For the reduction of O to R, kinetic boundary condition (Equation (2.22)) substitutes the Nernstian condition for the irreversible system when no equilibrium is retained at the electrode surface.

$$\frac{i}{FA} = D_O \left[\frac{\partial C_O(x,t)}{\partial x}\right]_{x=0} = k_f(t) C_O(0,t) \qquad \text{Equation (2.22)}$$

where k_f is the rate constant.

In an irreversible electro-reduction process, no currents flow until the potential is considerably more negative than E_e. To drive the reduction of O to R, it requires a larger overpotential compared to that required to start the reduction of O species in the reversible electron transfer process. Therefore, the peak potential ($E_{p,c}$) appears at more negative potentials in irreversible systems [21]. In case of the irreversible electro-oxidation reaction, the peak potential ($E_{p,a}$) shifts to more positive potentials due to the effect of the kinetic limitations [27]. The peak current for an irreversible one-electron process at 298 K is given as:

$$\left|i_{p,c}\right| = (2.99 \times 10^5)\, \alpha^{1/2} A C_O D_O^{1/2} \nu^{1/2} \qquad \text{Equation (2.23)}$$

where $i_{p,c}$ is the cathodic peak current (A), ν is the scan rate (V s^{-1}), A is the electrode area (cm^2), D_O is the diffusion coefficient of the analyte (cm^2 s^{-1}), and C_O is the concentration of the analyte in bulk solution (mol cm^{-3}).

The peak potential and the difference between the peak potential and half-peak potential for electro-reduction are given by Equations (2.24) and (2.25):

$$E_{p,c} = E^{\ominus'} - \frac{RT}{\alpha_c n' F}\left[0.780 + ln\left(\frac{D_O^{1/2}}{k_0}\right) + 0.5 ln\left(\frac{\alpha_c n' F \nu}{RT}\right)\right] \qquad \text{Equation (2.24)}$$

$$\left|E_p - E_{p/2}\right| = \frac{1.857RT}{\alpha_c F} \qquad \text{Equation (2.25)}$$

where $E^{\ominus'}$ is the formal electrode potential and n' is the number of electrons in the rate-determining step [27].

Noticeably, for the irreversible electro-reduction systems, the peak current is dependent on the scan rate and shifts to more negative potentials at faster scan rates. It is estimated that E_p shifts by *ca.* -1.16(RT/αF) for each tenfold increase in the scan rate.

2.10 Cyclic Voltammetry with Electrochemically Quasi-reversible Systems

Electrochemical systems which are intermediate between reversible and irreversible systems are called quasi-reversible systems [22]. For electrode reactions with quasi-reversible behaviour, the surface concentrations of O and R species depend on the forward and reverse electron transfer rates and the rate of mass transfer. In comparison to the case of reversible kinetics, the separation of the forward and reverse current peaks in the systems with quasi-reversible kinetics is dependent on the scan rate and the peak current is non-proportional to the $\nu^{1/2}$. A noticeable reverse peak can be seen if only a considerably fast scan rate is used. This is possibly because almost all the product formed in the forward scan will diffuse into bulk solution and it is not available for the reverse reaction at slow scan rates [21].

Figure 2.9 shows the cyclic voltammograms for a reversible, a quasi-reversible, and an irreversible electron transfer reaction.

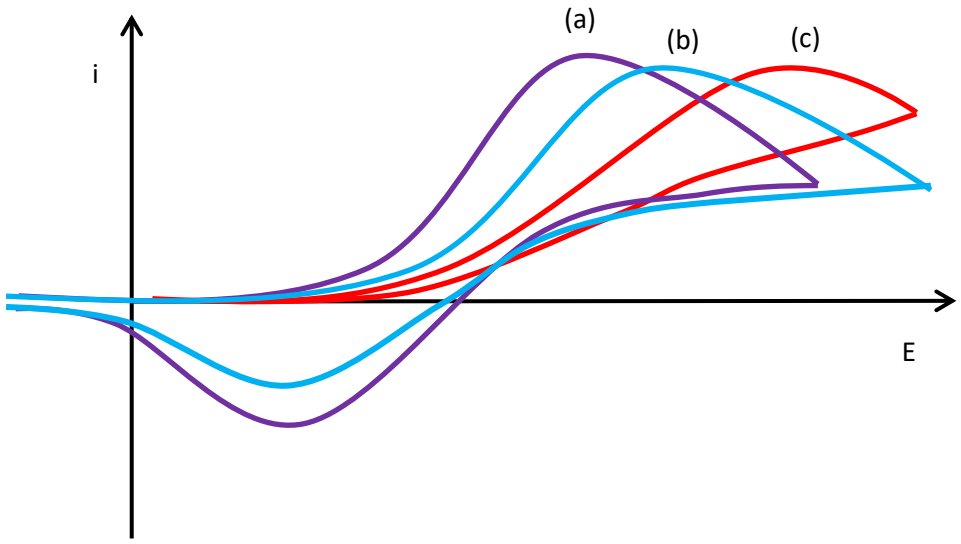


Figure 2.9 - Cyclic voltammograms for (a) a reversible, (b) a quasi-reversible, and (c) an irreversible electron transfer reaction [21].

Consider the one-electron, one-step reaction,

$$O_{(aq)} + e^- \underset{k_b}{\overset{k_f}{\rightleftharpoons}} R_{(aq)} \qquad \text{Equation (2.26)}$$

The boundary condition for a quasi-reversible reaction is given by Equation (2.27):

$$D_O \left(\frac{\partial C_O(x,t)}{\partial x}\right)_{x=0} = k_0 e^{-\alpha f[E(t)-E^0]}\{C_O(0,t) - C_R(0,t)e^{f[E(t)-E^0]}\} \qquad \text{Equation (2.27)}$$

The current, $i_{p,c}$, for a quasi-reversible electron transfer reaction is given by Equation (2.28):

$$|i_{p,c}| = FAD_O^{1/2} C_O f^{1/2} \nu^{1/2} \Psi(E) \qquad \text{Equation (2.28)}$$

where $f = \frac{F}{RT}$, ψ(E) is the wave function of a quasi-reversible system, A is the electrode area (cm^2), D_O is the diffusion coefficient of O ($cm^2\ s^{-1}$), C_O is the concentration of O in bulk solution (mol cm^{-3}), and v is the scan rate (V s^{-1}).

Heterogeneous Reactions

In electrocatalysis, a number of coupled heterogeneous chemical reactions can occur. The processes which take place on an electrode surface include electrode/electrolyte interactions and substrate adsorption/desorption, which can also be associated with mass transport [21]. For the reversible electrochemical reaction of a chemical species uniformly adsorbed onto an electrode surface ($O_{ad} + ne^- \rightleftharpoons R_{ad}$), changes in the shape of the cyclic voltammogram compared with that of a non-adsorbed species case are observed. This is because adsorbed species do not have to diffuse to the electrode surface [27]. Figure 2.10 shows the cyclic voltammogram for the reversible reaction of a surface-adsorbed species. On the anodic scan, the peak observed is attributed to the oxidation of the adsorbed species (R_{ad}) to form a product (O_{ad}). On the reverse (cathodic) scan, the product, which remains adsorbed to the electrode surface, is reduced to form the original reactant and reductive currents are generated. At potentials significantly more positive and negative than the oxidation and reduction potentials, respectively, the current drops back to zero. This phenomenon can be explained by a limited quantity of the adsorbed species, R_{ad}, presence on the surface. Once B_{ad} species has been converted electrochemically to O_{ad} species, no further electron transfer occurs. It is in contrast to the case of the solution phase reaction in which a fresh reactant is transported from bulk solution to the electrode surface by diffusion [21]. The shape of the cyclic voltammogram seen in Figure 2.10 is symmetrical with coincident oxidation and reduction peak potentials. This feature is characteristic of the electrode reaction controlled only by electron transfer kinetics [21, 27].

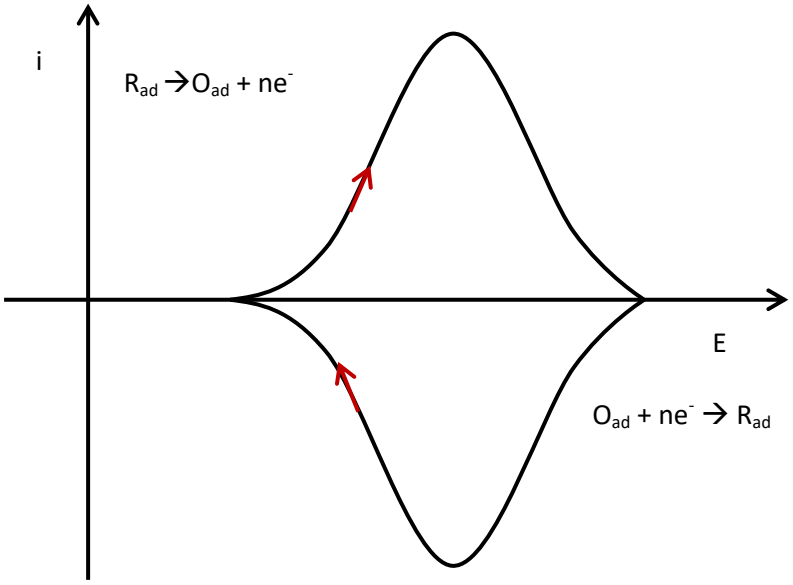


Figure 2.10 Cyclic voltammogram for the reversible reaction of adsorbed species [21].

For all electron transfer reactions of adsorbed species, the peak current is proportional to the scan rate (ν) not the square root of the scan rate ($\nu^{1/2}$) as exemplified by Equation (2.29).

$$i_{p,a} = \frac{n^2 F^2 \nu A \Gamma_{R_{ad},i}}{4RT} \qquad \text{Equation (2.29)}$$

where $\Gamma_{R_{ad},i}$ is the surface excess of R_{ad} before the sweep and $i_{p,a}$ is the oxidation peak current for a reversible process.

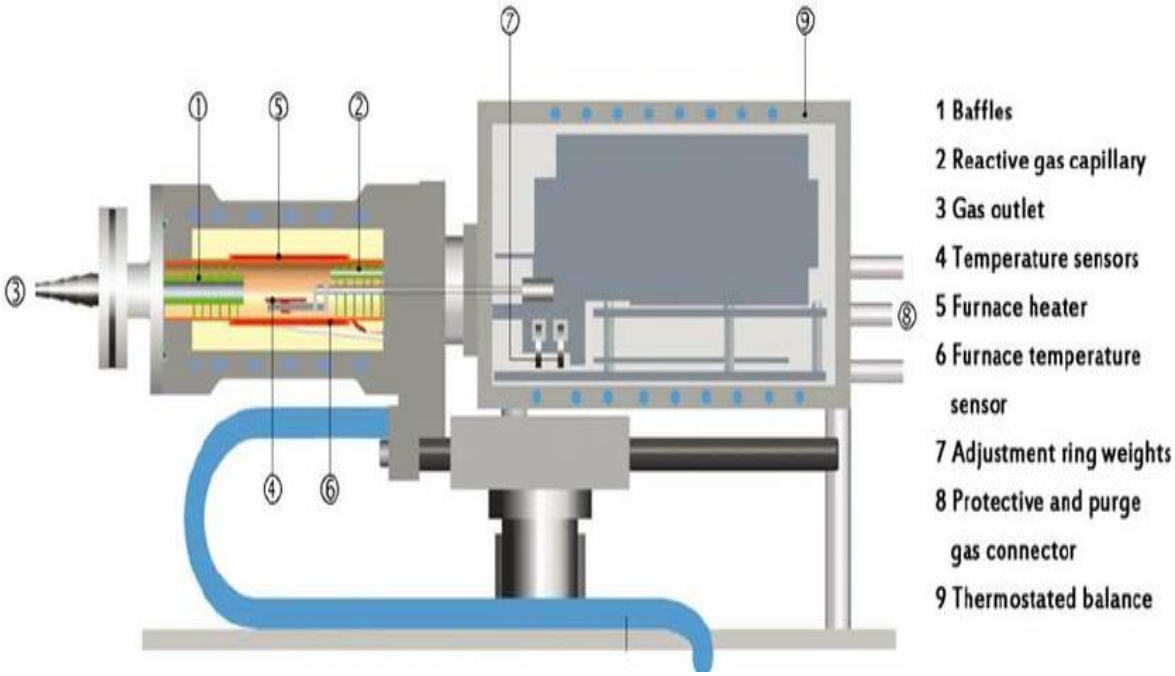
In cases of slower kinetics, desorption of the unstable surface-adsorbed species from the electrode surface, and replenishment of the electroactive species at the electrode surface by mass transfer from bulk solution during the potential cycling, deviation from a total symmetry of the cyclic voltammogram will occur. Any deviation in the voltammetric behaviour can be used to investigate the stability and nature of the bond between the surface and adsorbed species [21].

2.11 Thermogravimetric Analysis

Thermogravimetric analysis (TGA) is an analytical technique which is used to evaluate the thermal stability of materials and to determine a fraction of their volatile components by monitoring weight changes as a sample is heated. Thermogravimetric measurements are normally conducted in air or an inert atmosphere such as He or Ar. The weight of remaining residues in a sample holder (i.e. TGA pan) is recorded as a function of increasing temperature (see Figure 2.11). Additionally, some TGA instruments can record the temperature difference between the sample and one or more reference pans or the heat flow difference between the sample pan and the reference pan. TGA can be employed to determine loadings of metal catalysts supported on carbon materials such as carbon nanotubes. The weight loss in this case is typically due to oxidation of carbon to carbon dioxide gas and the weight gain is due to oxidation of metal catalyst to solid oxides. In general, TGA instruments can be categorised into two types: vertical and horizontal balance. The vertical balance instruments have a sample pan hanging from, or located above, the balance, and do not have a reference pan except in the case of some models. The horizontal balance instruments have both sample and reference pans and are capable of performing differential thermal analysis (DTA) and differential scanning calorimetry (DSC) measurements. The optimal maximum temperature (T_{max}) is assigned for TGA measurements. Theoretically, all chemical reactions must be complete and stable sample weight must be obtained at T_{max} [4].



A



B

Figure 2.11 – Mettler Toledo TGA/DSC 1 [18] (A) and schematic diagram of Mettler Toledo TGA/DSC 1 [36] (B)

2.12 X-ray Diffraction

2.12.1 Generation of X-rays

X-rays are electromagnetic waves with photon energies typically in the range of 100 eV to 100 keV. The short wavelength X-rays or hard X-rays are used for diffraction applications. Their photon wavelengths are in the range of a few Angstroms to 0.1 Angstrom, equivalent to approximately 1 keV to 120 keV. The wavelengths of X-rays are ideally suitable for examining the structural arrangement of atoms or molecules in a wide variety of materials because they are comparable to the size of atoms. The X-rays are able to penetrate deep into the materials. Thus, the information about the bulk structure can be determined. X-rays can be generated by either X-ray tubes as shown in Figure 2.12 or synchrotron radiation. In laboratory X-ray instruments, they are produced in an X-ray tube by bombarding a stationary or rotating target with an electron beam accelerated across a high voltage field. When the collision between electrons and atoms occurs, electrons are slowed down or deflected by the electric field around the atoms in the target and a continuous spectrum of X-ray emissions termed “Bremsstrahlung radiation” is obtained (see Figure 2.13). The inner shell electrons in atoms are also ejected by the high energy electrons. As a consequence, electrons from the higher energy levels then fill up the vacancies and X-ray photons are emitted. Cu and Mo are the common targets used in X-ray tubes and they can emit 8 keV ($\lambda \sim 1.54$ Å) and 14 keV ($\lambda \sim 0.8$ Å) X-rays, respectively [33].

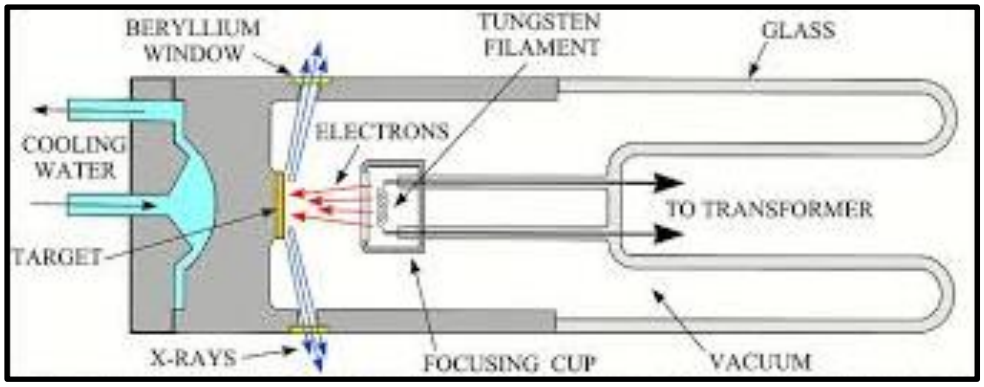


Figure 2.12- Diagram of a modern X-ray tube [15].

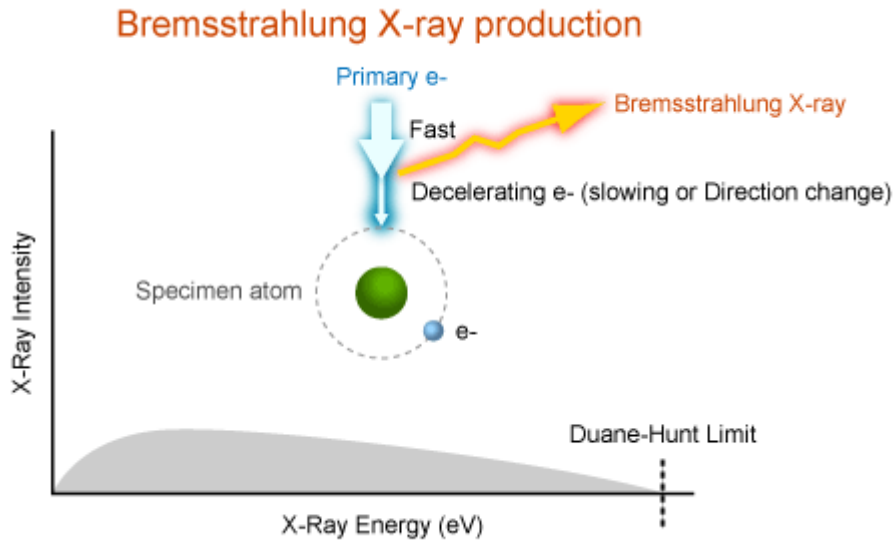


Figure 2.13 - Bremsstrahlung X-ray generation [6].

2.12.2 X-ray Diffraction Pattern

As X-rays travel through atoms, they initially interact with the electrons. The collision of X-ray photons with electrons in atoms results in the deflection of some photons from the original direction of the incident beam. In diffraction experiments, the elastically scattered X-rays are measured because they carry information about the electron distribution in materials. Diffracted waves from different atoms are able to interfere with each other. As a result, the intensity distribution is strongly dependent on this interaction. The diffracted waves in crystals consist of sharp interference maxima referred to as peaks with symmetry that is the same as in the distribution of atoms due to a periodic arrangement of atoms. The measurement of the diffraction pattern allows the distribution of atoms in a material to be logically concluded, accordingly. The positions of the peaks in an X-ray diffractogram are directly related to atomic distances. Figure 2.14 illustrates the arrangement of atoms in a periodic manner in 2 dimensions and the interaction of atoms with an incident X-ray beam.

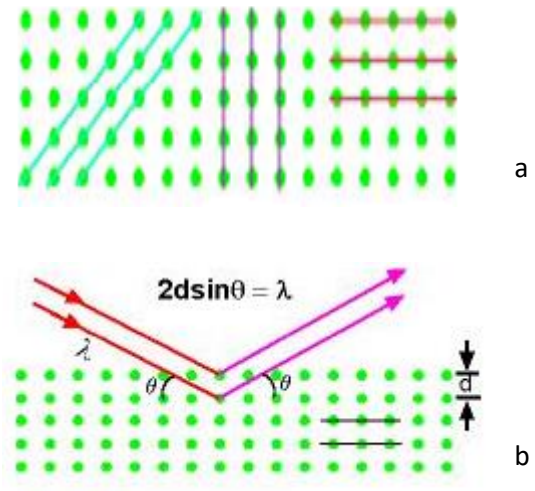


Figure 2.14- (a) Lattice planes and (b) Bragg's law [33].

For a given set of lattice planes with an inter-plane distance of d, the condition for a diffraction (peak) to occur can be simply written as:

$$2dsin\theta = n\lambda \qquad \text{Equation (2.30)}$$

where λ is the X-ray wavelength, θ is the scattering angle, and n is the integer representing the order of the diffraction peak. This equation is known as the Bragg's law. Bragg's law also applies to scattering centres consisting of any periodic distribution of electron density. In other words, the law holds true if the atoms are replaced by molecules or collections of molecules such as colloids, polymers, proteins and virus particles [33].

2.12.3 Powder Diffraction

Powder X-ray Diffraction (PXRD) is one of the most widely used X-ray diffraction techniques for materials characterisation. The specimen is usually in a powdery form comprised of fine grains of a crystalline material. This technique is also used to study particles in liquid suspension or polycrystalline solids (bulk or thin film materials).

The term "powder" refers to crystalline domains randomly oriented in the sample. Thus, when the 2-D diffraction pattern is recorded, it displays concentric rings of scattering peaks related to the various d-spacings in the crystal lattice. An XRD diffractogram shows diffraction peaks of varied intensities at different 2θ positions (see Figure 2.15). The peak positions and intensities are used for identification of the underlying structures or phases of materials. Identifying the phases is important as the properties of a material are highly dependent on its structure. Powder diffraction data can be collected by using either transmission or reflection geometry. These two methods provide the same data owing to the random orientation of the particles in the powder sample [33].

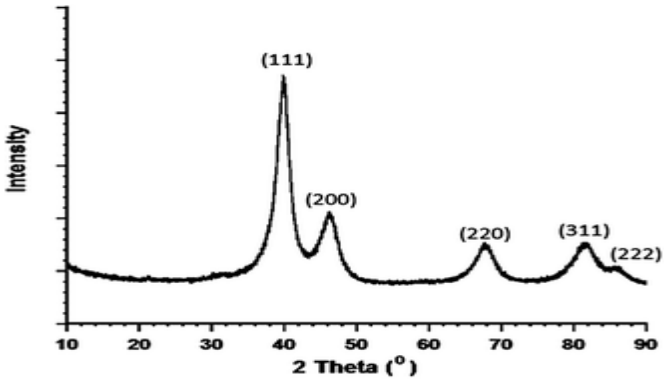


Figure 2.15 - Powder X-ray diffraction pattern of amylamine stabilised Pt nanoparticles [32].

2.14 Energy Dispersive X-ray Spectroscopy

Energy dispersive X-ray spectroscopy (EDS) is a characterisation technique which is used to identify elements present in a material by detecting X-rays emitted from atoms or ions. A specimen is first excited by a high energy electron beam or other electromagnetic radiation. The inner shell electrons are then ejected to vacuum, creating a vacancy in the inner shell as shown in Figure 2.16.

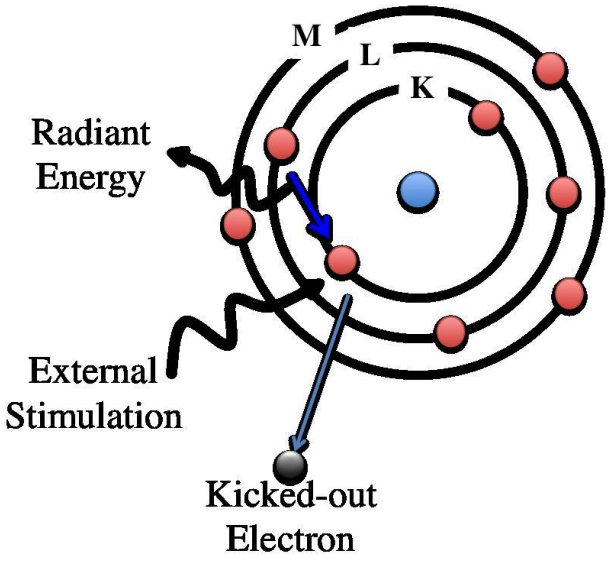


Figure 2.16 - Schematic diagram of X-ray generation in EDS [11].

The vacant site is later filled with an electron from the outer shell. During the electron transition process, an X-ray of energy corresponding to the energy difference between the initial state and the final state is emitted. Because each atom has unique and discretised energy levels, the emitted X-ray is a characteristic of individual atoms. EDS is typically attached to a scanning electron microscope or a transmission electron microscope in which a high energy electron beam is also required. Only elements with an atomic number above 4 can be detected by this technique. It is because, for atomic numbers of 4 or lower, the high rate of energy loss due to inelastic interaction overrides the backscatter coefficient, resulting in the premature loss of beam electrons prior to ionisation leading to X-ray production [37]. The obtained EDS spectra need to be carefully analysed as energy overlapping can arise when several atoms emitting X-rays of similar energy are present in the characterised samples. In EDS experiments, SiLi detectors at liquid nitrogen (LN_2) temperature are commonly used. When an X-ray strikes the detector, it produces photoelectrons which induce the formation of electron-hole pairs within the Si. The produced electrons and holes then migrate to the opposite end of the detector via the applied electric field of 1.5 kV, generating a current pulse with size proportional to the energy of the emitted X-ray [11].

2.15 X-ray Photoelectron Spectroscopy

X-ray photoelectron spectroscopy (XPS) is a surface-sensitive spectroscopic technique which is used to measure elemental compositions, empirical formulae, chemical states, and electronic states of elements present in a material. Figure 2.17 shows the diagram of an X-ray photoelectron spectrometer. To obtain an XPS spectrum, a studied material is irradiated by an X-ray beam and a measurement of the kinetic energy and the number of escaping electrons is simultaneously conducted. XPS is capable of determining elements present within a depth of

10 nm from the sample surface. A required condition for XPS measurement is a high vacuum (P ~ 10^{-8} millibar) or ultra-high vacuum (UHV; P is less than 10^{-9} millibar) [3].

2.15.1 Physical Principle

Photoelectron spectroscopy is based on a single photon in/electron out process [2]. XPS experiments can be carried using an X-ray photoelectron spectrometer as shown in Figure 2.16. In XPS measurements, X-ray photon is absorbed by an atom in a molecule or solid. The photon then interacts with a core electron leading to the ionisation. The emitted photoelectrons can be detected by the electron energy analyser and a photoelectron spectrum can thus be recorded. The overall photo-ionisation process occurring in XPS measurements is given by Equation 2.31.

$$A + h\upsilon \rightarrow A^{+} + e^{-} \qquad \text{Equation (2.31)}$$

By the law of conservation of energy:

$$E(A) + h\upsilon = E(A^{+}) + E(e^{-}) \qquad \text{Equation (2.32)}$$

As the energy of the electron is dependent solely on the kinetic energy (KE), Equation (2.32) can be rearranged to give the expression for the KE of the photoelectron:

$$KE = h\upsilon - \left(E(A^{+}) - E(A)\right) \qquad \text{Equation (2.33)}$$

The difference in energy between the ionised and neutral atoms represented by the bracketed term in Equation (2.33) is generally called the binding energy (BE) of the electron.

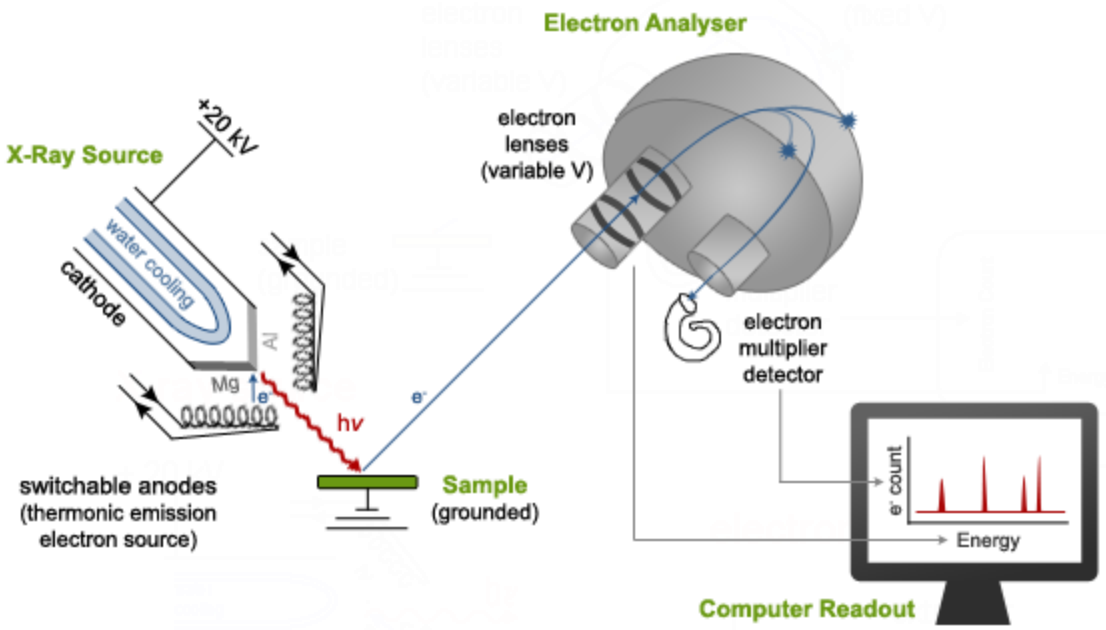


Figure 2.17 - Schematic diagram of an X-ray photoelectron spectrometer [19].

2.16 Transmission Electron Microscopy

Transmission Electron Microscopy (TEM) is one of the electron microscopy techniques used to observe the morphology of a specimen. An electron beam in a transmission electron microscope is usually generated by a thermionic emission process from a filament composed of a material such as tungsten (W). The transmitted beam which contains electron density, phase, and periodicity information is used for image formation. The emitted electrons are accelerated by an electric potential (in volts) and focused by electrostatic and electromagnetic lenses onto an ultra-thin sample. The electrons pass through and interact with the sample, leading to image formation. An image is then magnified and focused onto an imaging device such as a fluorescent screen, or is detected by a sensor such as a charge coupled device (CCD) camera (see Figure 2.18) [1, 29].

Theoretically, the obtainable maximum resolution, d, for a light microscope is limited by the photon wavelength used to probe the sample, λ, and the numerical aperture (NA) of the system [14]:

$$d = \frac{\lambda}{2n \sin \alpha} \approx \frac{\lambda}{2NA} \qquad \text{Equation (2.34)}$$

To avoid the limitations of visible light which has a relatively large wavelength of about 400 to 700 nm, electrons are used. Because of their wave-like properties, it is possible to make electrons behave similarly to a beam of electromagnetic radiation [10]. The wavelength of electrons is expressed by Equation (2.35):

$$\lambda_e \approx \frac{h}{\sqrt{2m_0 E(1 + \frac{E}{2m_0 c^2})}} \qquad \text{Equation (2.35)}$$

where E is the energy of the accelerated electrons, h is Planck's constant, m_0 is the rest mass of an electron, and c is the speed of light.

2.16.1 Limitations of TEM

For a number of materials, extensive sample preparation is required to produce a sufficiently thin specimen in order to be electron transparent. Therefore, TEM analysis is considered time-consuming with a low quantity of sample processed in a given period of time. During the sample preparation process, a change in sample structure may occur. Additionally, as the field of view is relatively small, it is possible that the analysed region may not be representative of the whole sample. Also, some samples, especially biological materials, can potentially be damaged by the electron beam.

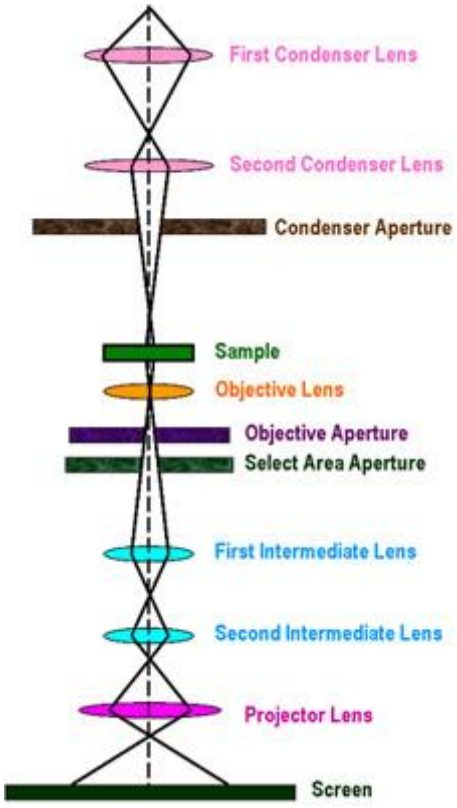


Figure 2.18- Diagram of typical TEM working [34].

References

1. Introduction to TEM. https://cfamm.ucr.edu/documents/tem-intro.pdf. (accessed 25 September 2014)
2. Photoelectron Spectroscopy. http://www.chem.qmul.ac.uk/surfaces/scc/scat5_3.htm. (accessed 25 September 2014)
3. Research Methods and Procedures. http://scholarbank.nus.edu.sg/bitstream/10635/23747/4/CHAPTER%203%20Research%20Methods%20and%20Procedures.pdf. (accessed 25 September 2014)
4. Thermogravimetric Analysis (TGA). https://www.perkinelmer.com/lab-solutions/resources/docs/faq_beginners-guide-to-thermogravimetric-analysis_009380c_01.pdf. (accessed 25 September 2014).
5. *Oxford dictionary of Chemistry*. Oxford University Press: 2004.
6. Australian Microscopy & Microanalysis Research Facility, Bremsstrahlung X-ray generation. http://www.ammrf.org.au/myscope/analysis/eds/xraygeneration/bremsstrahlung/. (accessed 25 September 2014)
7. Bard, A. J.; Faulkner, L. R., *Electrochemical Methods:Fundamentals and Applications*. 2 ed.; John Wiley & Sons: New York 2000.
8. Bard, A. J., *J. Electroanal. Chem.* **1973,** *6*, 187.
9. Brett, C. M. A.; Brett, A. M. O.; Christopher, M. A., *Electrochemistry : Principles, Methods and Applications* Oxford University Press: 1993.
10. Champness, P. E., *Electron Diffraction in the Transmission Electron Microscope*. Garland Science: 2001.
11. Christians, J. Energy Dispersive X-ray Spectroscopy (EDX) http://www3.nd.edu/~kamatlab/facilities_physchar.html#Pos5. (accessed 5 January 2015)
12. Department of Chemical Engineering and Biotechnology, Mass Transport. https://www.ceb.cam.ac.uk/research/groups/rg-eme/teaching-notes/mass-transport. (accessed 5 January 2015)
13. Department of Chemical Engineering and Biotechnology, Potential Step Voltammetry http://www.ceb.cam.ac.uk/research/groups/rg-eme/teaching-notes/potential-step-voltammetry. (accessed 5 January 2015)
14. Fultz, B.; Howe, J., *Transmission Electron Microscopy and Diffractometry of Materials*. Springer: 2007.
15. X-ray tube image. 2010. http://pubs.usgs.gov/of/2001/of01-041/htmldocs/images/xrdtube.jpg (accessed 30 August 2018)
16. Hamann, C. H.; Hamnett, A.; Vielstich, W., *Electrochemistry*. Weinheim: Wiley-VCH: 1997.
17. Hind, A. R.; Bhargava, S. K.; McKinnon, A., *Advances in Colloid and Interface Science* **2001,** *93* (1–3), 91-114.
18. Department of Chemistry – University of Oxford, Surface Analysis Facility – TGA/DSC. 2017. http://saf.chem.ox.ac.uk/tgadsc.aspx. (accessed 1 September 2017)
19. Horton, J. H., X-ray photoelectron spectroscopy. http://faculty.chem.queensu.ca/people/faculty/horton/research.html. (accessed 25 September 2014)

20. Larsen, D., ATR-FTIR. http://chemwiki.ucdavis.edu/Analytical_Chemistry/Instrumental_Analysis/Spectrometer/ATR-FTIR. (accessed 5 January 2015).
21. Fisher, A. C., Electrode Dynamics. Oxford University Press Inc.: New York, the United States, 2009; p 85.
22. Matsuda, H.; Ayabe, Y., *Z. Electrochem.* **1955,** *59*, 494.
23. Nicholson, R. S., *Analytical Chemistry* **1965,** *37* (11), 1351-1355.
24. Nicholson, R. S.; Shain, I., *Analytical Chemistry* **1964,** *36* (4), 706-723.
25. Nicholson, R. S.; Shain, I., *Analytical Chemistry* **1965,** *37* (2), 178-190.
26. Olmstead, M. L.; Hamilton, R. G.; Nicholson, R. S., *Analytical Chemistry* **1969** *41*, 260.
27. Brett, C. M. A.; Brett, A. M. O., Electroanalysis. Oxford University Press: New York, the United States, 2005; p 88.
28. Rieger, P. H., *Electrochemistry*. Chapman & Hall: New York, 1994.
29. Rodenburg, J. Learn to use TEM: an introductory guide by John Rodenburg. http://www.rodenburg.org/guide/t700.html.
30. Sakshat Virtual Labs, Theory of Cyclic Voltammetry. http://vlab.amrita.edu/?sub=3&brch=41&sim=126&cnt=65. (accessed 25 September 2014)
31. Schwarz, M. W.; Irving, S., *Analytical Chemistry* **1963,** *35*, 1770.
32. Sen, F.; Karatas, Y.; Gulcan, M.; Zahmakiran, M., *RSC Advances* **2014,** *4* (4), 1526-1531.
33. UC Santa Barbara Materials Research Laboratory, X-ray Basics. http://www.mrl.ucsb.edu/centralfacilities/x-ray/basics. (accessed 25 September 2014)
34. Williams, D.; Carter, C. B., *Transmission Electron Microscopy*. 1 - Basics ed.; Plenum Press: 1996.
35. Zhao, F.; Slade, R. C. T.; Varcoe, J. R., *Chemical Society Reviews* **2009,** *38* (7), 1926-1939.
36. Mettler-Toledo AG, Analytical TGA-Sorption System. http://sk.mt.com/dam/mt_ext_files/Editorial/Generic/4/TGA_DSC_1_Product_Brochure_Editorial-Generic_1186143058785_files/51724559_tga_dsc1brosche.pdf. (accessed 1 September 2017)
37. Hafner, B., Energy Dispersive Spectroscopy on the SEM: A Primer. http://www.charfac.umn.edu/instruments/eds_on_sem_primer.pdf. (accessed 1 September 2017)
38. Cammarata, L.; Kazarian, S. G.; Salterb, P. A.; Welton, T., *Physical Chemistry Chemical Physics* **2001,** *3*, 5192-5200.

Chapter 3

Synthesis and Characterisation

3.1 Introduction

Metal nanoparticle materials with different compositions, particle sizes, and particle morphologies can be obtained by using different synthesis methods and conditions. Two approaches namely top-down and bottom-up have been applied to prepare metal nanoparticles. The bottom-up technology is based on a chemical reduction of metal precursors, mostly in the form of metal salts, or decomposition in a controlled manner of metastable organometallic compounds in an organic or water solution [46]. In order to control compositions, sizes, and morphologies of nanoparticles prepared by the chemical reduction of metal salts, synthesis parameters such as solvents, metal salts, reducing agents, reduction temperatures, and a reduction time need to be optimised. One of the chemical reduction methods which have been used to prepare metal nanoparticles is a sodium borohydride ($NaBH_4$) reduction method. Sodium borohydride is a strong reducing agent which can reduce almost all metal cations. Also, it can be dissolved in water and some organic solvents such as ethylene glycol. Accordingly, it is suitable to be used for metallic nanoparticles preparation. As a reduction step is conducted in solution phase, a solvent used to prepare metal precursor(s) solution needs to be carefully chosen. Ethylene glycol has been widely used as the solvent because it is good to prevent the oxidation and aggregation of nanoparticles [47]. To study the physico-chemical properties of synthesised nanoparticles, a number of characterisation techniques are employed. Powder X-ray Diffraction (PXRD) technique is able to identify crystalline phases present in powder nanoparticle samples. Analyses of PXRD patterns provide some information about the lattice parameters and mean crystallite

size of crystal units. Energy Dispersive X-ray Spectroscopy (EDS) can be used to determine bulk compositions of nanoparticle materials. To determine surface compositions, X-ray Photoelectron Spectroscopy (XPS) should be used instead. An EDS machine typically equipped with a transmission electron (TE) microscope or a scanning electron (SE) microscope detects an X-ray emitted from individual excited atoms. In the case of XPS, emitted core-level photoelectrons of elements present in a surface layer are detected. The different oxidation states of surface species can be identified by using XPS, while EDS is unable to differentiate the oxidation states of bulk constituents. In order to study morphologies of nanoparticles and quantify loading of nanoparticles on carbon support, TE microscope and Thermogravimetric Analysis (TGA) technique can be employed.

In this chapter, the synthesis of PtSn/C (3:1) and PtSnCo/C (3:1:1 to 3:1:4) catalysts is presented. The method used to prepare these carbon-supported nanoparticle catalysts is the sodium borohydride reduction method. The results from characterisation of the resultant catalyst samples by the PXRD, EDS, Transmission Electron Microscopy (TEM), XPS, and TGA techniques are also presented. The PXRD technique was used to identify crystalline phases present in the PtSn/C (3:1) and all the synthesised PtSnCo/C catalysts. The EDS technique was employed to quantify the amount of Pt and Sn present in the bulk of the PtSn/C (3:1) catalyst and Pt, Sn, and Co existing in the bulk of all the synthesised PtSnCo/C catalyst samples. The transmission electron microscope was used to study morphologies of the as-prepared nanoparticles. Moreover, particle size, particle size distribution, and particle dispersion was observed using the TE microscope. To determine surface compositions of all the catalysts, XPS measurement was carried out. The determined bulk and surface compositions were used to help elucidate nanoparticle structures as the ratios between Pt and Sn or Pt and Co both in the bulk and the surface can suggest the sites of these species in the

nanoparticles. The TGA technique was used in order to determine total metal loading on carbon support of the as-prepared PtSn/C (3:1) and all PtSnCo/C catalysts.

3.2 Synthesis of the Pt/C, PtSn/C, and PtSnCo/C nanoparticle catalysts

3.2.1 Chemicals

1. Ethylene glycol (EG, anhydrous, 99.8%, Sigma-Aldrich)

2. Hexachloroplatinate hydrate ($H_2PtCl_6.xH_2O$, ~38% Pt basis, Aldrich)

3. Tin(II)chloride dihydrate ($SnCl_2.2H_2O$, puriss. p.a., ACS reagent, ISO, reag.Ph.Eur., ≥ 98%, Sigma-Aldrich)

4. Cobalt(II)chloride hexahydrate ($CoCl_2.6H_2O$, ACS reagent, 98%, Sigma-Aldrich)

5. Sodium hydroxide (NaOH, reagent grade, ≥98%, pellets (anhydrous), Sigma-Aldrich)

6. Sodium borohydride ($NaBH_4$, granular, 99.99% trace metals basis, Aldrich)

7. De-ionised water

8. Ethanol (puriss. p.a., absolute, ≥99.8% (GC) (Sigma-Aldrich)

9. Vulcan® XC-72R (Cabot Company Limited)

3.2.2 EG solution of Pt precursor

1 g of $H_2PtCl_6.xH_2O$ (~38% Pt basis) was dissolved in liquid ethylene glycol and the obtained solution was transferred to a 25-mL volumetric flask. The solution volume was adjusted to 25 mL using ethylene glycol. The concentration of Pt(IV) in the solution was *ca.*15.2 mg/mL.

3.2.3 EG solution of NaOH

0.1M NaOH solution was prepared by dissolving 1 g of NaOH pellets in liquid ethylene glycol. The mixture was heated at 60 ^{o}C to increase the solubility of NaOH. The obtained NaOH solution was cooled to room temperature and then transferred to a 250-mL volumetric flask. The final volume of 250 mL was adjusted with ethylene glycol.

3.2.4 Alkaline EG solution of $NaBH_4$

0.1M $NaBH_4$ solution was prepared by dissolving about 38 mg of solid $NaBH_4$ in 0.1M NaOH in EG solution. The obtained solution was transferred to a 10-mL volumetric flask and the final volume of 10 mL was adjusted with the same solvent.

3.2.5 Preparation of Pt/C

The Pt/C catalyst with the nominal Pt loading of 20 wt.% was synthesised by the following procedure. The Pt precursor solution of 965 µL was pipetted and added into a 50-mL three-neck round bottom flask. The total volume of 15 mL was made up of liquid ethylene glycol. The EG solution of the Pt precursor was stirred in an oil bath at 25±1 ^{o}C for 20 minutes with a flow of N_2.Then, 3 mL of 0.1M $NaBH_4$ solution was added into the Pt precursor solution dropwise while the solution was purged with N_2 gas. Following the reduction step, as purchased Vulcan®XC-72R carbon black was added to the colloidal solution. Liquid ethylene glycol was then added on top to obtain final solution volume to 30 mL. The pH of the mixture was adjusted to ~10 using the prepared 0.1M NaOH solution. The alkaline mixture was stirred at 25±1 ^{o}C for 5 hours with N_2 flow. After 5 hours, the mixture was filtered with a copious amount of DI-water and ethanol. Finally, the obtained Pt/C catalyst was dried at 80 ^{o}C for 12 hours under vacuum. Prior to characterisation and activity testing, the dried Pt/C catalyst was ground to fine powder and transferred to a vial.

3.2.6 Preparation of the PtSn/C and PtSnCo/C catalysts

PtSn/C catalyst with the nominal Pt:Sn atomic ratio of 3:1 and the total metal loading (Pt+Sn) of 20 wt.% was prepared by the same method and procedure used to synthesise the Pt/C catalyst. In this case, the pre-determined amount of solid Sn precursor was added into the Pt precursor solution. For the PtSnCo/C catalysts with different atomic ratios as shown in Table 1 and the total metal loading (Pt+Sn+Co) of 20 wt.% were also prepared by the same method and procedure except all three metal salts were present in the precursors solution.

Table 3.1- A number of moles of Pt(IV), Sn(II), and Co(II) in EG solution for the catalysts preparation

catalyst	mmole of Pt(IV)	mmole of Sn(II)	mmole of Co(II)	volume of 0.1M $NaBH_4$ solution (mL)
Pt/C	0.075	N/A	N/A	3
PtSn/C (3:1)	0.075	0.025	N/A	4
PtSnCo/C (3:1:1)	0.075	0.025	0.025	5
PtSnCo/C (3:1:2)	0.075	0.025	0.050	6
PtSnCo/C (3:1:3)	0.075	0.025	0.075	7
PtSnCo/C (3:1:4)	0.075	0.025	0.100	8

3.3 Results and discussion

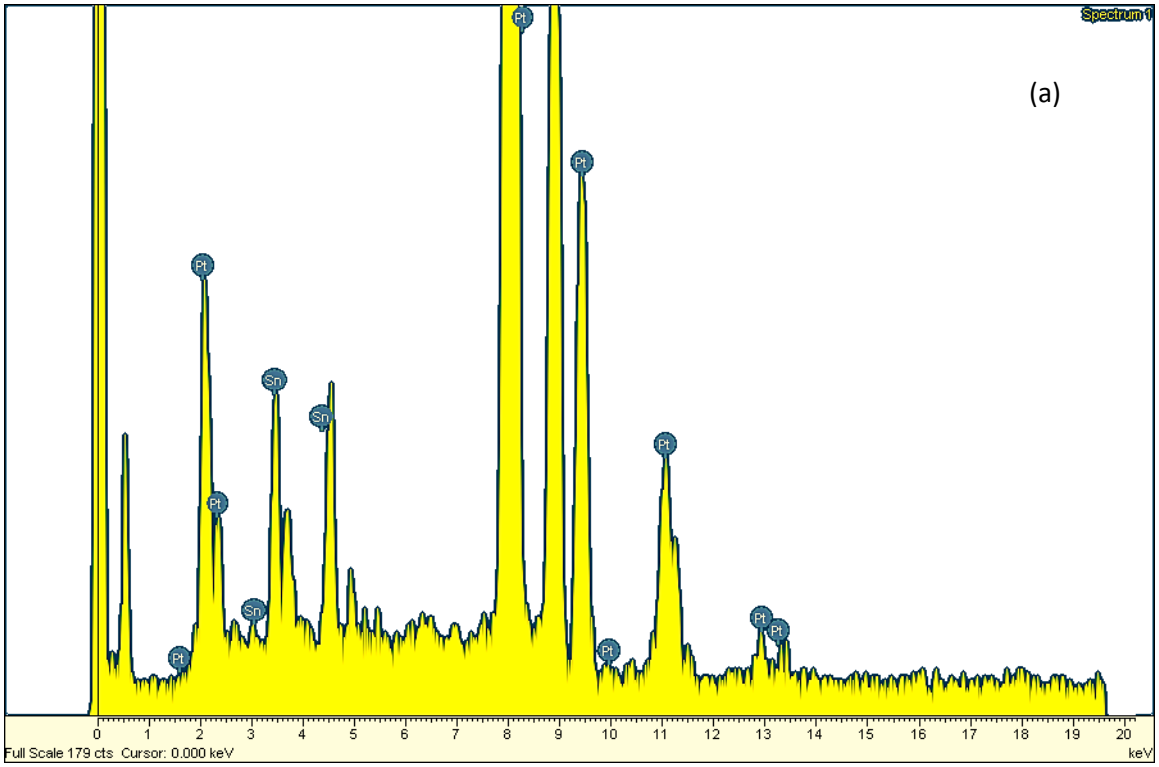
3.3.1 Chemical compositions of the as-prepared PtSn/C and PtSnCo/C catalysts by energy dispersive X-ray spectroscopy (EDS)

The EDS spectra of the as-synthesised PtSn/C (3:1) and all PtSnCo/C catalysts are shown in Figures 3.1-3.3 and the bulk chemical compositions of the catalysts are summarised in Table 3.2.

Table 3.2 - Bulk compositions of PtSn/C (3:1) and all PtSnCo/C (3:1:1 to 3:1:4)

catalyst (nominal atomic ratio)	Pt (at.%)	Pt (wt.%)	Sn (at.%)	Sn (wt.%)	Co (at.%)	Co (wt.%)	Pt : Sn : Co actual atomic ratio
PtSn/C (3:1)	75.18	83.27	24.82	16.73	-	-	3 : 1
PtSnCo/C (3:1:1)	66.95	79.64	23.26	16.84	9.79	3.52	3 : 1 : 0.4
PtSnCo/C (3:1:2)	57.52	75.84	17.92	14.38	24.56	9.78	3 : 1 : 1.4
PtSnCo/C (3:1:3)	42.98	66.94	13.07	12.39	43.95	20.68	3 : 1 : 3.4
PtSnCo/C (3:1:4)	39.22	63.94	12.26	12.16	48.52	23.90	3 : 1 : 4.0

at.% = atomic %, wt.% = weight %



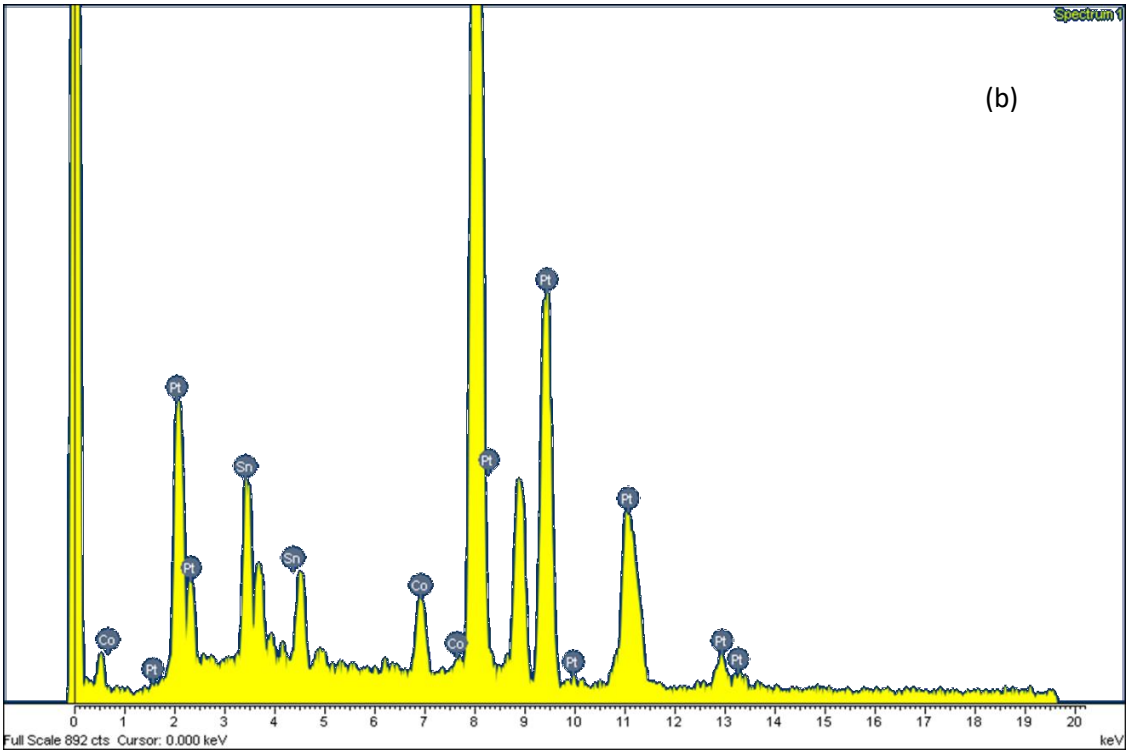
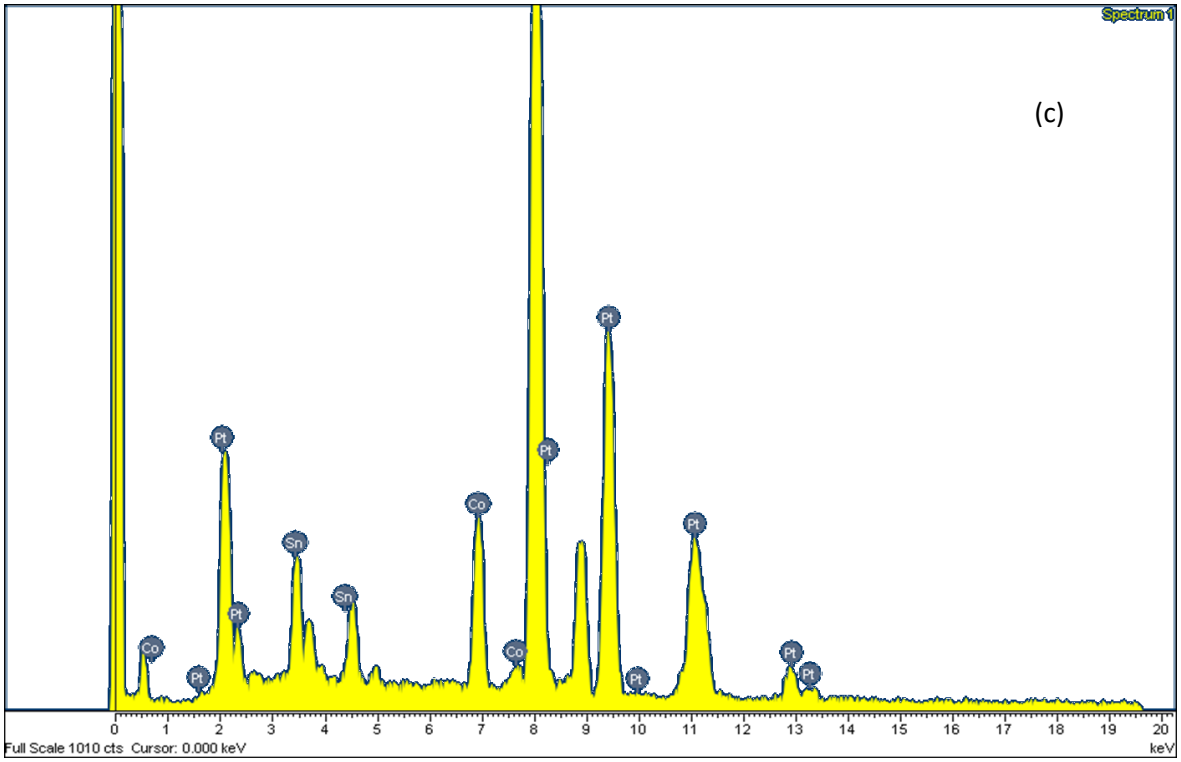


Figure 3.1- EDS spectra of the PtSn/C (3:1) (a) and PtSnCo/C (3:1:1) (b) catalysts



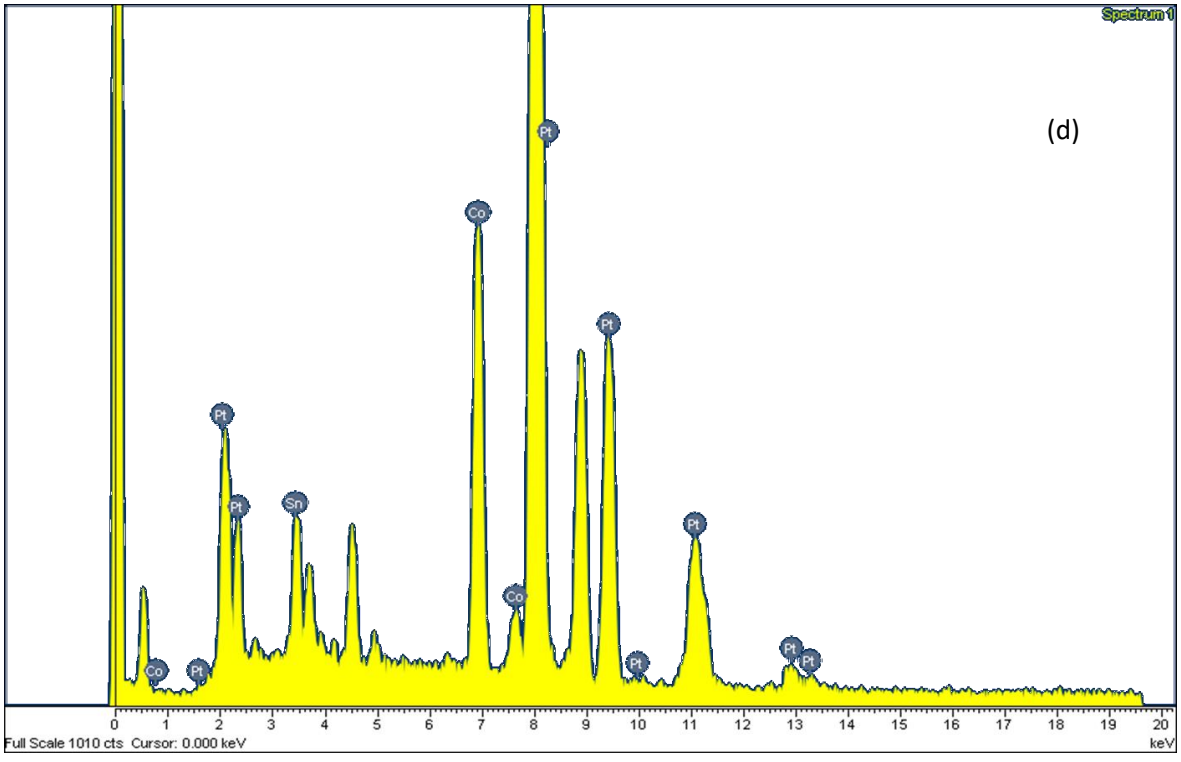


Figure 3.2-EDS spectra of the PtSnCo/C (3:1:2) (c) and PtSnCo/C (3:1:3) (d) catalysts

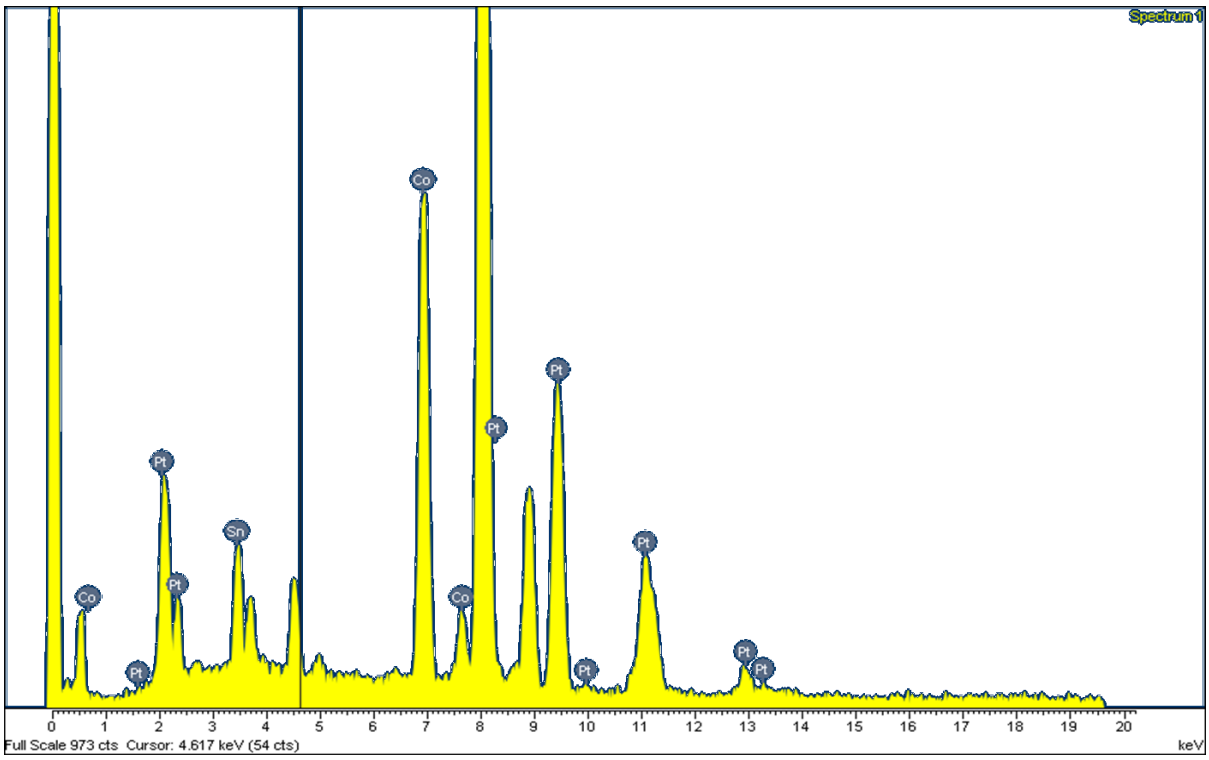


Figure 3.3-EDS spectrum of the PtSnCo/C (3:1:4) catalyst

The actual Pt:Sn atomic ratio obtained from the EDS measurement on the PtSn/C (3:1) sample was in good agreement with the nominal ratio. It was found that the actual Pt:Sn atomic ratio of each as-prepared PtSnCo/C catalyst also agreed with the nominal Pt:Sn ratio of 3:1. These results showed the effectiveness of the modified sodium borohydride reduction method in controlling the Pt:Sn atomic ratio. Although the Pt:Sn atomic ratio could be well-controlled for all the as-prepared PtSnCo/C catalysts, the Co content of PtSnCo/C (3:1:1) and PtSnCo/C (3:1:2) was not in good agreement with the nominal values. The Co content of PtSnCo/C (3:1:1) and PtSnCo/C (3:1:2) was found to be lower than the expected values by 0.6. These results were corresponding to the actual Pt:Sn:Co atomic ratios determined by ICP-MS. The loss of cobalt would be due to the incomplete reduction of Co^{2+} in the mixtures of Pt, Sn, and Co precursors. Furthermore, the cobalt species attached to the carbon support with a weak interaction would be washed out during the filtration [26, 38].

In this thesis, the compositions of the PtSn/C and all PtSnCo/C catalysts are referred to the nominal atomic ratios.

3.3.2 Total metal loadings and bulk chemical compositions of the as-prepared PtSn/C (3:1) and all PtSnCo/C electrocatalysts by ICP-MS

The bulk chemical compositions and total metal loadings of the as-prepared PtSn/C (3:1) and all PtSnCo/C electrocatalysts were determined by inductively coupled plasma mass spectrometry (ICP-MS). All catalysts samples were digested using aqua regia solution with assistance of microwave radiation. The total metal loadings and bulk chemical compositions of all the as-prepared catalysts are presented in Table 3.3.

Table 3.3 Total metal loadings and bulk chemical compositions of the as-prepared catalysts

catalyst (nominal atomic ratio)	total metal loading (Pt+Sn+Co) (%)	Pt:Sn:Co atomic ratio from ICP-MS	Pt:Sn:Co atomic ratio from EDS
PtSn/C (3:1)	23.42	3:1	3:1
PtSnCo/C (3:1:1)	22.31	3:1:0.5	3:1:0.4
PtSnCo/C (3:1:2)	21.30	3:1:1.1	3:1:1.4
PtSnCo/C (3:1:3)	21.12	3:1:1.9	3:1:3.4
PtSnCo/C (3:1:4)	19.33	3:1:2.6	3:1:4.0

The total metal loadings of all the as-prepared catalysts were close to the nominal percentage of 20, indicating that the employed reduction method using sodium borohydride as a reducing agent can load the desirable metal elements of the expected amount on the carbon black support. The bulk chemical compositions determined by ICP-MS were close to those determined by EDS except for the PtSnCo/C (3:1:3) and PtSnCo/C (3:1:4) catalysts. This result indicates an uneven distribution of the metal elements on as-synthesised nanoparticles.

3.3.3 Thermogravimetric Analysis

The as-synthesised PtSn/C (3:1) and all the PtSnCo/C electrocatalysts were heated from 25 ^{o}C to 800 ^{o}C in air with a heating rate of 10 ^{o}C/min in order to study the thermal behaviours of the catalysts. The obtained thermograms are shown in Figure 3.4.

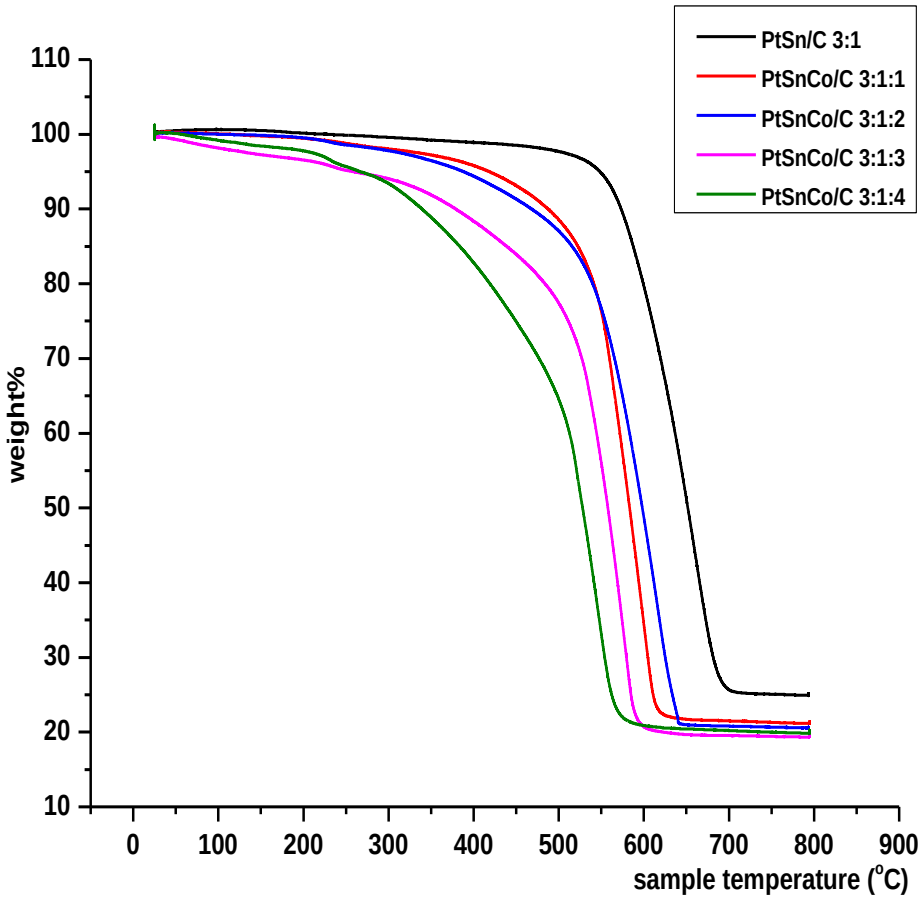


Figure 3.4 –TGA profiles of the as-prepared PtSn/C (3:1) and all PtSnCo/C catalysts

Table 3.4 - Summary of percentages of weight loss in different temperature ranges for the as-prepared PtSn/C (3:1) and PtSnCo/C (3:1:1 to 3:1:4) catalysts

catalyst (nominal atomic ratio)	temperature range (^{o}C)	weight loss (%)
PtSn/C (3:1)	246 - 507	2.87
	507 - 602	18.24
	602 - 712	54.09
PtSnCo/C (3:1:1)	195 - 410	4.40
	410 - 551	19.75
	551 - 635	54.07
PtSnCo/C (3:1:2)	218 - 352	3.24
	352 - 550	19.53
	550 - 647	55.94
PtSnCo/C (3:1:3)	63 - 341	6.71
	341 - 535	25.31
	535 - 635	47.85
PtSnCo/C (3:1:4)	102 - 337	8.81
	337 - 518	32.41
	518 - 630	37.65

The thermogram of the PtSn/C (3:1) catalyst shows that there was a small mass loss of 2.87 % in the temperature range between 246^{o}C and 507 ^{o}C. The second mass loss occurred in the range of 507 ^{o}C to 602 ^{o}C and it was followed by the abrupt loss of mass starting at about 602 ^{o}C. Finally, a constant mass was reached at about 712 ^{o}C. The mass loss in three regions are associated with the oxidation of Vulcan XC-72R carbon support to form CO_2 since the total weight loss of 75.20 % was close to the expected carbon loading of the catalyst. The mass loss at the other temperature ranges would be due to the combustion of carbon in different states [27]. For the PtSnCo/C (3:1:1) catalyst, three regions of mass loss were observed with the total weight loss of 78.22 %. The temperature for the initial mass loss of the PtSnCo/C (3:1:1) catalyst was lower than that of PtSn/C (3:1) and the same result was obtained for the

other three PtSnCo/C catalysts. The presence of cobalt species may attribute to the decrease in initial mass loss temperature. The total weight loss of 78.71 %, 79.87 %, and 78.87 % were obtained for the PtSnCo/C (3:1:2), PtSnCo/C (3:1:3), and PtSnCo/C (3:1:4) catalysts, respectively. By considering the temperature ranges of the sudden mass loss of the PtSn/C (3:1) and all PtSnCo/C catalysts, the decomposition of carbon started at temperatures lower than 602 ^{o}C for the PtSnCo/C catalysts. Moreover, the temperature shifted to more negative values as the Co content increased, suggesting that high Co content can decrease the thermal stability of the carbon support. Baturina et al. [48] investigated the thermal decomposition of Vulcan XC72 carbon black and the Vulcan XC72 supported Pt catalysts with different Pt loadings in flowing air. They found that the oxidation of the carbon black could be accelerated by Pt. Furthermore, the onset temperatures of initial and sudden mass loss decreased with an increase in the Pt loading. The negative shift of the carbon decomposition temperature was attributed to the changes of the total reaction rate due to the larger Pt surface area available at higher loadings [49]. Since the carbon support used in the preparation of the PtSn/C (3:1) and all PtSnCo/C catalysts is Vulcan XC-72R which is analogous to Vulcan XC72, its decomposition in air could be accelerated by Pt in contact with the carbon support. The lower onset temperatures of initial and sudden mass loss associated with the decomposition of the Vulcan XC-72R carbon support for all the PtSnCo/C catalysts would be because each PtSnCo/C catalyst has higher Pt surface area than PtSn/C (3:1). The higher Pt surface area would be associated with the presence of cobalt species on the surfaces of the PtSnCo/C catalysts. The weight of each catalyst sample began to be constant prior to 800 ^{o}C, indicating complete oxidation of the carbon support. The total metal loadings of all the as-prepared catalysts determined by the TGA method can be overestimated due to the oxidation of Pt, Sn, and Co components. It is known that metallic Pt can undergo the oxidation with oxygen at temperatures between 600 and 800 ^{o}C to yield PtO_x species [27]. In the same

temperature range, the oxidation of Sn, Co, and their oxides can also occur. Therefore, the weight of residues remaining on an alumina pan on completion of TGA measurement does not reflect the real total metal loading of the as-prepared catalyst.

Table 3.5 – Summary of the total weight of residues and the temperature for complete oxidation of the carbon support

catalyst (nominal atomic ratio)	nominal metal loading (Pt+Sn or Pt+Sn+Co) (wt.%)	temperature (^{o}C)	total weight of residues (wt.%)
PtSn/C (3:1)	20	712	25.06
PtSnCo/C (3:1:1)	20	635	21.63
PtSnCo/C (3:1:2)	20	647	20.92
PtSnCo/C (3:1:3)	20	635	19.27
PtSnCo/C (3:1:4)	20	630	20.18

Although the total weight of remaining substances after the combustion of the as-prepared catalyst shown in Table 3.5cannot represent its real total metal loading, the obtained value implies that the real total metal loading would be close to a nominal value of 20 wt.% and the method used to synthesise the PtSn/C (3:1) and all PtSnCo/C nanoparticle catalysts would be considered as effective in loading metal elements on the carbon support.

3.3.4 Powder X-ray Diffraction

The X-ray diffraction patterns of all the as-prepared catalysts are shown in Figures 3.5 and 3.6. To identify the crystalline phases formed and determine the formation of alloys in the binary PtSn/C (3:1) and all ternary PtSnCo/C catalysts, the XRD patterns of the as-prepared PtSn/C (3:1) and all PtSnCo/C catalysts were compared to that of Pt/C synthesised by the same method.

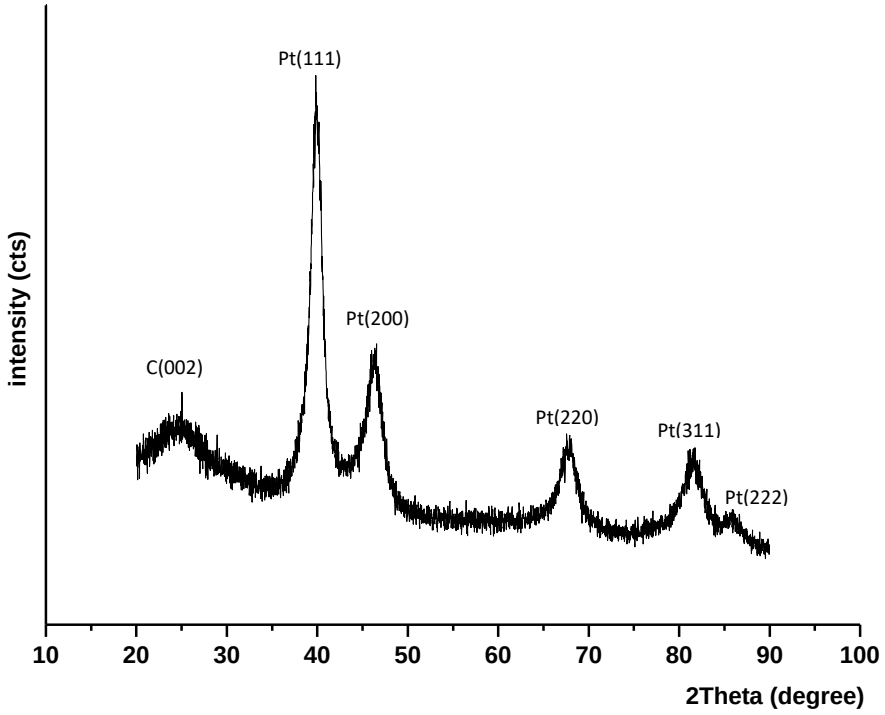


Figure 3.5 - XRD pattern of the Pt/C catalyst with the nominal Pt loading of 20 wt.%

The displayed diffractogram of Pt/C in Figure 3.5 showed peaks at 2θ ≈ 40°, 46°, 67°, 82°, and 85° characteristic of the face-centred cubic (fcc) structure of polycrystalline Pt. The diffraction peak observed at 2θ ≈ 25° is associated with C(002) crystal plane of the hexagonal structure of Vulcan XC-72R carbon support [50]. The lattice parameter of the fcc lattice of Pt calculated using Pt(220) diffraction peak was 0.3910 nm and the mean crystallite size calculated from Scherrer equation was 3.9 nm. The position of Pt(220) was used in the lattice parameter and mean crystallite size calculation because it is not interfered by the carbon peak and the other Pt diffraction peaks.

For a cubic lattice system, the lattice parameter can be calculated by the following expression:

$$a = d_{hkl}\sqrt{h^2 + k^2 + l^2} \qquad \text{Equation (3.1)}$$

where a is the lattice parameter of the cubic system, hkl is the Miller's index of a crystal plane [11].

The lattice parameter of the fcc Pt crystal structure (a_{fcc}) based on the Pt(220) peak can be calculated from Equation (3.2) which is derived from Equation (3.1) by substituting the Bragg's d-spacing and the Miller's index of the Pt(220) crystal plane.

$$a_{fcc} = \frac{\sqrt{2}\lambda_{K\alpha 1}}{sin\theta} \qquad \text{Equation (3.2)}$$

where $\lambda_{K\alpha 1}$ is the X-ray wavelength (1.54 Å for Cu K_α radiation) and θ is the diffraction angle corresponding to the peak maximum.

The average or mean crystallite size of nanoparticles can be calculated from the Scherrer's equation (Equation (3.3)) with the full width at half maximum (FWHM) of the Pt(220) peak.

$$L = \frac{0.9\lambda}{B_{1/2}\cos\theta} \qquad \text{Equation (3.3)}$$

where L is the average crystallite size and $B_{1/2}$ is the full width at half maximum [27].

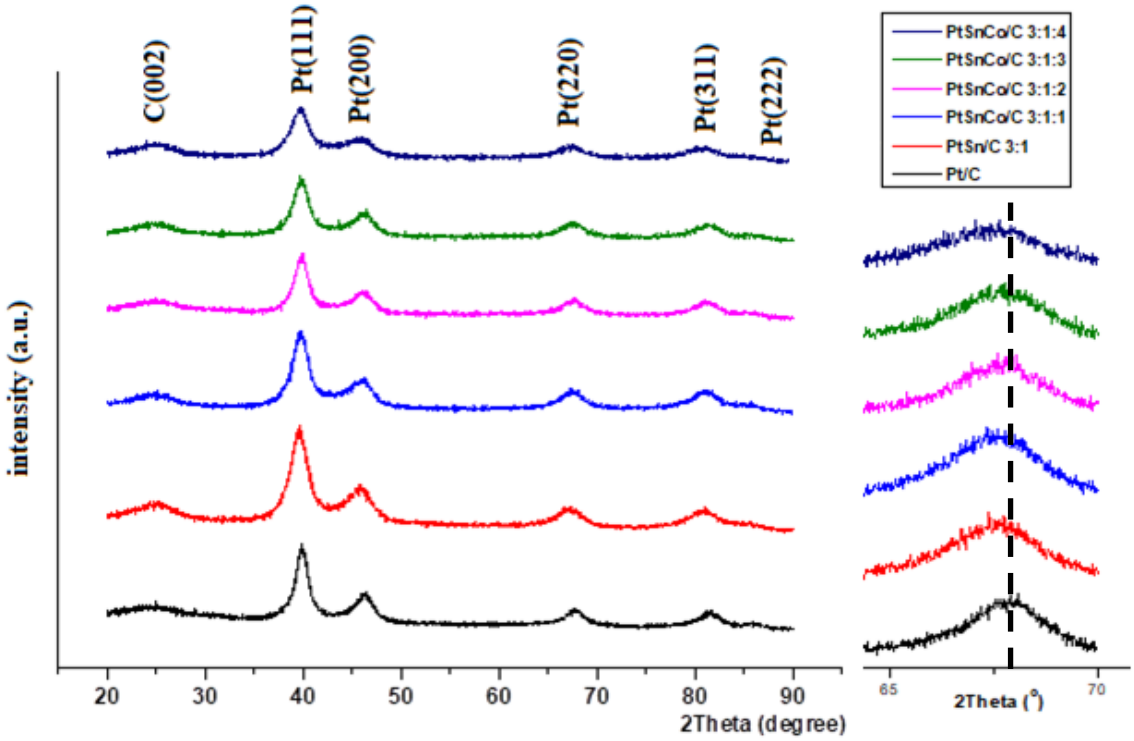


Figure 3.6 - XRD patterns of the Pt/C, PtSn/C (3:1), and PtSnCo/C (3:1:1 to 3:1:4) catalysts

The XRD patterns of the as-prepared PtSn/C (3:1) and all PtSnCo/C catalysts (see Figure 3.6) showed peaks corresponding to the fcc structure of Pt. No peak indicative of the presence of pure Sn and pure Co phases was observed for the PtSn/C (3:1) and all PtSnCo/C (3:1:1 to 3:1:4) samples. Furthermore, the peaks attributed to crystalline SnO_x especially the tetragonal SnO_2 phase at $2\theta \sim 34^o$ and 52^o which are associated with $SnO_2(101)$ and $SnO_2(211)$, respectively [20] were not observed in the XRD patterns of the as-prepared PtSn/C (3:1) and all PtSnCo/C (3:1:1 to 3:1:4) catalysts. In addition, for the PtSnCo/C catalysts at all atomic

ratios, the crystalline cobalt oxide (CoO_x) phases were not observed either. The presence of those phases cannot be discarded as the amount of each phase may be too small to be detected or they may exist in an amorphous form [38].

Table 3.6 - Lattice parameters of the fcc structure of Pt and the average crystallite sizes of the carbon supported Pt, PtSn (3:1), and all PtSnCo (3:1:1 to 3:1:4) nanoparticle catalysts

catalyst	nominal atomic ratio	actual atomic ratio from EDS	Pt fcc lattice parameter (a_{fcc}) based on Pt(220) diffraction peak (nm)	average crystallite size (D) (nm)
Pt/C	-	-	0.3910	3.9
PtSn/C	3:1	3:1	0.3938	3.4
PtSnCo/C	3:1:1	3:1:0.4	0.3925	3.8
PtSnCo/C	3:1:2	3:1:1.4	0.3918	3.7
PtSnCo/C	3:1:3	3:1:3.4	0.3918	3.7
PtSnCo/C	3:1:4	3:1:4.0	0.3931	3.0

The mean crystallite size based on the FWHM of the Pt(220) diffraction peak and the Pt fcc lattice parameters of all the as-prepared catalysts are summarised in Table 3.6. The mean crystallite sizes of the carbon supported PtSn (3:1), PtSnCo (3:1:1), PtSnCo (3:1:2), PtSnCo (3:1:3), and PtSnCo (3:1:4) nanoparticles were comparable. This result indicates that the modified sodium borohydride reduction method used to prepare the nanoparticle catalysts is effective in controlling mean crystallite size. Therefore, the effects of mean crystallite size on the electro-oxidation activity for alcohols can be excluded. It is known that the mean crystallite size from XRD is usually equal or smaller than that from TEM [39]. The mean crystallite sizes from XRD and TEM are in good agreement when the particles are described by well-defined boundary or a small degree of agglomeration [1]. It would be expected that with a small degree of agglomeration and a narrow particle size distribution the mean particle size of the PtSn (3:1) nanoparticles would be about 3.4 nm and the mean particle sizes of the

PtSnCo (3:1:1), PtSnCo (3:1:2), PtSnCo (3:1:3), and PtSnCo (3:1:4) nanoparticles are approximately 3.8, 3.7, 3.7, and 3.0 nm, respectively.

It can be seen in Table 3.6 that the lattice parameter of the PtSn/C (3:1) nanoparticles is higher than that of Pt/C. The increase in the lattice parameter indicates the expansion of the fcc lattice of Pt due to the incorporation of Sn atom ,whose size is bigger than that of Pt, into the Pt structure [32] (Sn atomic radius = 151 pm, Pt atomic radius = 138.5 pm, and Co atomic radius = 125 pm [12]).

It has been reported that the Pt fcc lattice parameter of the tri-metallic PtSn-based nanoparticle catalyst prepared by incorporating a third metal such as Pd, Ni, Ru, and Rh, whose atomic radius is smaller than that of Sn, was lower compared to that of the PtSn/C catalyst at the same Pt:Sn atomic ratio [3, 8, 32, 38]. The lattice contraction was attributed to formation of ternary PtSnM alloys where M = Pd, Ni, Ru, and Rh. The lattice parameter of each synthesised PtSnCo/C catalyst with the Pt:Sn atomic ratio of 3:1 was smaller than that of PtSn/C with the same Pt:Sn atomic ratio. As Co can be alloyed with Pt [16] and its smaller atomic radius compared to that of Pt can cause the lattice contraction, the co-existence of Co and Sn in fcc structure of Pt can reduce the lattice parameter due to the opposite effect (lattice contraction versus lattice expansion) induced by Co and Sn, respectively. In the following section, the hypothesis of formation of ternary PtSnCo alloy in all the PtSnCo/C catalysts is tested.

To examine the hypothesis, the analysis used to deduce the formation of the ternary PtSnRu alloy in the PtSnRu catalyst was applied [38]. The calculation of the lattice parameters of the ternary PtSnCo/C catalysts is based on the hypothesis that the amount of alloyed Sn and Co in the ternary catalysts is the same as the amount of alloyed Sn and Co in the binary PtSn and

PtCo catalysts. Following Vegard's law, the lattice parameter can be calculated from Equation (3.4):

$$a_{PtSnCo} = a_{PtSn} - k_{PtSnCo}\chi_{Co} \qquad \text{Equation (3.4)}$$

where a_{PtSnCo} is the lattice parameter of PtSnCo, a_{PtSn} is the lattice parameter of PtSn at the same Pt to Sn atomic ratio, χ_{Co} is the atomic fraction of alloyed Co. By assuming the dependence of a_{PtSnCo} on the Co content in the binary alloy (k_{PtCo}), Equation (3.4) becomes

$$a_{PtSnCo} = a_{PtSn} - k_{PtCo}\chi_{Co} = a_{PtSn} + a_{PtCo} - a_{Pt} \qquad \text{Equation (3.5)}$$

where a_{PtSn} and a_{PtCo} are the lattice parameters of the binary PtSn and PtCo catalysts which have the same Sn and Co content as in the corresponding PtSnCo/C catalysts, and a_{Pt} is the lattice parameter of pure Pt. The lattice parameters of the PtCo materials with the Co content of 9.79 %, 24.56 %, 43.95 %, and 48.52 % as determined for PtSnCo/C (3:1:1), PtSnCo/C (3:1:2), PtSnCo/C (3:1:3), and PtSnCo/C (3:1:4), respectively, were estimated by the following linear correlation between the Co content and the lattice parameter [31].

$$a_{PtCo} = a_{Pt} - k_{PtCo}\chi_{Co} \qquad \text{Equation (3.6)}$$

where a_{Pt} is 0.3910 nm and k_{PtCo} is 0.0165 , and χ_{Co} = 0.098/(0.098+ 0.670) = 0.128 for the PtSnCo/C (3:1:1) catalyst. By substituting a_{Pt}, k_{PtCo} , and χ_{Co} into eq. (6) with the above numbers, a_{PtCo} of 0.3889 nm was obtained. The lattice parameter of the binary PtSn catalyst containing 23.26 % Sn, which is the same as in PtSnCo/C (3:1:1), was estimated based on the linear correlation between the lattice parameter and the Sn content in the binary PtSn/C catalysts [24].

$$a_{PtSn} = a_{Pt} + 0.0123\chi_{Sn} \qquad \text{Equation (3.7)}$$

The a_{PtSn} value of 0.3942 nm was obtained. By substituting a_{Pt}, a_{PtCo} and a_{PtSn} into Equation (3.5), a_{PtSnCo} of 0.3921 nm was obtained. This value is reasonably in good agreement with that of the as-prepared ternary PtSnCo/C (3:1:1) catalyst (a_{PtSnCo}= 0.3925 nm), suggesting that Co is alloyed with PtSn. The lattice parameters of the PtSnCo/C (3:1:1), PtSnCo/C (3:1:2), PtSnCo/C (3:1:3), and PtSnCo/C (3:1:4) catalysts obtained from the algorithm above is tabulated in Table 3.7.

Table 3.7 – Summary of the calculated lattice parameters of all the PtSnCo/C catalysts

catalyst	χ_{Sn}	χ_{Co}	a_{PtSn} (nm)	a_{PtCo} (nm)	a_{PtSnCo} (nm)	a_{PtSnCo} (nm) experimental
PtSnCo/C (3:1:1)	0.258	0.128	0.3942	0.3889	0.3921	0.3925
PtSnCo/C (3:1:2)	0.237	0.300	0.3939	0.3861	0.3890	0.3918
PtSnCo/C (3:1:3)	0.234	0.506	0.3939	0.3827	0.3856	0.3918
PtSnCo/C (3:1:4)	0.239	0.553	0.3939	0.3819	0.3848	0.3931

For the PtSnCo/C (3:1:2), PtSnCo/C (3:1:3), and PtSnCo/C (3:1:4) catalysts, the calculated lattice parameters are not reasonably in good agreement with the experimental lattice parameters of these catalysts. The difference between the two values is more distinct as the bulk Co content increases. As observed in other ternary catalysts [40][23][26], a decrease in the degree of alloying of atoms in the binary catalysts can be caused by the presence of a third non-alloyed metal. The decrease in lattice parameter when the bulk Co content increases could be due to the lower amount of alloyed Sn in the fcc structure of Pt and the presence of non-alloyed Co oxides. By assuming that only Sn is alloyed with Pt in the PtSnCo/C catalysts except PtSnCo/C (3:1:1), the Sn atomic fraction ($X_{Sn)}$ in the Pt-Sn alloys and the degree of alloying can be calculated from the following equations [9, 26]:

$$X_{Sn} = \left(\frac{(a - a_0)}{(a_s - a_0)}\right) X_s \qquad \text{Equation (3.8)}$$

where a_s is the lattice parameter of the Pt_3Sn/C ETEK catalyst (0.4002 nm)

X_s is the Sn atomic fraction in the Pt_3Sn/C ETEK catalyst (0.25)

a_0 is the lattice parameter of the Pt/C catalyst (0.3910 nm)

The degree of alloying between Pt and Sn (Sn_{al}/Sn_{tot}) indicating an alloyed Sn (Sn_{al}) to total Sn (Sn_{tot}) ratio in catalysts is expressed as:

$$\frac{Sn_{al}}{Sn_{tot}} = \frac{X_{Sn}}{(1 - X_{Sn})} \cdot \frac{Pt_{EDS}}{Sn_{EDS}} \qquad \text{Equation (3.9)}$$

where Pt_{EDS} and Sn_{EDS} are the Pt and Sn content determined by the EDS measurement, respectively.

The alloyed Sn atomic fraction and degree of alloying for the PtSn/C (3:1) catalyst and all the PtSnCo/C catalysts are shown in Table 6. X_{Sn} of about 0.076 indicates that about one-third of the total Sn content is present in the $Pt_{92}Sn_8$ alloy phase and it co-exists with SnO_x species as confirmed by XPS. The deconvolution of the Sn 3d peak appearing in the XPS spectrum of PtSn/C (3:1) reveals that only Sn oxide species are present on the catalyst surface. It could, therefore, be suggested that the PtSn nanoparticles consist of a core-shell structure particle with $Pt(O_x)$-SnO_x shell and PtSn alloy core and a small amount of crystalline SnO_x phase and/or amorphous SnO_x.

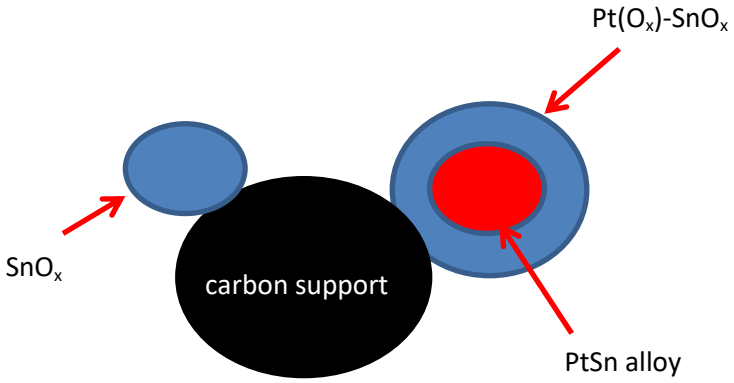


Figure 3.7- Proposed structure of the PtSn (3:1) nanoparticles based on the XRD and XPS results

It can be seen that the alloyed Sn atomic fraction decreased with increasing Co content up to the bulk composition of 3:1:2. Further increase in the Co content resulted in the increase in the lattice parameter. The same trend was also observed for the degree of alloying and the PtSnCo/C (3:1:2) catalyst had the lowest degree of alloying. The fcc lattice parameter-EDS-determined Co content plot is shown in Figure 3.8.

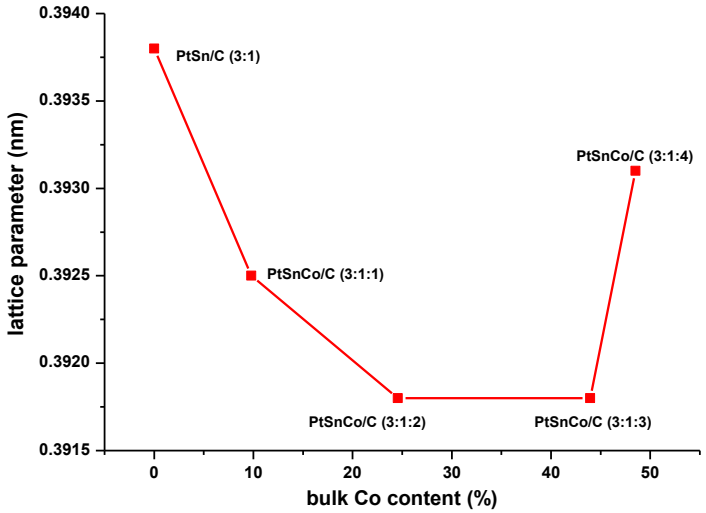


Figure 3.8- Plot of fcc lattice parameters versus actual bulk Co content (atomic %) obtained from the EDS measurements.

The XRD results with some findings from the XPS analysis, which will be discussed in details in the XPS section, can be used to primarily propose the structure of the PtSnCo nanoparticles in all the PtSnCo/C catalysts. The XPS analyses revealed that no metallic Co was found on the surfaces of all the PtSnCo/C catalysts. Based on the observed binding energy, cobalt (II) oxide (CoO) was the predominant Co species in the surface layers of the PtSnCo/C catalysts. The core-shell structured nanoparticles with PtSn alloy core and Pt(O_x)-SnOx-CoO shell would be on the carbon support. The small amount of oxides/hydroxides of Sn and Co in a crystalline and/or amorphous form may also be deposited on the carbon support for all the PtSnCo/C catalysts. To precisely identify the structures of the as-prepared PtSnCo nanoparticles, HRTEM technique is required.

Table 3.8 - XRD analysis of PtSn/C (3:1) and PtSnCo/C (3:1:1 to 3:1:4)

catalyst	lattice parameter, a_{fcc} (nm)	Sn atomic fraction, X_{Sn}	degree of alloying, Sn_{al}/Sn_{tot} (%)
PtSn/C (3:1)	0.3938	0.076	24.94
PtSnCo/C (3:1:1)	0.3925	n.d.	n.d.
PtSnCo/C (3:1:2)	0.3918	0.022	7.13
PtSnCo/C (3:1:3)	0.3918	0.022	7.31
PtSnCo/C (3:1:4)	0.3931	0.057	19.36

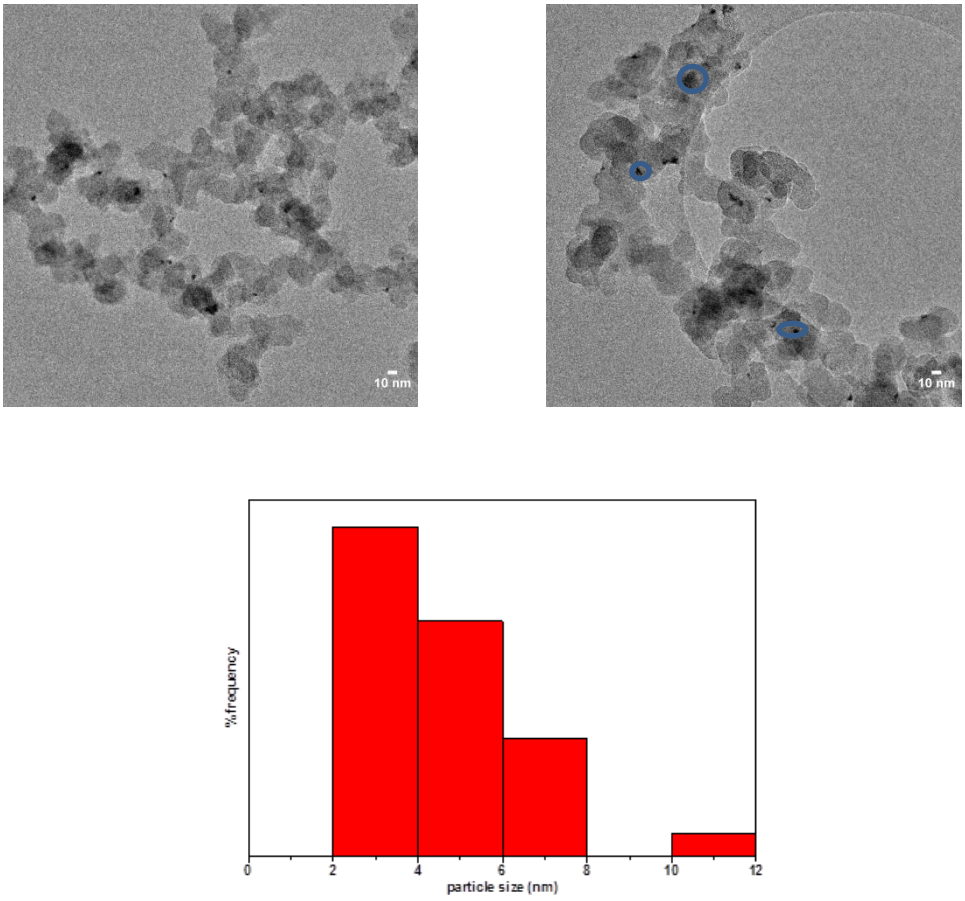
n.d. = not determined

3.3.5 Transmission Electron Microscopy

Transmission electron microscope was used to study morphologies, particle size, particle size distribution, and particle dispersion of the as-prepared PtSn (3:1) and the PtSnCo nanoparticles. TEM micrographs were obtained with the magnifications of 40k and 150k. The histograms of the particle size distribution were generated by analyses of nanoparticles in several different regions of the studied catalysts. The mean particle size, d, was calculated by the following equation:

$$d = \sum(k)\frac{n_k d_k}{n_k} \qquad \text{Equation (3.10)}$$

where n_k is the frequency of particles with size d_k.



Note: dots in the blue circles are as-synthesised PtSn nanoparticles

Figure 3.9 – TEM images and the histogram of particle size distribution for the PtSn/C (3:1) catalyst

The morphology of the as-synthesised PtSn (3:1) nanoparticles was spherical as seen in the TEM images in Figure 3.9. The particles were well-dispersed on the support. The mean particle size of the nanoparticles was 4.7±1.8 nm. The observed mean particle size was higher than the crystallite size measured by using the PXRD technique, indicative of some degree of particle agglomeration.

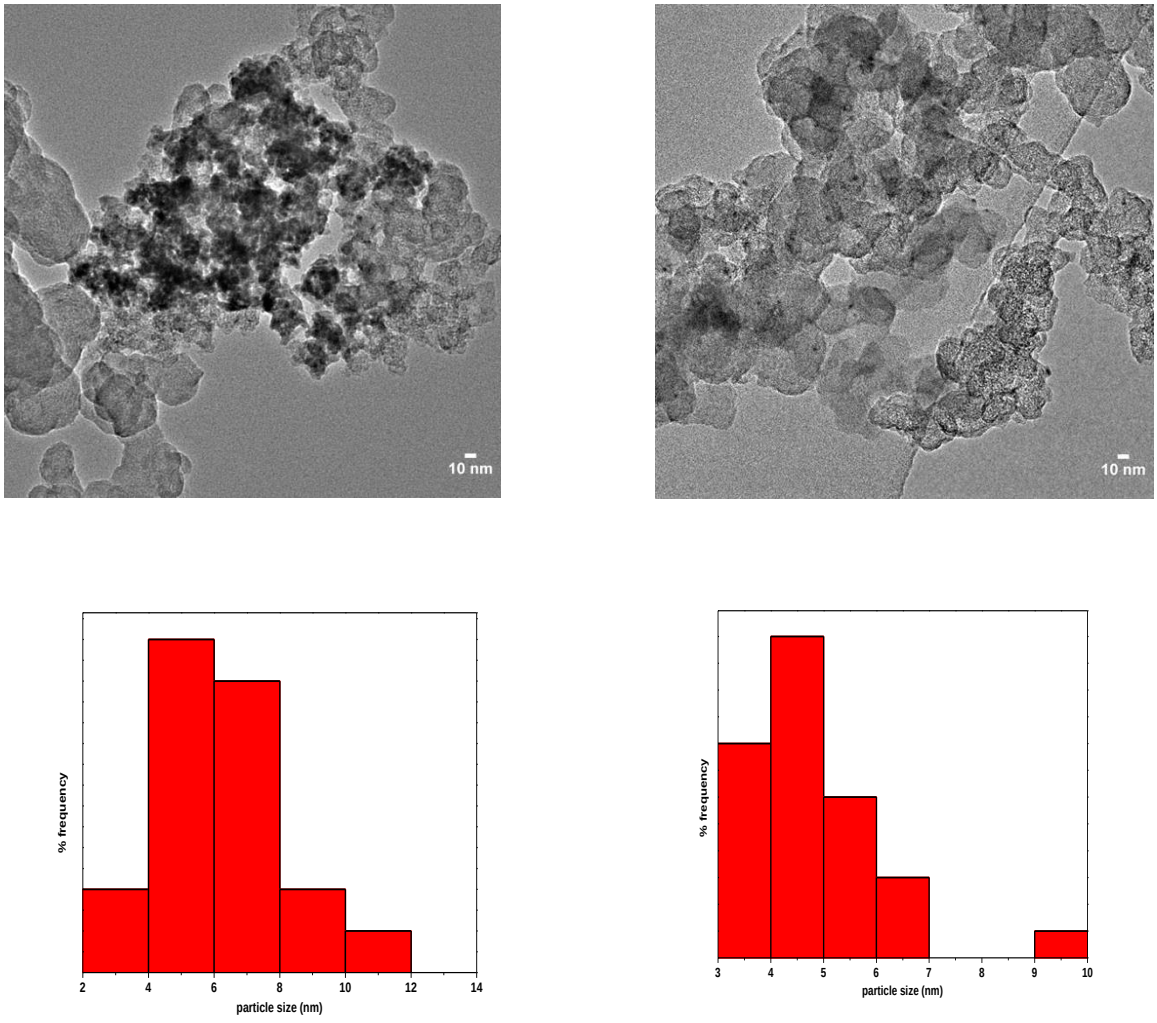


Figure 3.10 – TEM images and particle size distribution histograms of the PtSnCo/C (3:1:2) (left) and PtSnCo/C (3:1:4) (right)

The shape of the observed nanoparticles for both the PtSnCo/C (3:1:2) and PtSnCo/C (3:1:4) was also spherical. The average particle sizes and the corresponding standard deviations for PtSnCo/C (3:1:2) and PtSnCo/C (3:1:4) were 6.4±1.9 nm and 4.8 ±1.2 nm, respectively (see Figure 3.10). These values were higher than the mean crystallite sizes obtained from PXRD. The higher values can be ascribed to particle agglomeration. F. Colmati et al. [10] reported that the size of the Pt-Sn nanoparticles increased with increasing Sn content in the catalyst. E. Antolini et al. [3] synthesised the PtSnPd/ C nanoparticle catalysts using formic acid method and found that the addition of Pd decreased the amount of Sn in the catalyst as well as the particle size. This result was in good agreement with the result reported by F. Colmati et al. However, for the PtSnCo/C catalysts presented in this thesis, provided the total metal loading of each ternary PtSnCo catalyst is fairly constant (about 20 wt. %), the addition of Co decreased the Sn content, but the particle size did not decrease with decreasing Sn content. These results demonstrate that the type of a third metal added to PtSn nanoparticles, catalyst preparation methods and conditions, and chemical compositions determine the particle size of a catalyst.

3.3.6 X-ray Photoelectron Spectroscopy

The surface compositions of the PtSn/C (3:1) and all PtSnCo/C catalysts were determined by XPS which is a surface-sensitive technique. Prior to deconvolution of peaks associated with surface Pt, Sn, and Co species, binding energies corresponding to those peaks were calibrated to compensate the charging effect. The calibration was conducted by applying a binding energy difference between the binding energy of the core-level C1s electron in non-functionalised carbon atoms of Vulcan XC-72R carbon black and the standard binding energy of the core-level C 1s electron of 284.5 eV [24] to the XPS spectrum of the as-prepared catalyst.

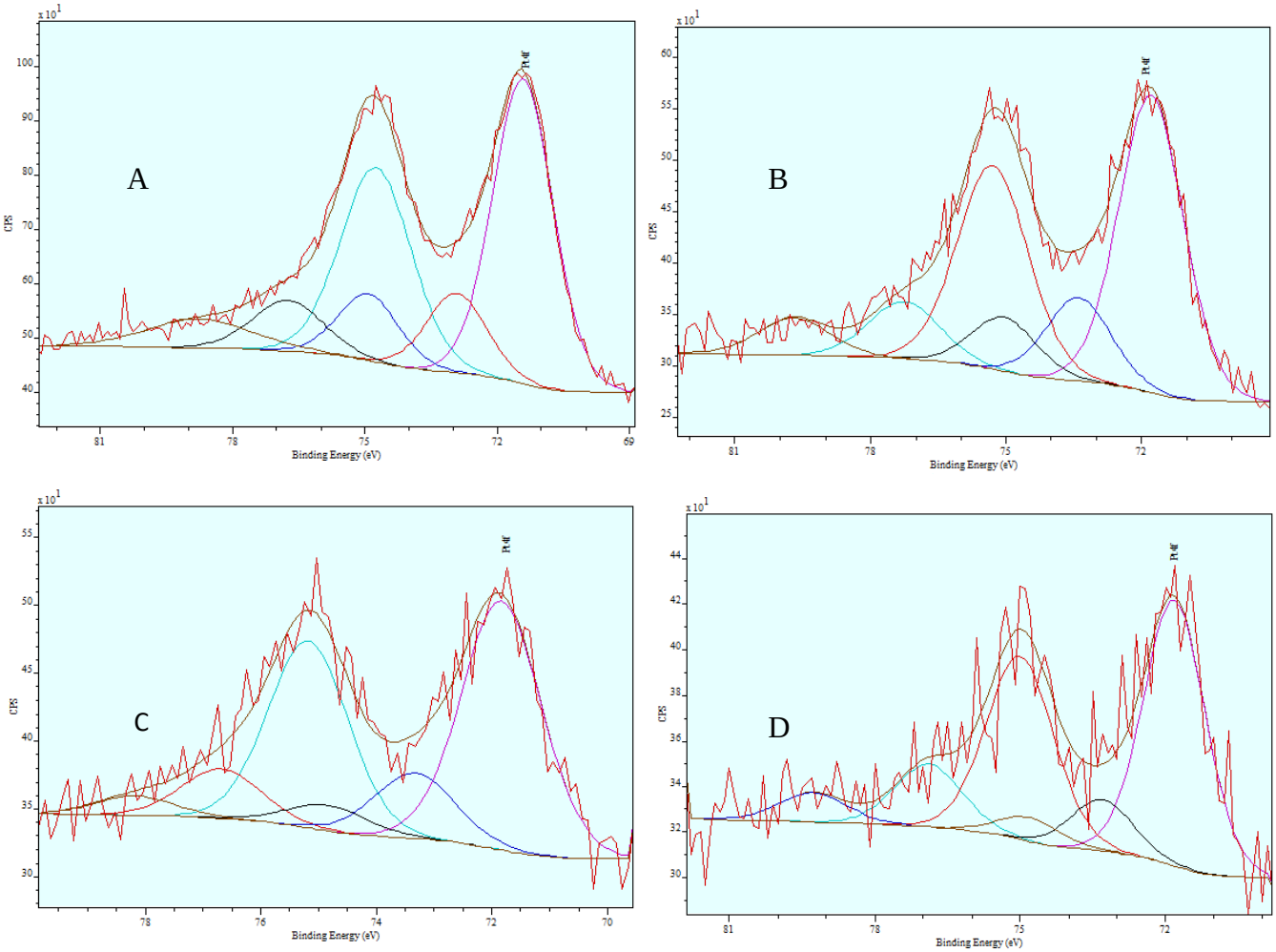


Figure 3.11 - XPS spectra of the Pt 4f region of the Pt/C (A), PtSn/C (3:1) (B), PtSnCo/C (3:1:1 and 3:1:2) (C-D) electrocatalysts

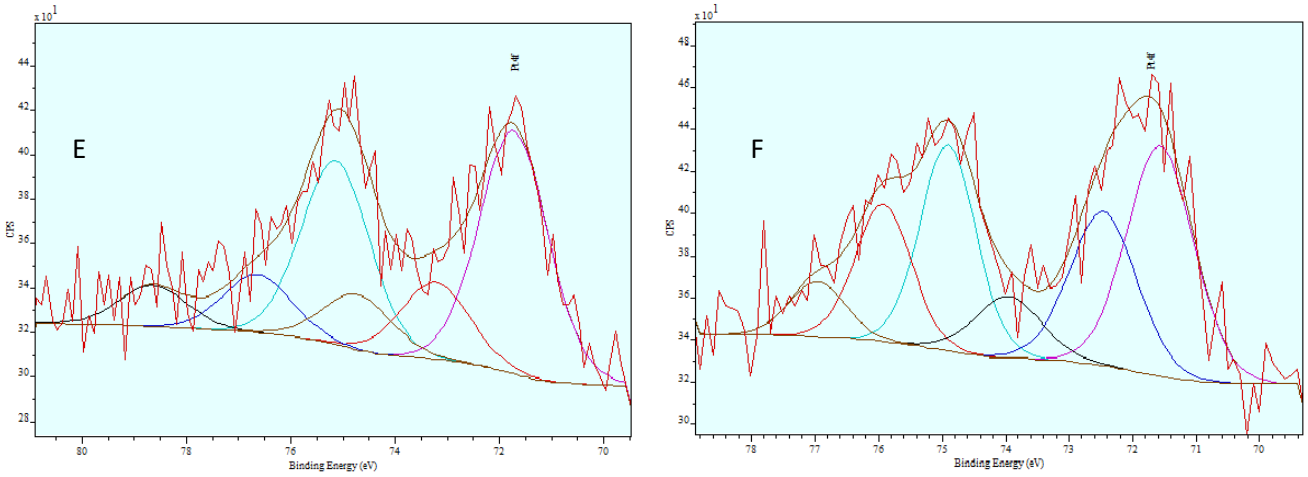


Figure 3.12 - XPS spectra of the Pt 4f region of the PtSnCo/C (3:1:3 and 3:1:4) (E-F) electrocatalysts

The doublet of the Pt 4f peak, which is originated from a spin-orbit splitting phenomenon, observed in the XPS spectrum of the individual catalyst was deconvoluted into three pairs. The peak appearing in the lower binding energy region is attributed to the core-level Pt $4f_{7/2}$ electron, while the signal from the core-level Pt $4f_{5/2}$ electron appears in the upper binding energy region. For interpretation of the results obtained from fitting the Pt 4f spectra, only the binding energies of the Pt $4f_{7/2}$ peaks were taken into account. The Pt $4f_{7/2}$ binding energies of all the as-prepared catalysts is tabulated in Table 3.9. It can be seen for the Pt/C catalyst that three Pt $4f_{7/2}$ peaks obtained from the deconvolution appeared at the binding energy values of 71.42, 72.92, and 74.42 eV which can be assigned to Pt in metallic state (Pt(0)), Pt(II) as PtO or $Pt(OH)_2$, and Pt(IV) as PtO_2 species, respectively [26][28][21][18]. The binding energy of Pt(0) species of 71.42 eV is higher than that of Pt(0) species for the bulk Pt reported in the literature [44]. The higher binding energy could be due to the Pt-carbon interaction and small particle effect [2][35]. For the PtSn/C (3:1) electrocatalyst, the binding energy of Pt(0) species is 0.37 eV higher than that of Pt/C synthesised by the same method.

Table 3.9 - XPS analysis of the deconvoluted Pt 4f $_{7/2}$ peaks of the Pt/C and carbon supported Pt-based electrocatalysts

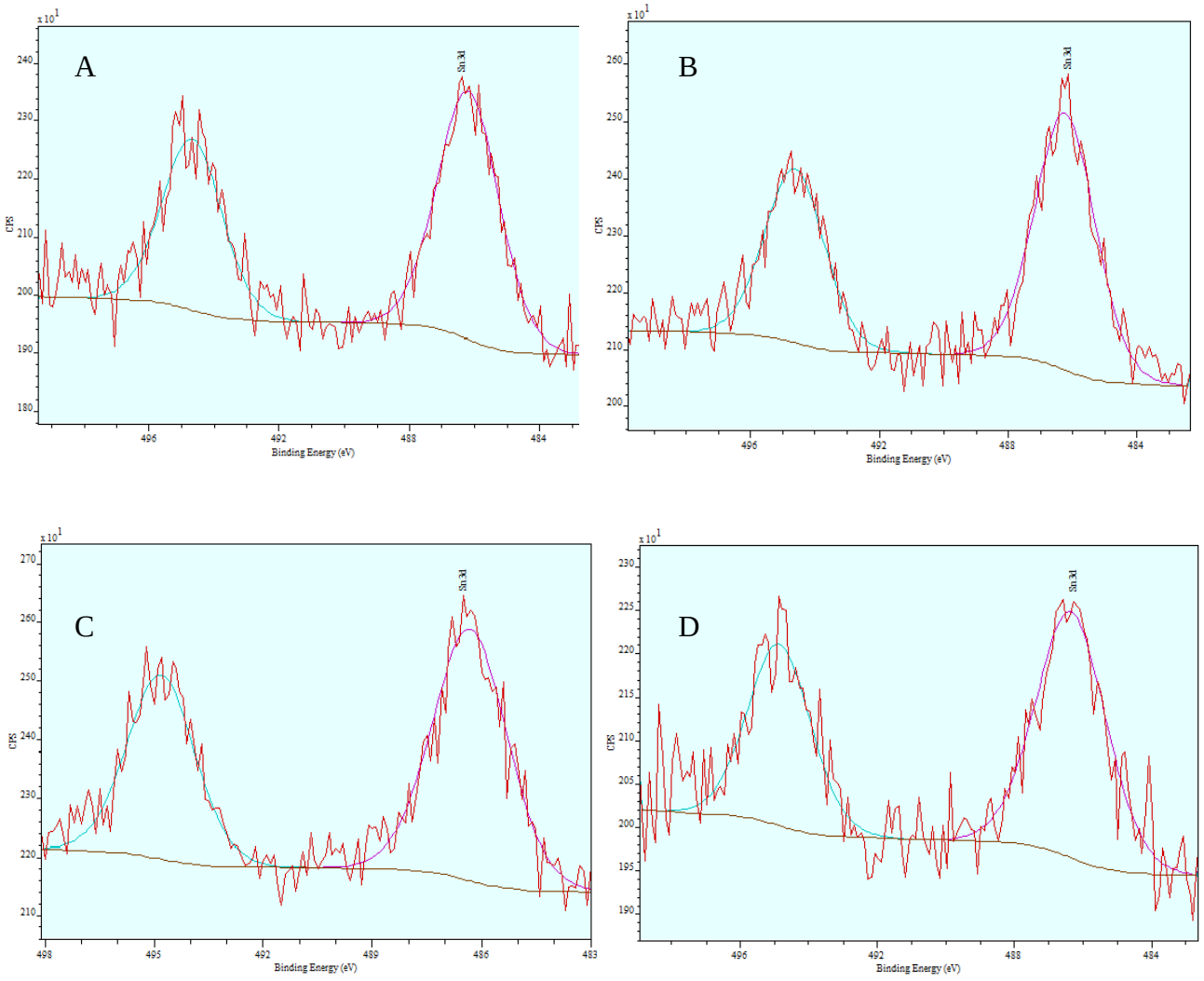
electrocatalyst (nominal atomic ratio)	Pt 4f $_{7/2}$ binding energy (BE) (eV)	Pt species and proportion (%)
Pt/C	71.42	Pt(0) , 63.57
	72.92	Pt(II) , 16.88
	74.42	Pt(IV) , 19.55
PtSn/C (3:1)	71.79	Pt(0) , 68.45
	73.39	Pt(II) , 19.15
	75.04	Pt(IV) , 12.40
PtSnCo/C (3:1:1)	71.84	Pt(0) , 73.17
	73.34	Pt(II) , 19.31
	74.84	Pt(IV) , 7.52
PtSnCo/C (3:1:2)	71.82	Pt(0) , 78.04
	73.32	Pt(II) , 15.00
	74.82	Pt(IV) , 6.96
PtSnCo/C (3:1:3)	71.72	Pt(0) , 64.87
	73.22	Pt(II) , 20.52
	74.72	Pt(IV) , 14.62
PtSnCo/C (3:1:4)	71.57	Pt(0) , 51.69
	72.46	Pt(II) , 34.53
	73.96	Pt(IV) , 13.77

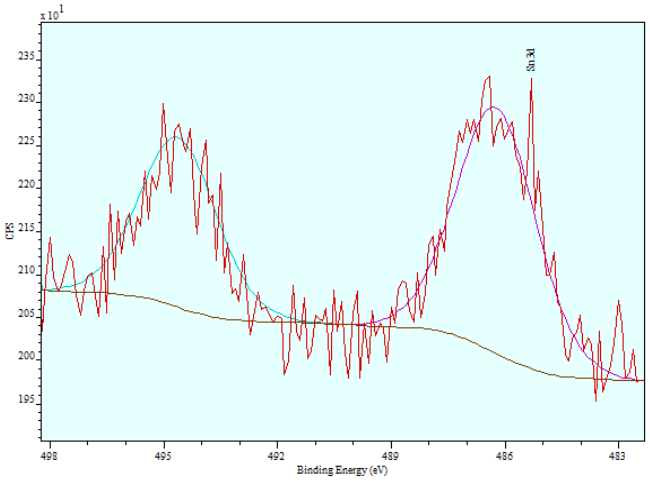
The shift of the binding energy of Pt(0) upon the addition of Sn has been reported. Kim J. H. et al. [24] characterised the as-prepared PtSn/C catalysts by XPS and they found that the binding energy of metallic Pt of the PtSn/C catalyst was lower by 0.3-1.0 eV compared to that of Pt/C. They suggested that the difference between the electronegativity of Pt (EN = 2.28)and Sn (EN = 1.96) leading to charge transfer from Sn to Pt [41] may cause the negative shift of the binding energy. The negative shift of Pt(0) binding energy based on the electronegativity difference of Pt and Sn was emphasised by Y. Ma et al. [29]. Hence, the positive shift to the higher Pt(0) binding energy observed for the PtSn/C (3:1) catalyst cannot

be explained by the charge transfer from Sn to Pt. P. Justin et al. [22] studied the Pt-Nb_2O_5/C electrocatalyst by the XPS technique and found that the Pt $4f_{7/2}$ binding energy of metallic Pt (Pt^0) shifted to the higher value compared to that of pure Pt [17]. The positive shift of 0.5 eV was attributed to the positive charge induced on the Pt particles which interacted with the niobium (V) oxide support [27][33][25]. Moreover, Villullas et al. [42] and other researchers [34][4] also found that the positive shift of Pt(0) binding energy was caused by the interaction between Pt nanoparticles and the particles of oxides. In the case of the PtSn nanoparticles supported on carbon, Y. Ma et al. [29] reported the positive shift of the Pt(0) binding energy of the PtSn/C EDTA and PtSn/C glycine catalysts compared to that of Pt/C (71.3eV). They concluded that the positive shift could be due to the interaction between Pt and tin oxide species. According to the literatures, the positive shift of the Pt(0) binding energy observed for the as-prepared PtSn/C (3:1) could arise from the interaction between Pt and tin oxide species. To clarify, the Sn 3d spectrum of PtSn/C (3:1) was deconvoluted and only one component at Sn $3d_{5/2}$ binding energy of 486.19 eV, which is attributed to tin oxide species [45][38][27][24][29], was obtained. The PtSnCo/C (3:1:1) and (3:1:2) electrocatalysts were analysed by XPS and the binding energies of the Pt $4f_{7/2}$ peaks corresponding to metallic Pt shifted positively to 71.84 and 71.82 eV, respectively, when compared with that of PtSn/C (3:1). The shift towards a higher binding energy was not observed for PtSnCo/C (3:1:3) and (3:1:4). The binding energy of metallic Pt, instead, shifted to the lower values. Interestingly, the amount of metallic Pt in the surface layers of all the as-prepared catalysts increases from 63.57 % to 78.04 % from Pt/C to PtSnCo/C (3:1:2) then it decreased with increasing Co content.

The XPS spectra of PtSn/C (3:1) and all PtSnCo/C (3:1:1 to 3:1:4) displayed in Figure 3.13 show the deconvoluted Sn $3d_{5/2}$ and Sn $3d_{3/2}$ peaks. It is clearly seen from the spectra that all Sn $3d_{5/2}$ peaks were deconvoluted into one single component with the binding energy of

about 486 eV which can be assigned to tin oxide (SnO and/or SnO_2) species [6][37][43]. Due to a very small difference in Sn 3d $_{5/2}$ binding energy (about 0.7 eV [15]), the distinct separation of Sn(II) from Sn(IV) species is not possible [24][19]. The analysis of the Sn 3d $_{5/2}$ spectra of all electrocatalysts can confirm that only tin oxide species are present in the surface layers of the as-prepared nanoparticles. Partly, tin oxides in the surface layers could be formed by the oxidation of Sn atoms with O_2 and/or H_2O in the atmosphere because of the high oxophilicity of Sn [24].





E

Figure 3.13 - XPS spectra of the Sn 3d region of the PtSn/C (3:1) (A), PtSnCo/C (3:1:1 to 3:1:4) (B-E) electrocatalysts

Table 3.10 – Sn 3d $_{5/2}$ binding energies of the PtSn/C (3:1) and all PtSnCo/C (3:1:1 to 3:1:4) electrocatalysts

electrocatalyst (nominal atomic ratio)	Sn 3d $_{5/2}$ binding energy (eV)	Sn species
PtSn/C (3:1)	486.19	Sn(II) and Sn(IV)
PtSnCo/C (3:1:1)	486.23	Sn(II) and Sn(IV)
PtSnCo/C (3:1:2)	486.31	Sn(II) and Sn(IV)
PtSnCo/C (3:1:3)	486.34	Sn(II) and Sn(IV)
PtSnCo/C (3:1:4)	486.22	Sn(II) and Sn(IV)

The Co 2p signal was observed for all the PtSnCo/C catalysts (Figure 3.14). Co $2p_{3/2}$ and Co $2p_{1/2}$ peaks were deconvoluted into three doublets with two of them in the satellite region. A Co 2p XPS spectrum is slightly more complicated than Pt 4f and Sn 3d spectra as a broad peak or satellite interferes with a main line. The broadened structure observed in Co $2p_{3/2}$ spectra is due to the spin-orbit splitting effect. Moreover, the binding energies for most cobalt oxides and hydroxides (i.e. CoO, Co_3O_4, Co_2O_3, CoOOH) are known to be very similar [7]. As a result, assignment of a specific cobalt species based purely on binding energy is

unlikely. Nonetheless, the oxidation states of Co can be assigned by the detailed analysis of the Co $2p_{3/2}$ shake-up or satellite structure. All Co(II) compounds are paramagnetic high spin complexes with total electron spin, s, of 3/2, whereas all Co(III) complexes are diamagnetic (s = 0). The intense broad satellites or shake-up peaks to higher binding energy of the main $2p_{3/2}$ curves can, therefore, only be seen for Co(II) compounds. These features are not observed for diamagnetic Co(III) complexes [5, 7, 13-14, 30].

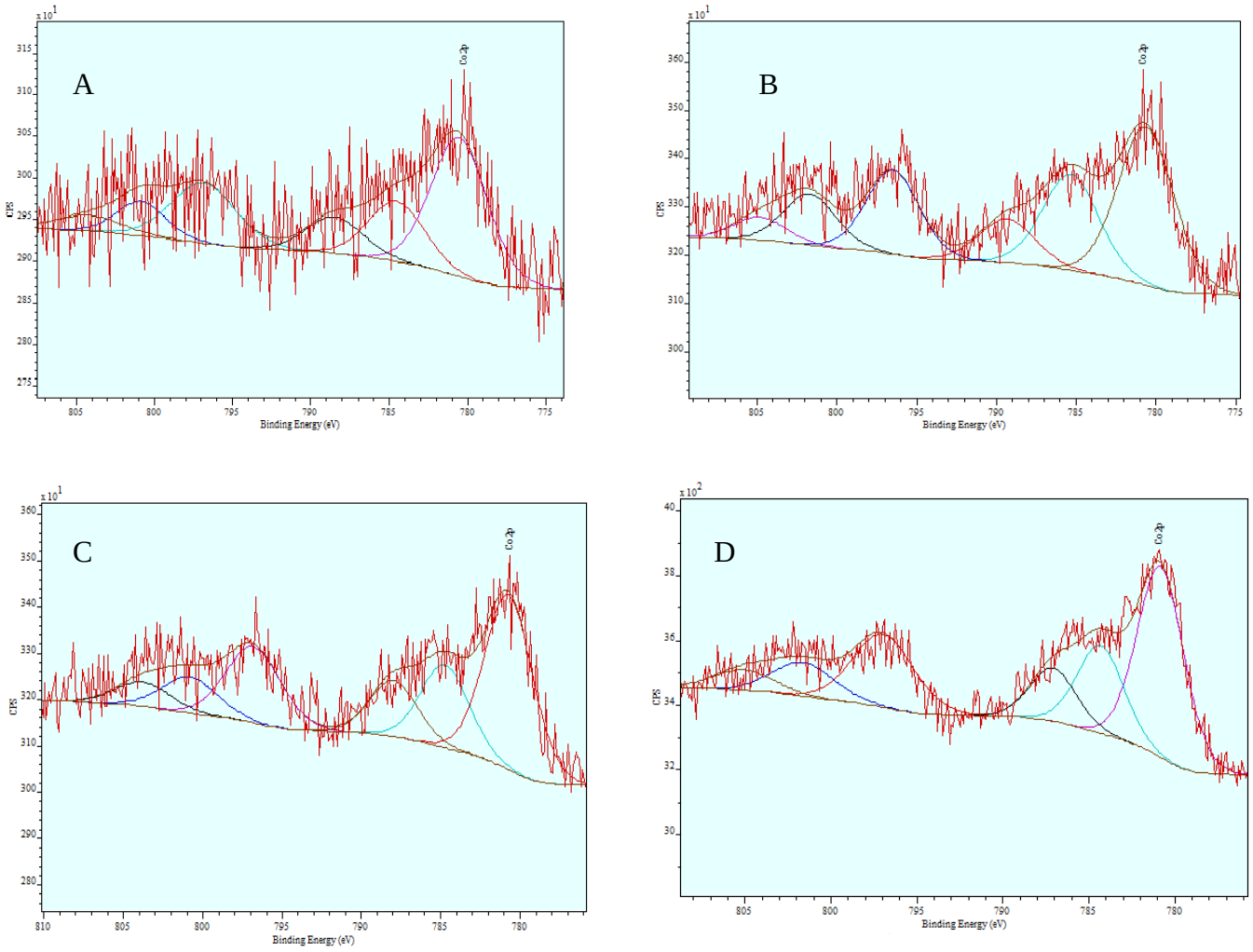


Figure 3.14 - XPS spectra of Co 2p region of the PtSnCo/C (3:1:1 to 3:1:4) (A-D) electrocatalysts

Table 3.11 - Co 2p $_{3/2}$ binding energies of all PtSnCo/C electrocatalysts

electrocatalyst (nominal atomic ratio)	Co 2p $_{3/2}$ binding energy (eV)	Co species
PtSnCo/C (3:1:1)	780.52	CoO
PtSnCo/C (3:1:2)	780.64	CoO
PtSnCo/C (3:1:3)	780.73	CoO
PtSnCo/C (3:1:4)	780.84	CoO

Table 3.11 summarises the results obtained from fitting the Co 2p spectum of the individual PtSnCo/C catalyst. The broad satellites to higher binding energy of the main 2p $_{3/2}$ curves were observed in all Co 2p spectra of the as-prepared PtSnCo/C catalysts, indicating no Co(III) compounds are present in the surface layers of the catalysts. The Co $2p_{3/2}$ binding energies from deconvolution of the main Co $2p_{3/2}$ peaks were 780.52, 780.64, 780.73, and 780.84 eV for PtSnCo/C (3:1:1), PtSnCo/C (3:1:2), PtSnCo/C (3:1:3), and PtSnCo/C (3:1:4), respectively. Based on the binding energies of different Co oxidation states, it is unlikely for metallic Co to be present in the surface layers of the as-prepared PtSnCo/C catalysts. Three possible Co(II) compounds namely CoO, Co_3O_4, and $Co(OH)_2$ are considered the major Co species in the surface layers of the PtSnCo/C catalysts. According to the Co $2p_{3/2}$ binding energy taken from three different references (Table 3.12), it can be concluded that CoO was present as a predominant surface cobalt species in all the as-prepared PtSnCo/C catalysts.

Table 3.12 - Co $2p_{3/2}$ binding energies (eV) of different cobalt species [36]

cobalt species	Schenck and Dillard (1983)	Cataldi et al. (1992)	Moulder et al. (1992)
metallic Co	-	-	778.3
CoO	780.0±0.1	779.8	780.4
Co_3O_4	779.9±0.1	-	779.5
$Co(OH)_2$	781.0±0.1	781.4	781.0
CoOOH	780.0±0.1	-	780.0

The surface compositions of the PtSn/C (3:1) and all PtSnCo/C catalysts were determined by the XPS measurement. Since all the XPS spectra were obtained from the measurement performed under the same conditions, the relative intensity ratio of the different peaks acquired can represent the relative content of the Pt, Sn, and Co species present in the surface layers [51].

Table 3.13- Surface compositions of the PtSn/C (3:1) and all PtSnCo/C catalysts

electrocatalyst	surface composition from XPS Pt:Sn:Co (atomic %)	Pt/Sn ratio	Pt/Co ratio
PtSn/C (3:1)	55.67:44.33	1.26	-
PtSnCo/C (3:1:1)	23.81:34.35:41.84	0.69	0.57
PtSnCo/C (3:1:2)	10.10:27.66:62.24	0.37	0.16
PtSnCo/C (3:1:3)	12.84:19.82:67.33	0.65	0.19
PtSnCo/C (3:1:4)	10.06:16.19:73.74	0.62	0.14

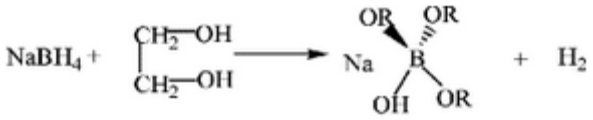
Table 3.14 – Comparison of the bulk and surface Pt/Sn and Pt/Co ratios

catalyst	bulk Pt/Sn ratio[a]	surface Pt/Sn ratio	bulk Pt/Co ratio[a]	surface Pt/Co ratio
PtSn/C (3:1)	3.03	1.26	-	-
PtSnCo/C (3:1:1)	2.88	0.69	6.84	0.57
PtSnCo/C (3:1:2)	3.21	0.37	2.34	0.16
PtSnCo/C (3:1:3)	3.29	0.65	0.98	0.19
PtSnCo/C (3:1:4)	3.20	0.62	0.81	0.14

[a]EDS bulk compositions

It can be seen in Table 3.14 that the surface Pt/Sn ratio of each as-prepared catalyst was significantly lower than the bulk Pt/Sn ratio. Likewise, the surface Pt/Co ratio of the as-prepared PtSnCo/C catalyst was smaller compared to the bulk Pt/Co ratio. These results demonstrate that the surface layers of the as-prepared PtSn/C (3:1) and all the PtSnCo/C catalysts are enriched with Sn and Co species.

Based on the results from catalyst characterisation, the formation of the Pt-based nanoparticles supported on carbon for the synthesised PtSn/C (3:1) and all PtSnCo/C catalysts can be proposed as follows. In the case of the PtSnCo/C catalysts, Pt(IV), Sn(II), and Co(II) ions in the precursor solutions initially form the metal ion-EG complexes. In the alkaline EG solution of $NaBH_4$, ethylene glycol was reported to react with sodium borohydride to produce the weakly basic complex macromolecule (A) as shown below [52].



Equation (3.11)

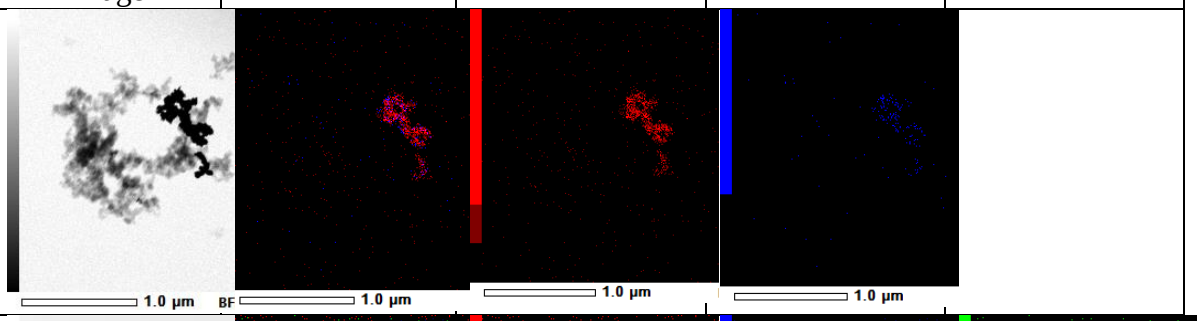
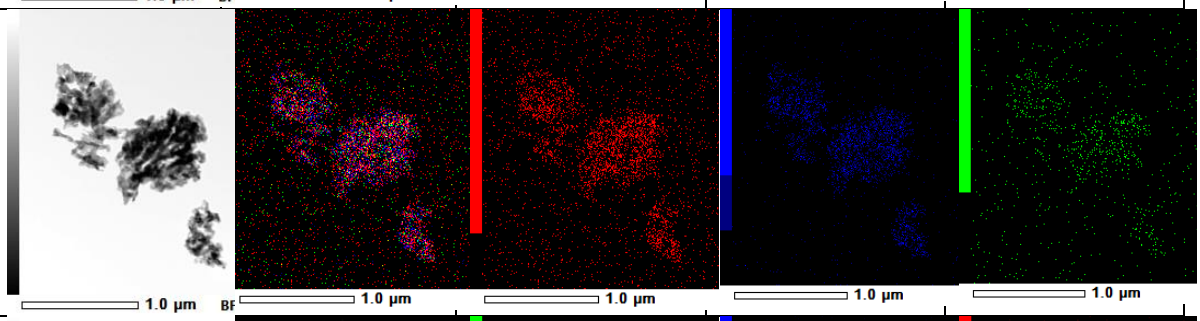
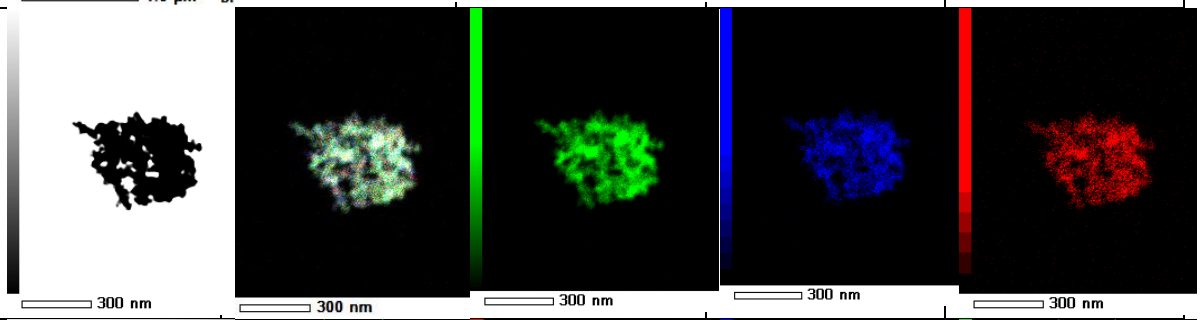
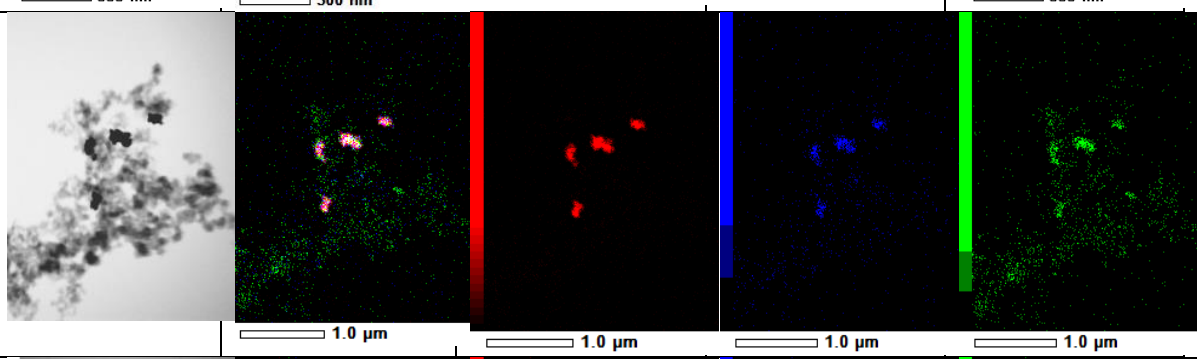
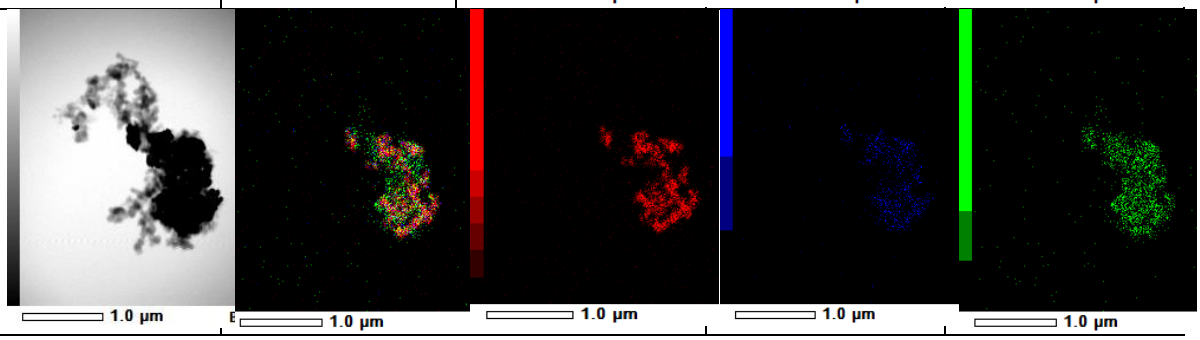
A

Because sodium hydroxide does not react with $NaBH_4$ and EG, the alkaline EG solution of $NaBH_4$ with EG in excess consists of the complex A, sodium hydroxide, and ethylene glycol. During the reduction step, Pt(IV) ions in $[PtCl_6]^{2-}$ are reduced to Pt first due to the most positive standard reduction potential at 25 ^oC of $[PtCl_6]^{2-}$ species. Pt atoms then aggregate to form Pt nanoparticles. Some Sn(II) and Co(II) ions are reduced to metallic Sn and Co by excess $NaBH_4$. The obtained Sn atoms or Sn and Co atoms incorporate into the Pt structure to form alloys. Upon the addition of NaOH-EG solution to raise the pH of the mixtures to 10, non-reduced Sn(II) and Co(II) ions react with hydroxide species to form solid $Sn(OH)_2$ and $Co(OH)_2$ [Phys. Chem. Chem. Phys. 15 (2013) 1014]. The analysis of the XRD results showed that no Co was alloyed with Pt and Sn atoms except for the PtSnCo/C (3:1:1) catalyst. The solid $Sn(OH)_2$ and $Co(OH)_2$ species, under the employed reduction conditions, transform into SnO, SnO_2, and CoO and deposit on the Pt-based nanoparticles formed, as suggested by the XPS results. The concentrations of $[PtCl_6]^{2-}$, Sn(II), and Co(II) species as well as the Pt:Sn:Co atomic ratios in the precursor EG solutions would have an effect on the formation of Pt-based alloys and the degree of alloying. Detailed studies will be carried out to reveal the mechanisms for formation of nanoparticles for PtSn/C (3:1) and all PtSnCo/C (3:1:1, 3:1:2, 3:1:3, and 3:1:4) catalysts.

3.3.7 Bright Field Scanning Transmission Electron Microscopy (BF-STEM)

BF-STEM method equipped with EDS was used to study the distribution of nanoparticles on Vulcan XC-72R carbon black of the as-prepared PtSn/C (3:1) and all PtSnCo/C catalysts. BF-STEM micrographs and corresponding EDS maps are shown in Table 3.15.

Table 3.15 BF-STEM images and EDS elemental maps

catalyst	BF-STEM image	overlay	Pt	Sn	Co
PtSn/C (3:1)					
PtSnCo/C (3:1:1)					
PtSnCo/C (3:1:2)					
PtSnCo/C (3:1:3)					
PtSnCo/C (3:1:4)					

It can be seen from the EDS maps generated from the BF-STEM micrograph of the PtSn/C (3:1) sample that Pt and Sn elements were in close proximity on the carbon support. This finding confirms the co-existence of PtSn alloys and SnO_x species in the as-synthesised nanoparticles. A Co element in all the as-synthesised PtSnCo/C samples was found close to where Pt and Sn were detected. The close proximity of Co to Pt and Sn can be certain based on these findings. Unlike the case of PtSn/C (3:1), these results cannot be used to confirm that Co exists only in form of CoO with Pt and Sn. It may be present as binary PtCo alloys, or ternary PtSnCo alloys.

3.3.8 X-ray Absorption Spectroscopy (XAS)

X-ray absorption spectroscopy is a widely used method to investigate atomic local structures and electronic states. Generally, an X-ray strikes an atom, resulting in promotion of an excited core electron to an unoccupied valence level, or into the continuum. The transition of an excited core electron to a higher energy unoccupied state is studied by XAS [53]. X-ray absorption spectra consist of two main spectral regions namely X-ray Absorption Near Edge Structure (XANES) or Near Edge X-ray Absorption Fine Structure (NEXAFS) and Extended X-ray Absorption Fine Structure (EXAFS) [54]. Each region in an X-ray absorption spectrum is a result of the transitions of three different types of photoelectrons. The NEXAFS region emerges due to transition of an excited core electron with the wave vector (k) of zero to an unoccupied valence state, or transition of a photoelectron with $0 < k < 2/R$, where R is the distance between the X-ray absorbing atom and its nearest neighbour, to the continuum. The EXAFS region is also a result of transition from a core level to the continuum of a photoelectron, but the photoelectron involved has the k value greater than 2/R. The photoelectron of this type has considerably high kinetic energy and weak backscattering

occurs in a single scattering process from only one neighbouring atom. Figure 3.15 shows the transitions of photoelectrons upon absorption of an X-ray quantum.

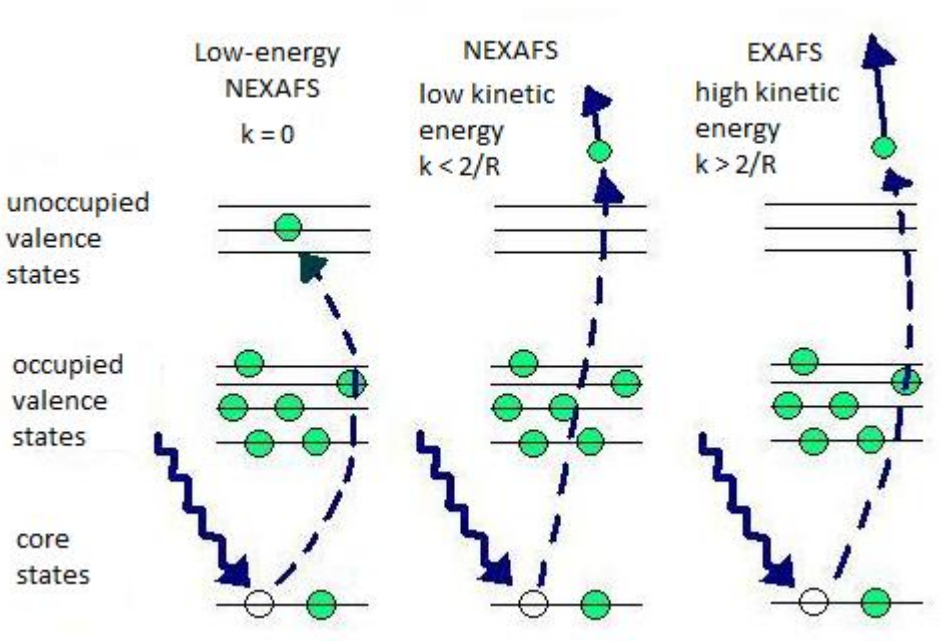


Figure 3.15 -Transitions of three different types of photoelectrons upon absorption of an X-ray quantum [53]

The as-synthesised PtSnCo/C catalysts were characterised using the XAS technique at room temperature. Figure 3.16 shows the Co K-edge XANES spectra of all the as-prepared PtSnCo/C catalysts and the standard Co foil. These spectra were energy calibrated, background corrected, and normalised using Athena software. XANES is appreciably sensitive to the co-ordination number of a central atom and symmetries. It can be used to determine the oxidation state of a probed element [55]. The shapes of all the XANES spectra shown in Figure 3.16 were similar, but different from that of the XANES spectrum of the standard Co foil. The pre-edge features, which arise from 1s to 3d transition due to 3d to 4p orbital mixing as well as direct quadrupolar coupling [53], were observed in all spectra at the same photon energy and with almost the same intensity. The close pre-edge intensity is indicative of similar co-ordination symmetries of the absorbing Co species [55].

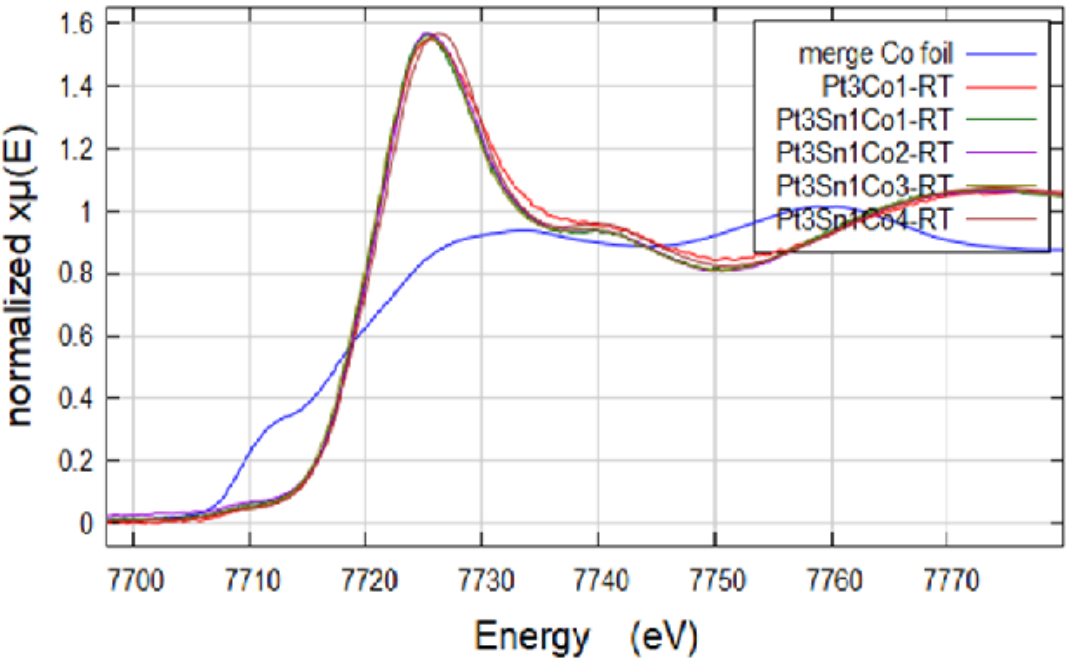


Figure 3.16 – Co K-edge XANES spectra of the standard Co foil and all the as-prepared PtSnCo/C catalysts obtained from XAS measurements at room temperature

The edge absorption energy for all the as-synthesised PtSnCo/C nanoparticle materials was much higher than that for the Co foil. This indicates that the oxidation state of absorbing Co in all the as-prepared PtSnCo/C materials is more positive compared to that of Co atoms in the Co foil. The strong peaks above the edge energy position called the white line peak were present at about 7.725 keV, corresponding to the white line energy of CoO species [55, 56]. It can be concluded from the Co K-edge XANES spectra that the majority of Co species in the as-prepared PtSnCo/C materials is CoO. After the XAS measurements at room temperature were conducted, the as-synthesised PtSnCo/C materials were heated under the reducing atmosphere of H_2 to 400 ^oC at a H_2 flow rate of 15 mL/min and retained at this temperature for 2 hours. The *in-situ* XAS measurements on the heat-treated samples were then carried out. Figure 3.17 shows the Co K-edge XANES spectra of the thermally treated PtSnCo/C samples.

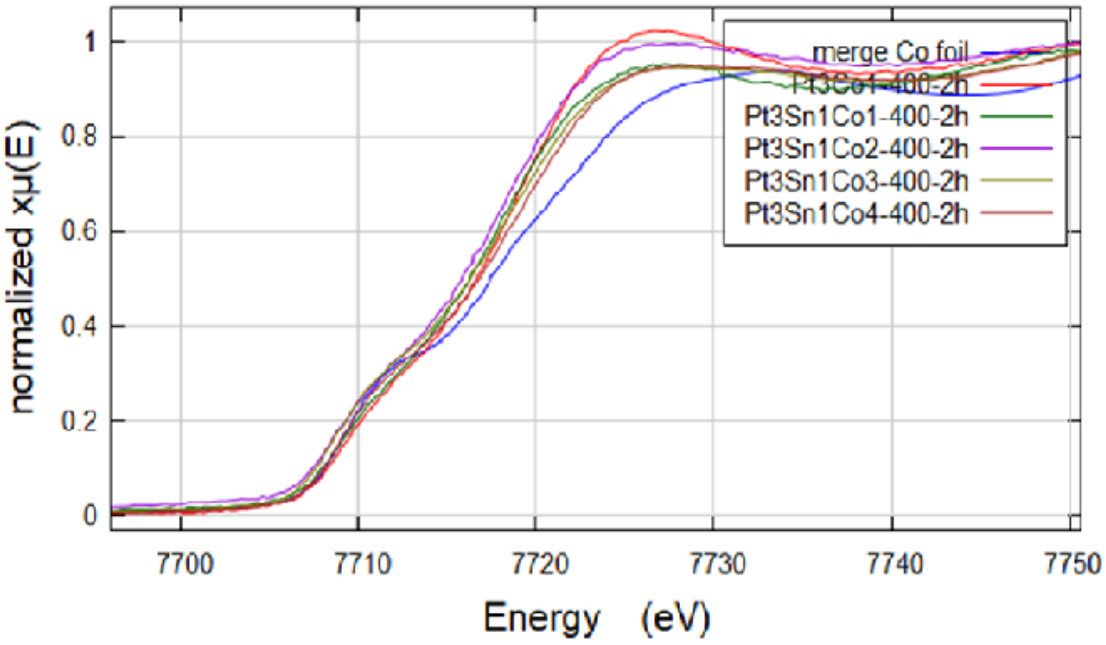


Figure 3.17 – Co K-edge XANES spectra of the PtSnCo/C samples thermally treated at 400 ^{o}C for 2 hours in a H_2 atmosphere at a flow rate of 15 mL/min.

The shapes of the XANES spectra shown in Figure 3.17 for all the thermally treated samples were similar. The pre-edge structures previously observed in the as-prepared PtSnCo/C samples were not present in the XANES spectra of all the thermally treated samples. This would be due to changes in the co-ordination symmetries of the absorption sites upon reduction at 400 ^{o}C. The intensity of the white line decreased and the peak position shifted to the higher photon energy value, possibly due to CoO reduction to metallic Co in all the thermally treated samples. However, the edge energies for the thermally treated samples were slightly higher than that for the Co foil. An explanation for this incident would be the existence of a trace amount of CoO species, or charge transfer from Co atoms to Pt or Sn. The results obtained from analysis of the XANES spectra of the thermally treated samples point out that reducing reaction conditions can alter phases of nanoparticles which could lead to changes in the catalytic activity of a nanoparticle material.

For an in-depth investigation of the local structures of both as-prepared and thermally treated samples, the EXAFS data extracted from the XAS spectra of the two sample sets were analysed using the standard data analysis procedure (ARTEMIS software). The EXAFS spectra were firstly transformed from k space to R space to obtain the radial distribution function (RDF). Fourier transform of the RDF was performed over the appropriate region to isolate one or several coordination shells. The isolated coordination shells were then fitted using the single scattering EXAFS equation. Figures 3.18 and 3.19 show Fourier transformed (FT) EXAFS profiles for all the as-prepared and thermally treated PtCo/C (3:1) and PtSnCo/C catalysts, respectively.

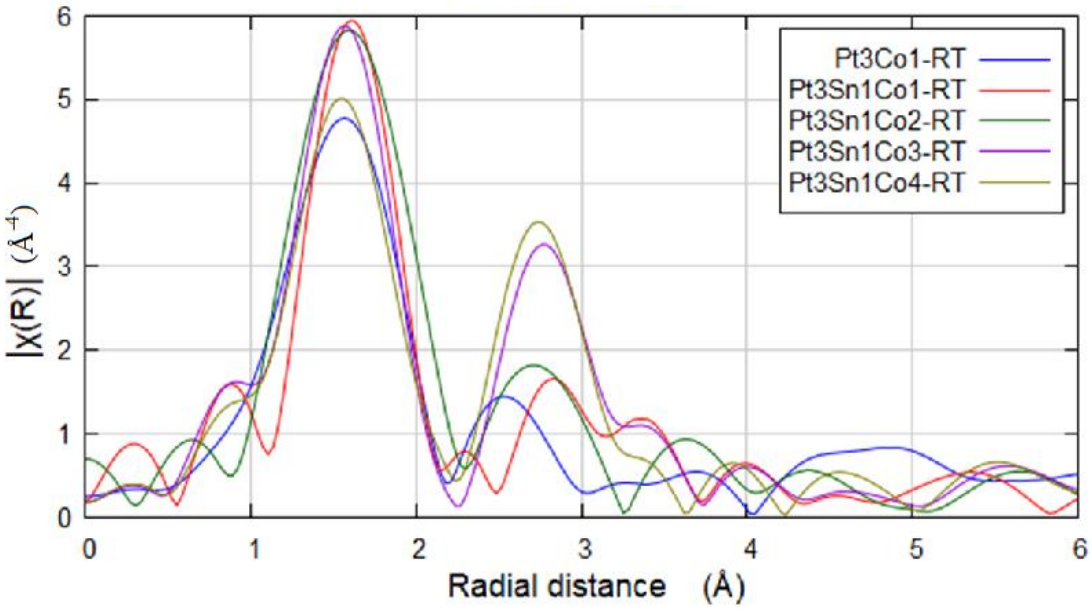


Figure 3.18 – Fourier transformed (FT) EXAFS profiles for all the as-prepared PtCo/C (3:1) and PtSnCo/C catalysts

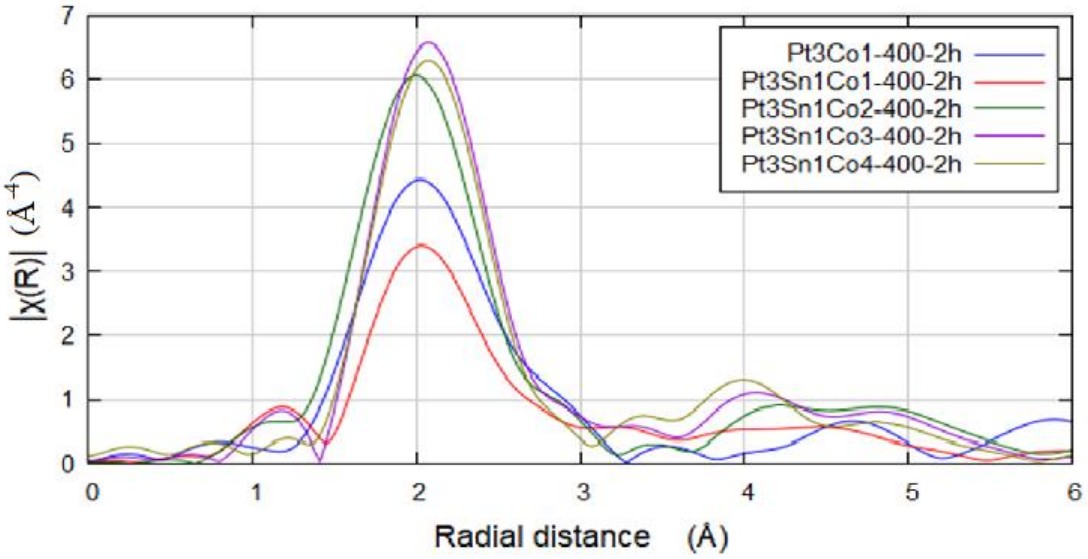


Figure 3.19 – FT-EXAFS profiles for all the thermally treated PtCo/C (3:1) and PtSnCo/C catalysts

The fitted data summarised in Table 3.16 show that the as-prepared PtCo/C (3:1) and all PtSnCo/C samples contained CoO as a predominant species of Co. The total coordination numbers, which are a summation of the coordination numbers of both Co-O and Co-Co interactions, were in the range of 7 to 12. The Co-Co inter-atomic distance for all the as-prepared PtSnCo/C samples was similar and it was higher than that for the as-prepared PtCo/C (3:1) sample. The presence of Sn with Pt and Co may cause dilation in Co-Co distance. The main peaks located at a radial distance between 2 and 3 Å, which are likely due to the first shell of Co-Co interaction, were significantly different in intensity. The peak intensity for PtSnCo/C (3:1:3) and PtSnCo/C (3:1:4) was close, but higher than that for the other three investigated catalysts. This may be due to a larger particle size or better crystallinity. Upon reduction under the atmosphere of H_2 at 400 ^oC for 2 hours, metallic Co and cubic Pt_3Co alloy phases were detected in the PtCo/C (3:1) and PtSnCo/C (3:1:1) samples with a higher coordination number of Co-Pt interaction for PtSnCo/C (3:1:1).

Interestingly, only metallic Co phase was detected in the thermally treated PtSnCo/C (3:1:2), PtSnCo/C (3:1:3), and PtSnCo/C (3:1:4) samples. The existence of PtCo alloy phases cannot be discarded. They may be present in an undetectable amount or their particle size may be too small to be detected. The total coordination number of absorbing Co for all the heat-treated samples was in the range of 5 to 8, which is smaller than the coordination number value of 12 for bulk Co. These results would mean that metallic Co is mainly on the surface of nanoparticles, or Co metal and PtCo alloys present in a small particle.

It was suspected that ternary PtSnCo alloys were formed and present in the as-synthesised PtSnCo/C catalysts. The application of XAS in a transmission mode for K-edge of Co (7709 eV) using a synchrotron-based X-ray could not yield a solid evidence to prove the existence of the ternary PtSnCo alloys. Although a solid proof was not obtained, the existence of the ternary PtSnCo alloys cannot be ruled out. To solve this problem, XAS measurements in a transmission mode for Pt L_{III}-edge (11564 eV) and Sn K-edge (29200 eV) should be carried out. Sn K-edge and Pt L_{III}-edge EXAFS profiles could reveal additional information such as Pt-Pt, Pt-Sn, Pt-Co, Sn-Sn, and Sn-Co interactions which can assist to confirm whether the ternary PtSnCo alloys exist in the as-synthesised PtSnCo/C catalysts.

Table 3.16 EXAFS fitting results of all the as-prepared and thermally treated PtCo/C (3:1) and PtSnCo/C catalysts

Catalyst	Interaction	C.N.	Bond length (Å)	ss	R factor (%)
as-prepared PtCo/C (3:1)	Co-O	6.0(2)	2.05(1)	0.009(1)	0.7
	Co-Co	1.4(3)	3.01(2)	0.008(2)	
thermally treated PtCo/C (3:1)	Co-Co1	4.7(3)	2.47(1)	0.011(1)	1.7
	Co-Pt1	1.3(4)	2.68(3)	0.007(3)	
as-prepared PtSnCo/C (3:1:1)	Co-O	4.4(4)	2.08(1)	0.005(2)	0.9
	Co-Co	2.9(4)	3.13(2)	0.015(3)	
thermally treated PtSnCo/C (3:1:1)	Co-Co1	2.8(3)	2.50(1)	0.008(1)	1.0
	Co-Pt1	4.2(4)	2.76(1)	0.011(3)	
as-prepared PtSnCo/C (3:1:2)	Co-O	7.1(5)	2.05(1)	0.011(1)	0.9
	Co-Co	2.4(6)	3.08(3)	0.014(4)	
thermally treated PtSnCo/C (3:1:2)	Co-Co1	5.6(4)	2.43(1)	0.011(1)	1.3
as-prepared PtSnCo/C (3:1:3)	Co-O	7.3(5)	2.06(1)	0.011(1)	0.5
	Co-Co	5.3(4)	3.10(1)	0.013(3)	
thermally treated PtSnCo/C (3:1:3)	Co-Co1	7.3(4)	2.47(1)	0.013(1)	1.3
as-prepared PtSnCo/C (3:1:4)	Co-O	7.2(5)	2.07(1)	0.012(1)	0.5
	Co-Co	4.6(2)	3.10(1)	0.009(2)	
thermally treated PtSnCo/C (3:1:4)	Co-Co1	7.8(3)	2.48 (1)	0.014(1)	0.9

Note: C.N. and ss refer to the average coordination number for the coordination shell and single scattering factor, respectively.

Conclusions

-The Pt/C (20 wt. % of Pt loading), PtSn/C (3:1), and PtSnCo/C (3:1:1 to 3:1:4) catalysts were successfully synthesised by the $NaBH_4$ reduction method.

-The bulk compositions determined by EDS for the PtSn/C (3:1) and all PtSnCo/C (3:1:1 to 3:1:4) catalysts were in close agreement with the nominal atomic ratios.

-ICP-MS analysis confirmed that the total metal loading was close to 20 wt.% for all the as-synthesised catalysts.

-All the synthesised catalysts showed the face-centred cubic (fcc) structure of PtSn alloy. The average crystallite sizes of the as-prepared nanoparticles were relatively close, indicating the effectiveness of the synthesis method in controlling the mean crystallite size.

-The ternary PtSnCo alloy was only formed in the PtSnCo/C (3:1:1) catalyst. The fcc lattice parameters and the degree of alloying for the PtSnCo/C catalysts were lower than those for PtSn/C (3:1). The decrease in the lattice parameter and the degree of alloying could be caused by lower amount of alloyed Sn and the presence of non-alloyed Sn and Co.

-The degree of alloying decreased continuously with increasing Co content up to the actual bulk composition of 3:1:3.4.

-The core-shell structure with PtSn alloy core and metal oxides shell was proposed for all the as-prepared catalysts based on the PXRD and XPS results.

-TEM results showed that the nanoparticles of the studied catalysts were in spherical shape. Some degree of particle agglomeration was observed for the PtSn/C (3:1), PtSnCo/C (3:1:2), and PtSnCo/C (3:1:4) catalysts. The mean particle size increased with increasing Co content.

-The XPS results showed that the binding energy of metallic Pt present in the PtSn/C (3:1) and all PtSnCo/C catalysts was higher than that in the Pt/C catalyst. The increase in the core-level binding energy of Pt (0) could be due to interactions between Pt and oxides of Sn and Co. The Sn and Co enriched surface was deduced for all the as-prepared nanoparticle catalysts.

-BF-STEM method equipped EDS showed that Sn and Co elements were in close proximity with Pt in all the as-synthesised PtSn/C (3:1) and all PtSnCo/C catalyst samples.

-XANES and EXAFS data for the as-prepared PtCo/C (3:1) and all PtSnCo/C catalysts showed that CoO was the predominant phase of Coin all the as-prepared catalyst samples. Upon reduction at 400 ^{o}C for 2 hours under the atmosphere of H_2, CoO was reduced to metallic Co. Only thermally treated PtCo/C (3:1) and PtSnCo/C (3:1:1) in which a PtCo alloy phase was found.

References

1. Akbari, B.; Tavandashti, M. P.; Zandrahimi, M., *Iranian Journal of Materials Science & Engineering* **2011,** *8* (2).
2. Alderucci, V.; Pino, L.; Antonucci, P. L.; Roh, W.; Cho, J.; Kim, H.; Cocke, D. L.; Antonucci, V., *Materials Chemistry and Physics* **1995,** *41* (1), 9-14.
3. Antolini, E.; Colmati, F.; Gonzalez, E. R., *Journal of Power Sources* **2009,** *193* (2), 555-561.
4. Awasthi, R.; Singh, R. N., *International Journal of Hydrogen Energy* **2012,** *37* (3), 2103-2110.
5. Barr, T. L., *The Journal of Physical Chemistry* **1978,** *82* (16), 1801-1810.
6. Beyhan, S.; Coutanceau, C.; Léger, J.-M.; Napporn, T. W.; Kadırgan, F., *International Journal of Hydrogen Energy* **2013,** *38* (16), 6830-6841.
7. Casella, I. G.; Guascito, M. R., *Journal of Electroanalytical Chemistry* **1999,** *476* (1), 54-63.
8. Colmati, F.; Antolini, E.; Gonzalez, E. R., *Journal of Alloys and Compounds* **2008,** *456* (1–2), 264-270.
9. Colmati, F.; Antolini, E.; Gonzalez, E. R., *Applied Catalysis B: Environmental* **2007,** *73* (1–2), 106-115.
10. Colmati, F.; Antolini, E.; Gonzalez, E. R., *Journal of Solid State Electrochemistry* **2001,** *5*.
11. De Souza, R. F. B.; Parreira, L. S.; Rascio, D. C.; Silva, J. C. M.; Teixeira-Neto, E.; Calegaro, M. L.; Spinace, E. V.; Neto, A. O.; Santos, M. C., *Journal of Power Sources* **2010,** *195* (6), 1589-1593.
12. Dean, J. A., Lange's Handbook of Chemistry 15th ed.; Dean, J. A., Ed. McGraw-Hill: New York, N.Y., 1999.
13. Desimoni, E.; Casella, G. I.; Salvi, A. M., *Carbon* **1992,** *30* (4), 521-526.
14. Frost, D. C.; McDowell, C. A.; Woolsey, I. S., *Chemical Physics Letters* **1972,** *17* (3), 320-323.
15. Hanyš, P.; Janeček, P.; Matolı´n, V.; Korotcenkov, G.; Nehasil, V., *Surface Science* **2006,** *600* (18), 4233-4238.
16. Huang, Q.; Yang, H.; Tang, Y.; Lu, T.; Akins, D. L., *Electrochemistry Communications* **2006,** *8* (8), 1220-1224.
17. Hüfner, S., Photoelectron Spectroscopy: Principles and Applications. Springer, Heidelberg: 1996.
18. Hull, R. V.; Li, L.; Xing, Y.; Chusuei, C. C., *Chemistry of Materials* **2006,** *18* (7), 1780-1788.
19. Hung, W.-Z.; Chung, W.-H.; Tsai, D.-S.; Wilkinson, D. P.; Huang, Y.-S., *Electrochimica Acta* **2010,** *55* (6), 2116-2122.
20. Jiang, L.; Sun, G.; Sun, S.; Liu, J.; Tang, S.; Li, H.; Zhou, B.; Xin, Q., *Electrochimica Acta* **2005,** *50* (27), 5384-5389.
21. Jiang, S.; Ma, Y.; Jian, G.; Tao, H.; Wang, X.; Fan, Y.; Lu, Y.; Hu, Z.; Chen, Y., *Advanced Materials* **2009,** *21* (48), 4953-4956.

22. Justin, P.; Hari Krishna Charan, P.; Ranga Rao, G., *Applied Catalysis B: Environmental* **2010,** *100* (3–4), 510-515.
23. Jusys, Z.; Schmidt, T. J.; Dubau, L.; Lasch, K.; Jörissen, L.; Garche, J.; Behm, R. J., *Journal of Power Sources* **2002,** *105* (2), 297-304.
24. Kim, J. H.; Choi, S. M.; Nam, S. H.; Seo, M. H.; Choi, S. H.; Kim, W. B., *Applied Catalysis B: Environmental* **2008,** *82*, 89-102.
25. Kongkanand, A.; Vinodgopal, K.; Kuwabata, S.; Kamat, P. V., *The Journal of Physical Chemistry B* **2006,** *110* (33), 16185-16188.
26. Lee, E.; Murthy, A.; Manthiram, A., *Electrochimica Acta* **2011,** *56* (3), 1611-1618.
27. Lim, D.-H.; Choi, D.-H.; Lee, W.-D.; Lee, H.-I., *Applied Catalysis B: Environmental* **2009,** *89* (3–4), 484-493.
28. Ma, Y.-w.; Liu, Z.-r.; Wang, B.-l.; Zhu, L.; Yang, J.-p.; Li, X.-a., *New Carbon Materials* **2012,** *27* (4), 250-257.
29. Ma, Y.; Wang, H.; Ji, S.; Linkov, V.; Wang, R., *Journal of Power Sources* **2014,** *247* (0), 142-150.
30. McIntyre, N. S.; Cook, M. G., *Analytical Chemistry* **1975,** *47* (13), 2208-2213.
31. Zhao, Y.; Liu, J.; Zhao, Y.; Wang, F., *Physical Chemistry Chemical Physics* **2014,** *16*, 19298-19306.
32. Parreira, L. S.; da Silva, J. C. M.; D'Villa -Silva, M.; Simões, F. C.; Garcia, S.; Gaubeur, I.; Cordeiro, M. A. L.; Leite, E. R.; dos Santos, M. C., *Electrochimica Acta* **2013,** *96* (0), 243-252.
33. Pereira, A.; Laplante, F.; Chaker, M.; Guay, D., *Advanced Functional Materials* **2007,** *17* (3), 443-450.
34. Qu, W.-L.; Wang, Z.-B.; Jiang, Z.-Z.; Gu, D.-M.; Yin, G.-P., *RSC Advances* **2012,** *2* (1), 344-350.
35. Roth, C.; Goetz, M.; Fuess, H., *Journal of Applied Electrochemistry* **2001,** *31* (7), 793-798.
36. Salimon, J.; Riyanto, R.; Othman, M. R., *Indonesian Journal of Chemistry* **2011,** *11* (1).
37. Tabet-Aoul, A.; Mohamedi, M., *Journal of Alloys and Compounds* **2013,** *553* (0), 113-118.
38. Thepkaew, J.; Therdthianwong, S.; Therdthianwong, A.; Kucernak, A.; Wongyao, N., *International Journal of Hydrogen Energy* **2013,** *38* (22), 9454-9463.
39. Ungár, T.; Tichy, G.; Gubicza, J.; Hellmig, R. J., *Powder Diffraction* **2005,** *20* (04), 366-375.
40. Venkataraman, R.; Kunz, H. R.; Fenton, J. M., *Journal of The Electrochemical Society* **2003,** *150* (3), A278-A284.
41. Viderama, S. Periodic Table - Electronegativity - Noble Gases. http://secrets-of-periodic-table.blogspot.co.uk/2012/09/pauling-electronegativity-values.html.

42. Villullas, H. M.; Mattos-Costa, F. I.; Bulhões, L. O. S., *The Journal of Physical Chemistry B* **2004,** *108* (34), 12898-12903.
43. Wang, R.; Liu, Z.; Ma, Y.; Wang, H.; Linkov, V.; Ji, S., *International Journal of Hydrogen Energy* **2013,** *38* (31), 13604-13610.
44. Zhou, Y.; Nakashima, M.; White, J. M., *The Journal of Physical Chemistry* **1988,** *92* (3), 812-818.
45. Zhu, M.; Sun, G.; Xin, Q., *Electrochimica Acta* **2009,** *54* (5), 1511-1518.
46. Leite, E. R., Nanocrystals Assembled from the Bottom Up. In *Encyclopedia of Nanoscience and Nanotechnology*, Nalwa, H. S., Ed. American Scientific: 2004**,** Vol. 6, pp 537-554.
47. Zhang, H.-X.; Siegert, U.; Liu, R.; Cai, W.-B., *Nanoscale Research Letters* **2009,** *4* (7), 705-708.
48. Baturina, O. A.; Aubuchon, S. R.; Wynne, K. J., *Chemistry of Materials* **2006,** *18* (6), 1498-1504.
49. Stevens, D. A.; Dahn, J. R., *Carbon* **2005,** *43* (1), 179-188.
50. Jiang, L.; Zang, H.; Sun, G.; Xin, Q., *Chinese Journal of Catalysis* **2006,** *27* (1), 15-19.
51. Zhang, X.; Wang, H.; Key, J.; Linkov, V.; Ji, S.; Wang, X.; Lei, Z.; Wanga, R., *Journal of The Electrochemical Society* **2012,** *159* (3).
52. Liu, M.; Chang, J.; Sun, J.; Gao, L., *Electrochimica Acta* **2013,** *107* (0), 9-15.
53. Gee, S., XAS: Theory. https://chem.libretexts.org/Core/Physical_and_Theoretical_Chemistry/Spectroscopy/X-ray_Spectroscopy/XAS%3A_Theory (accessed 8 April 2018)
54. Ascone, I., X-ray absorption spectroscopy for beginners. https://www.iucr.org/__data/assets/pdf_file/0004/60637/IUCr2011-XAFS-Tutorial_-Ascone.pdf (accessed 8 April 2018)
55. Das, B.; Reddy, M. V.; Chowdari, B. V. R., *Nanoscale* **2013**, 5 (5), 1961-1966.
56. Chen, L.; Mashimo, T.; Iwamoto, C.; Okudera, H.; Omurzak, E.; Ganapathy,H. S.; Ihara, H.; Zhang, J.; Abdullaeva, Z.; Takebe, S.; Yoshiasa, A., *Nanotechnology* **2013**, 24 (4), 045602.

Chapter 4

Ethanol Electro-oxidation Reaction (EOR) on the PtSn/C and PtSnCo/C Electrodes

4.1 Introduction

The ethanol electro-oxidation reaction in acidic media on carbon supported binary and ternary Pt-based nanoparticle catalysts has been extensively investigated using both voltammetric techniques and a single direct ethanol fuel cell (DEFC) test [1-10]. In the case of carbon supported bi-metallic PtSn and PtSn-based tri-metallic nanoparticle catalysts, Pt, a catalytic metal for ethanol electro-oxidation, is mostly in the polycrystalline form. In order to understand the ethanol electro-oxidation reaction on PtSn and ternary PtSn-based nanoparticle catalysts, the reaction mechanisms for ethanol electro-oxidation on polycrystalline Pt electrodes will be discussed. R. B. Kutz et al. [11] investigated reaction pathways of ethanol electro-oxidation on the polycrystalline Pt electrodes in both H_2SO_4 and $HClO_4$ electrolyte solutions. The proposed reaction mechanisms based on the spectroscopic and voltammetric observations are shown in Figure 4.1.

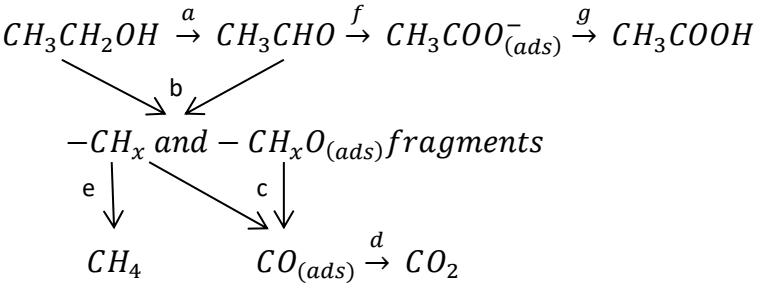


Figure 4.1 - Schematic diagram of the proposed reaction pathways of ethanol electro-oxidation on polycrystalline Pt catalysts in acidic media

It can be summarised from the experimental results [11] that there are two main pathways for the electro-oxidation of ethanol on polycrystalline Pt electrodes based on a final product. One oxidation pathway occurring at low potentials (E < 0.4 V vs. Ag/AgCl) led to the formation of adsorbed CO species. The other (E > 0.4 V) led to the formation of acetate which is the main surface product of ethanol electro-oxidation. They also found that the oxidation of the adsorbed CH_x fragment to CO was more difficult than that of adsorbed CH_xO. At low potentials, the electro-oxidation of the adsorbed CH_x species was expected to be less efficient and competed with the electro-reduction of $CH_{x,ad}$ to CH_4. J. Melke et al. summarised the reaction mechanisms investigated by spectroscopic techniques of ethanol electro-oxidation on Pt electrodes [12]. The oxidation of ethanol to acetaldehyde and acetic acid took place on a Pt(111) surface or at all Pt sites in the case of high surface coverage. Moreover, a part of ethanol electro-oxidation to acetaldehyde was found to be reversible. The adsorbed intermediates found on a Pt(111) surface were acetate ($CH_3COO^-_{ad}$) and acetyl (CH_3CO_{ad}). It was also found that further dehydrogenation of acetyl was hindered on Pt(111). For the oxidation of ethanol towards CO_2, it could take place only at low coverage on open or stepped surfaces such as Pt(110), Pt(100), and Pt(211). The formation of acetaldehyde could be avoided by promoting the dehydrogenation on α-C of the ethanol molecule. The second dehydrogenation on the α-C atom possibly led to further dehydrogenation and made the C-C bond breaking possible. The C-C bond cleavage occurred within either adsorbed CHCO or CH_2CO species and it led to the formation of strongly adsorbed CH_x and CO intermediates (see Figure 4.2).

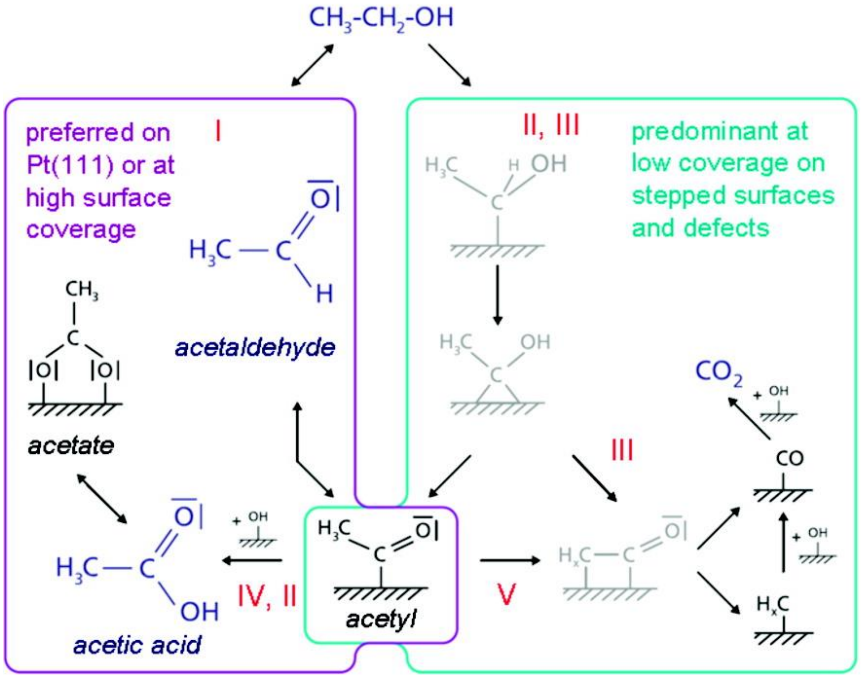


Figure 4.2 – Summary of the reaction mechanisms of ethanol oxidation on the Pt electrodes [12]. Reproduced from ref. 12 with permission from ACS

To study the electro-oxidation reaction of ethanol on PtSn/C and carbon supported PtSn-based tri-metallic nanoparticle catalysts in terms of the catalytic activity of the catalysts and the EOR mechanism, Linear Sweep Voltammetry (LSV), Cyclic Voltammetry (CV), and Chronoamperometry (CA) are employed for a half-cell test. These three techniques can provide information about surface structures and stability of nanoparticle catalysts during the ethanol electro-oxidation reaction.

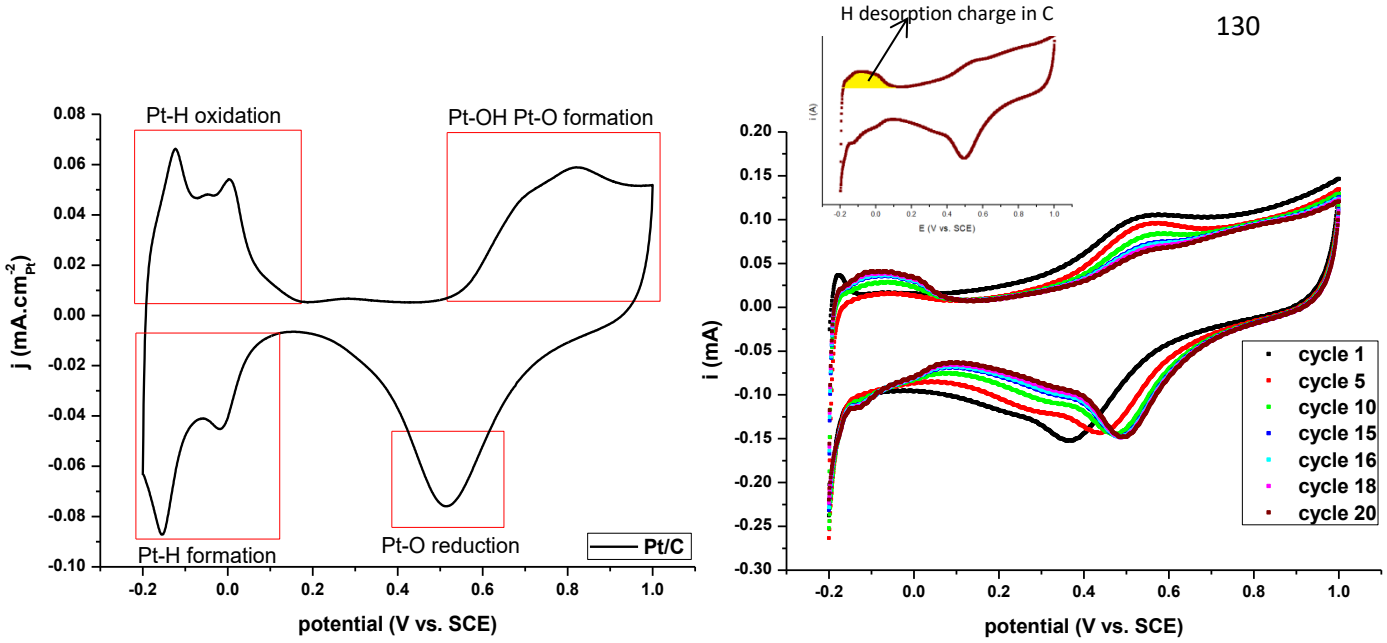
In this chapter, the ethanol electro-oxidation activity in the acidic medium of the PtSnCo/C catalysts investigated by LSV, CV, and CA is presented. Their activity for ethanol electro-oxidation and stability are compared with that of PtSn/C prepared using the same method in order to study the effect of Co on the ethanol electro-oxidation reaction.

4.2 Electrochemical Measurement

4.2.1 Characteristics of a Catalyst Surface

The characteristics of the surfaces of PtSn/C (3:1) and all the investigated PtSnCo/C catalysts under the employed electrochemical conditions were studied. The glassy carbon electrodes with PtSn/C (3:1) and all PtSnCo/C electrocatalysts were potential cycled in 0.5M H_2SO_4 supporting electrolyte solution to obtain stable cyclic voltammograms. The applied potential range was between -0.2 and 1.0 V vs. SCE. Potential values reported in this thesis, unless otherwise stated, are with respect to a saturated calomel electrode (SCE). The potential cycling process was conducted at room temperature (23 ^{o}C) with a scan rate of 50 mV/s.

The PtSn/C (3:1) and all the investigated PtSnCo/C electrodes were potential cycled in a N_2-purged 0.5M H_2SO_4 supporting electrolyte solution for 20 cycles. The obtained cyclic voltammograms are presented in Figures 4.3 and 4.4. The voltammetric features of the PtSn/C (3:1) electrode varied with an increase in a number of potential scanning cycles. The shapes and sizes of the first fifteen cyclic voltammograms observed during the entire potential scanning range were clearly different. After 15 scanning cycles, the shapes and sizes of the following voltammograms did not change significantly. Typical features including H adsorption and desorption on surface Pt, formation of Pt-OH and Pt-O species, and reduction of surface Pt-O species were observed in the steady-state cyclic voltammogram (cycle 20 in Figure 4.3) of PtSn/C (3:1). The charge of hydrogen desorption or oxidation from the Pt surface, which can be calculated from the peak area between -0.2 and 0.1 V (vs. SCE), increased with an increase in the number of potential scanning cycles, indicating that the Pt sites for H adsorption are more available upon potential cycling.



(A) (B)

Figure 4.3 Cyclic voltammograms of the Pt/C (A) and PtSn/C (3:1) (B) electrodes recorded in 0.5M H_2SO_4 supporting electrolyte solution at a scan rate of 50 mV/s with an inset showing H desorption charge.

The hydrogen adsorption and desorption features of Pt-based catalysts are influenced by a surface composition [10]. According to the XPS analysis of tin (see chapter 3), only tin oxide (SnO_x) species were detected in the surface region of the as-prepared PtSn/C (3:1). The smaller number of the Pt active sites for hydrogen adsorption on the surface of the as-prepared PtSn/C (3:1) electrode compared to that of the stable surface can be ascribed to the blockage of SnO_x species. J. Sobkowski et al. [13] carried out CV measurements on Pt and Pt with deposited tin electrodes in 0.5M H_2SO_4 solution at a scan rate of 50 mV/s between 0 and 1.4 V (vs. RHE) corresponding to a potential range of -0.26 to 1.14 V (vs. SCE). The obtained polarisation curve of the Pt with deposited tin electrode showed a broad oxidation peak centred at about 0.75 V (vs. RHE) or *ca.* 0.50 V (vs. SCE) in the forward scan and a reduction peak centred at *ca.* 0.50 V (vs. RHE) or *ca.* 0.24 V (vs. SCE) in the reverse scan. The observed redox couple was found outside a Pt oxidation/reduction region. They

attributed the oxidation peak at 0.75 V to the oxidation of adsorbed Sn(II) to adsorbed Sn(IV) species and the reduction peak at 0.50 V to the reversible reduction of the adsorbed Sn(IV) to Sn(II) (see Equation 4.1).

$Sn(II)_{ads} \rightleftharpoons Sn(IV)_{ads} + 2e^-$ Equation (4.1)

The electrochemical conditions set for the CV measurements on the Pt with deposited Sn electrode are identical to those applied for the CV measurements on the PtSn/C (3:1) and all investigated PtSnCo/C electrodes. The broad oxidation and reduction peaks appearing at approximately 0.50 V and 0.25 V (vs. SCE), respectively, in the first cyclic voltammogram of PtSn/C (3:1) could be attributed to the oxidation of deposited SnO species to probably adsorbed $Sn(OH)_4$ [13] and its reversible reduction. After prolonged cyclic polarisation between -0.2 V and 1.0 V, SnO species preferentially deposited on the Pt active sites for hydrogen adsorption could be dissolved into the acid medium as suggested by the disappearance of the adsorbed Sn(II)/Sn(IV) redox couple. The stable surface of the PtSn/C (3:1) electrode could contain mostly SnO_2 species as suggested by the broad shoulders between 0.4 and 0.6 V (vs. SCE) in the forward scan and between 0.2 and 0.4 V (vs. SCE) in the reverse scan which are ascribed to the O_2 adsorption and desorption from the dissociation of water onto SnO_2 [14].

The polarisation curves from potential cycling the PtSnCo/C (3:1:1), PtSnCo/C (3:1:2), PtSnCo/C (3:1:3), and PtSnCo/C (3:1:4) electrodes in 0.5 M H_2SO_4 supporting electrolyte solution, as shown in Figure 4.4, exhibit changes of current with applied potentials and a number of potential scanning cycles. After the 15^{th} potential scan of all the investigated Co-containing PtSn/C electrodes, no severe changes in the shape and size were observed, indicating that the electrode surfaces were stable after 15 cycles of potential scanning between -0.2 and 1.0 V (vs. SCE). According to the results from the potential cycling

process, the cycle 16 to cycle 20 voltammograms of the individual electrodes can represent the stable surfaces of the catalysts. In this thesis, the 20th cyclic voltammograms of all the investigated electrodes were selected. The changes in voltammetric features during the entire potential cycling process on PtSnCo/C (3:1:1) and the other cobalt-containing PtSn/C electrodes were similar to those on PtSn/C (3:1) including an increase in hydrogen desorption charge, a disappearance of the redox couple centred at *ca.* 0.50 V and 0.25 V (vs. SCE) in the forward and reverse scans, respectively, from the polarisation curves, and the presence of the small peak shoulders between 0.4 V and 0.6 V (vs. SCE) in the forward scans and 0.2 V and 0.4 V (vs. SCE) in the reverse scans on the polarisation curves. The corresponding voltammetric behaviours in the double layer and surface Pt oxidation/reduction regions of the PtSnCo/C catalysts to those of PtSn/C (3:1) suggest that SnO deposited on the outermost layer of the PtSnCo nanoparticles dissolved in the acid medium upon repeated potential cycling, while SnO_2 remained on the stable surfaces of the PtSnCo/C catalysts. Two small peaks centred at *ca.* -0.10 V in the H adsorption/desorption region were observed on the steady-state cyclic voltammograms of PtSnCo/C (3:1:1), PtSnCo/C (3:1:2), and PtSnCo/C (3:1:3). These two peaks are characteristic of hydrogen adsorption/desorption on a Pt(110) crystal plane [15]. The presence of the peaks at -0.10 V would be indicative of surface Pt reconstruction during the potential sweeping process. For the PtSn/C (3:1) and PtSnCo/C (3:1:4) electrodes, such features were not clearly observed on their steady-state cyclic voltammograms, indicating that a Pt(111) facet is possibly a predominant Pt crystal plane present on the stable surfaces of both catalysts. In comparison with the steady-state cyclic voltammogram of Pt/C (Figure 4.3), a well-defined H adsorption/desorption feature of polycrystalline Pt was not observed on the steady-state cyclic voltammograms of all the investigated electrodes. This may be due to high degree of surface alloying, or co-existence of Pt and oxide species of Sn and Co.

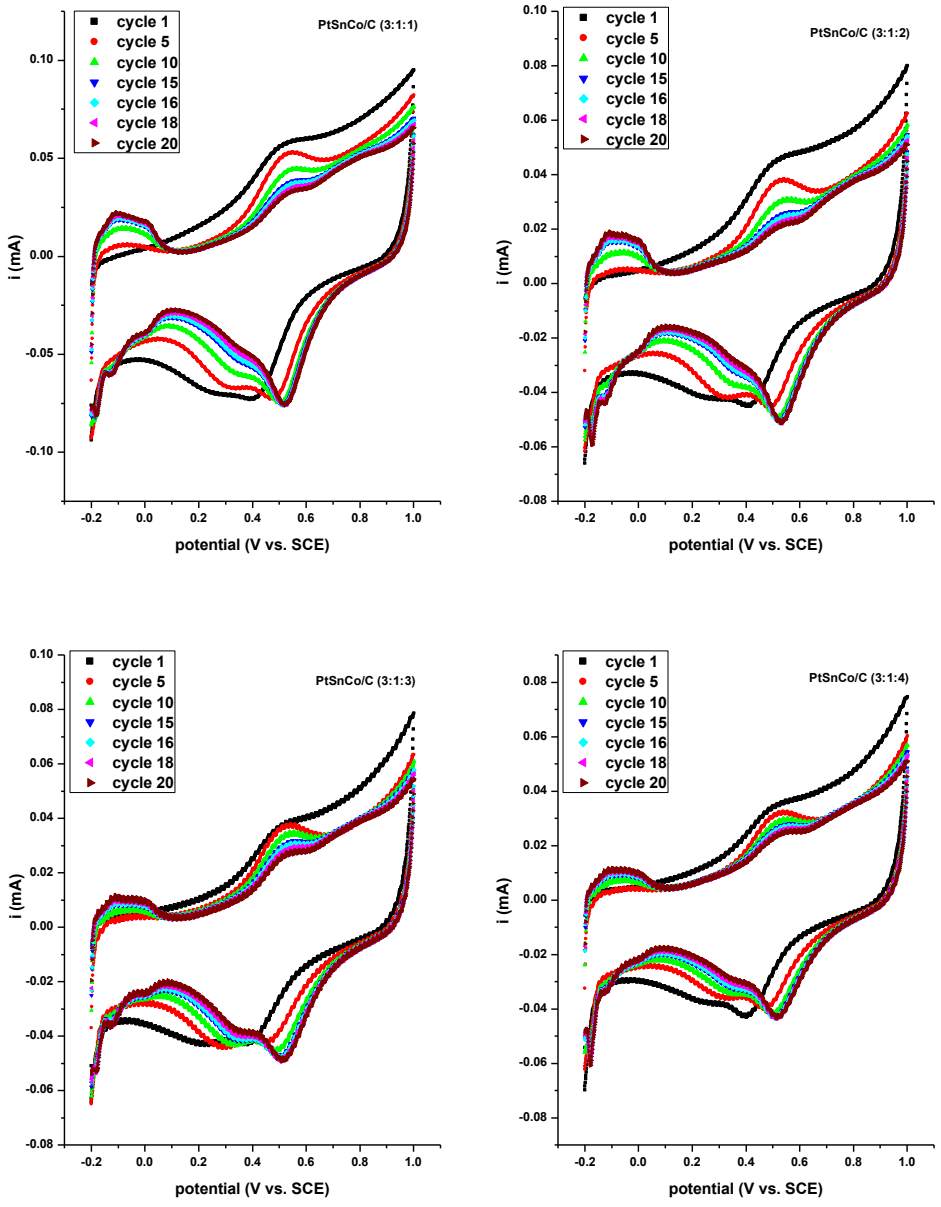


Figure 4.4 Cyclic voltammograms of all the investigated PtSnCo/C electrodes recorded in 0.5M H_2SO_4 supporting electrolyte solution at a scan rate of 50 mV/s.

Apart from tin oxide species, the as-prepared PtSnCo/C catalysts contained CoO as a predominant Co species on the outermost layer of the catalyst surfaces. The Pourbaix diagram for cobalt-water system (Figure 4.5) shows that cobalt is present in form of Co^{2+} at pH = 0.24 and the applied potentials between 0.0 and 1.2 V (vs. SHE). These conditions are similar to those for the CV measurements of the PtSnCo/C electrodes. N. Kristian et al. (2010) [17] studied the surface characteristics of a PtCo/C electrode prepared at pH 4 before and after potential cycling in 0.1M $HClO_4$ electrolyte solution. It was concluded from the cyclic voltammograms recorded in 0.1M KOH solution that the surface of the as-prepared PtCo/C electrocatalyst consisted of cobalt oxide species. After the acid treatment, the cobalt oxide species dissolved in the acid medium and the surface became Pt-enriched. It can, therefore, be assumed that potential cycling the PtSnCo/C electrodes in 0.5M H_2SO_4 supporting electrolyte solution between -0.2 and 1.0 V (vs. SCE) results in the dissolution of CoO into the acid medium.

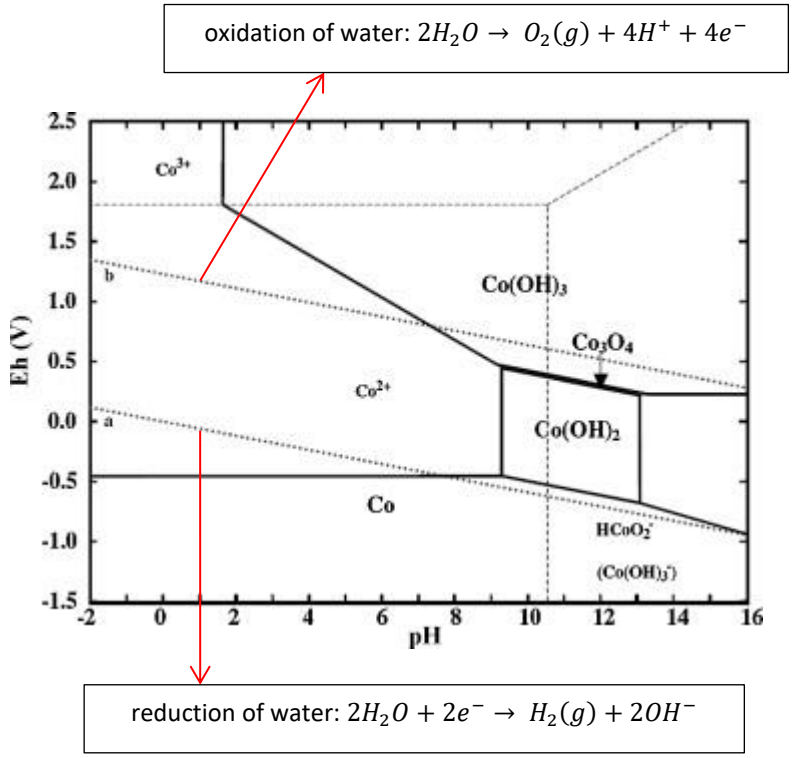


Figure 4.5 The Pourbaix diagram for the cobalt-water system [16]

The dissolution of CoO in sulphuric acid solution is represented by Equation 4.2 [18]:

$CoO + H_2SO_4 \rightarrow CoSO_4 + H_2O$ Equation (4.2)

Despite the possibility of CoO dissolution from the surfaces of the investigated PtSnCo/C catalysts during the potential cycling process, CoO could remain in some amount on the stable surfaces of the catalysts due to strong interactions between CoO and SnO_2.

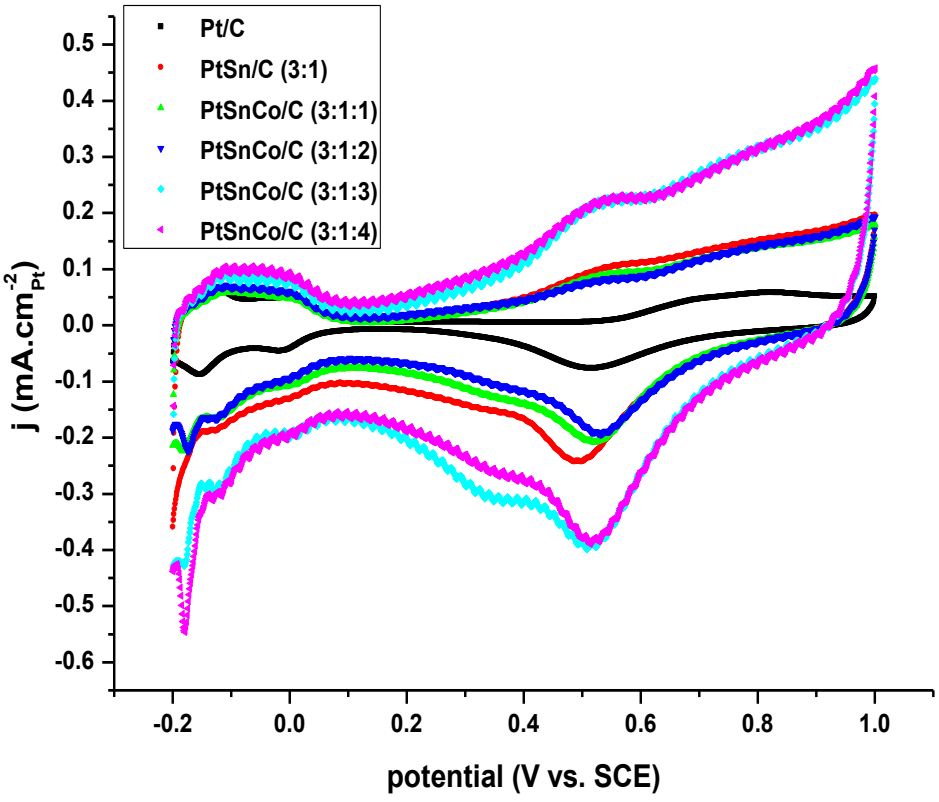


Figure 4.6 Steady-state cyclic voltammograms (cycle 20) of the Pt/C, PtSn/C (3:1) and all PtSnCo/C electrodes recorded in N_2-purged 0.5M H_2SO_4 supporting electrolyte solution at a scan rate of 50 mV/s.

The steady-state cyclic voltammograms of the PtSn/C (3:1) and all PtSnCo/C electrodes were compared (Figure 4.6). The currents were normalised by the electrochemically active surface area (EASA) based on hydrogen desorption charge (S_H) of Pt-H oxidation, denoted as Pt-EASA, which can be calculated by the following equation:

$$S_H = \frac{Q_H\ (\mu C)}{210\ \mu C.cm_{Pt}^{-2}} \qquad \text{Equation (4.3)}$$

where Q_H is hydrogen desorption charge with no contribution from the capacitive charge in the double layer region and 210 μC.cm$^{-2}_{Pt}$ is the charge required to oxidise a monolayer of hydrogen on the smooth Pt surface [8]. The roughness of the investigated electrodes was obtained by dividing the Pt-EASA with the apparent surface area of a 3-mm diameter glassy carbon electrode (GCE) (0.071 cm^2) [10]. The hydrogen desorption charge was obtained by integrating the hydrogen desorption peak located in a potential range from -0.2 (vs. SCE) to an applied potential (*ca.* 0.1 V vs. SCE) corresponding to a current response, in A or mA, with negligible capacitive contribution due to charge separation in the electrical double layer (see Figure 4.3).

Table 4.1 Summary of the hydrogen desorption charge (Q_H), Pt-EASA, and roughness of the stable catalyst surfaces

catalyst	Q_H (μC)	Pt-EASA (cm$^2_{Pt}$)	roughness
Pt/C	697.98	3.32	46.76
PtSn/C (3:1)	128.60	0.61	8.59
PtSnCo/C (3:1:1)	76.64	0.36	5.14
PtSnCo/C (3:1:2)	55.61	0.26	3.66
PtSnCo/C (3:1:3)	26.01	0.12	1.74
PtSnCo/C (3:1:4)	23.40	0.11	1.55

Table 4.1 shows that the stable surface of each investigated PtSnCo/C electrode had the real electrode surface area (Pt-EASA) lower than the PtSn/C (3:1) electrode. The decrease in Pt-EASA may be due to a greater amount of surface oxide species on the Pt active sites for hydrogen adsorption, or a lower number of the active sites for Pt-H formation arising from surface alloying. Agglomeration of nanoparticles during the potential cycling process may also associate with the reduction of the real electrode surface area. The capacitive charging currents in the double layer region (0.1 to 0.6 V (vs. SCE)) of PtSn/C (3:1), PtSnCo/C (3:1:1), and PtSnCo/C (3:1:2) (Figure 4.6) were similar, but lower than those of the investigated PtSnCo/C (3:1:3) and PtSnCo/C (3:1:4) electrodes. Since the capacitive charging current is usually from the dissociation of water on surface oxides [19][10], a greater amount of oxides present on a catalyst surface can result in higher capacitive charging current. Accordingly, the greatest amount of oxides can be found on the stable surface of PtSnCo/C (3:1:4), while the least amount is found on the stable surface of PtSn/C (3:1).

Table 4.2 Summary of surface Pt oxidation and Pt-O reduction potentials

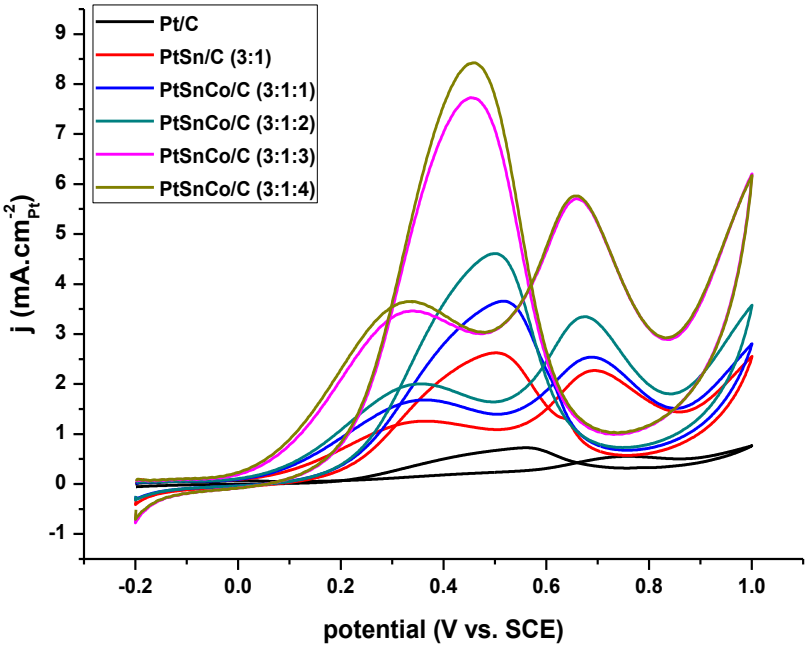
Electrocatalyst	onset potential of Pt-OH formation (V vs SCE)	peak potential of Pt-O reduction (V vs SCE)
Pt/C	0.53	0.52
PtSn/C (3:1)	0.60	0.49
PtSnCo/C (3:1:1)	0.60	0.52
PtSnCo/C (3:1:2)	0.60	0.53
PtSnCo/C (3:1:3)	0.60	0.51
PtSnCo/C (3:1:4)	0.60	0.52

Table 4.2 shows the onset potentials for Pt-OH formation and Pt-O reduction on the PtSn/C (3:1) and all the investigated PtSnCo/C electrodes. The formation of Pt-OH species from water dissociation on all electrodes commenced at *ca.* 0.60 V. In the reverse potential sweep, Pt-O species formed on the stable surfaces of all PtSnCo/C catalysts in a high potential region was reduced at more positive potentials compared to the reduction of Pt-O on the stable

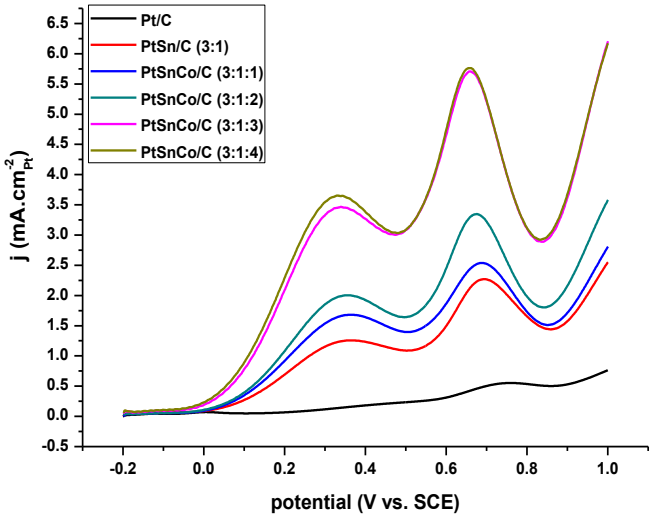
surface of the PtSn/C (3:1) catalyst. These results indicate that Pt on the stable surface of PtSn/C (3:1) is more oxophilic than that on the stable surfaces of the other four PtSnCo/C catalysts. Pt atoms on the stable surface of PtSn/C (3:1) could bind more strongly with oxygenated species than surface Pt on the other catalysts, resulting in a slower rate of intermediate removal.

4.3 Ethanol Electro-oxidation Activity by Cyclic Voltammetry

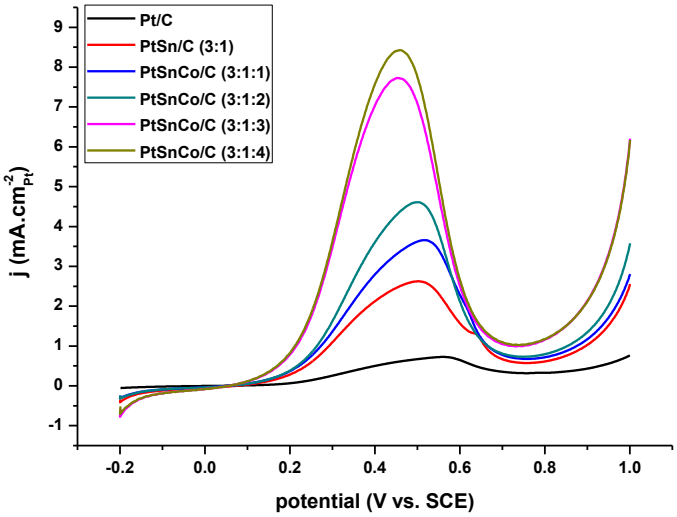
The electrocatalytic activities for ethanol oxidation of the Pt/C, PtSn/C (3:1) and all investigated PtSnCo/C catalysts were evaluated using the CV technique. Firstly, all the studied electrodes were potential cycled in 0.5M H_2SO_4 solution between -0.2 and 1.0 V (vs. SCE) for 20 cycles to obtain stable surfaces. The electrochemically treated electrodes were then potential swept between -0.2 and 1.0 V (vs. SCE) in 0.5M H_2SO_4 + 1M EtOH solution to investigate the ethanol electro-oxidation activities of the catalysts. The oxidation currents from the first cycle of the potential sweeping process in an ethanol-containing 0.5M H_2SO_4 solution were normalised by Pt-EASA of the stable surface. These area-based current densities were the ethanol electro-oxidation activities at different applied potentials of the catalyst. The measurements for the ethanol electro-oxidation activity of each catalyst sample were made in triplicate. The activities for ethanol electro-oxidation of the studied catalysts are presented in Figure 4.7.



(A)



(B)



(C)

Figure 4.7 - Cyclic voltammograms exhibiting the ethanol electro-oxidation activities of the Pt/C, PtSn/C (3:1) and all PtSnCo/C catalysts. CV conditions: 0.5M H_2SO_4 + 1M EtOH electrolyte solution, potential range from -0.2 to 1.0 V (vs. SCE), and a scan rate of 50 mV/s. (A) full voltammograms (B) forward scans (C) reverse scans

Figure 4.7 shows the ethanol electro-oxidation activities of the Pt/C, PtSn/C (3:1) and all PtSnCo/C catalysts. Ethanol electro-oxidation on PtSn/C (3:1) and all the ternary PtSnCo/C catalysts started at about 160 – 170 mV before the commencement of ethanol electro-oxidation on Pt/C. The onset potential for ethanol electro-oxidation on the stable surface of PtSn/C (3:1) was similar to that of PtSnCo/C (3:1:2), but it was about 15-20 mV higher than those of PtSnCo/C (3:1:1), PtSnCo/C (3:1:3), and PtSnCo/C (3:1:4). The negative shift of the onset potential indicates faster electron transfer kinetics of ethanol electro-oxidation on the binary PtSn/C (3:1) and ternary PtSnCo/C catalysts [20]. Sn and Co species present on the stable surfaces of PtSn/C (3:1) and all the investigated PtSnCo/C electro-catalysts could facilitate a dehydrogenation reaction upon adsorption of ethanol molecules on the catalyst surface.

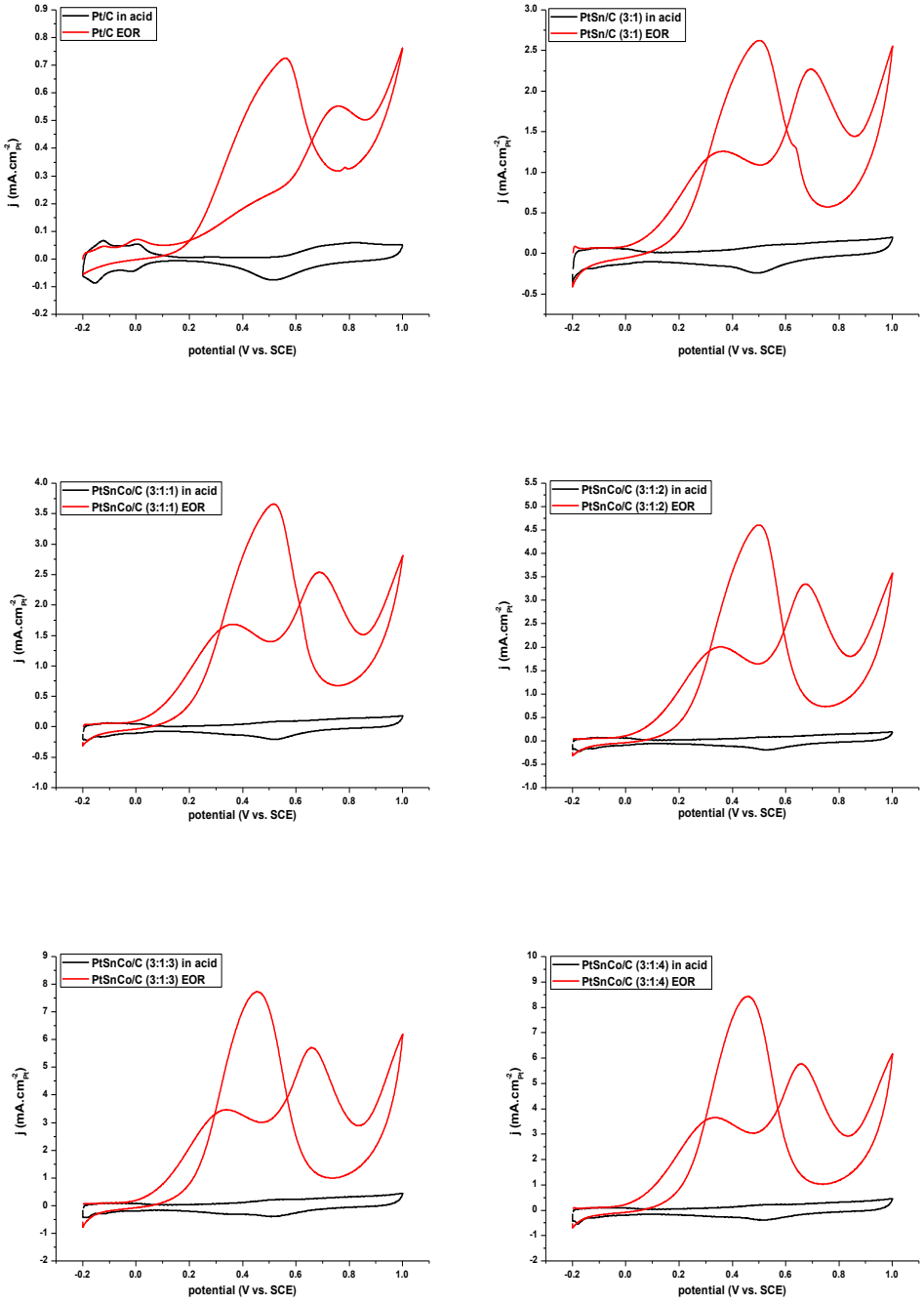


Figure 4.8 Cyclic voltammetric profiles of ethanol electro-oxidation on the investigated Pt/C, PtSn/C (3:1) and all PtSnCo/C electrodes. CV conditions: 0.5M H_2SO_4 + 1M EtOH electrolyte solution, potential range from -0.2 to 1.0 V (vs. SCE), and a scan rate of 50 mV/s.

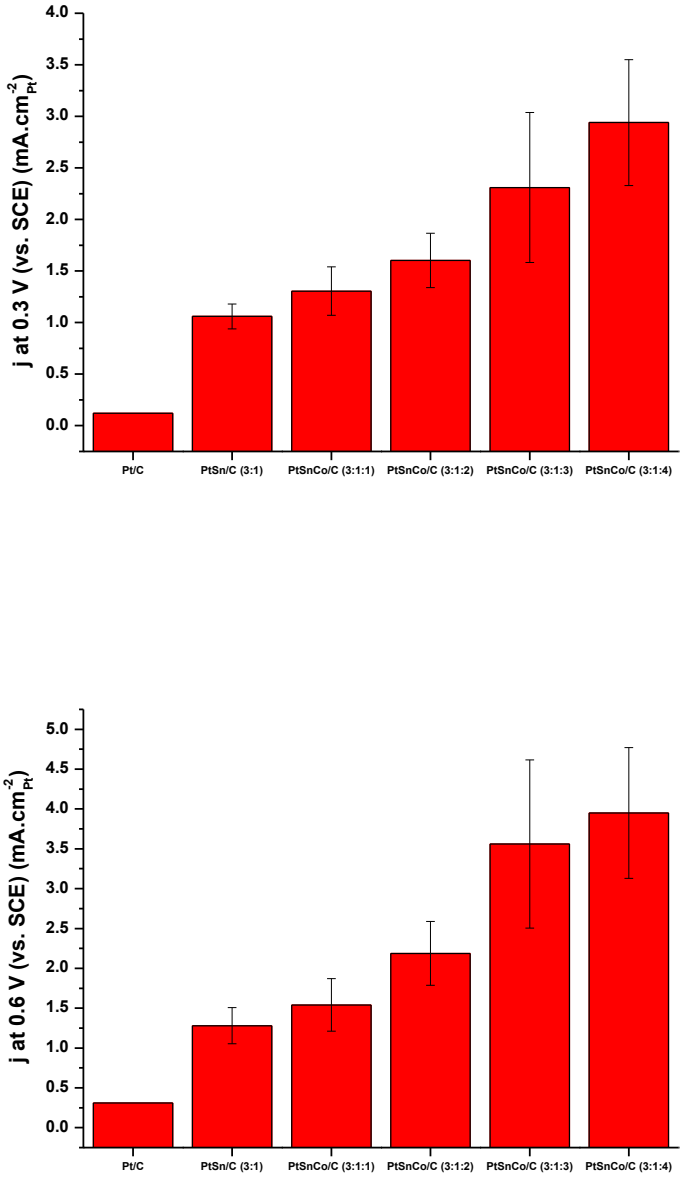


Figure 4.9 Ethanol electro-oxidation activities of the Pt/C, PtSn/C (3:1) and all PtSnCo/C catalysts at 0.3 V and 0.6 V (data taken from the first cyclic voltammograms recorded in N_2-purged 0.5M H_2SO_4 + 1M EtOH solution at room temperature after electrochemical treatment of each electrode between -0.2 V and 1.0 V (vs. SCE) for 20 cycles in N_2-purged 0.5M H_2SO_4 supporting electrolyte solution)

The current densities at 0.6 V (vs. SCE) presented in Figure 4.9 were average values from three measurements and the error bars were standard deviations (S.D.) of the measurements.

Table 4.3 Summary of the ethanol electro-oxidation activities of the Pt/C, PtSn/C (3:1) and all PtSnCo/C catalysts

electrocatalyst with nominal atomic ratio	onset potential (V vs. SCE)	forward peak current density (j_f) ($mA.cm^{-2}_{Pt}$)	reverse peak current density (j_b) ($mA.cm^{-2}_{Pt}$)	j_f/j_b*	forward peak potential (E_f) (V)	reverse peak potential (E_b) (V)
Pt/C	0.191	0.55	0.72	0.76	0.76	0.56
PtSn/C (3:1)	0.037	2.28	2.62	0.87	0.70	0.50
PtSnCo/C (3:1:1)	0.015	2.54	3.66	0.69	0.69	0.52
PtSnCo/C (3:1:2)	0.034	3.35	4.62	0.73	0.67	0.50
PtSnCo/C (3:1:3)	0.020	5.71	7.73	0.74	0.66	0.45
PtSnCo/C (3:1:4)	0.023	5.75	8.43	0.68	0.66	0.46

*a ratio between peak oxidation current density produced in the forward scan (j_f) and peak oxidation current density generated in the reverse scan (j_b)

Figure 4.8 shows that the hydrogen adsorption/desorption features previously observed on the steady-state cyclic voltammogram of the Pt/C electrode were noticeable on the first cyclic voltammogram from the activity test for ethanol electro-oxidation. Unlike the case of PtSn/C (3:1) and all ternary PtSnCo/C electrodes, the hydrogen adsorption/desorption features were completely suppressed. These results indicate stronger adsorption of ethanol molecules on the stable surfaces of PtSn/C (3:1) and all the investigated PtSnCo/C catalysts. The peak oxidation current density in the forward scan, which corresponds to the maximum rate of ethanol electro-oxidation achieved by a studied catalyst, for ethanol electro-oxidation on PtSnCo/C (3:1:3) and PtSnCo/C (3:1:4) was the highest among all the investigated catalysts. The peak current density achieved by PtSnCo/C (3:1:3) and PtSnCo/C (3:1:4) was about 2.5 and 10 times higher than that achieved by PtSn/C (3:1) and Pt/C, respectively. These results

demonstrated that the presence of both SnO_x and CoO on the surfaces of the as-synthesised PtSnCo/C catalysts with the actual Pt:Sn:Co atomic ratios of 3:1:1.9 and 3:1:2.6 can lead to formation of the stable surfaces which achieved the highest ethanol electro-oxidation activity. The j_f/j_b ratios, which indicate an efficiency in removing surface-poisoning species of an electrocatalyst, for ethanol electro-oxidation on PtSnCo/C (3:1:3) and PtSnCo/C (3:1:4) were lower than that for the EOR on PtSn/C (3:1) by 17.57 % and 27.94 %, respectively. Despite, the lower j_f/j_b ratios for the EOR on PtSnCo/C (3:1:3) and PtSnCo/C (3:1:4), the peak current density achieved by these two catalysts, which was *ca.* 150 % higher than that achieved by PtSn/C (3:1), make them a strong competitor to the carbon supported binary PtSn (3:1) catalyst for direct ethanol fuel cells operating at low temperatures. At the applied potentials of 0.3 and 0.6 V (vs. SCE) at which low-temperature direct ethanol fuel cells normally operate, the electrochemically treated PtSnCo/C (3:1:3) and PtSnCo/C (3:1:4) persistently exhibited superior activity for ethanol electro-oxidation than the other investigated electrocatalysts (see Figure 4.9). Figure 4.10 shows numerically the ethanol electro-oxidation activities of the ternary PtSnCo/C (3:1:3) and PtSnCo/C (3:1:4) in comparison to that of the monometallic Pt/C and binary PtSn/C (3:1) electrocatalysts. The exceptionally high current density for ethanol electro-oxidation on both PtSnCo/C (3:1:3) and PtSnCo/C (3:1:4) strongly suggests that the PtSnCo/C (3:1:3) and PtSnCo/C (3:1:4) prepared by the sodium borohydride method in alkaline ethylene glycol and treated under the employed electrochemical conditions are suitable to be used as an anode electrocatalyst for direct ethanol fuel cells.

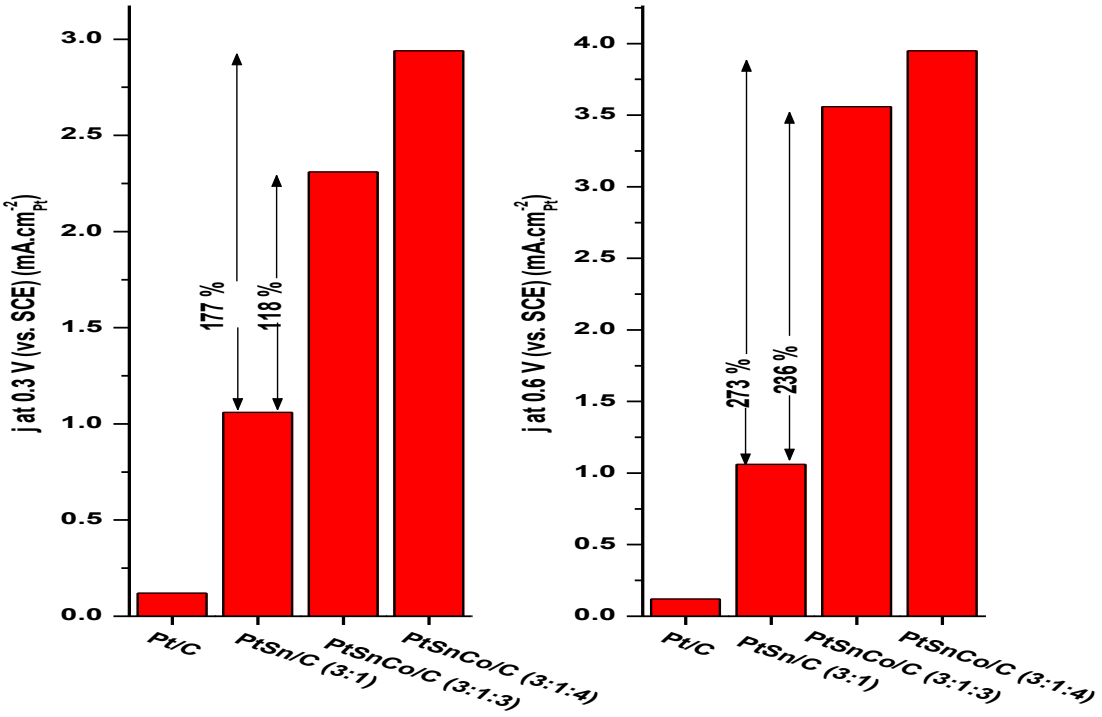


Figure 4.10 Ethanol electro-oxidation activities of the Pt/C, PtSn/C (3:1), PtSnCo/C (3:1:3), and PtSnCo/C (3:1:4) catalysts at 0.3 V and 0.6 V (vs. SCE)

To explain the ethanol electro-oxidation activity enhancement of PtSnCo/C (3:1:3) and PtSnCo/C (3:1:4) at 0.6 V (vs. SCE), the Pt^0 $4f_{7/2}$ binding energies of the as-prepared catalyst samples and the oxidation current densities at 0.6 V were plotted against the bulk Co/Pt atomic ratios of the investigated catalysts (see Figure 4.11). The trend of the oxidation current density is not strongly correlated to that of the Pt^0 $4f_{7/2}$ binding energy. It can be seen that the core-level binding energies for surface Pt of PtSnCo/C (3:1:3) and PtSnCo/C (3:1:4) were lower than that of PtSn/C (3:1). The lower Pt^0 $4f_{7/2}$ binding energies indicate that the activity enhancement on PtSnCo/C (3:1:3) and PtSnCo/C (3:1:4) could arise from the electronic effects. According to the Hammer-Nørskov model and a direct correlation between the d-band centre and the Pt^0 core-level binding energy [22][23], chemisorption strengths between adsorbed species and Pt with lower core-level binding energy are weaker due to a downshift of the Pt d-band centre. The weaker chemisorption strengths cause surface adsorbed species to be removed more easily, resulting in more available Pt active sites for electro-oxidation of ethanol. Since the core-level binding energies of Pt on the stable surfaces of PtSnCo/C (3:1:3) and PtSnCo/C (3:1:4) are lower than that of PtSn/C (3:1), the chemisorption strengths between Pt and intermediates produced by dissociative adsorption of ethanol are weaker compared to those between Pt on the stable surface of PtSn/C (3:1) and reaction intermediates. The adsorbed intermediates on the catalytic surface of PtSnCo/C (3:1:3) and that of PtSnCo/C (3:1:4) can then be removed more easily, leading to more available Pt active sites for ethanol electro-oxidation. Moreover, the stable surfaces of PtSnCo/C (3:1:3) and PtSnCo/C (3:1:4) contained more oxide species than that of PtSn/C (3:1). These surface oxides supply oxygenated species necessary for removal of reaction intermediates. A greater amount of surface oxide species can lead to more surface oxygenated species formed by dissociation of water. Due to the fact that oxide species are more oxophilic that Pt, adsorbed OH species formed at 0.6 V (vs. SCE) on Pt will be likely to diffuse to surface oxide sites. As

a result, more Pt sites are available for the electro-oxidation of ethanol. The higher ethanol electro-oxidation activity observed for PtSnCo/C (3:1:1) and PtSnCo/C (3:1:2) in comparison to that observed for PtSn/C (3:1) cannot be explained by the Hammer-Nørskov model due to the higher Pt^0 $4f_{7/2}$ core-level binding energy. Therefore, the enhanced activity towards the ethanol electro-oxidation on the stable surfaces of PtSnCo/C (3:1:1) and PtSnCo/C (3:1:2) would result from reconstruction of Pt atoms upon potential cycling to create more active sites for dissociative adsorption of ethanol.

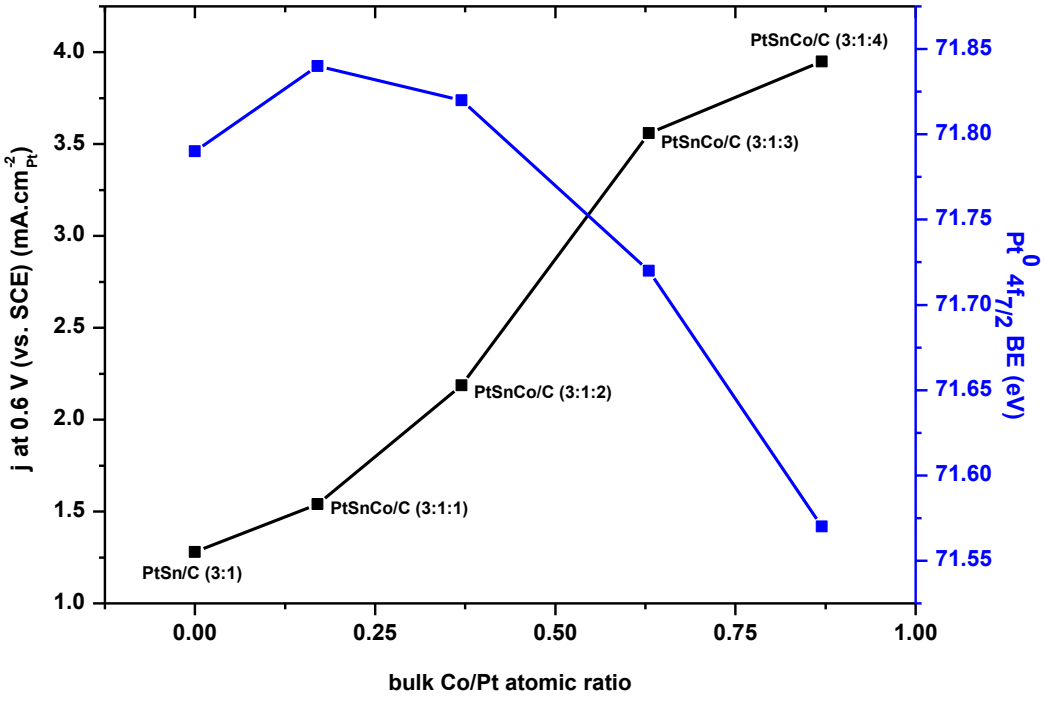


Figure 4.11 Plots showing relationships of the bulk Co/Pt atomic ratio to the oxidation current density for ethanol electro-oxidation at 0.6 V (vs. SCE) and Pt^0 $4f_{7/2}$ core-level binding energy

In addition to electronic effects, the particle size effect also plays an important role in promotion of the ethanol electro-oxidation activity of Pt-based catalysts. It was found that the particle size of Pt-based nanoparticles had an influence on the binding energy of CO_{ad} to Pt atoms. Carbon monoxide adsorbed on a small Pt nanoparticle, whose terrace to edge ratio of surface Pt atoms was lower compared to that of a larger particle, more strongly than a larger Pt nanoparticle [24-26]. Moreover, the terrace to edge ratio decreased with decreasing particle size [27]. In the case of PtSn/C (3:1), PtSnCo/C (3:1:3), and PtSnCo/C (3:1:4), the particle size would not play a major role in activity enhancement due to comparable mean crystallite and particle sizes of these three catalysts.

4.4 Chronoamperometry

The durability of anode electrocatalysts is one of the most important factors determining the performance of DEFCs. Anode electrocatalysts with high tolerance to poisoning species produced by the dissociative adsorption of ethanol molecules under operational conditions for fuel cells are desirable. To investigate the stability of the catalysts studied for ethanol electro-oxidation, chronoamperometry, an electrochemical technique in which the current resulting from faradaic processes taking place at the electrode under a constant potential is measured as a function of time [29], was employed. The stability test was performed on the stable surfaces of all the investigated catalysts. The PtSn/C (3:1) and all PtSnCo/C electrodes were polarised at 0.6 V (vs. SCE) for 600 s. Figure 4.12 shows the j-t plots for ethanol electro-oxidation on the PtSn/C (3:1) and all PtSnCo/C electrodes.

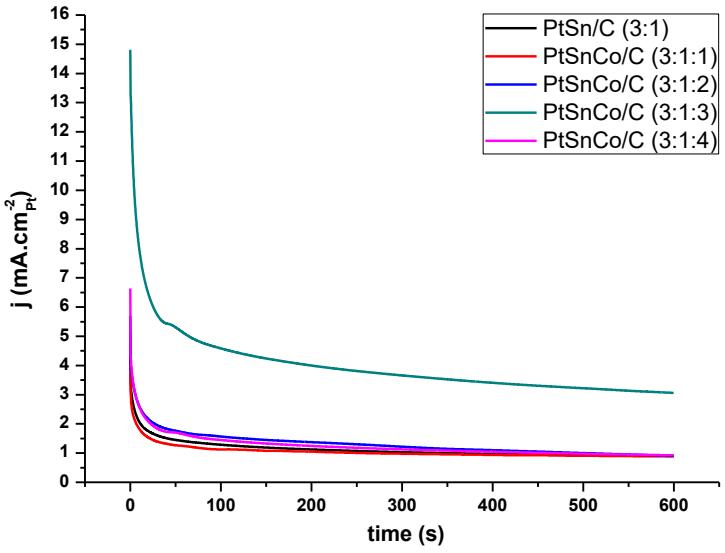


Figure 4.12 j-t plots for the ethanol electro-oxidation on the PtSn/C and all PtSnCo/C electrocatalysts recorded in 0.5M H_2SO_4 + 1M EtOH solution at 0.6V (vs. SCE) for 500 s after electrochemical treatment in 0.5M H_2SO_4 supporting electrolyte solution

It can be seen from the chronoamperometric profiles in Figure 4.12 that the all the investigated electrodes showed similar behaviour towards ethanol electro-oxidation. The oxidation current sharply decreased in the first 50-second time interval and started to slowly decay after 50 s. The decrease in the oxidation current density is ascribed to a rapid increase in the surface coverage by incompletely oxidised species which block Pt surfaces. The blockage causes the lowering of the ability to electro-oxidise ethanol of Pt [8][30-32]. A pseudo-steady state oxidation current was attained after 250 s. PtSnCo/C (3:1:3) exhibited the highest oxidation current density for ethanol electro-oxidation after 600 s. The other PtSnCo/C electrocatalysts and PtSn/C (3:1) showed comparable oxidation current density values. These results were in good agreement with those from the CV measurements for ethanol electro-oxidation on the stable catalyst surfaces at 0.6 V (vs. SCE) (see Figure 4.9). The exceptionally higher pseudo-steady state oxidation current density obtained from the ethanol electro-oxidation on the stable surface of PtSnCo/C (3:1:3) compared to that of PtSnCo/C (3:1:4) indicates that the as-prepared PtSnCo/C (3:1:3) catalyst is more promising as an anode electrocatalyst for a direct ethanol fuel cell application.

4.5 CO electro-oxidation by CO stripping voltammetry

Carbon monoxide is one of the intermediates identified as the main poisoning species of electrode active sites for the electro-oxidation of organic molecules [33]. According to J. Melke [12], CO and CH_3COO^- are stable adsorbed species on the active sites for ethanol oxidation of Pt electrodes. In order to evaluate the CO electro-oxidation activities of the synthesised PtSn/C and all four PtSnCo/C electrodes, CO stripping voltammetry was employed. The CO stripping experiment was also conducted on the Pt/C electrode to investigate the effects of tin and cobalt species on the CO electro-oxidation activity of Pt. The freshly prepared PtSn/C electrode was immersed into a deaerated 0.5M H_2SO_4 supporting electrolyte solution. CO gas was then bubbled through the electrolyte solution for 30 minutes while the electrode potential was held at -0.2 V vs SCE. The electrolyte solution was purged with N_2 gas for 30 minutes after the CO adsorption step to remove the dissolved CO. The potential scanning on the electrode was then carried out between -0.2 and 1.0 V vs SCE to completely oxidise the adsorbed CO species at a scan rate of 50 mV/s. The electrode was potential scanned for one more cycle to obtain a background cyclic voltammogram. The same procedure was repeated with the different PtSnCo/C and Pt/C electrodes. Figure 4.13 shows the cyclic voltammograms for CO electro-oxidation on the Pt/C and PtSn/C (3:1) electrodes after the underpotential CO adsorption.

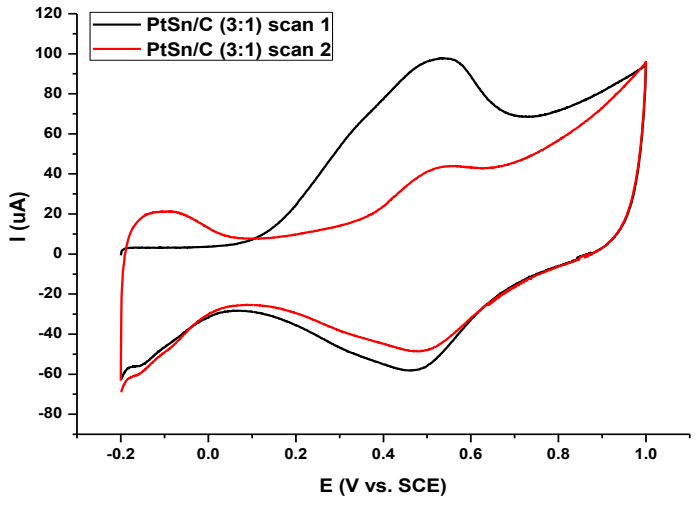


Figure 4.13 CO stripping voltammogram of the PtSn/C (3:1) electrode

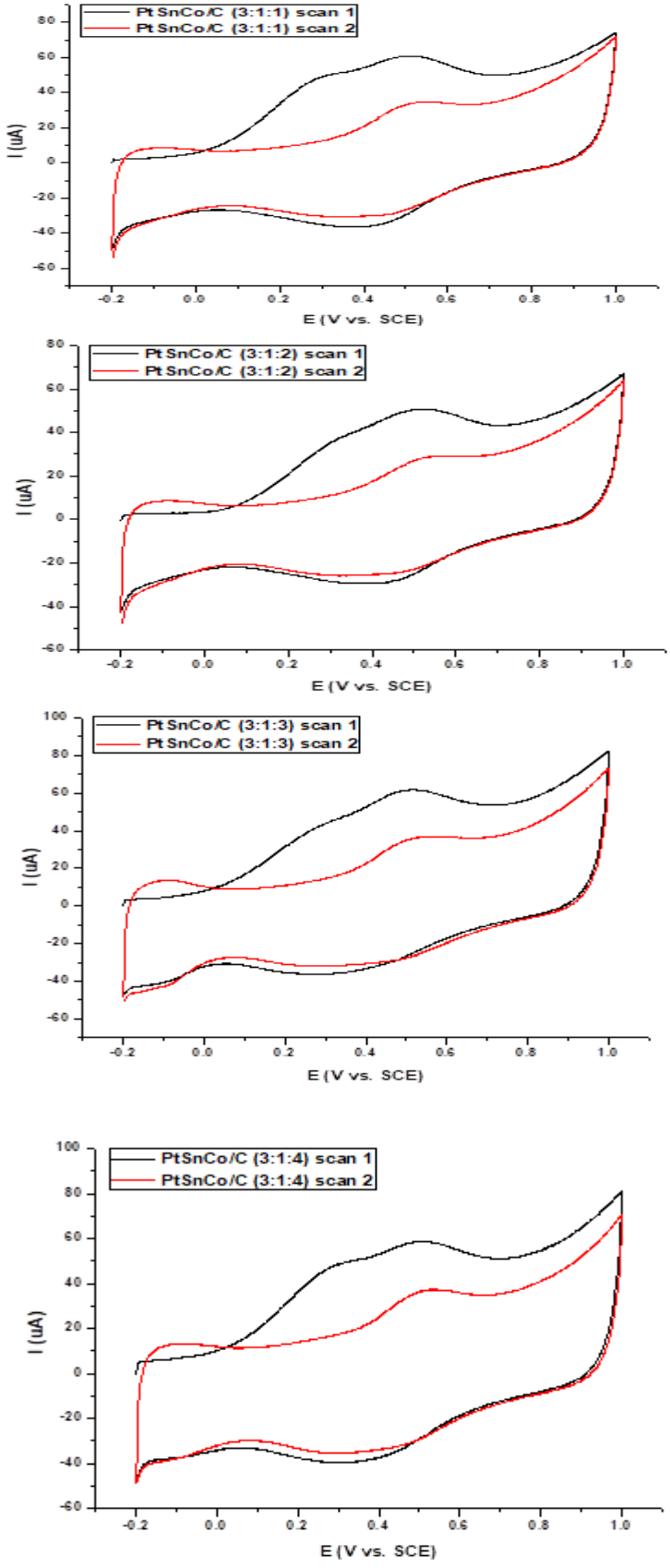


Figure 4.14 CO stripping voltammograms of all the PtSnCo/C electrodes

Figures 4.13 and 4.14 show the voltammograms obtained by the potential sweep of the PtSn/C (3:1) and all PtSnCo/C electrodes after underpotential CO adsorption. The second voltammogram of each electrode displayed features similar to those observed in the second polarisation curve from the CV measurement in 0.5M H_2SO_4 supporting electrolyte solution, indicating complete oxidation of CO pre-adsorbed on the surface of the as-prepared catalyst.

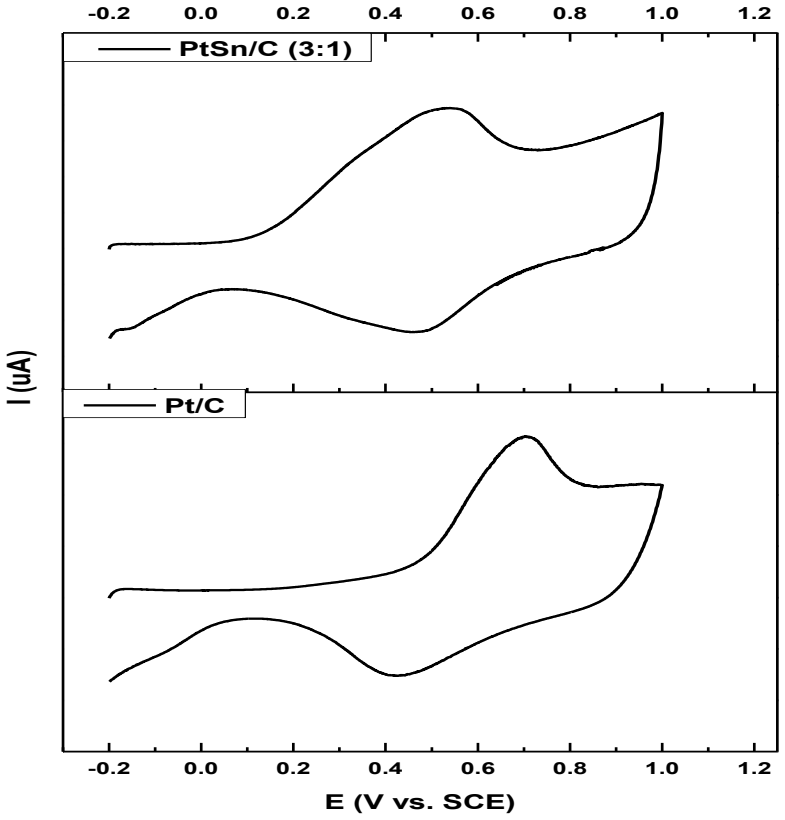


Figure 4.15 Comparison of the CO stripping voltammograms of the PtSn/C (3:1) and Pt/C electrodes

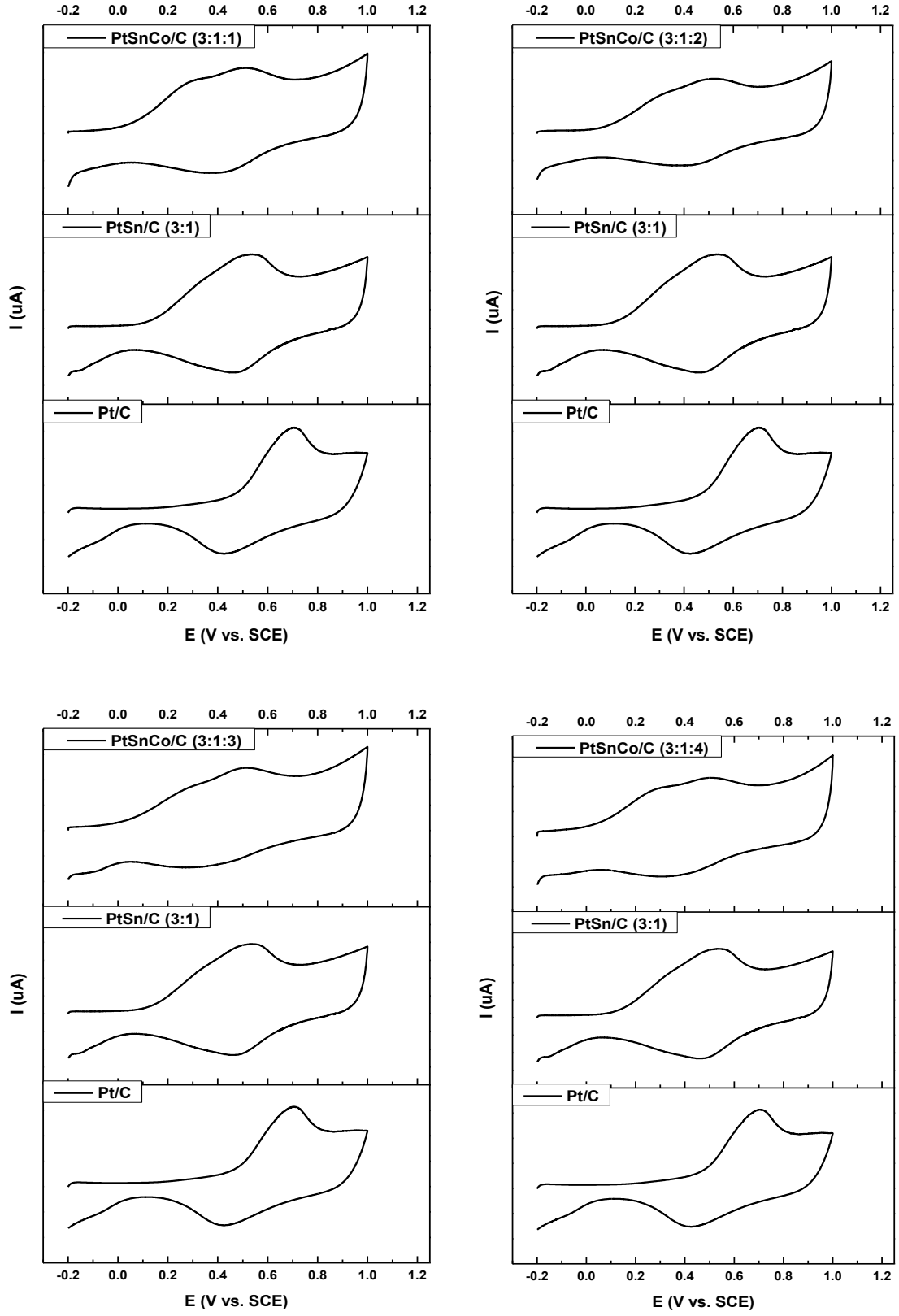


Figure 4.16 Comparison of the CO stripping voltammograms of the investigated electrodes

The voltammogram for CO electro-oxidation on the surface of the Pt/C electrode (Figure 4.15) showed only one strong peak at 0.7 V and the adsorbed CO species started to be oxidised at ca. 0.4 V. For the PtSn/C (3:1) electrode, a broad CO oxidation peak between 0.1 and 0.7 V was observed with a small shoulder and strong peak at ca. 0.35 V and 0.55 V ascribed to the oxidation of weakly and strongly adsorbed CO, respectively [34]. The weakly adsorbed CO can be oxidised by combining with OH_{ad} species formed on the surface of SnO_x as presented in the following reactions.

$$SnO_x + H_2O \rightarrow SnO_x - OH + H^+ + e^- \qquad \text{Equation (4.4)}$$

$$Pt - CO + SnO_x - OH \rightarrow Pt + SnO_x + CO_2 + H^+ + e^- \qquad \text{Equation (4.5)}$$

The lower onset potential for the CO electro-oxidation on PtSn/C (3:1) compared to that on Pt/C is indicative of the faster kinetics of CO electro-oxidation on the stable surface of the PtSn/C (3:1) electrode [35]. In addition, the negative shift of the peak potential for the electro-oxidation of strongly adsorbed CO is a clear evidence that the as-synthesised PtSn/C (3:1) catalyst is able to promote the oxidation of strongly adsorbed CO at a lower potential likely by either consuming adsorbed OH species formed on Pt or SnO_x through bifunctional mechanism [36]. A broad peak with a small shoulder and a main peak at a higher potential were observed for the electro-oxidation of adsorbed CO on the surfaces of the individual as-prepared PtSnCo/C catalysts. The onset potential for CO electro-oxidation on the individual catalysts was close and it was slightly lower than that on PtSn/C (3:1). Furthermore, the peak potentials for the electro-oxidation of both weakly and strongly adsorbed CO shifted to more negative values i.e. 0.3 V and 0.5 V, respectively, in comparison to PtSn/C (3:1). Such peak potential values were independent to the compositions of the catalysts. The reduction in the onset potential and the peak oxidation potential for the CO electro-oxidation on the PtSnCo/C electrodes is a clear indication of higher CO electro-oxidation activity compared to PtSn/C

(3:1) and Pt/C. The electro-oxidation of CO weakly adsorbed on the surfaces of the PtSnCo/C electrodes at 0.3 V could occur by the reaction of the adsorbed CO and OH_{ad} species formed on SnO_x or CoO, while strongly adsorbed CO could be oxidised by combining with OH_{ad} formed on SnO_x or CoO or Pt through the bifunctional mechanism. The superior activity for CO electro-oxidation of the as-prepared PtSnCo/C catalysts to PtSn/C (3:1) suggests that promotional effects of cobalt and tin species co-existing in the catalysts would not compete, instead complement each other, leading to higher electrocatalytic activity for CO oxidation [35]. Moreover, the absence of the CO oxidation peak at a potential of *ca.* 0.7 V on the CO stripping voltammograms of PtSn/C (3:1) and all PtSnCo/C emphasises that Pt/SnO_2 and Pt/SnO_2/CoO clusters have synergistic properties for CO_{ad} oxidation [37]. According to the CO electro-oxidation activities of the as-synthesised catalysts, it can be assumed that the stable surfaces obtained from potential cycling the as-prepared PtSnCo/C catalysts would exhibit higher CO electro-oxidation activity than that obtained from potential cycling the as-prepared PtSn/C (3:1) catalyst due to the presence of both CoO and SnO_2 species on their stable surfaces.

4.6 Ethanol Electro-oxidation Mechanism on the PtSnCo/C Electrocatalysts

Ethanol electro-oxidation reactions in acidic media on polycrystalline Pt electrodes have been investigated [11, 38]. The two pathways namely partial oxidation and total or complete oxidation have been established. In brief, the partial oxidation pathway (Equation (4.7)) involves the oxidation of ethanol to acetaldehyde ($2e^-$ process) and acetic acid ($4e^-$ process) while the total oxidation pathway (Equation (4.6)) involves the C-C bond breaking which leads to the formation of CO_2 ($12e^-$ process).

$$CH_3CH_2OH \rightarrow [CH_3CH_2OH]_{ad} \rightarrow C_{1ad,}\, C_{2ad} \rightarrow CO_2 \qquad \text{Equation (4.6)}$$

$$CH_3CH_2OH \rightarrow [CH_3CH_2OH]_{ad} \rightarrow CH_3CHO \rightarrow CH_3COOH \qquad \text{Equation (4.7)}$$

To obtain high current density from operating DEFCs, the Pt-based electrocatalysts for ethanol electro-oxidation at anodes should promote the complete oxidation pathway. The mechanism of ethanol electro-oxidation reaction on the PtSn/C (3:1) and that on each PtSnCo/C electrode was studied by CV in acetaldehyde and acetic acid solutions. The studies of acetaldehyde electro-oxidation reaction (AALOR) on PtSn/C (3:1) and all PtSnCo/C were conducted by means of CV. All tested electrodes were potential cycled in a N_2-purged 0.5M H_2SO_4 solution between -0.2 and 1.0 V (vs. SCE) until steady-state cyclic voltammograms were obtained. The electrochemically treated electrodes were then potential cycled between -0.2 and 1.0 V (vs. SCE) in a 0.5M H_2SO_4 + 0.5M acetaldehyde (AAL) solution purged with N_2 prior to the measurements. The acetaldehyde electro-oxidation activities of the catalysts were normalised by their electrochemically active surface areas. The acetic acid electro-oxidation reaction (AAOR) on the electrochemically treated electrodes was also studied. The procedure for acetic acid electro-oxidation studies was the same as for acetaldehyde electro-oxidation except the electrodes were potential cycled between -0.2 and 1.0 V (vs. SCE) in a N_2-purged 0.5M H_2SO_4+0.5M acetic acid (AA) solution.

Figure 4.17 shows cyclic voltammograms recorded for acetaldehyde electro-oxidation on the investigated electrodes. It can be seen in the voltammograms that the features of hydrogen adsorption/desorption on Pt were suppressed, indicative of adsorption of acetaldehyde molecules on surface Pt.

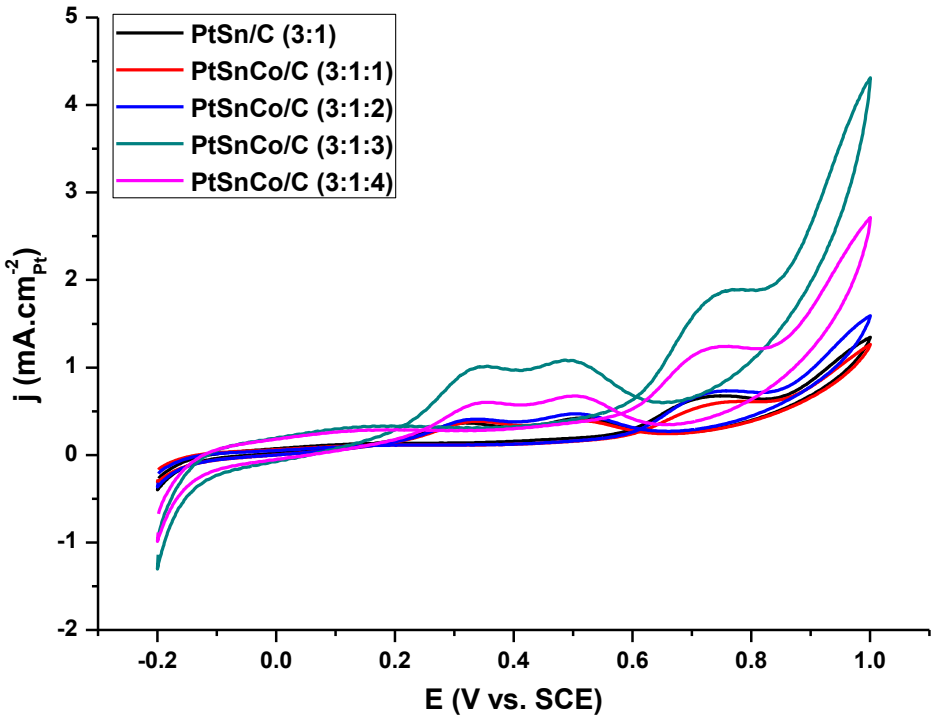


Figure 4.17 Cyclic voltammograms for acetaldehyde electro-oxidation on the PtSn/C (3:1) and all PtSnCo/C electrocatalysts recorded in 0.5M H_2SO_4+0.5M AAL with a scan rate of 50 mV/s

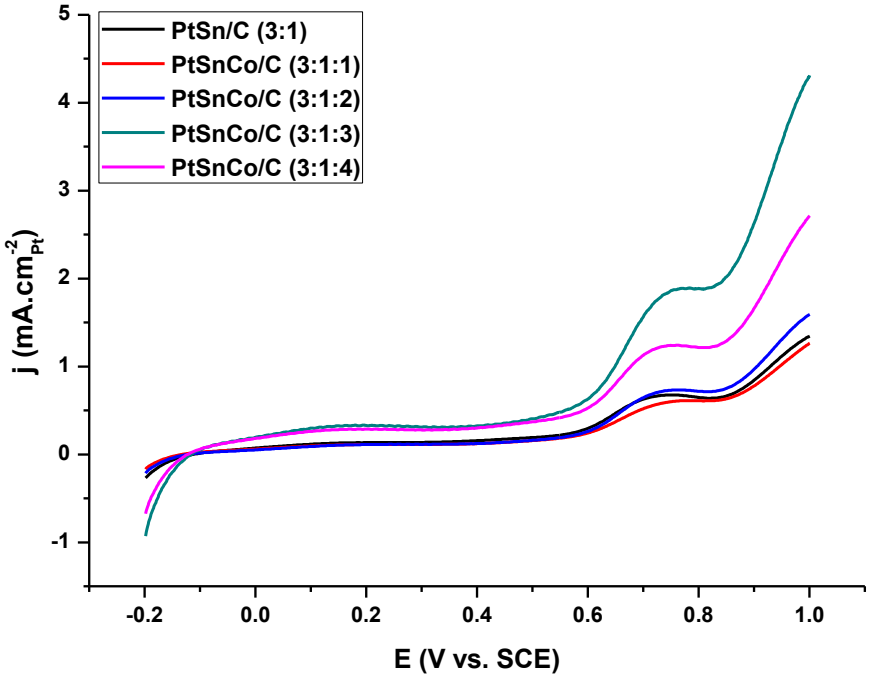


Figure 4.18 Forward scans of the cyclic voltammograms for acetaldehyde electro-oxidation reaction on the stable surfaces of the PtSn/C (3:1) and all PtSnCo/C electrocatalysts

Acetaldehyde adsorbed on the stable surfaces of the PtSn/C (3:1) and all PtSnCo/C electrocatalysts started to be oxidised at potentials between 0.35 and 0.47 V (vs. SCE). The lowest and highest onset potentials of 0.35 and 0.47 V were characteristic of acetaldehyde electro-oxidation on PtSn/C (3:1) and PtSnCo/C (3:1:3), respectively. The oxidation current density increased with an increase in applied potential. The peak oxidation current density for acetaldehyde electro-oxidation on the stable surface of each investigated catalyst was attained at 1.0 V. The increase in oxidation peak current density at higher potentials suggests that adsorbed species and intermediates produced from dissociative adsorption of acetaldehyde molecules are further oxidised by reacting with the adsorbed oxygen species (Pt-O_{ads}) produced at high potentials on the surfaces of PtSn/C (3:1) and all the PtSnCo/C catalysts. In the reverse scans, a single broad oxidation peak with two humps was observed for each investigated electrode between 0.20 and 0.60 V (vs. SCE). The j_f/j_b ratios were greater than 1

for all the investigated electrodes, indicating that the catalyst surfaces would not be poisoned by intermediates formed. S. Beyhan et al. [44] studied the adsorption and electro-oxidation of acetaldehyde on $Pt_{90}Sn_{10}$/C and $Pt_{80}Sn_{10}Co_{10}$/C using *in situ* FTIR spectroscopy. They found that PtSn/C (9:1) was not very selective to the production of CO_2. Furthermore, the electro-oxidation of acetaldehyde on both PtSn/C (9:1) and PtSnCo/C (8:1:1) electrodes occurred via a 2-electron process to form acetic acid or through the oxidation of adsorbed CO formed by the dissociative adsorption of CH_3CO species. According to the studies of Beyhan [44], the electro-oxidation of acetaldehyde on the catalytic surfaces of all the investigated PtSn/C (3:1) and all PtSnCo/C electrodes would take place via the oxidation of acetyl intermediate to form CO_2 and acetic acid. The stable surfaces of the investigated PtSn/C (3:1) and all PtSnCo/C catalysts showed no activity for acetic acid electro-oxidation as evidenced by the features of the voltammograms shown in Figures 4.19 and 4.20 which are similar to those of the voltammograms obtained from the CV measurements in the absence of acetic acid. This result indicates that acetic acid produced by the partial oxidation of ethanol could be present in bulk solution rather than on the surface of Pt as an adsorbed acetate (CH_3COO^-) species [12].

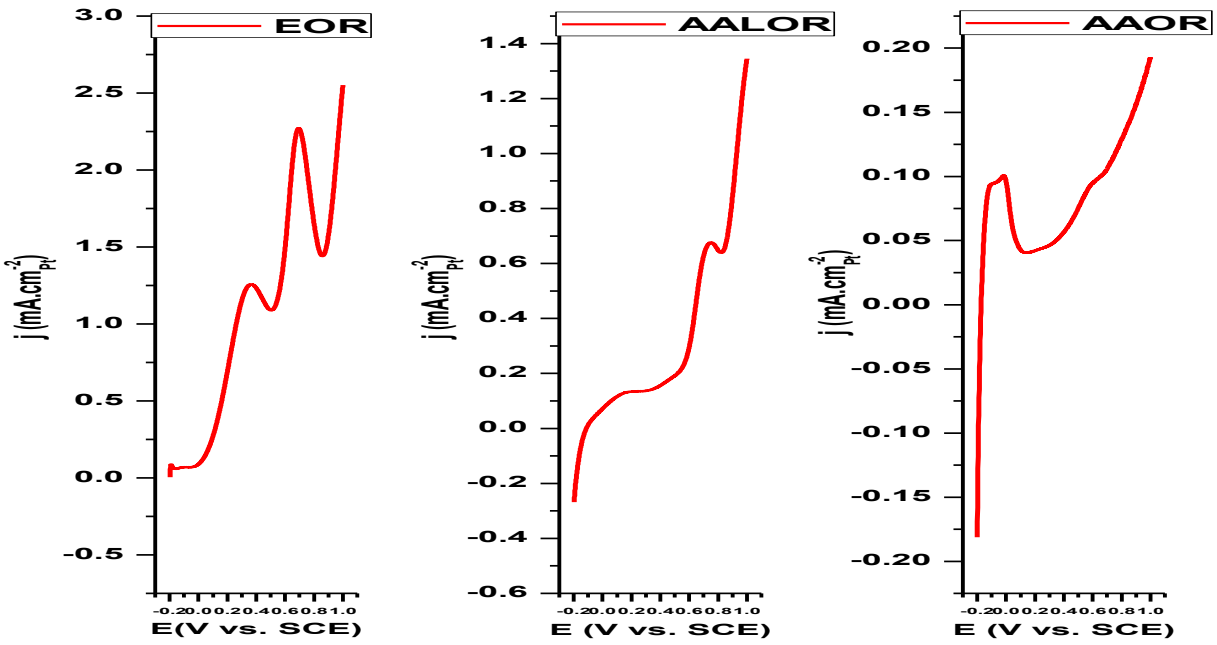


Figure 4.19 Ethanol, acetaldehyde (AAL), and acetic acid (AA) electro-oxidation activity of the PtSn/C (3:1) electrode measured by CV in 1.0M EtOH+0.5M H_2SO_4, 0.5M AAL+0.5M H_2SO_4, and 0.5M AA+0.5M H_2SO_4 electrolyte solutions with a scan rate of 50 mV/s

Based on the voltammetric profiles of ethanol, acetaldehyde, and acetic acid electro-oxidation on the stable surface of PtSn/C (3:1) electrode (see Figure 4.19), the mechanism of ethanol electro-oxidation can be proposed as follows. Upon reaching the surface of PtSn/C (3:1) ethanol molecules physisorb on the catalyst surface before it starts to be oxidised at about 0.04 V. After the first dehydrogenation at the α-carbon, the adsorbed intermediates including acetyl and CO species undergo further oxidation to acetaldehyde or acetic acid, and CO_2, respectively. The peak appearing at the potential of *ca.* 0.6 V during the ethanol electro-oxidation reaction on the surface of PtSn/C (3:1) could be attributed mainly to the production of acetic acid from acetaldehyde electro-oxidation. To support the proposed mechanisms, *in situ* techniques such as differential electrochemical mass spectroscopy (DEMS), attenuated total reflectance – Fourier transform infrared spectroscopy (ATR-FTIR) equipped with an electrochemical cell, single potential alteration infrared reflectance spectroscopy (SPAIRS),

and subtractively normalised interfacial Fourier transform infrared reflectance spectroscopy (SNIFTIRS) can be used. These techniques can provide information about the presence of reaction intermediates and the formation of reaction products, such as CO_2, on and in the vicinity of the electrode [39].

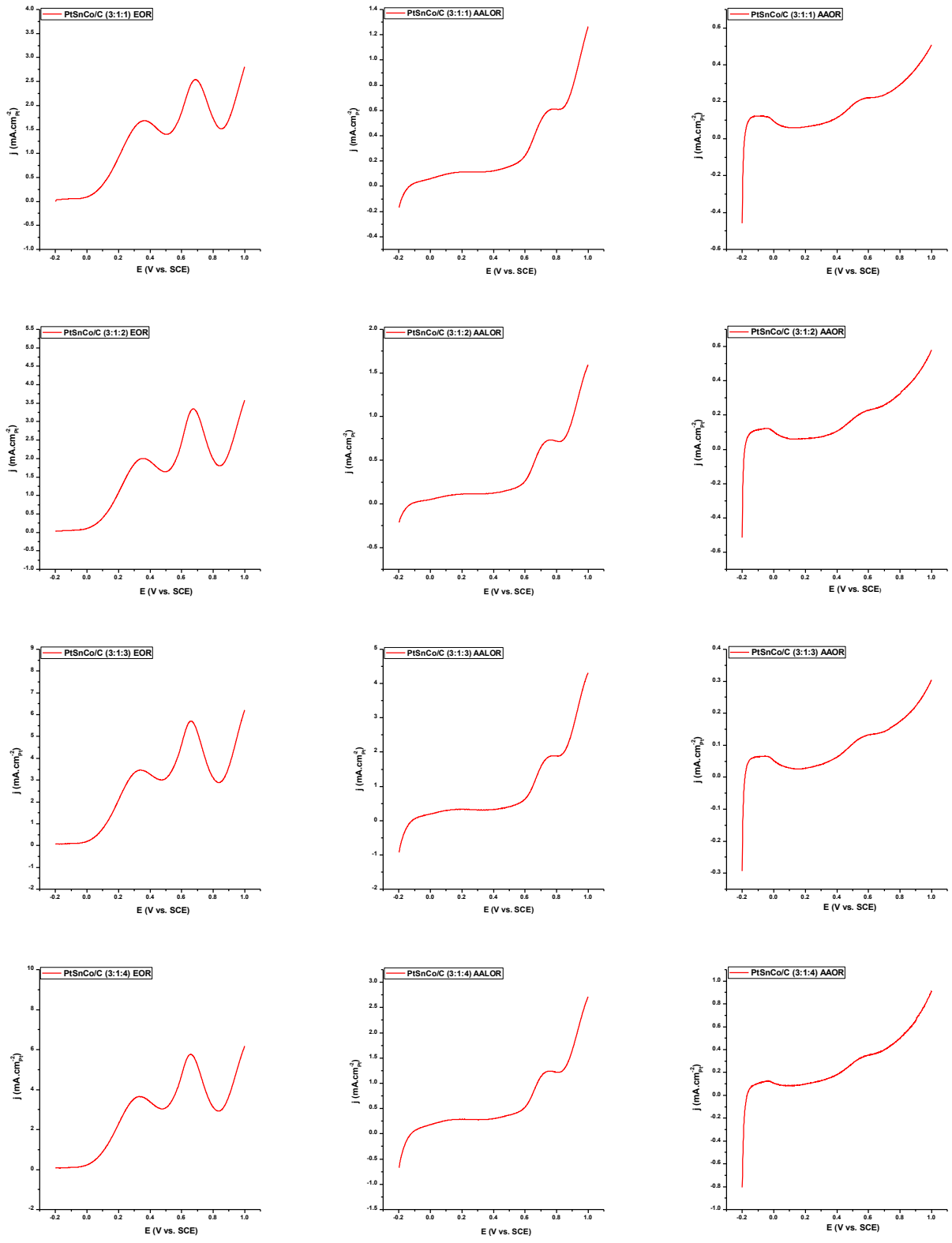


Figure 4.20 Ethanol, AAL, and AA electro-oxidation activities of all the PtSnCo/C electrodes

By taking the voltammetric profiles of the ethanol, acetaldehyde, and acetic acid electro-oxidation on the surfaces of all the investigated PtSnCo/C electrodes into account, the proposed reaction mechanisms for ethanol electro-oxidation on PtSn/C (3:1) can be proposed for the PtSnCo/C electrodes since the voltammetric profiles of ethanol, acetaldehyde, and acetic acid electro-oxidation for all PtSnCo/C cases are similar to those for PtSn/C (3:1). However, electrochemical oxidation of ethanol on the surfaces of the PtSnCo/C catalysts begins at potentials 10 to 30 mV earlier than that on the surface of the PtSn/C (3:1) catalyst. These results suggest that the stable surfaces of PtSn/C (3:1) and all PtSnCo/C catalysts are similar in terms of the attributes of catalytic sites, but the catalysts with the presence of Co species in their as-synthesised form possess a greater number of electrochemically active sites for ethanol electro-oxidation after the electrochemical treatment in an acid supporting electrolyte.

Conclusions

-The stable surfaces of the PtSn/C (3:1) and all PtSnCo/C catalysts were derived by repeatedly potential cycling the as-prepared PtSn/C (3:1) and all PtSnCo/C catalysts for 20 scans under the employed CV conditions.

-The obtained surfaces were formed possibly by the reconstruction of surface Pt atoms and dissolution of surface SnO and CoO species.

-The PtSnCo/C (3:1:3) and PtSnCo/C (3:1:4) electrocatalysts exhibited the highest peak current density for ethanol electro-oxidation for an employed potential range with the onset potential as low as 0.02 V (vs. SCE). Their activities at 0.6 V (vs. SCE) were superior to that of PtSn/C (3:1) and that of Pt/C, suggesting that PtSnCo/C (3:1:3) and PtSnCo/C (3:1:4) are alternative anode electrocatalysts for application in a direct ethanol fuel cell. The superior activity for ethanol electro-oxidation compared to that of the binary PtSn/C (3:1) and monometallic Pt/C catalysts could be due to the unique Pt electronic structures, which would lead to a surface that binds less strongly to reaction intermediates, resulting in easier removal of surface species. More active sites for ethanol electro-oxidation are available on the catalyst surfaces, accordingly. In addition, CoO species present on the stable surfaces of the PtSnCo/C (3:1:3) and PtSnCo/C (3:1:4) can assist the removal of surface poisoning species, such as CO_{ad}, by the bi-functional mechanism and synergistic effects.

-The ethanol electro-oxidation on the stable surface of each investigated catalyst was proposed to occur via both partial and total oxidation pathways. At potentials lower than 0.4 V, the formation of acetaldehyde and CO_{ad} species probably occurs in parallel with no production of acetic acid. At potentials higher than 0.4 V, intermediates from the dissociative adsorption of ethanol can be oxidised by combining with adsorbed OH species supplied by CoO, SnO_2, and Pt on the catalyst surface.

References

1. Sieben, J. M.; Duarte, M. M. E., *International Journal of Hydrogen Energy* **2011,** *36* (5), 3313-3321.

2. Simões, F. C.; dos Anjos, D. M.; Vigier, F.; Léger, J. M.; Hahn, F.; Coutanceau, C.; Gonzalez, E. R.; Tremiliosi-Filho, G.; de Andrade, A. R.; Olivi, P.; Kokoh, K. B., *Journal of Power Sources* **2007,** *167* (1), 1-10.

3. Jiang, L.; Sun, G.; Sun, S.; Liu, J.; Tang, S.; Li, H.; Zhou, B.; Xin, Q., *Electrochimica Acta* **2005,** *50* (27), 5384-5389.

4. Bommersbach, P.; Mohamedi, M.; Guay, D., *Journal of The Electrochemical Society* **2007,** *154* (8), B876-B882.

5. Silva, J. C. M.; De Souza, R. F. B.; Parreira, L. S.; Neto, E. T.; Calegaro, M. L.; Santos, M. C., *Applied Catalysis B: Environmental* **2010,** *99* (1–2), 265-271.

6. García-Rodríguez, S.; Rojas, S.; Peña, M. A.; Fierro, J. L. G.; Baranton, S.; Léger, J. M., *Applied Catalysis B: Environmental* **2011,** *106* (3–4), 520-528.

7. Li, M.; Zhou, W. P.; Marinkovic, N. S.; Sasaki, K.; Adzic, R. R., *Electrochimica Acta* **2013,** *104* (0), 454-461.

8. Baranova, E.; Amir, T.; Mercier, P. J.; Patarachao, B.; Wang, D.; Le Page, Y., *Journal of Applied Electrochemistry* **2010,** *40* (10), 1767-1777.

9. Beyhan, S.; Léger, J.-M.; Kadırgan, F., *Applied Catalysis B: Environmental* **2014,** *144* (0), 66-74.

10. Beyhan, S.; Coutanceau, C.; Léger, J.-M.; Napporn, T. W.; Kadırgan, F., *International Journal of Hydrogen Energy* **2013,** *38* (16), 6830-6841.

11. Kutz, R. B.; Braunschweig, B.; Mukherjee, P.; Behrens, R. L.; Dlott, D. D.; Wieckowski, A., *Journal of Catalysis* **2011,** *278* (2), 181-188.

12. Melke, J.; Schoekel, A.; Dixon, D.; Cremers, C.; Ramaker, D. E.; Roth, C., *The Journal of Physical Chemistry C* **2010,** *114* (13), 5914-5925.

13. Sobkowski, J.; Franaszczuk, K.; Piasecki, A., *Journal of Electroanalytical Chemistry and Interfacial Electrochemistry* **1985,** *196* (1), 145-156.

14. Lim, D.-H.; Choi, D.-H.; Lee, W.-D.; Lee, H.-I., *Applied Catalysis B: Environmental* **2009,** *89*(3–4), 484-493.

15. Yamamoto, K.; Kolb, D. M.; Kötz, R.; Lehmpfuhl, G., *Journal of Electroanalytical Chemistry and Interfacial Electrochemistry* **1979,** *96* (2), 233-239.

16. Garcia, E. M.; Santos, J. S.; Pereira, E. C.; Freitas, M. B. J. G., *Journal of Power Sources* **2008,** *185* (1), 549-553.

17. Kristian, N.; Yu, Y.; Lee, J.-M.; Liu, X.; Wang, X., *Electrochimica Acta* **2010,** *56* (2), 1000-1007.

18. Hubli, R. C.; Mittra, J.; Suri, A. K., *Hydrometallurgy* **1997,** *44* (1), 125-134.

19. Li, H.; Sun, G.; Cao, L.; Jiang, L.; Xin, Q., *Electrochimica Acta* **2007,** *52* (24), 6622-6629.

20. Tabet-Aoul, A.; Mohamedi, M., *Journal of Alloys and Compounds* **2013,** *553*, 113-118.

21. Zhao, Y.; Liu, J.; Zhao, Y.; Wang, F., *Physical Chemistry Chemical Physics* **2014,** *16* (36), 19298-19306.

22. Wu, P.; Zhang, H.; Qian, Y.; Hu, Y.; Zhang, H.; Cai, C., *The Journal of Physical Chemistry C* **2013,** *117* (37), 19091-19100.

23. Hammer, B.; Nørskov, J. K., *Advances in Catalysis* **2000,** *45*, 71-129.

24. Baranova, E. A.; Bock, C.; Ilin, D.; Wang, D.; MacDougall, B., *Surface Science* **2006,** *600* (17), 3502-3511.

25. Park, S.; Wasileski, S. A.; Weaver, M. J., *The Journal of Physical Chemistry B* **2001,** *105* (40), 9719-9725.

26. Chang, S. C.; Weaver, M. J., *The Journal of Physical Chemistry* **1991,** *95* (14), 5391-5400.

27. Nashner, M. S.; Frenkel, A. I.; Somerville, D.; Hills, C. W.; Shapley, J. R.; Nuzzo, R. G., *Journal of the American Chemical Society* **1998,** *120* (32), 8093-8101.

28. Kim, J. H.; Choi, S. M.; Nam, S. H.; Seo, M. H.; Choi, S. H.; Kim, W. B., *Applied Catalysis B: Environmental* **2008,** *82* (1), 89-102.

29. Bard, A. J.; Faulkner, L. R., *Electrochemical Methods: Fundamentals and Applications*. 2 ed.; Wiley: 2000.

30. Jiang, L.; Colmenares, L.; Jusys, Z.; Sun, G. Q.; Behm, R. J., *Electrochimica Acta* **2007,** *53* (2), 377-389.

31. Bommersbach, P.; Chaker, M.; Mohamedi, M.; Guay, D., *The Journal of Physical Chemistry C* **2008,** *112* (37), 14672-14681.

32. Jiang, L.; Sun, G.; Zhou, Z.; Sun, S.; Wang, Q.; Yan, S.; Li, H.; Tian, J.; Guo, J.; Zhou, B.; Xin, Q., *The Journal of Physical Chemistry B* **2005,***109* (18), 8774-8778.

33. Soares, L. A.; Morais, C.; Napporn, T. W.; Kokoh, K. B.; Olivi, P., *Journal of Power Sources* **2016,** *315*, 47-55.

34. Marković, N. M.; Grgur, B. N.; Lucas, C. A.; Ross, P. N., *The Journal of Physical Chemistry B* **1999,** *103* (3), 487-495.

35. Wang, D.; Wang, J.; Lu, S.; Jiang, S. P., *Journal of Electroanalytical Chemistry* **2014,** *712* (0), 55-61.

36. Chen, Y.; Wang, J.; Meng, X.; Zhong, Y.; Li, R.; Sun, X.; Ye, S.; Knights, S., *International Journal of Hydrogen Energy* **2011,** *36* (17), 11085-11092.

37. Arenz, M.; Stamenkovic, V.; Blizanac, B. B.; Mayrhofer, K. J.; Markovic, N. M.; Ross, P. N., *Journal of Catalysis* **2005,** *232* (2), 402-410.

38. Antolini, E.; Gonzalez, E. R., *Catalysis Today* **2011,** *160* (1), 28-38.

39. Ozoemena, K. I.; Chen, S., *Nanomaterials for Fuel Cell Catalysis*. Springer International Publishing: 2016.

40. Du, W.; Wang, Q.; Saxner, D.; Deskins, N. A.; Su, D.; Krzanowski, J. E.; Frenkel, A. I.; Teng, X., *Journal of the American Chemical Society* **2011,** *133* (38), 15172-15183.

41. Zhu, M.; Sun, G.; Xin, Q., *Electrochimica Acta* **2009,** *54* (5), 1511-1518.

42. Corradini, P. G.; Antolini, E.; Perez, J., *Journal of Power Sources* **2015,** *275*, 377-383.

43. Jiang, L.; Hsu, A.; Chu, D.; Chen, R., *International Journal of Hydrogen Energy* **2010,** *35* (1), 365-372.

44. Beyhan, S.; Léger, J.-M.; Kadırgan, F., *Journal of Power Sources* **2013,** *242*, 503-509.

Chapter 5

Electrocatalytic Activities of the PtSnCo/C Nanoparticle Catalysts for Ethylene Glycol (EG), 2-Propanol (2P), and Methanol (MeOH) Oxidation in 0.5M H_2SO_4 Medium

5.1 Introduction

Ethylene glycol, 2-propanol, and methanol are promising fuels for electrical energy production by direct alcohol fuel cells due to their high energy densities and theoretical energy conversion efficiencies for alcohol oxidation in a DAFC (Table 1.1 of chapter 1). The individual alcohols also possess other advantages that make them a good choice fuel for DAFC applications. Methanol, which is considered the most promising fuel among the different alcohols, can be easily handled, stored and transported without the need of well-built infrastructures. Moreover, liquid methanol is readily available at low cost [1]. These could potentially reduce the cost of DMFCs. However, there are some drawbacks of methanol and its use in DMFCs that lead to the search for new types of alcohol [2]. Methanol is highly toxic and can be harmful to humans and animals. Highly concentrated methanol solutions can result in a crossover of methanol from the anode to the cathode, leading to a mixed potential at the cathode. The potential mixing incident, in turn, reduces the overall cell potential [3]. Ethylene glycol, a polyhydric alcohol, has gained attention from researchers as a potential fuel for a direct alcohol fuel cell application. Ethylene glycol can be electrochemically oxidised and produced from biomass. Furthermore, its supply chain has already been established as it has been widely used in the automobile industry [2]. In comparison with methanol, ethylene glycol has higher theoretical volume capacity in Ah/mL and is safer to handle due to its higher boiling point (198 ^{o}C vs. 64.7 ^{o}C). These benefits

make fuel cells based on EG as a fuel a promising alternative energy source. Another alcohol which has been used as a fuel for DAFCs is 2-propanol. 2-propanol or isopropanol, the smallest secondary alcohol, has been a focused topic in DAFC development [4,5] due to its intrinsic properties and particular molecular structure. 2-propanol is less toxic and shows lower overpotential compared to methanol. It can be electrochemically oxidised and produced from some renewable feed stocks in significant quantities [6]. Moreover, the fuel cells using 2-propanol showed higher performance and much lower crossover current than those using methanol [4-5, 7-10].

To generate electricity by DAFCs, the oxidation of alcohol fuels fed to anodes have to occur under the operating conditions. Thus, electrocatalysts capable of efficiently oxidising alcohol molecules are required. Pt has been used as a core material for the development of highly active anode electrocatalysts for DAFC applications [2, 6, 11-18]. It is because Pt has high activity towards oxidation of many small-molecule chemicals and it is highly stable in an acidic environment. It was clearly demonstrated that Pt could electro-catalytically oxidise ethylene glycol, 2-propanol, and methanol molecules. Therefore, it has been utilised as an anode electrocatalyst in direct ethylene glycol fuel cells (DEGFCs), direct 2-propanol fuel cells (D2PFCs), and direct methanol fuel cells (DMFCs). The electro-oxidation reactions of ethylene glycol, 2-propanol, and methanol on Pt catalysts have been studied by electrochemical and spectroscopic techniques to understand the electrocatalysis of Pt catalysts. To achieve the maximum current from a fuel cell, the total oxidation to CO_2 of an alcohol is required. The total oxidation reactions of ethylene glycol, 2-propanol, and methanol are expressed by Equations 5.1, 5.2, and 5.3, respectively:

$(CH_2OH)_2 + 2H_2O \rightarrow 2CO_2 + 10H^+ + 10e^-$ Equation (5.1)

$CH_3CH(OH)CH_3 + 5H_2O \rightarrow 3CO_2 + 18H^+ + 18e^-$ Equation (5.2)

$CH_3OH + H_2O \rightarrow CO_2 + 6H^+ + 6e^-$ Equation (5.3)

The complete oxidation of EG produces 10 electrons per one EG molecule, while the complete oxidation of 2-propanol and that of methanol release 18 electrons and 6 electrons per one alcohol molecule, respectively. Ethylene glycol electro-oxidation on Pt can proceed via two different pathways (see Figure 5.1) [19]. The first pathway involves C-C bond breaking and subsequent oxidation of the C_1 fragments. The second pathway involves sequential oxidation of the functional groups with no C-C bond scissoring. This results in the formation of a variety of C_2 molecules including glycolaldehyde, glyoxal, glycolic acid, glyoxylic acid, and oxalic acid. At room temperatures and potentials below 0.9 V in acid electrolyte, the sequential oxidation of the C_2 molecules terminates at the stage of oxalic acid formation [20]. The current efficiencies for CO_2 formation, a measure of complete oxidation, of the electro-oxidation of ethylene glycol and its C_2 oxidation products on a Pt/C catalyst at potentials lower than 0.7 V and ambient temperatures were between 6 % for EG, about 14% for glycolaldehyde, glyoxal, and glycolic acid, and *ca.* 35 % for glyoxylic acid. The current efficiency for CO_2 formation of about 100 % was attained at potentials greater than 0.95 V for oxalic acid oxidation [19]. These results imply that high operational potentials are required for direct ethylene glycol fuel cells with Pt as an anode electrocatalyst to achieve the highest possible power density. It is desirable that commercialised direct ethylene glycol fuel cells generate high current at the lowest possible potential. The use of pure Pt as an anode electrocatalyst would not fulfil the stated requirement. Therefore, novel multifunctional Pt-based electrocatalysts for ethylene glycol electro-oxidation which lead to generation of high current at low potentials are needed.

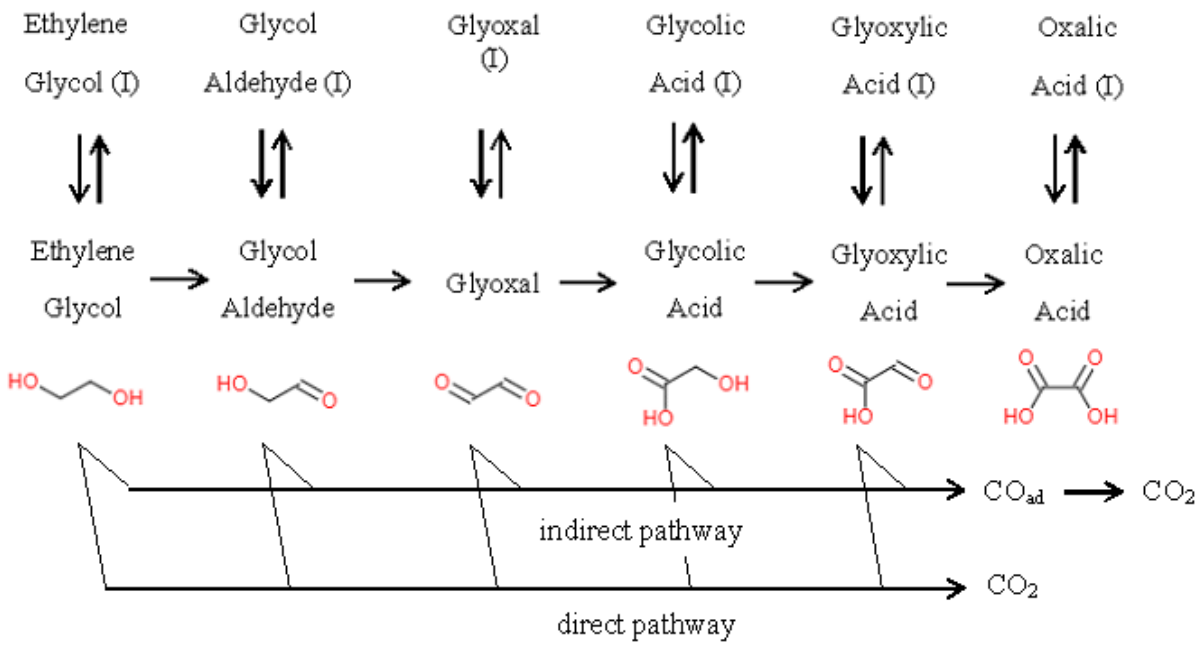


Figure 5.1 Schematic diagrams for the electro-oxidation reaction of ethylene glycol on the Pt catalysts in acidic media. (I) denotes the dissolved species.

Binary and ternary Pt-based electrocatalysts, such as PtSn, PtRu, PtSnX, and PtRuX where X is a precious or non-precious metal, could be used as anode electrocatalysts for DEGFCs as these materials have exhibited high activity for methanol and ethanol electro-oxidation. The activities for methanol electro-oxidation reaction (MOR) of carbon-supported Pt and Pt-based bi-metallic nanoparticle catalysts have been substantially studied by a half-cell and single direct methanol fuel cell test [16,21-23,28]. Among the investigated bi-metallic PtM catalysts, PtRu alloy offers the most promising catalytic activity for methanol electro-oxidation with strong tolerance to CO poisoning [24-27]. The performance of PtRu electrodes for methanol electro-oxidation can be improved by the addition of a third metal such as Ni, Mo, Sn, Fe, Co, and Rh [23]. The PtRuCo, PtRuNi, and PtRuFe electrodes show much improved activity for methanol electro-oxidation in acidic media compared to the binary PtRu catalyst [29,30]. Therefore, Ni, Co, and Fe can be considered potential third metals to

be added to binary Pt-based electrocatalysts for catalytic methanol electro-oxidation in acidic media.

Bi-metallic PtSn nanoparticle catalysts have also shown electrocatalytic activity for methanol oxidation in acidic media [31-38]. Their methanol electro-oxidation activities are dependent on the chemical states of Sn including oxidised tin (Sn (II) and Sn (IV)) and Sn (0) in PtSn alloys or Sn ad-atom. A. O. Neto et al. [31] examined the methanol electro-oxidation activity of the PtSn/C (50:50) and PtRu/C (50:50) electrocatalysts prepared by an alcohol-reduction process. The results from chronoamperometry measurement showed that PtSn/C exhibited higher activity than PtRu/C. Similar results were also found by A. N. Golikand et al. [39]. Thus, PtSn nanoparticle catalysts are an interesting alternative as anode electrocatalysts for DMFCs. Bi-metallic PtCo nanoparticle is another catalytic material for methanol electro-oxidation reaction in acidic media as its activity has been observed [14, 21, 40-43]. The ternary PtCo-based and PtSn-based catalysts for methanol electro-oxidation in acidic media such as PtCoPd/C [44], thin-filmed PtCoCr/C [45], PtSnRu/C [31], and PtSnCe/C [46] were studied. However, the catalytic methanol electro-oxidation activity of PtSnCo nanoparticle supported on carbon black has not been investigated.

The electro-oxidation of 2-propanol in acidic media has been studied on Pt and Pt-based catalysts. S-G. Sun and Y. Lin [18] conducted the measurements of activity for 2-propanol electro-oxidation of three Pt single crystal electrodes namely Pt(111), Pt(110), and Pt(100). The results showed that each Pt single crystal electrode had different activity. Furthermore, the Pt(110) and Pt(100) electrodes exhibited the highest and lowest activity for 2-propanol electro-oxidation, respectively. These obtained results indicate that 2-propanol electro-oxidation reaction is a surface structure sensitive reaction. A mechanistic study of 2-propanol electro-oxidation on the three single crystalline Pt electrodes was also carried out and it was concluded that the electro-oxidation of 2-propanol on the Pt single crystal electrodes did not

occur via the formation of adsorbed CO species. They also suggested that the dissociation of 2-propanol to adsorbed CO species could possibly not occur on other Pt(hkl) surfaces. The reaction mechanisms based-on the spectroscopic results for 2-propanol electro-oxidation on the Pt(111), Pt(110), and Pt(100) single crystal electrodes is summarised in figure 5.2. CO_2 was found to be a final product of 2-propanol electro-oxidation on all investigated electrodes. Additionally, acetone, which was produced from dehydrogenation, could be an oxidation product and a reaction intermediate.

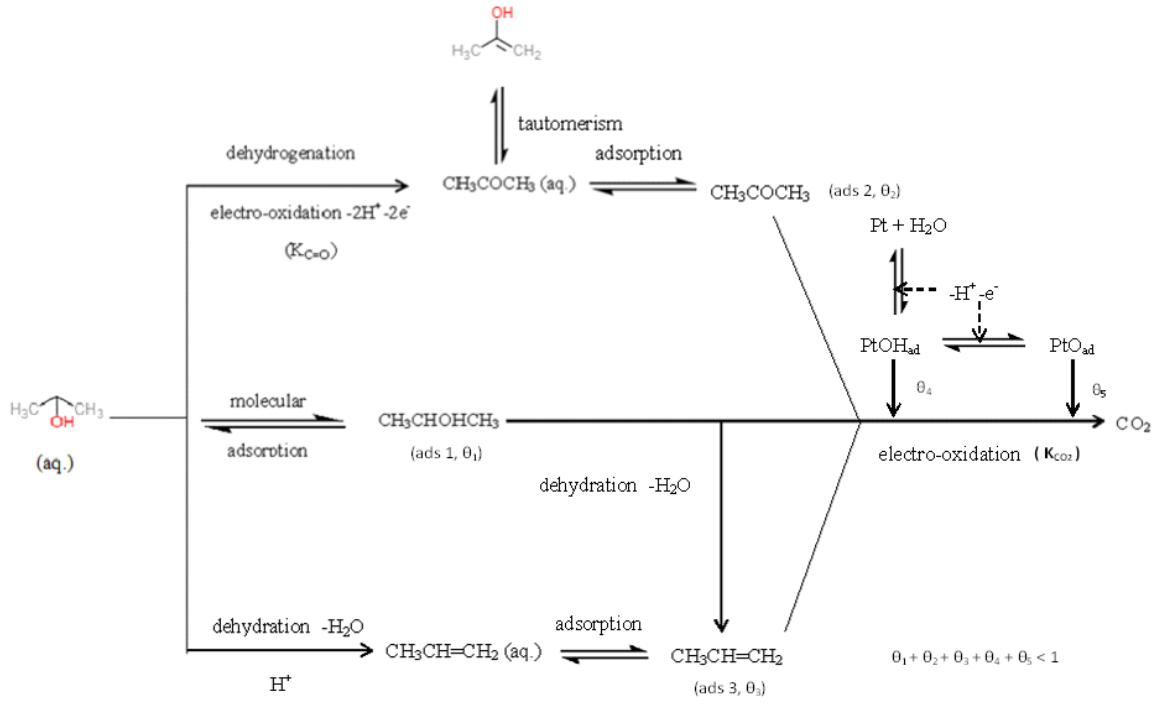


Figure 5.2 Proposed mechanism of 2-propanol electro-oxidation on the Pt single crystal electrodes

In this chapter, the electrocatalytic activities for ethylene glycol (EG), 2- propanol (2P) and methanol (MeOH) oxidation of the PtSn/C (3:1) and all PtSnCo/C catalysts are presented. The possible reaction mechanisms of the electro-oxidation of EG, 2P, and MeOH on the investigated catalysts are discussed.

5.2 Experiments

Cyclic voltammetry was employed to measure EG, 2P, and MeOH electro-oxidation activities of the PtSn/C (3:1) and all PtSnCo/C catalysts. For measurements of EG electro-oxidation activity, the studied electrodes prepared by coating the as-synthesised catalysts on a glassy carbon electrode were potential cycled in N_2-purged 0.5M H_2SO_4 supporting electrolyte solution between -0.2 V and 1.0 V (vs. SCE) for 20 scans. The electrochemically treated electrodes were then potential swept in N_2-purged 0.5M H_2SO_4 + 1M EtOH solution to test their EG electro-oxidation activities. The activities for EG electro-oxidation of the catalysts were specific activities obtained from normalisation of oxidation currents by the electrochemically active surface areas of the investigated catalysts. The activity tests for 2P and MeOH electro-oxidation on the PtSn/C (3:1) and all PtSnCo/C catalysts were conducted using the same procedure as for the EG electro-oxidation activity test, but 0.5M H_2SO_4 + 1M 2P and 0.5M H_2SO_4 + 1M MeOH solutions were used instead.

5.3 Results and Discussion

5.3.1 Ethylene glycol electro-oxidation activities of the PtSn/C (3:1) and all PtSnCo/C catalysts

The EG electro-oxidation activities of the PtSn/C (3:1) and all PtSnCo/C catalysts are shown in Figures 5.3 and 5.4.

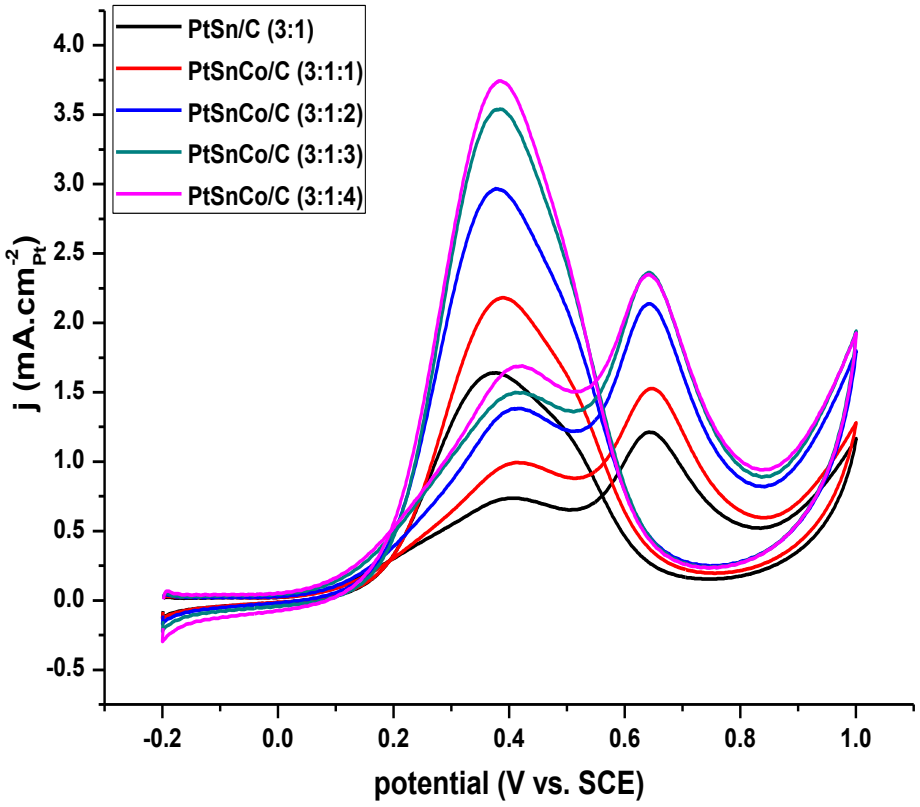


Figure 5.3 Cyclic voltammograms (cycle 1) recorded with the PtSn/C (3:1) and all PtSnCo/C electrodes in 0.5M H_2SO_4 + 1M EG electrolyte solution at a scan rate of 50 mV/s.

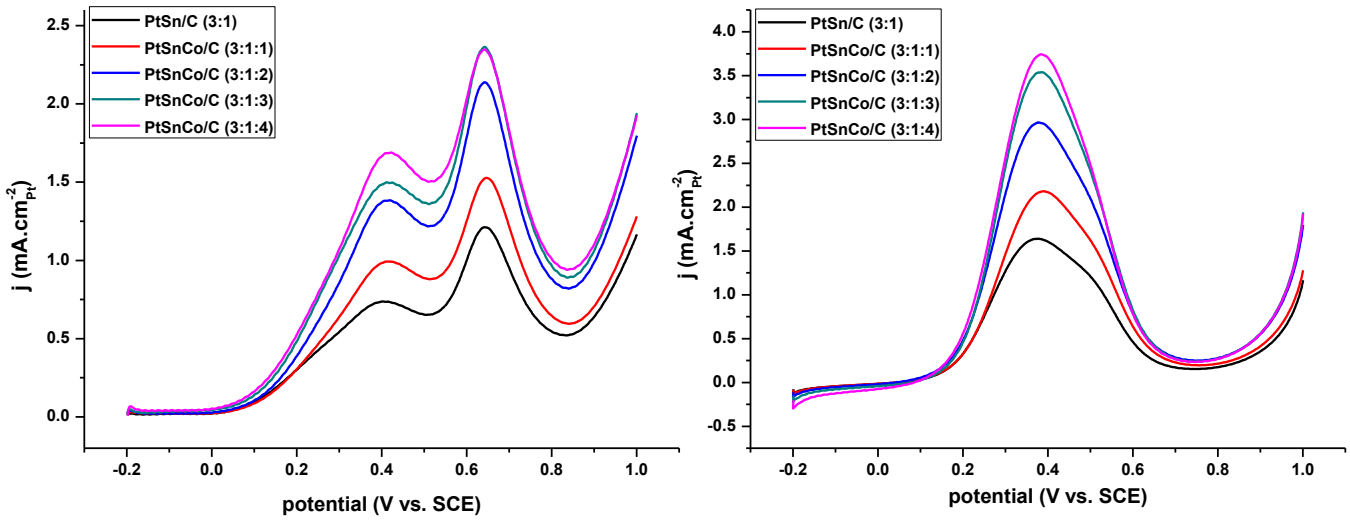


Figure 5.4 Forward scan (A) and reverse scan (B) voltammograms exhibiting the EG electro-oxidation activities of the PtSn/C (3:1) and all PtSnCo/C catalysts. CV conditions: 0.5M H_2SO_4 + 1M EG electrolyte solution and a scan rate of 50 mV/s.

The voltammetric profiles for ethylene glycol electro-oxidation on the stable surfaces of PtSn/C (3:1) and all PtSnCo/C electrocatalysts (Figures 5.3, 5.4) show two oxidation peaks centred at *ca.* 0.40 V and 0.65 V (vs. SCE) in the forward scans and one oxidation peak centred at *ca.* 0.40 V (vs. SCE) in the reverse scans. The EG electro-oxidation reaction on all ternary PtSnCo/C electrodes commenced at about 0.1 V (vs. SCE), indicating a similar rate of first electron transfer. This onset potential value was about 20 mV more positive than that for the EG electro-oxidation on PtSn/C (3:1). Table 5.1 presents the voltammetric data for EG electro-oxidation on all the investigated electrodes. The forward peak potential for EG electro-oxidation was independent to the compositions of the as-synthesised catalysts. The forward peak current density was in the following order: PtSn/C (3:1) < PtSnCo/C (3:1:1) < PtSnCo/C (3:1:2) < PtSnCo/C (3:1:3) ≈ PtSnCo/C (3:1:4). It can be observed that, for all studied electrodes, the peak current density for EG electro-oxidation in a higher potential

region was significantly higher than that for EG electro-oxidation in a lower potential range. Pt on the surfaces of the studied electrocatalysts started to be oxidised to form Pt-OH_{ad} species at the applied potential of *ca.* 0.6 V (vs. SCE). The increase in EG electro-oxidation activity in the higher potential region would originate from the oxidation of EG molecules and further oxidation of adsorbed species produced from dissociative adsorption of EG in the lower potential region by consuming adsorbed OH (OH_{ad}) species on both Pt and oxides of Sn and Co.

Table 5.1 Summary of the EG electro-oxidation activities of the PtSn/C (3:1) and all PtSnCo/C catalysts

electrocatalyst	onset potential (V vs. SCE)	E_f (V vs. SCE)	E_b (V vs. SCE)	j_f ($mA.cm^{-2}_{Pt}$)	j_b ($mA.cm^{-2}_{Pt}$)	j_f/j_b
PtSn/C (3:1)	0.079	0.64	0.38	1.21	1.64	0.74
PtSnCo/C (3:1:1)	0.095	0.65	0.39	1.52	2.18	0.70
PtSnCo/C (3:1:2)	0.087	0.64	0.38	2.14	2.96	0.72
PtSnCo/C (3:1:3)	0.100	0.64	0.38	2.37	3.54	0.67
PtSnCo/C (3:1:4)	0.092	0.64	0.38	2.35	3.74	0.63

Wang et al. [11] studied EG electro-oxidation on a Pt/C catalyst by differential electrochemical mass spectroscopy (DEMS). They concluded that, at low potentials, C_2 by-products (mainly glycolic and oxalic acids) were formed by catalytic EG electro-oxidation and EG molecules dissociated to CO_{ads} species. At high potentials, the formation of CO_2 was observed. A study to identify intermediates and reaction products of EG electro-oxidation on a Pt electrode was also conducted by Dailey et al. [47]. A Pt(111) single crystal electrode immersed in EG-containing 0.1M $HClO_4$ electrolyte solution was polarised at different

potentials for a designated time period and the obtained solutions were analysed. They concluded that glycolaldehyde, glycolic acid, and oxalic acid were detected at potentials between 0 and 0.6 V (vs. SCE). The mechanistic studies carried out by Wang et al. and Dailey et al. for EG electro-oxidation on the Pt catalysts in acid media can be adopted to propose the mechanism of EG electro-oxidation on the stable surfaces of the PtSn/C (3:1) and all PtSnCo/C catalysts. At the applied potentials from -0.2 V to 0.1 V (vs. SCE), EG molecules are adsorbed on the Pt surface sites without being oxidised. At about 0.1 V, for all PtSnCo/C and 0.08 V for PtSn/C (3:1), the adsorbed EG started to be oxidised via dehydrogenation. The electro-oxidation of EG at potentials lower than 0.65 V occurs in parallel through complete oxidation to CO_2 and partial oxidation to glycolaldehyde, glycolic acid, and oxalic acids. CO_{ads} and glycolic residues which are the intermediates for the formation of CO_2 and C_2 products, respectively, are removed by combining with OH_{ads} species formed on SnO_2 for PtSn/C (3:1) and SnO_2/CoO for all PtSnCo/C catalysts. The proposed mechanism for the complete oxidation pathway on the surfaces of the investigated catalysts can be described as follows.

At the potentials lower than 0.65 V on PtSn/C (3:1),

$$Pt + CH_2(OH)CH_2(OH) \rightarrow Pt - CH_2(OH)CH_2(OH) \qquad \text{Equation (5.4)}$$

$$2Pt - CH_2(OH)CH_2(OH) \rightarrow 2Pt - CO + 12H^+ + 12e^- \qquad \text{Equation (5.5)}$$

$$Pt - CO + SnO_2 - OH \rightarrow Pt + CO_2 + SnO_2 + H^+ + e^- \qquad \text{Equation (5.6)}$$

At the potentials lower than 0.65 V on all PtSnCo/C,

$$Pt + CH_2(OH)CH_2(OH) \rightarrow Pt - CH_2(OH)CH_2(OH) \qquad \text{Equation (5.7)}$$

$$2Pt - CH_2(OH)CH_2(OH) \rightarrow 2Pt - CO + 12H^+ + 12e^- \qquad \text{Equation (5.8)}$$

$$Pt - CO + SnO_2 - OH \rightarrow Pt + CO_2 + SnO_2 + H^+ + e^- \quad \text{Equation (5.9)}$$

$$Pt - CO + CoO - OH \rightarrow Pt + CO_2 + CoO + H^+ + e^- \quad \text{Equation (5.10)}$$

The current of EG electro-oxidation on PtSn/C (3:1) and all PtSnCo/C electrodes decreased after 0.65 V and began to increase at a potential of *ca.* 0.85 V. The oxidation current changes can be rationalised by a number of Pt active sites for the dissociative adsorption of EG. At potentials higher than 0.65 V, the majority of Pt sites could be occupied by oxygenated species mainly adsorbed OH which is formed as a result of water dissociation on Pt. Subsequently, the number of Pt surface sites for the dissociative adsorption of EG molecules is diminished. The oxidation of new EG molecules coming from the bulk solution is impeded, resulting in the decrease in oxidation current. At potentials greater than 0.85 V, Pt-OH_{ad} species could be further oxidised to Pt-O species. Some C_2 products in the bulk solution or near the electrode surface are catalytically oxidised by Pt-O species, resulting in the increase in oxidation current in this potential range. The ratio of the peak current density in the forward scan to the peak current density in the reverse scan (j_f/j_b) for EG electro-oxidation on each catalyst surface was found to be lower than 1. This result indicates that glycolic residues and other incompletely oxidised carbonaceous species formed in the forward scan accumulate largely on the catalyst surface. The highest j_f/j_b ratio for EG electro-oxidation, which indicates the best tolerance to surface poisoning species, was obtained using PtSn/C (3:1) as an electrocatalyst. The individual PtSnCo/C catalyst exhibited smaller degree of tolerance compared to PtSn/C (3:1). PtSnCo/C (3:1:1) and PtSnCo/C (3:1:2) had relatively similar tolerance to surface poisoning species and higher than that of PtSnCo/C (3:1:4). It can be concluded based on the tolerance to surface poisoning species that the presence of cobalt species both metallic cobalt which is alloyed with Pt and Sn for PtSnCo/C (3:1:1) and CoO on the surfaces of the as-prepared PtSnCo/C catalysts did not seem to lead to creation of stable surfaces with better tolerance to carbonaceous species produced by electro-oxidation of

EG than PtSn/C (3:1). However, the presence of cobalt species in the as-prepared catalysts could lead to formation of the surfaces with superior EG electro-oxidation activity at a potential of 0.5 V vs. SCE which is the practical potential for direct ethylene glycol fuel cell operation (Figure 5.5) [11].

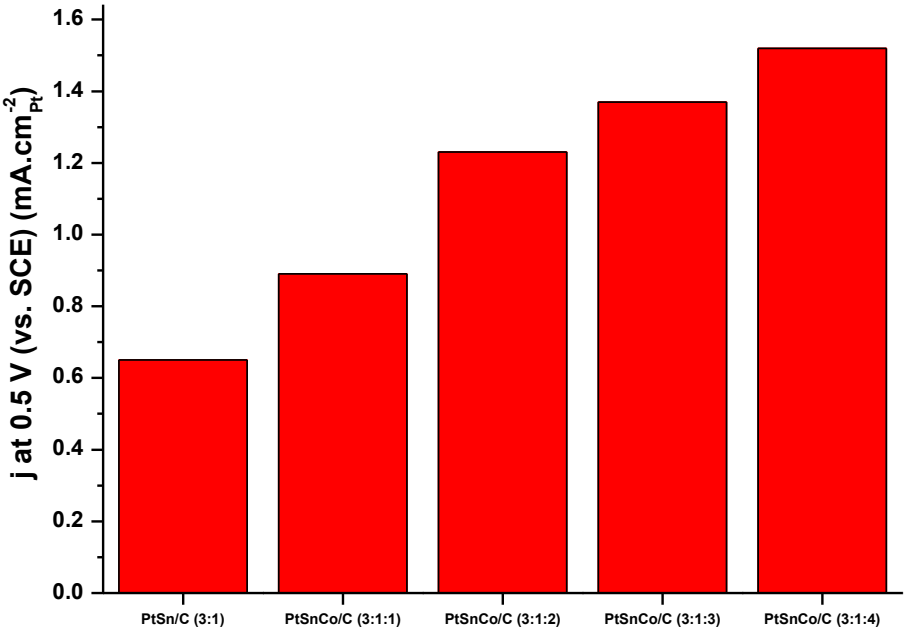


Figure 5.5 EG electro-oxidation activities of the PtSn/C (3:1) and all PtSnCo/C catalysts at 0.5 V (data were taken from the first cyclic voltammograms recorded in 0.5M H_2SO_4 + 1M EG solution after electrochemical treatment of each electrode in 0.5M H_2SO_4 for 20 cycles between -0.2 V and 1.0 V (vs. SCE))

The alcohol electro-oxidation activity of binary and ternary Pt-based catalysts is strongly dependent on spatial arrangements of surface Pt atoms (ensemble effect) and electronic structures of Pt clusters (electronic or ligand effect). Different arrangements and electronic structures can lead to formation of various types of reaction products, resulting in different catalytic activity.

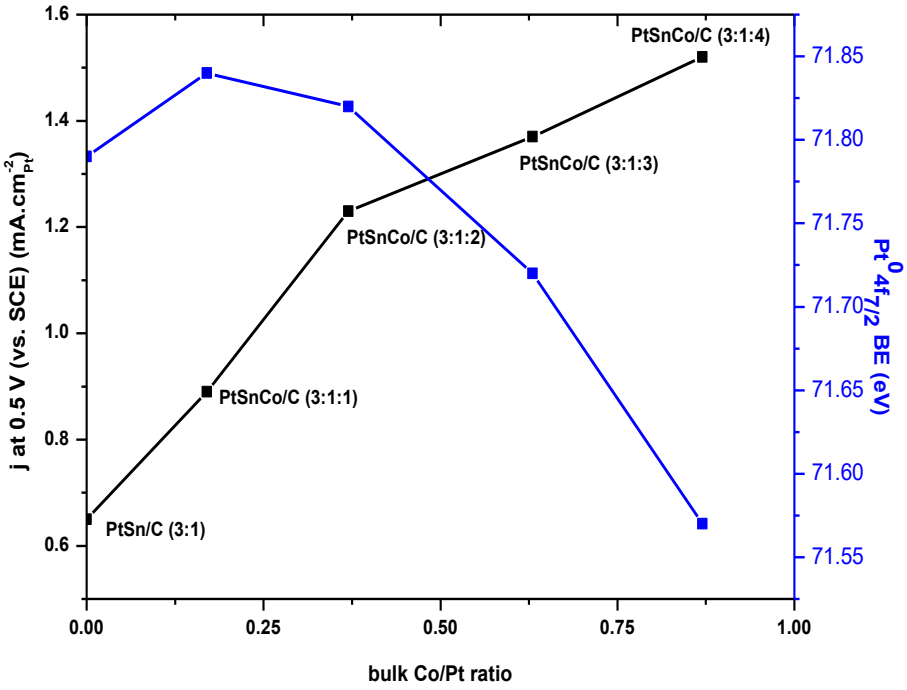


Figure 5.6 Plots of the Pt^0 $4f_{7/2}$ core-level binding energies and oxidation current densities at 0.5 V as a function of the bulk Co/Pt atomic ratio

Figure 5.6 shows a direct correlation between the bulk Co/Pt atomic ratio of the as-synthesised catalyst and the oxidation current density at 0.5 V. PtSnCo/C (3:1:4) with the bulk Co/Pt atomic ratio of 0.87 exhibited the highest EG electro-oxidation activity among the studied electrocatalysts. To determine whether the electronic effect is a main cause for an enhancement of EG electro-oxidation activity, the $4f_{7/2}$ core-level binding energies of Pt(0)

on the surfaces of the as-prepared catalysts were plotted against the bulk Co/Pt atomic ratios. This is based on the assumption that the binding energy of Pt 4f core-level electrons does not change significantly upon the electrochemical treatment applied to obtain the stable surfaces of the studied catalysts. It can be seen in Figure 5.6 that the Pt^0 $4f_{7/2}$ binding energy increased with an increase in the bulk Co/Pt atomic ratio to 0.17. The Pt^0 $4f_{7/2}$ binding energy decreased upon further increase in the bulk Co/Pt atomic ratio. The changes in the Pt^0 $4f_{7/2}$ binding energy suggest that the electronic structures of surface Pt atoms would possibly be modified by tin and cobalt oxides present on the catalyst surface. It is believed that changes in the d-band centre accompany the surface core-level shifts with similar variations and in the same direction [48]. A positive and a negative shift in Pt^0 $4f_{7/2}$ binding energy, therefore, correspond to an upshift and a downshift of the Pt d-band centre in relation to the Fermi level, respectively [49]. The Hammer-Nørskov model demonstrated that the d-band centre of a metal surface has a close correlation to the ability of the metal surface to form chemisorption bonds [50]. As the d-band centre shifts up, the chemisorption bonds become stronger. On the other hand, the chemisorption bonds become weaker as the d-band centre shifts down [49]. The investigated catalysts can be divided into two groups based on the Pt^0 $4f_{7/2}$ binding energy of PtSn/C (3:1). The first group consists of PtSnCo/C (3:1:1) and PtSnCo/C (3:1:2) and the second group consists of PtSnCo/C (3:1:3) and PtSnCo/C (3:1:4). The $4f_{7/2}$ binding energy of metallic Pt (Pt^0) of PtSn/C (3:1) was lower than that of the catalysts in group one, but greater than that of the catalysts in group two. Based on the Hammer-Nørskov model, the chemisorption strengths of EG and other intermediates such as CO_{ads} and glycolic residues to surface Pt of the PtSn/C (3:1), PtSnCo/C (3:1:1) and PtSnCo/C (3:1:2) catalysts would be greater than those of PtSnCo/C (3:1:3) and PtSnCo/C (3:1:4). Assuming the chemisorption strengths are sufficiently strong, surface Pt of PtSnCo/C (3:1:3) and PtSnCo/C (3:1:4) would be less vulnerable to poisoning species than that of the other three catalysts. Also, the d-band

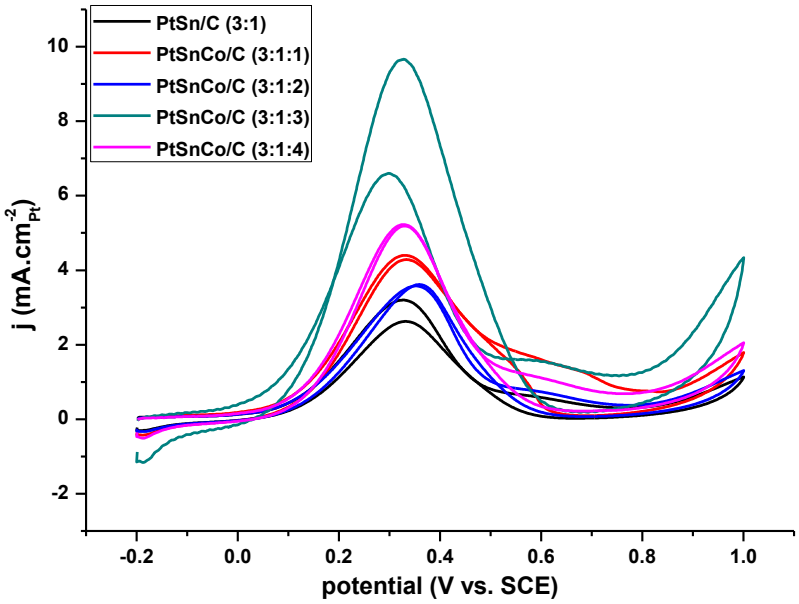
centre downshift in the PtSnCo/C (3:1:3) and PtSnCo/C (3:1:4) catalysts would weaken the chemisorption strength of the intermediates. This would cause the chemisorption bonds to break more easily, leading to improvement of the EG electro-oxidation activity. The higher EG electro-oxidation activity of PtSnCo/C (3:1:3) and PtSnCo/C (3:1:4) compared to that of the other three electrocatalysts may be originated from the electronic effects. The superior EG electro-oxidation activity of PtSnCo/C (3:1:1) and PtSnCo/C (3:1:2) in comparison to that of PtSn/C (3:1) is not in agreement with the tendency predicted by the model. This result can lead to conclude that the electronic effects may play a role but not significantly in determining the catalytic activity for EG electro-oxidation of the PtSnCo/C (3:1:1) and PtSnCo/C (3:1:2) electrocatalysts. The geometric or ensemble effects pertaining to surface arrangements of Pt atoms under the employed electrochemical conditions could outweigh the electronic effects and play a significant role in activity determination by providing more electrochemically active sites for EG electro-oxidation.

5.3.2 2-Propanol electro-oxidation activities of the PtSn/C (3:1) and all PtSnCo/C catalysts

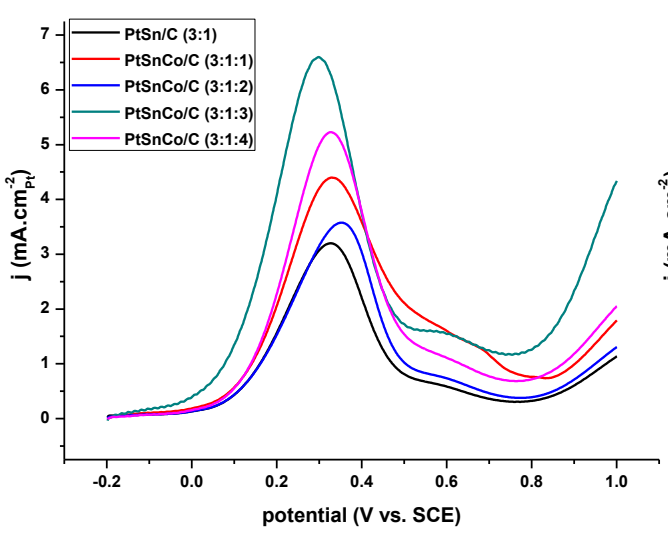
The catalytic activities for 2-propanol (2P) electro-oxidation of all the investigated PtSnCo/C and PtSn/C (3:1) catalysts measured by a CV technique are shown in Figure 5.7. The cyclic voltammogram for the 2-propanol electro-oxidation reaction (2POR) on the PtSn/C (3:1) electrode shows that there were two oxidation peaks centred at about 0.33 V (vs. SCE) in the forward and reverse scans. The same voltammetric features including the presence of two oxidation peaks with a similar peak potential were observed for the individual PtSnCo/C catalysts investigated. The forward oxidation peaks could be associated with the electro-oxidation of 2P molecules and intermediates produced by dissociative adsorption of 2P on the stable catalyst surfaces, while the oxidation peaks in the reverse scan could be due to the electro-oxidation of incompletely oxidised carbonaceous species adsorbed on the catalyst surfaces. The obtained cyclic voltammograms resembled those from the electro-oxidation of 2P on Pt single crystal electrodes [18], Pt, and Pt-based binary electrodes [6].

Table 5.2 Summary of 2P electro-oxidation activities of the PtSn/C (3:1) and PtSnCo/C catalysts

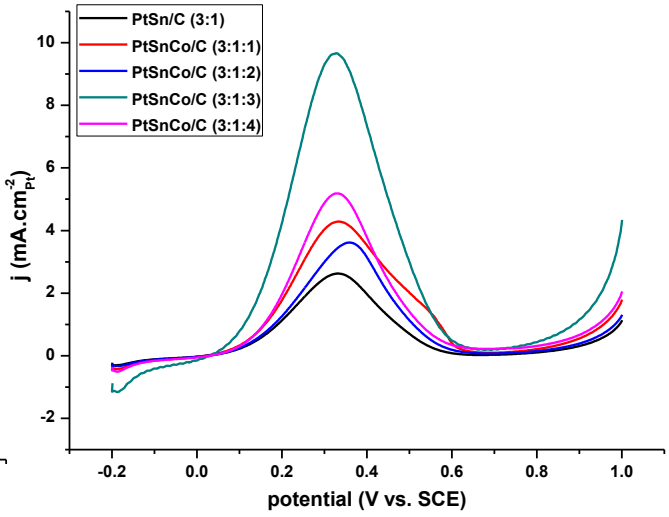
electrocatalyst	onset potential (V vs. SCE)	E_f (V vs. SCE)	E_b (V vs. SCE)	j_f ($mA.cm^{-2}_{Pt}$)	j_b ($mA.cm^{-2}_{Pt}$)	j_f/j_b
PtSn/C (3:1)	0.061	0.33	0.33	3.20	2.64	1.21
PtSnCo/C (3:1:1)	0.058	0.33	0.34	4.40	4.27	1.03
PtSnCo/C (3:1:2)	0.055	0.35	0.36	3.58	3.62	0.99
PtSnCo/C (3:1:3)	0.050	0.30	0.32	6.59	9.64	0.68
PtSnCo/C (3:1:4)	0.047	0.33	0.33	5.23	5.22	1.00



(A)



(B)



(C)

Figure 5.7 2P electro-oxidation activities of the PtSn/C (3:1) and all PtSnCo/C catalysts. (A) cycle 1, (B) forward scan, and (C) reverse scan cyclic voltammograms. CV conditions: 0.5M H_2SO_4 + 1M 2P electrolyte solution, a potential range from -0.2 to 1.0 V (vs. SCE), and a scan rate of 50 mV/s.

The onset potential of 2P electro-oxidation on the PtSn/C (3:1) electrode was higher than those of 2P electro-oxidation on the PtSnCo/C (3:1:1), PtSnCo/C (3:1:2), PtSnCo/C (3:1:3), and PtSnCo/C (3:1:4) electrodes. The negative shift of the onset potential for 2P electro-oxidation indicates faster rates of 2P dehydrogenation on the catalyst surface [6]. The lower onset potentials for 2P electro-oxidation on all PtSnCo/C may originally be due to the presence of Co and Sn species in the as-synthesised catalysts. The dissolution of CoO upon potential cycling the PtSnCo/C electrodes would create more active sites for dehydrogenation. The forward peak current densities (j_f) of 2P electro-oxidation on the stable surfaces of all the investigated PtSnCo/C catalysts was higher compared to that on the stable surface of PtSn/C (3:1). Similar to the electro-oxidation of EG, 2P electro-oxidation activity was strongly dependent on the chemical compositions of the as-prepared PtSnCo/C catalysts (see Figure 5.7). The stable surface obtained from potential cycling the as-synthesised PtSnCo/C (3:1:3) catalyst generated the highest current density. A j_f/j_b ratio, a measure of the tolerance to surface poisoning species of a catalyst, was *ca.* 1 or greater for all the investigated electrodes except PtSnCo/C (3:1:3). It is interesting to see that the most active surface for 2P electro-oxidation is the most vulnerable to surface poisoning species. This incident would be explained by the reaction pathways of 2P electro-oxidation on the stable surface of the PtSnCo/C (3:1:3) electrocatalyst. According to some previous reports about the electro-oxidation of 2-propanol on Pt and Pt-based electrocatalysts in acidic media [18, 51-54], it can be stated that the main electrochemical reaction is dehydrogenation, a conversion of 2-propanol to acetone, with the charge-transfer reaction of hydrogen. Besides, the electrochemical reaction involving further oxidation of intermediates formed by the dissociative adsorption of 2-propanol to CO_2 occurs in parallel to the main reactions. The intermediate is probably an acetone species or acetone itself [6]. Two parallel reaction

pathways of 2-propanol electro-oxidation on Pt and Pt-based electrocatalysts are shown in the diagram below.

$$Pathway\ 1: CH_3CHOHCH_3 \rightarrow CH_3COCH_3 + 2H^+ + 2e^-$$

$$Pathway\ 2: CH_3CHOHCH_3 \rightarrow (intermediate) + n_1H^+ + n_1e^- \xrightarrow{nH_2O} CO_2 + n_2H^+ + n_2e^-$$

Figure 5.8 Summary of 2-propanol electro-oxidation pathways on Pt and Pt-based electrocatalysts based on the findings of S.G. Sun et al., J. Otomo et al., and E.Pastor et al.

Pathway 1 shows the dehydrogenation of 2-propanol with the successive charge-transfer reaction of hydrogen and pathway 2 demonstrates the conversion of an intermediate to CO_2. The mechanistic studies of 2-propanol electro-oxidation on a smooth Pt electrode at low potentials (<0.4 V vs. RHE) [53-54] and high potentials [55] led to the conclusions that the major oxidation product for 2-propanol electro-oxidation at low potentials was acetone, while both pathways could occur at higher potentials than 0.4 V vs. RHE. Based on these findings, the oxidation peaks centred at *ca.*0.3 V (vs. SCE) which were observed in the forward potential scan for 2P-electro-oxidation on the stable surfaces of the PtSn/C (3:1) and all PtSnCo/C catalysts could be attributed to the oxidation of 2P molecules to acetone. The oxidation currents measured at potentials higher than 0.8 V (vs. SCE) could be associated with acetone formation (pathway 1) and complete oxidation to CO_2 (pathway 2). For the case of PtSnCo/C (3:1:3), the surface created after electrochemical treatment would suit the complete oxidation to CO_2 the most as suggested by a clear peak shoulder centred at *ca.*0.6 V (vs. SCE) and significantly high current density at potentials higher than 0.8 V (vs. SCE). The reaction pathway for complete oxidation could involve strongly bound intermediates which are difficult to be removed. As a result, the catalyst surface is heavily occupied by those intermediates. The large amount of adsorbed species being accumulated on the catalyst surface can yield high oxidation current upon a cathodic potential sweep. A considerably

higher peak current density value in the reverse scan compared to the peak current density value in the forward scan will lead to a small j_f/j_b ratio.The as-prepared PtSnCo/C (3:1:4) can be perceived as an alternative anode electrocatalyst for direct 2P fuel cells due to an exceptionally high peak current density and tolerance to surface poisoning species. The activity for 2-propanol electro-oxidation at 0.3 V (vs. SCE), a potential for practical operation of direct 2-propanol fuel cells, was taken into account for a selection of a potential catalyst suitable to be utilised as an anode electrocatalyst for direct 2-propanol fuel cells.

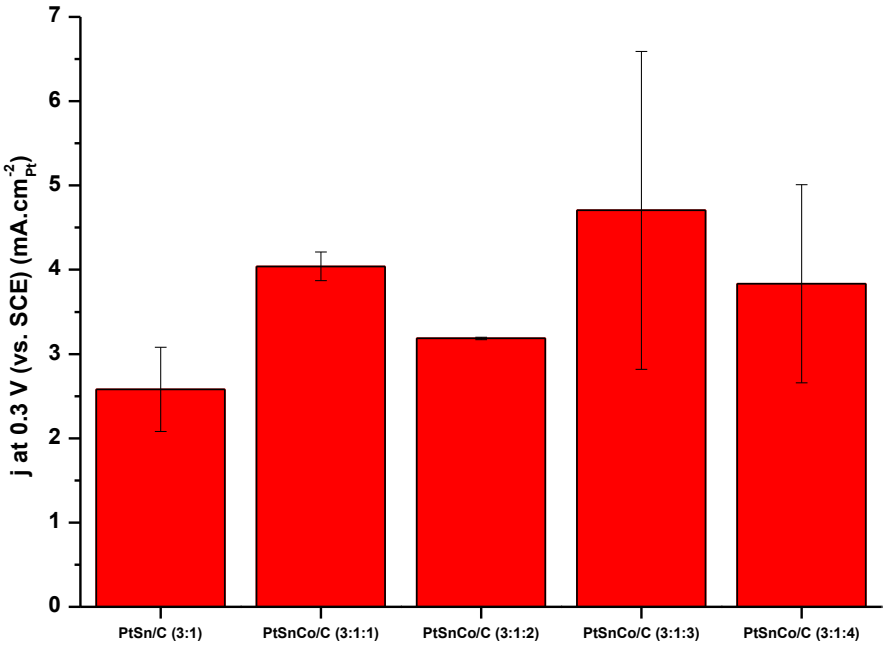


Figure 5.9 2-propanol electro-oxidation activities of the PtSn/C (3:1) and all PtSnCo/C catalysts at 0.3 V (vs. SCE)

It can be seen in figure 5.9 that all electrochemically treated PtSnCo/C electrocatalysts exhibited higher 2-propanol electro-oxidation activity than PtSn/C (3:1) at the applied potential of 0.3 V (vs. SCE). Among the PtSnCo/C electro-catalysts, the electrochemically treated PtSnCo/C (3:1:3) was the most active catalyst for 2P electro-oxidation due to its highest oxidation current density. Possible effects that would play a role in determining the activity for 2-propanol electro-oxidation of the studied catalysts at 0.3 V (vs. SCE) are discussed below.

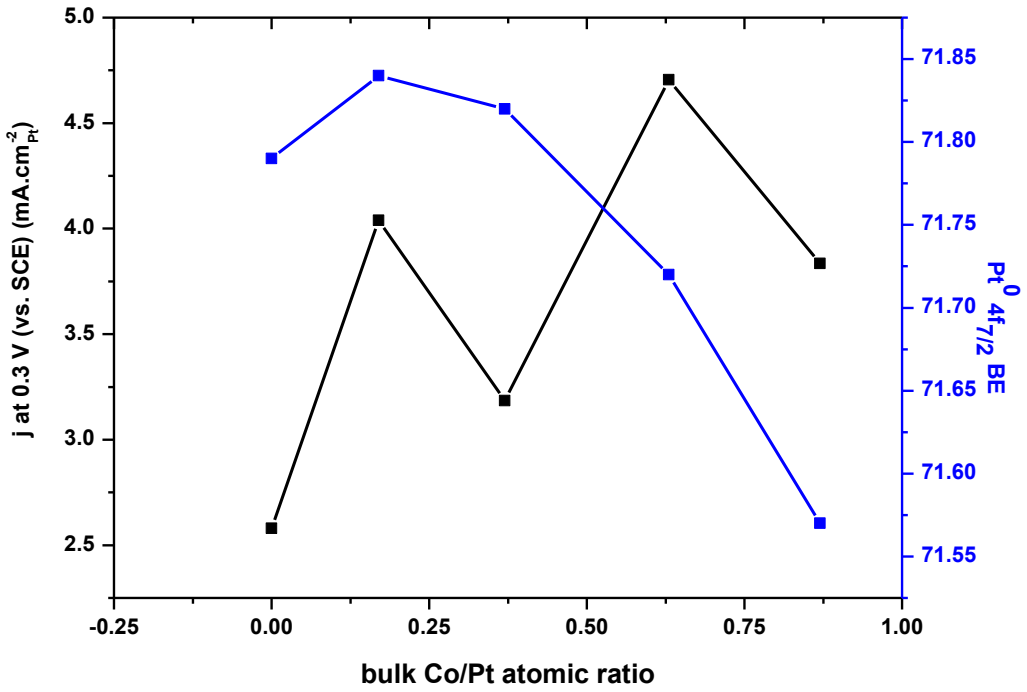
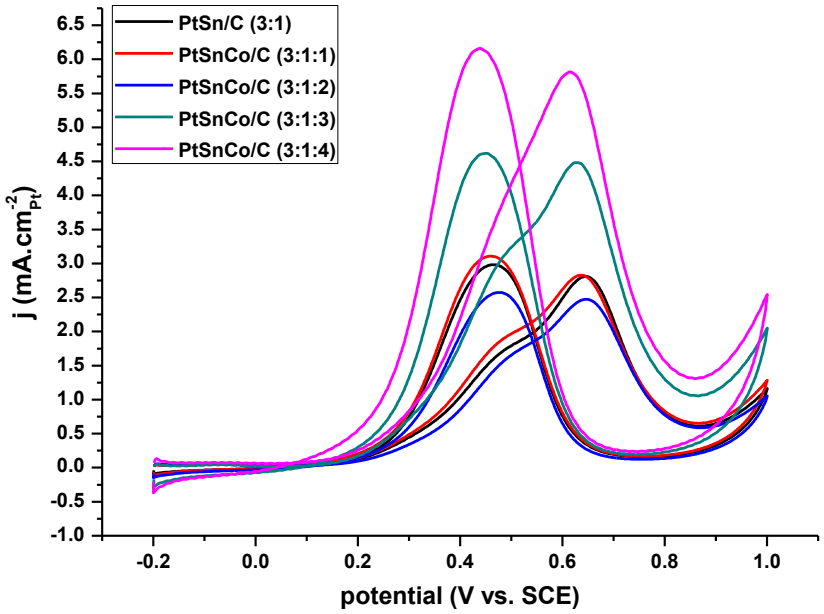


Figure 5.10 Plots of the Pt^0 4f7/2 core-level binding energies and oxidation current densities at 0.3 V as a function of the bulk Co/Pt atomic ratio

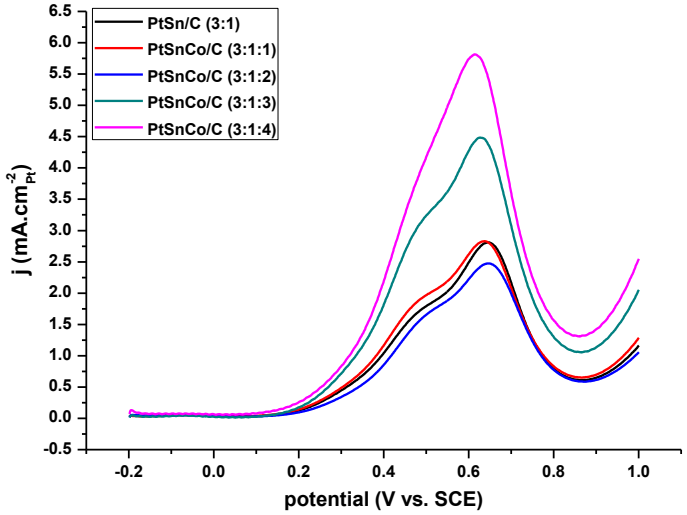
Figure 5.10 shows that there was no strong correlation between the trend of the core-level binding energy and that of the oxidation current density at 0.3 V. This indicates that changes of Pt electronic structures would not play a major role in activity enhancement observed for all the PtSnCo/C electrocatalysts compared to PtSn/C (3:1) [49]. The arrangements of surface Pt atoms upon potential cycling the investigated electrodes may form more electrochemically active sites for dissociative adsorption of 2-propanol. According to the literature, the oxidation current densities for 2P electro-oxidation on the stable surfaces of the investigated catalysts at 0.3 V could be attributed mainly to the oxidation of 2P to acetone. CoO species present on the stable surfaces of the PtSnCo/C catalysts would promote 2-propanol electro-oxidation activity via the hydrogen (H) spillover effect. The oxidation of 2-propanol to acetone occurs via dehydrogenation with successive charge-transfer reaction of hydrogen. The adsorbed hydrogen species on Pt migrates directly to adjacent CoO or it is passed along the surface OH groups formed on SnO_2 in a continuous exchange of covalent and hydrogen bonds between neighbouring OH groups to CoO, according to the bucket-brigade model. [56, 57].

5.3.3 Methanol electro-oxidation activities of the PtSn/C (3:1) and all PtSnCo/C catalysts

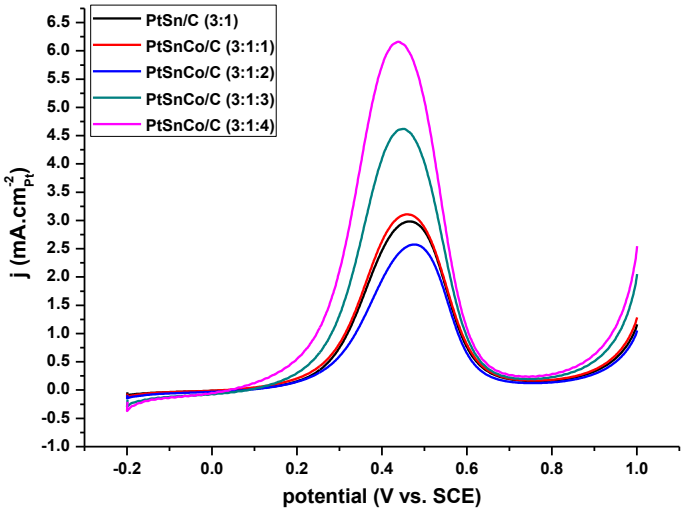
Figure 5.11 shows the methanol electro-oxidation activities of the PtSn/C (3:1) and all PtSnCo/C electrocatalysts measured by CV in 0.5M H_2SO_4 + 1M MeOH electrolyte solution.



(A)



(B)



(C)

Figure 5.11 Cyclic voltammograms (cycle 1) exhibiting the MeOH electro-oxidation activities of the PtSn/C (3:1) and all PtSnCo/C catalysts (A) forward scan voltammograms (B) reverse scan voltammograms (C). CV conditions: 0.5M H_2SO_4 + 1M MeOH solution and a scan rate of 50 mV/s.

Table 5.3 Summary of the MeOH electro-oxidation activities of the PtSn/C (3:1) and PtSnCo/C catalysts

electrocatalyst	onset potential (V vs. SCE)	E_f (V vs. SCE)	E_b (V vs. SCE)	j_f ($mA.cm^{-2}_{Pt}$)	j_b ($mA.cm^{-2}_{Pt}$)	j_f/j_b
PtSn/C (3:1)	0.197	0.64	0.47	2.81	2.99	0.94
PtSnCo/C (3:1:1)	0.189	0.64	0.46	2.83	3.11	0.91
PtSnCo/C (3:1:2)	0.194	0.64	0.47	2.48	2.56	0.97
PtSnCo/C (3:1:3)	0.194	0.63	0.45	4.48	4.61	0.97
PtSnCo/C (3:1:4)	0.191	0.61	0.44	5.81	6.16	0.94

The onset potential of methanol electro-oxidation on the stable surfaces of the investigated catalysts was similar. The forward peak current density (j_f) of methanol electro-oxidation on the stable surface of PtSn/C (3:1) was significantly lower than the j_f value of PtSnCo/C (3:1:3), and that of PtSnCo/C (3:1:4), but comparable to those of PtSnCo/C (3:1:1) and PtSnCo/C (3:1:2). The peak potential of methanol electro-oxidation on PtSn/C (3:1) was close to that of methanol electro-oxidation on all the PtSnCo/C catalysts. The anodic peak current density in the forward scan to anodic peak current density in the reverse scan (j_f/j_b) ratios for methanol electro-oxidation on the PtSn/C (3:1) and all PtSnCo/C electrodes are prsented in Table 5.3. The j_f/j_b ratio indicates the catalytic performance for methanol electro-oxidation in terms of CO tolerance of electrocatalysts and the degree of accumulation of

carbonaceous species on catalyst surfaces. A higher j_f/j_b ratio is an indication of better CO tolerance during the anodic scan and less accumulation of carbonaceous species on a catalyst surface [58]. The j_f/j_b ratios for methanol electro-oxidation on the stable surfaces of all the tested catalysts were about 1 and comparable, indicating similar tolerance to surface poisoning species of all the investigated catalysts. The j_f/j_b value close to 1 indicate an excellent capability of the catalysts in removal of adsorbed CO (CO_{ad}) and other carbonaceous species such as CHO_{ad} and $COOH_{ad}$ species formed during the anodic scan [16]. PtSnCo/C (3:1:4) catalyst is considered a suitable catalyst for methanol electro-oxidation. It is because PtSnCo/C (3:1:4) achieved the highest peak current density for methanol electro-oxidation and its j_f/j_b ratio is acceptable. In accordance with the CV measurements on the PtSn/C (3:1) and all PtSnCo/C electrodes in 0.5M H_2SO_4 supporting electrolyte solution, the stable surface of PtSn/C (3:1) consisted of Pt and SnO_2 species, while, the stable surfaces of all the investigated PtSnCo/C electrodes consisted of Pt, SnO_2, and CoO species. Due to the presence of SnO_2 and CoO on the stable catalyst surfaces with Pt, the methanol electro-oxidation reaction on the stable catalyst surfaces could occur via the bi-functional and the complete MOR mechanisms [59]. It is generally accepted in the complete MOR mechanism that the adsorbed CO species, which acts as a surface poison, is produced from the dehydrogenation of methanol molecules and dominates the MOR reaction. The three elementary steps of the complete methanol electro-oxidation reaction are shown below.

$$CH_3OH \xrightarrow{k_{ads}} CO_{ads} + 4H^+ + 4e^- \qquad \text{Equation (5.11)}$$

$$H_2O \rightleftharpoons OH_{ads} + H^+ + e^- \qquad \text{Equation (5.12)}$$

$$CO_{ads} + OH_{ads} \xrightarrow{k_{ox}} CO_2 + H^+ + e^- \qquad \text{Equation (5.13)}$$

The methanol electro-oxidation reaction as described by the bi-functional mechanism involves the dissociation of water on the surface of oxides of second and third metals (MO_x) and removal of adsorbed CO species ($-CO_{ads}$) formed on a Pt surface at low potentials.

$$Pt + CH_3OH \longrightarrow Pt - CH_3OH_{ads} \quad \text{Equation (5.14)}$$

$$Pt - CH_3OH_{ads} \longrightarrow Pt - CO_{ads} + 4H^+ + 4e^- \quad \text{Equation (5.15)}$$

$$MO_x + H_2O \longrightarrow MO_x - H_2O_{ads} \quad \text{Equation (5.16)}$$

$$MO_x - H_2O_{ads} \longrightarrow MO_x - OH_{ads} + H^+ + e^- \quad \text{Equation (5.17)}$$

$$Pt - CO_{ads} + MO_x - OH_{ads} \longrightarrow Pt + MO_x + CO_2 + H^+ + e^- \quad \text{Equation (5.18)}$$

M in the case of PtSn/C (3:1) is Sn, while it is Sn and Co in the case PtSnCo/C. The variations in the methanol electro-oxidation activities of the catalysts with different Co content can be rationalised by considering the electronic (ligand effect) and geometric (ensemble effect) effects. The electronic effect pertains to the electronic structures of Pt, while the geometric effect corresponds to a number of surface Pt atoms and their arrangements. The electronic structures of Pt can be modified by alloying Pt with other elements. Alloying Pt with less electronegative elements such as Sn and Co leads to charge transfer from Sn and Co to Pt which may cause the shift of a binding energy of Pt to lower values [60]. The absence of XPS peaks attributed to metallic Sn and Co would not rule out the existence of metallic Sn and Co in nanoparticles. It would be possible that Sn and/or Co atoms form ternary PtSnCo alloys, or binary Pt-based alloys which are at a depth greater than 10 Å from the surface of nanoparticles. Pt atoms on the catalyst surfaces can be considered electronically unaffected by Sn and Co atoms present at such depth. Due to the location of metallic Sn and Co, potential cycling the PtSn/C (3:1) and all PtSnCo/C electrodes between -0.2 and 1.0 V (vs. SCE) in 0.5M H_2SO_4 solution does not alter the proportion of the alloy

phases in all investigated catalysts. The dissolution of surface oxides during the potential cycling of the electrodes would not affect significantly the electronic structures of Pt present on the stable surfaces compared to those existing on the as-synthesised catalysts. Accordingly, the Pt^{o} $4f_{7/2}$ binding energy from the XPS measurements on the as-prepared electrocatalysts can be assumed to be the same for metallic Pt on the stable surfaces upon potential cycling. In other words, Pt electronic structures do not change significantly upon electrode potential cycling.

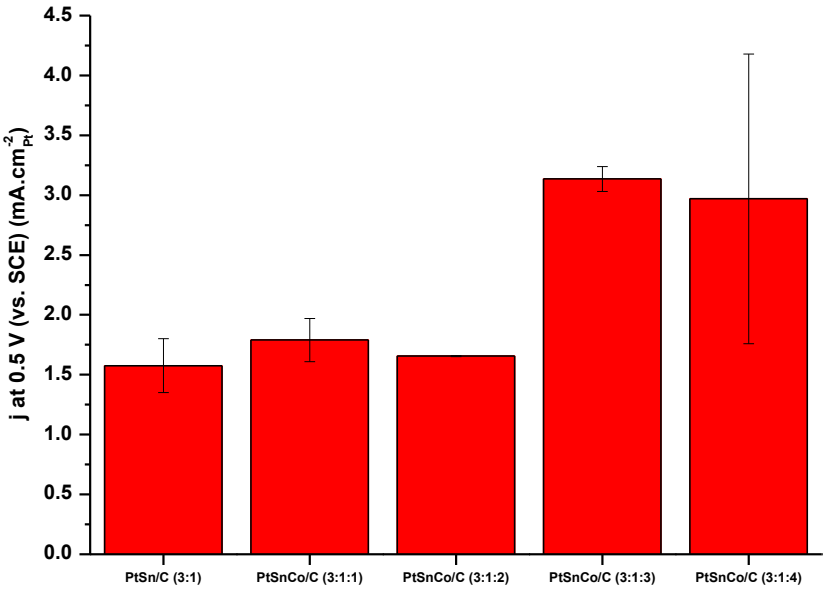


Figure 5.12 Methanol electro-oxidation activities of the PtSn/C (3:1) and all PtSnCo/C catalysts at 0.5 V (vs. SCE)

Figure 5.12 displays the oxidation current densities of methanol electro-oxidation on the stable surfaces of PtSn/C (3:1) and all the PtSnCo/C catalysts. PtSn/C (3:1), PtSnCo/C (3:1:1), and PtSnCo/C (3:1:2) exhibited comparable activity. PtSnCo/C (3:1:3) exhibited the highest methanol electro-oxidation activity. By considering the oxidation current density measured at 0.5 V and the j_f/j_b ratio, PtSnCo/C (3:1:3) with the stable surface is a promising candidate for an anode electrocatalyst for direct methanol fuel cells (DMFCs) operating at low temperatures.

Conclusions

-The stable surfaces obtained from potential cycling the investigated PtSn/C (3:1) and all PtSnCo/C electrodes between -0.2 V and 1.0 V (vs. SCE) exhibited different electro-oxidation activities for ethylene glycol, 2-propanol, and methanol in 0.5M H_2SO_4 medium.

-The chemical compositions of the as-synthesised catalysts had an effect on the structures of the stable surfaces and electro-oxidation activities for EG, 2P, and MeOH.

-The electrochemically treated PtSnCo/C (3:1:3) and PtSnCo/C (3:1:4) electrodes exhibited the highest peak current density for ethylene glycol electro-oxidation among all the investigated catalysts.

-At 0.5 V, the electrochemically treated PtSnCo/C (3:1:4) catalyst was a potential anode electrocatalyst for direct ethylene glycol fuel cell application.

-The highest peak current density for 2-propanol electro-oxidation was obtained from the electrochemically treated PtSnCo/C (3:1:3) catalyst.

-At 0.3 V, 2-propanol electro-oxidation on the stable surface of the PtSnCo/C (3:1:3) electrode yielded the highest oxidation current density.

-The electrochemically treated PtSnCo/C (3:1:4) had highest peak current density for methanol electro-oxidation.

-The electrochemically treated PtSnCo/C (3:1:3) and PtSnCo/C (3:1:4) catalysts were considered promising anode electrocatalysts for direct methanol fuel cell application due to superior methanol electro-oxidation activities at 0.5 V (vs. SCE) compared to the other three electrocatalysts.

References

1. Cui, X.; Cui, F.; He, Q.; Guo, L.; Ruan, M.; Shi, J., *Fuel* **2010,** *89* (2), 372-377.

2. Serov, A.; Kwak, C., *Applied Catalysis B: Environmental* **2010,** *97* (1–2), 1-12.

3. Ravikumar, M. K.; Shukla, A. K., *Journal of The Electrochemical Society* **1996,** *143* (8), 2601-2606.

4. Cao, D.; Bergens, S. H., *Journal of Power Sources* **2003,** *124* (1), 12-17.

5. Qi, Z.; Hollett, M.; Attia, A.; Kaufman, A., *Electrochemical and Solid-State Letters* **2002,** *5* (6), A129-A130.

6. Habibi, B.; Dadashpour, E., *Electrochimica Acta* **2013,** *88* (0), 157-164.

7. Xu, C.; Tian, Z.; Chen, Z.; Jiang, S. P., *Electrochemistry Communications* **2008,** *10* (2), 246-249.

8. Wang, J.; Wasmus, S.; Savinell, R. F., *Journal of The Electrochemical Society* **1995,** *142* (12), 4218-4224.

9. Markiewicz, M. E. P.; Bergens, S. H., *Journal of Power Sources* **2010,** *195* (21), 7196-7201.

10. Qi, Z.; Kaufman, A., *Journal of Power Sources* **2002,** *112* (1), 121-129.

11. Wang, H.; Jusys, Z.; Behm, R. J., *Journal of Electroanalytical Chemistry* **2006,** *595* (1), 23-36.

12. Orts, J. M.; Fernandez-Vega, A.; Feliu, J. M.; Aldaz, A.; Clavilier, J., *Journal of Electroanalytical Chemistry and Interfacial Electrochemistry* **1990,** *290* (1–2), 119-133.

13. Xu, Y.; Han, L., *International Journal of Hydrogen Energy* **2014,** *39* (14), 7278-7290.

14. Xu, C.; Hou, J.; Pang, X.; Li, X.; Zhu, M.; Tang, B., *International Journal of Hydrogen Energy* **2012,** *37* (14), 10489-10498.

15. Radmilovic, V.; Gasteiger, H. A.; Ross, P. N., *Journal of Catalysis* **1995,** *154* (1), 98-106.

16. Iwasita, T., *Electrochimica Acta* **2002,** *47* (22–23), 3663-3674.

17. Long, N. V.; Yang, Y.; Minh Thi, C.; Minh, N. V.; Cao, Y.; Nogami, M., *Nano Energy* **2013,** *2* (5), 636-676.

18. Sun, S.-G.; Lin, Y., *Electrochimica Acta* **1996,** *41* (5), 693-700.

19. Wang, H.; Jusys, Z.; Behm, R. J., *Electrochimica Acta* **2009,** *54* (26), 6484-6498.

20. Johnson, J. W.; Wroblowa, H.; Bockris, J. O. M., *Electrochimica Acta* **1964,** *9* (5), 639-651.

21. Ahmadi, R.; Amini, M. K.; Bennett, J. C., *Journal of Catalysis* **2012,** *292* (0), 81-89.

22. Jarvi, T. D.; Stuve Jr., E. M., Electrocatalysis. In *Frontiers of Electrochemistry*, Lipkowski, J.; Ross Jr., P. N., Eds. Wiley-VCH: New York, 1998; Vol. 4.

23. Zhao, Y.; Fan, L.; Ren, J.; Hong, B., *International Journal of Hydrogen Energy* **2014,** *39* (9), 4544-4557.

24. Basnayake, R.; Li, Z.; Katar, S.; Zhou, W.; Rivera, H.; Smotkin, E. S.; Casadonte, D. J.; Korzeniewski, C., *Langmuir* **2006,** *22* (25), 10446-10450.

25. Ahn, S. H.; Choi, I.; Kwon, O. J.; Kim, J. J., *Chemical Engineering Journal* **2012,** *181* (Supplement C), 276-280.

26. Li, B.; Higgins, D. C.; Zhu, S.; Li, H.; Wang, H.; Ma, J.; Chen, Z., *Catalysis Communications* **2012,** *18* (Supplement C), 51-54.

27. Salgado, J. R. C.; Alcaide, F.; Álvarez, G.; Calvillo, L.; Lázaro, M. J.; Pastor, E., *Journal of Power Sources* **2010,** *195* (13), 4022-4029.

28. Velázquez-Palenzuela, A.; Centellas, F.; Garrido, J. A.; Arias, C.; Rodríguez, R. M.; Brillas, E.; Cabot, P.-L., *Journal of Power Sources* **2011,** *196* (7), 3503-3512.

29. Huang, T.; Liu, J.; Li, R.; Cai, W.; Yu, A., *Electrochemistry Communications* **2009,** *11* (3), 643-646.

30. Jeon, M. K.; Lee, K. R.; Daimon, H.; Nakahara, A.; Woo, S. I., *Catalysis Today* **2008,** *132* (1–4), 123-126.

31. Neto, A. O.; Dias, R. R.; Tusi, M. M.; Linardi, M.; Spinacé, E. V., *Journal of Power Sources* **2007,** *166* (1), 87-91.

32. Liu, Z.; Guo, B.; Hong, L.; Lim, T. H., *Electrochemistry Communications* **2006,** *8* (1), 83-90.

33. Zheng, L.; Xiong, L.; Sun, J.; Li, J.; Yang, S.; Xia, J., *Catalysis Communications* **2008,** *9* (5), 624-629.

34. Wei, Z.; Guo, H.; Tang, Z., *Journal of Power Sources* **1996,***58* (2), 239-242.

35. Zheng, L.; Xiong, L.; Liu, Q.; Han, K.; Liu, W.; Li, Y.; Tao, K.; Niu, L.; Yang, S.; Xia, J., *Electrochimica Acta* **2011,** *56* (27), 9860-9867.

36. Herranz, T.; García, S.; Martínez-Huerta, M. V.; Peña, M. A.; Fierro, J. L. G.; Somodi, F.; Borbáth, I.; Majrik, K.; Tompos, A.; Rojas, S., *International Journal of Hydrogen Energy* **2012,** *37* (8), 7109-7118.

37. Antolini, E.; Gonzalez, E. R., *Electrochimica Acta* **2010,** *56* (1), 1-14.

38. Antolini, E.; Gonzalez, E. R., *Catalysis Today* **2011,** *160* (1), 28-38.

39. Golikand, A. N.; Golabi, S. M.; Maragheh, M. G.; Irannejad, L., *Journal of Power Sources* **2005,** *145* (2), 116-123.

40. Huang, H.; Fan, Y.; Wang, X., *Electrochimica Acta* **2012,** *80* (0), 118-125.

41. Lu, Y.; Reddy, R. G., *International Journal of Hydrogen Energy* **2008,** *33* (14), 3930-3937.

42. Mathe, N. R.; Scriba, M. R.; Coville, N. J., *International Journal of Hydrogen Energy* **2014,** *39* (33), 18871-18881.

43. Xu, C.; Su, Y.; Tan, L.; Liu, Z.; Zhang, J.; Chen, S.; Jiang, S. P., *Electrochimica Acta* **2009,** *54* (26), 6322-6326.

44. Wang, Y.-X.; Chen, T.-H., *Chinese Chemical Letters* **2014,** *25* (6), 907-911.

45. Jeon, M. K.; Cooper, J. S.; McGinn, P. J., *Journal of Power Sources* **2009,** *192* (2), 391-395.

46. Murthy, A.; Lee, E.; Manthiram, A., *Applied Catalysis B: Environmental* **2012,** *121–122* (0), 154-161.

47. Dailey, A.; Shin, J.; Korzeniewski, C., *Electrochimica Acta* **1998,** *44* (6–7), 1147-1152.

48. Wu, P.; Zhang, H.; Qian, Y.; Hu, Y.; Zhang, H.; Cai, C., *The Journal of Physical Chemistry C* **2013,** *117* (37), 19091-19100.

49. Zhao, Y.; Liu, J.; Zhao, Y.; Wang, F., *Physical Chemistry Chemical Physics* **2014,** *16* (36), 19298-19306.

50. Hammer, B.; Nørskov, J. K., *Advances in Catalysis* **2000,** *45*, 71-129.

51. Otomo, J.; Li, X.; Kobayashi, T.; Wen, C.-j.; Nagamoto, H.; Takahashi, H., *Journal of Electroanalytical Chemistry* **2004,** *573* (1), 99-109.

52. Sun, S.-G.; Lin, Y., *Electrochimica Acta* **1998,** *44* (6), 1153-1162.

53. Sun, S.-G.; Lin, Y., *Journal of Electroanalytical Chemistry* **1994,** *375* (1), 401-404.

54. Pastor, E.; González, S.; Arvia, A. J., *Journal of Electroanalytical Chemistry* **1995,** *395* (1), 233-242.

55. Rodrigues, I. d. A.; De Souza, J. P. I.; Pastor, E.; Nart, F. C., *Langmuir* **1997,** *13* (25), 6829-6835.

56. Nabaho, D.; Niemantsverdriet, J. W.; Claeys, M.; van Steen, E., *Catalysis Today* **2016,** *261* (Supplement C), 17-27.

57. Phaahlamohlaka, T. N.; Kumi, D. O.; Dlamini, M. W.; Forbes, R.; Jewell, L. L.; Billing, D. G.; Coville, N. J., *ACS Catalysis* **2017,** *7* (3), 1568-1578.

58. Viswanathan, B.; Neel, P. I.; Varadarajan, T. K., *Catalysis Surveys from Asia* **2009,***13* (3), 164-183.

59. Zhang, X.; Wang, H.; Key, J.; Linkov, V.; Ji, S.; Wang, X.; Lei, Z.; Wang, R., *Journal of The Electrochemical Society* **2012,** *159* (3), B270-B276.

60. Kim, J. H.; Choi, S. M.; Nam, S. H.; Seo, M. H.; Choi, S. H.; Kim, W. B., *Applied Catalysis B: Environmental* **2008,** *82* (1), 89-102.

Chapter 6

Conclusions

The binary PtSn/C and ternary PtSnCo/C catalysts with the nominal Pt:Sn and Pt:Sn:Co atomic ratios of 3:1, 3:1:1, 3:1:2, 3:1:3, and 3:1:4 were synthesised by the modified sodium borohydride reduction method. The Pt:Sn atomic ratio of the as-prepared PtSn/C (3:1) electrocatalyst and the Pt:Sn:Co atomic ratios of the as-prepared PtSnCo/C (3:1:1), PtSnCo/C (3:1:2), PtSnCo/C (3:1:3), PtSnCo/C (3:1:4) electrocatalysts determined by EDS and ICP-MS were in close agreement with the nominal ratios. The results from ICP-MS analysis showed that the total metal loadings of all the as-prepared catalysts were close to the nominal 20 wt.%. The mean crystallite size of the PtSn/C (3:1) and all PtSnCo/C nanoparticle catalysts from XRD was comparable. The as-synthesised carbon-supported nanoparticles of the binary PtSn/C (3:1) catalyst were heterostructured. The particles consisted of PtSn alloy core and Pt shell of a few layers with the co-existence of Pt, its oxides, and SnO_x species on the outermost surface of the particles. The carbon-supported heterostructured nanoparticles of the PtSnCo/C (3:1:1) catalyst comprised of ternary PtSnCo alloy and Pt shell with the presence of $Pt(O_x)/SnO_x/CoO$ species on the outermost surface of the catalyst particles. For the ternary PtSnCo/C (3:1:2), PtSnCo/C (3:1:3), and PtSnCo/C (3:1:4) electrocatalysts, the as-synthesised nanoparticles were composed of PtSn alloy core and Pt shell with $Pt(O_x)/SnO_x/CoO$ species on the outermost surface. The CV studies on the individual catalysts were conducted in 0.5M H_2SO_4 supporting electrolyte solution in the absence and presence of ethanol between -0.2 V and 1.0 V (vs. SCE). After potential cycling the electrodes for 15 scans in the acid solution, the steady-state cyclic voltammograms were obtained. The catalyst surfaces corresponding to the 20^{th} cyclic voltammograms were referred to as the stable surfaces. The specific oxidation current density obtained from the electro-

oxidation of ethanol, ethylene glycol, 2-propanol, and methanol on the stable surfaces of the investigated electrocatalysts was the electro-oxidation activities for ethanol, ethylene glycol, 2-propanol, and methanol of the electrocatalysts. The catalytic surfaces of the investigated electrodes formed during the potential sweep process were a result of surface SnO dissolution and partial dissolution of surface CoO with reconstruction of surface Pt atoms. The surface area of electrochemically active Pt of the stable surface of PtSn/C (3:1) was higher compared to that of the Co-containing electrode. The highest capacitive charging current was measured on PtSnCo/C (3:1:4), indicative of the greatest amount of oxides on the stable surface of the PtSnCo/C (3:1:4) electrocatalyst. The CO stripping voltammograms of the as-prepared catalysts demonstrated that the catalytic nanoparticles of PtSn/C (3:1) and all PtSnCo/C had synergistic properties between the surface components for removal of adsorbed CO species. The ethanol electro-oxidation activities of the binary PtSn/C (3:1) and all ternary PtSnCo/C electrocatalysts in terms of peak current density were considerably higher than that of Pt/C. Among all the PtSnCo/C electrocatalysts, PtSnCo/C (3:1:3) and PtSnCo/C (3:1:4) exhibited the highest peak current density for ethanol electro-oxidation and it was higher than that of the binary PtSn/C (3:1), signifying the merit of a three-component PtSn-based catalyst towards ethanol electro-oxidation in acidic media. The ethanol electro-oxidation activities of the electrochemically treated Pt/C, PtSn/C (3:1), PtSnCo/C (3:1:3), and PtSnCo/C (3:1:4) at 0.6 V (vs. SCE), a practical operational potential for direct ethanol fuel cells, were compared and it was found that the electrochemically treated PtSnCo/C (3:1:4) catalyst was the most active based on its highest current density. The higher ethanol electro-oxidation activities of PtSnCo/C (3:1:3) and PtSnCo/C (3:1:4) compared to that of PtSn/C (3:1) is primarily due to the unique electronic structures of surface Pt which would cause reaction intermediates to be removed more easily from the catalyst surfaces, leading to more available electrochemically active sites for ethanol electro-oxidation. The differences of the Pt electronic structures of

PtSnCo/C (3:1:4) and PtSnCo/C (3:1:3) from those of PtSn/C (3:1) could be due to CoO species present on the surface of both the as-prepared electrocatalysts. CoO in contact with Pt on the catalyst surface may alter the Pt electronic structures by electron transfer (electronic effect) or rearrangement of surface Pt atoms (geometric effect) due to its partial dissolution during the potential sweep process. Moreover, more adsorbed OH species on the catalytic surface of PtSnCo/C (3:1:4) necessary for the oxidation of intermediates, such as CO_{ad} and CH_3CO_{ad}, produced by the dissociative adsorption of ethanol could contribute to the higher ethanol electro-oxidation activity of PtSnCo/C (3:1:4). The results from the chronoamperometry measurements at 0.6 V (vs. SCE) of the catalytic surfaces of all the investigated electrodes demonstrated the highest stability towards ethanol electro-oxidation of PtSnCo/C (3:1:3). The electro-oxidation activities for ethylene glycol, 2-propanol, and methanol of the binary PtSn/C (3:1) and all ternary PtSnCo/C electrocatalysts were investigated. All examined electrodes had the electro-oxidation activity towards the three types of alcohol. The electrochemically treated PtSnCo/C (3:1:4) nanoparticle catalyst is a potential candidate for application as an anode electrocatalyst in a direct ethylene glycol fuel cell due to its highest activity at 0.5 V (vs. SCE). The PtSnCo/C (3:1:3) and PtSnCo/C (3:1:4) exhibited excellent activity for methanol electro-oxidation at 0.5 V (vs. SCE) and can be seen as promising anode catalysts for direct methanol fuel cell application. For application as an anode electrocatalyst in a direct 2-propanol fuel cell, the electrochemically treated PtSnCo/C (3:1:3) nanoparticle catalyst is a suitable choice due to its highest 2-propanol electro-oxidation activity at 0.3 V (vs. SCE).

Chapter 7

Experiments

Catalyst Preparation

Chemicals

1. Ethylene glycol (EG, anhydrous, 99.8%, Sigma-Aldrich)

2. Hexachloroplatinate hydrate ($H_2PtCl_6.xH_2O$, ~38% Pt basis, Aldrich)

3. Tin(II)chloride dihydrate ($SnCl_2.2H_2O$, puriss. p.a., ACS reagent, ISO, reag.Ph.Eur., ≥ 98%, Sigma-Aldrich)

4. Cobalt(II)chloride hexahydrate ($CoCl_2.6H_2O$, ACS reagent, 98%, Sigma-Aldrich)

5. Sodium hydroxide (NaOH, reagent grade, ≥98%, pellets (anhydrous), Sigma-Aldrich)

6. Sodium borohydride ($NaBH_4$, granular, 99.99% trace metals basis, Aldrich)

7. De-ionised water

8. Ethanol (puriss. p.a., absolute, ≥99.8% (GC) (Sigma-Aldrich)

9. Vulcan® XC-72R (Cabot Company Limited)

EG solution of Pt precursor

1 g of $H_2PtCl_6.xH_2O$ (~38% Pt basis) was dissolved in liquid ethylene glycol and the obtained solution was transferred to a 25-mL volumetric flask. The solution volume was made up to 25 mL using ethylene glycol. The concentration of Pt(IV) in the solution was *ca.*15.2 mg/mL.

EG solution of NaOH

0.1M NaOH solution was prepared by dissolving 1 g of NaOH pellets in liquid ethylene glycol. The mixture was heated at 60 ^oC to increase the solubility of NaOH. The obtained NaOH solution was cooled to room temperature and then transferred to a 250-mL volumetric flask. The final volume of 250 mL was made up with ethylene glycol.

Alkaline EG solution of $NaBH_4$

0.1M $NaBH_4$ solution was prepared by dissolving about 38 mg of solid $NaBH_4$ in 0.1M NaOH in EG solution. The obtained solution was transferred to a 10-mL volumetric flask and the final volume of 10 mL was adjusted with the same solvent.

Preparation of Pt/C

Pt/C catalyst with nominal Pt loading of 20 wt.% was synthesised by the following procedure. The Pt precursor solution of 965 µL was pipetted and added into a 50-mL three-neck round bottom flask. The total volume of 15 mL was adjusted with liquid ethylene glycol. The EG solution of Pt precursor was stirred in an oil bath at 25±1 ^{o}C for 20 minutes with N_2 flow. Then, 3 mL of 0.1M $NaBH_4$ solution was added into the Pt precursor solution dropwise while the solution was purged with N_2 gas. Following the reduction step, as purchased Vulcan®XC-72R carbon black was added to the colloidal solution. Liquid ethylene glycol was then added on top to adjust the solution volume to 30 mL. The pH of the mixture was adjusted to ~10 using the prepared 0.1M NaOH solution. The alkaline mixture was stirred at 25±1 ^{o}C for 5 hours with N_2 flow. After 5 hours, the mixture was filtered with a copious amount of DI-water and ethanol. Finally, the obtained Pt/C catalyst was dried at 80 ^{o}C for 12 hours under vacuum. Prior to characterisation and activity testing, the dried Pt/C catalyst was ground to fine powder and transferred to a vial.

Preparation of PtSn/C and PtSnCo/C catalysts

PtSn/C catalyst with the nominal Pt:Sn atomic ratio of 3:1 and total metal loading (Pt+Sn) of 20 wt.% was prepared by the same method and procedure used to synthesise the Pt/C catalyst. In this case, pre-determined amount of solid Sn precursor was added into the Pt precursor solution. For PtSnCo/C catalysts with different atomic ratios as shown in Table 1 and total metal loading (Pt+Sn+Co) of 20 wt.% were also prepared by the same method and procedure except all three metal salts were present in the precursors solution.

Table 7.1 A number of moles of Pt(IV), Sn(II), and Co(II) in EG solution for catalysts preparation

catalyst	mmole of Pt(IV)	mmole of Sn(II)	mmole of Co(II)	volume of 0.1M $NaBH_4$ solution (mL)
Pt/C	0.075	N/A	N/A	3
PtSn/C (3:1)	0.075	0.025	N/A	4
PtSnCo/C (3:1:1)	0.075	0.025	0.025	5
PtSnCo/C (3:1:2)	0.075	0.025	0.050	6
PtSnCo/C (3:1:3)	0.075	0.025	0.075	7
PtSnCo/C (3:1:4)	0.075	0.025	0.100	8
PtSnCo/C (3:1:5)	0.075	0.025	0.125	9

Powder X-ray Diffraction (PXRD)

Crystal structure of the as-prepared carbon supported Pt, PtSn, and all PtSnCo nanoparticle catalysts was investigated by powder X-ray diffraction technique using a PANalytical X-ray diffractometer with Cu K_α radiation. Prior to the measurement, fine powder sample was mounted on a glass slide with another glass slide until it became flat. The XRD machine was programmed to run from $2\theta = 20^{o}$ to 90^{o}.

X-ray Photoelectron Spectroscopy (XPS)

Surface compositions and chemical states of surface species of the as-prepared catalysts were studied by X-ray photoelectron spectroscopy technique. X-ray photoelectron spectra of the catalyst samples were collected using a VG Escalab II spectrometer with Aluminium Kα radiation (1486.6 eV) and a hemispherical analyser for detection of electrons. The Pass Energy was set at 50 eV for survey scan of the samples, and 20 eV for the high resolution scan of specific areas. The resulting spectra were analysed using CasaXPS peak fitting software. The background and sample charging were corrected using the Shirley method and the binding energy (BE) at 284.5 eV of C 1s peak [1] as a reference, respectively.

[1] Applied Catalysis B: Environmental 82 (2008) 89-102

Thermogravimetric Analysis (TGA)

The thermal stability and nanoparticles loadings of the catalysts were determined by thermogravimetric analysis using TGA 4000 PerkinElmer model. The catalyst samples were weighed and put into an alumina pan. The measurement was performed in air with the heating rate of 10 ^{o}C/min. The TGA conditions are shown below.

Start temperature 25 ^{o}C

-isothermal for 3 minutes

-heating rate 10 ^{o}C / min

-air flow rate = 25 mL/min

Final temperature 800 ^{o}C

-isothermal for 30 minutes

-cooling down to25^{o}C at the rate of 10 ^{o}C /min

-isothermal for 5 minutes at 25 ^{o}C

Transmission Electron Microscopy (TEM) and Energy Dispersive X-ray Spectroscopy (EDX)

Transmission electron microscope was employed to study the morphology of the as-prepared catalysts. TEM was performed using a Jeol 2010 microscope operating at 200 kV with LaB_6 crystal as the source of the electron beam. To determine the bulk compositions of the catalysts, EDX equipped with TE microscope was used. EDX analysis was performed using an Oxford Instruments LZ5 windowless EDX spectrometer.

Electrochemical Measurements

Working electrode preparation

Glassy Carbon Electrode (GCE) with diameter of 3 mm (geometric area = 0.071 cm^2) was used as a substrate to prepare a working electrode. Prior to the working electrode preparation, a glassy carbon electrode was polished with 0.05 µm alumina suspension on a polishing pad, followed by ultrasonication in DI-water. 5 µL of the catalyst ink, which was prepared by sonicating the mixture of 5.0 mg catalyst, 100 µL perfluorosulfonic acid PTFE copolymer (5% w/w, Alfa Aesar), 100 µL absolute ethanol, and 850 µL DI-water for 30 minutes at 30 ^oC, was dropped onto the polished glassy carbon substrate. Finally, the catalyst ink was dried at room temperature under vacuum for 30 minutes.

Electrochemical cell setting

Electrochemical measurements were carried out in a conventional three-electrode cell. Saturated Calomel Electrode (SCE, +0.241 V vs. SHE) and Pt wire were used as a reference and a counter electrode, respectively. All potentials were recorded with respect to the SCE. Prior to the measurements, 0.5M H_2SO_4 solution with or without the analytes was purged with N_2 gas for 20 minutes to remove the dissolved oxygen. All solutions were prepared with MilliQ Millipore water (18.2 MΩ.cm). Electrochemical experiments were performed using a Metrohm AUTOLAB potentiostat equipped with a PC. All electrochemical data were processed using NOVA 1.11 software.